A polarimetric study of the reflection nebulae NGC 2068 and NGC 2023 in the Orion R1 association

Mannion, Michael David

A polarimetric study of the reflection nebulae NGC 2068 and NGC 2023 in the Orion R1 association

Michael David Mannion

Department of Physics
University of Durham
Science Laboratories
South Road
Durham DH1 3LE

A thesis submitted to the University of Durham for the degree of Doctor of Philosophy

30 January 1987

A polarimetric study of the reflection nebulae NGC 2068 and NGC 2023 in the Orion R1 association

Michael David Mannion

ABSTRACT

Polarimetry studies of two reflection nebulae in the Orion R1 association are used to determine the nature of the dust in which recently formed stars are embedded in, and show the geometry of the surrounding dust cloud.

The data reductions presented are on NGC 2068 and NGC 2023, which are centres of recent low-mass star formation and are embedded on the nearside of L1630. In the case of NGC 2068, it appears that there is a single illuminating star which illuminates a foreground tilted slab of varying dust density from the rear. A simple tilted slab model assuming single Mie scattering from homogeneous spherical grains was used to fit visual data of traces of polarization, polarized intensity and total intensity through HD 38563N in a north-south direction. The model favoured metallic grains; the best fit being for iron grains and a slab 0.5 parsecs in front of HD 38563N tilted at an angle 55 degrees to the line-of-sight. In the case of NGC 2023, multicolour polarimetry is presented in B,V,R,I and Z. The star HD 37903 was found to be the sole illuminating star. A model to fit the spectral dependence of polarization gave low refractive index grains assuming a power law size distribution. Associated with NGC 2023 are Herbig-Haro objects HH-1, 4, which were found not to be polarized.

PREFACE

The work undertaken for this doctoral thesis was done while the author was a postgraduate member of the Astronomy Group in the Department of Physics at Durham University under the supervision of Dr. S.M. Scarrott between February 1983 and January 1987. During this time the author reduced and analysed electronographic polarimetry data on NGC 2068 in the V waveband, and electronographic (B,V,R) and CCD (R,I,Z) data on NGC 2023. Models were devised to fit a) the observations of visual polarization in NGC 2068 as a function of offset distance and b) the observed wavelength dependence of polarization in NGC 2023.

No part of this thesis has previously been submitted for a degree in this or any other university and all work is due to the author unless otherwise acknowledged.

Michael David Mannion

CONTENTS

CONTENTS

CONTENTS

CONTENTS

CONTENTS

TABLES

TABLES

LIST OF FIGURES

LIST OF FIGURES

LIST OF FIGURES

LIST OF PLATES

CHAPTER 1 Introduction

1.1 Observations

Astronomical data that are derived from the detection of quanta of electromagnetic radiation are intrinsically of four types due to the nature of the propagating photons. The information carried by photons is essentially: (1) spatial information - a function of their arrival direction F(x,y); (2) intensity information - a function of their rate of arrival F(t); (3) spectroscopic information - a function of the photon's energy F(ν); and (4) polarimetric information, which is uniquely defined by the four Stokes parameters F(I,Q,U,V). In this thesis the main observational data will be polarimetric observations of the reflection nebulae, NGC 2068 and NGC 2023.

Polarization studies of reflection nebulae give indications on the physical conditions and processes in the interstellar medium; for example: the nature of interstellar dust grains, grain sizes and size distribution, composition of dust and the spatial distribution of dust around the illuminating star. Moreover, in certain compact reflection nebulae, the interaction of recently formed stars with the surrounding interstellar dust from which the stars condensed may be studied. This can lead to an understanding of the initial conditions in the interstellar medium (ISM) in which star formation occurs in our Galaxy.

The scope of this thesis will not only include both polarization data in the visible bands B, V, and R and the near-infrared I and Z bands, but examine far-infrared, submillimetre and radio work done on reflection nebulae in the Orion R1 association. This is in order to fully understand the Orion region of medium-mass star formation using all the present-day data available.

Near-infrared (0.8 - 5 micron) observations enable one to see into the dark dust clouds and globules which are optically thick in the visible bands so that pre-main sequence stars may be studied, especially low-mass stars (1-2 Mo - Hyland 1981; Sellgren 1983). The medium-infrared (10 - 30 micron) waveband is useful in making spectroscopic observations of dust as many identifiable bands can be found, e.g. 10 micron silicate band. The far-infrared (40 - 450 micron) can map out the extent of molecular clouds due to the ultraviolet radiation from hot young OB stars being absorbed and reradiated by the dust in molecular clouds in this wavelength region. At longer wavelengths, submillimetre radio observations (100 - 1000 micron) of giant molecular clouds have provided information on gas cloud dynamics, and recently have indicated regions of molecular outflow in star formation regions (Bally and Lada 1983). Radio observations from 1 mm to 50 cm include observations of recombination lines from Stromgren spheres: here one can derive physical parameters of the ionized region such as electron density and excitation temperature. The neutral hydrogen content of clouds is mapped out using the 21-cm

emission line while ionized hydrogen in HII regions, which have mean temperatures of 8000 K, produce thermal bremsstrahlung radiation at radio wavelengths. Thus, the total extent of the interactions of the gas, dust and radiation fields in the ISM (in the molecular clouds where star formation is occurring) can be fully analysed.

1.2 Star Formation

Star formation is still continuing today as is evident from observations of: young stars - such as in OB and R associations; pre-main sequence stars - T Tauri; progenitors of OB associations like massive (1 E3 - 1 E6 solar mass) dense clouds e.g. giant molecular clouds, Orion A and B; and the possible by-products of stellar formation, Herbig-Haro objects. If one looks at other spiral galaxies besides our own, one sees the spiral structure delineated by bright blue supergiants that are ~ 1 E6 years old, bright HII regions that are excited by recently formed O and B stars, as well as many dark molecular clouds. Thus, it is apparent that recent star formation is concentrated in the spiral arms of spiral galaxies. However, in irregular galaxies like the Magellanic Clouds, star formation appears to be triggered randomly, so there are different mechanisms operating in the spiral arms of our Galaxy and other spirals compared with other parts of the Galaxy and other types of galaxies. What the different mechanisms are for triggering star formation in molecular clouds and which types of molecular clouds give rise to

which type of stars is still unknown.

Present-day research into star formation is directed towards understanding nearby star formation regions and the important questions to be answered are: 1) What is the initial mass function (IMF) of the stars first formed in interstellar clouds? 2) How do star formation regions then evolve and what is the range in ages of stars of different mass formed? 3) What are the processes involved in forming clusters of stars in molecular clouds?

This thesis will be concerned with observations of star formation in our Galaxy, in particular, with evidence of medium-mass star formation in the Orion complex. The observational evidence for star formation regions has been increased with the use of radio and infrared wavelengths. Besides the optical data of massive, young OB stars and the ionized HII regions, the radio and infrared data have shown what the astrophysical conditions are in the giant molecular clouds, and is now leading to an understanding of how stars form and evolve to the main sequence. The signposts to regions of recent and continuing star formation in molecular clouds are summarized below.

Giant Molecular Clouds (GMCs): These are the most massive structures in the Galaxy with masses in the range E5-6 Mo and linear dimensions up to 100 pc. They are concentrated in the spiral arms of the Galaxy. It is believed that 90% of stars in our Galaxy are formed in GMCs (Margulis and Lada 1984). The lifetime

of a giant molecular cloud is subject to conjecture; Blitz and Shu (1980) argue they have ages < 3 E7 years, while Solomon and Sanders (1980) put forward an age in excess of 2 E8 years. Both values are, however, much longer than the gravitational free-fall time of ~1 million years.

Bok globules: The globules described by Bok (1977) are small, dense, isolated dark nebulae, often round in shape, and which could be the birthplaces of single or multiple stars. They are between 3 - 30 arcminutes in diameter or 0.1 - 1 parsec and have masses in the range 20 - 800 Mo, but many appear to be gravitationally stable (Hyland 1981) so their evolutionary status is uncertain at present.

OB associations: They are groups of young massive stars (M > 10 Mo) which have spectral types in the range O - B3 and are usually closely associated with giant molecular clouds. Blitz (1980) has surveyed a number of molecular cloud complexes and found that the OB associations are generally located at the sides of the clouds. The total number of stars in these associations average several thousand and many associations contain smaller subgroups which have different ages, but the oldest subgroups are usually in the range 10 - 15 million years old (Blaauw 1964).

Compact HII regions: These are very small, dense HII regions with typical sizes ~0.5 parsec and electron densities > E4 /cm3. They are associated with high luminosity energy sources: L > E4

Lo. This amount of energy requires one or more O type stars, and from observations of the rapid expansion of these regions, this implies short lifetimes of ~E5 years, and so the smallest and densest compact HII regions are the youngest (Habing and Israel 1979). They are usually found in groups or close to OH maser sources, but they are always located near the edge of molecular clouds.

Herbig emission stars (Herbig 1960): Like T Tauri stars, these are believed to be pre-main sequence stars, but have masses > 3 Mo. They are A or B type stars located above and to the right of the Zero Age Main Sequence and presumed to have ages between E5 - E6 years. Their optical characteristics include: irregular variability, infrared excess and association with a dust cloud.

T Tauri stars: They are low mass (< 3 Mo) stars having late K type spectra with strong Balmer and sometimes H + K CaII emission lines. They are probably pre-main sequence stars (PMSS) approaching the main sequence and from their observed P Cygni profiles these stars are undergoing large mass loss E-7 - E-8 Mo/yr. The prototype T Tauri and most of the stars in this class are found to be irregular variables and show an ultraviolet and infrared excess. Their ages have been estimated to be between E5 - E7 years.

Herbig-Haro objects: These objects are small, isolated emission nebulae with typical sizes <~ 1 arcminute or 0.01 parsec.

They are characterised by a weak continuum and strong, low-excitation emission lines, and are found in heavily obscured dark cloud regions. As these objects appear to be associated with supersonic, bipolar outflows from T Tauri stars that are embedded in molecular clouds, the general consensus of opinion on their origin is that they are excited by interstellar shock waves originating from the associated T Tauri star (Schwartz 1983).

Reflection nebulae: The early B type stars that illuminate reflection nebulae, that have neither dispersed the dense cloud from which they were formed, nor have moved great distances from their birthplaces, will have ages less than or equal to E6 years.

Young clusters: Nascent star clusters with stars later than B3 cannot be detected through radio continuum measurements as no compact HII regions can be produced (the stars are not hot enough) and, due to the large dust extinction in the visible (Av > 10 m), can only be detected in the infrared. The first infrared survey to search for young star clusters was carried out by Grasdalen et al. (1973) at 2.2 micron in the Rho Ophiuchi dark cloud.

CO hot spots: These are regions of enhanced CO emission in molecular clouds that are due to radiation from newly formed stars, either heating the surrounding dust, which in turn is thermally coupled to the molecular gas, e.g. NGC 2068 (White et al. 1981), or through the production of a photoionized carbon II region like that observed in NGC 2023 (Knapp et al. 1975). The

temperature in these regions has been increased from an average 10 - 20 K up to 50 K.

Masers: Astronomical masers have been observed over the last 20 years. The main molecular species which are seen in maser emission are the water and hydroxyl molecule. Both water and hydroxyl masers have been found in star forming molecular clouds usually where gas densities are E5 - E11 cm-3 and their central energy source has been calculated to be E4 - E5 Lo. As they are very small (masers sources consist of groups of spots whose cluster size is < E17 cm with individual spots ~ E14 cm) they represent excellent probes of the dynamical and physical conditions around recently formed stars (probably OB stars - Reid and Moran 1981). From their large expansion velocities their ages have been estimated to be not more than E5 years.

Star formation regions usually have several of these signposts and their relation to one another will be discussed in chapter 3.

1.3 The Orion Complex

One region in our Galaxy where recent star formation has occurred is in the direction of Orion, towards the spur off the Orion-Cygnus local arm. This region is dominated masswise by two large molecular cloud complexes, Ori A and B (Kutner et al. 1977), and by the expanding shell of ionized gas known as Barnard's Loop. Newly formed stars make up the I Orion OB association and include

stars in Gould's Belt and The Trapezium in the Great Nebula of Orion. The I Orion association lies north-west from the dust cloud Lynds 1641 (Lynds 1962) and contains four subgroups that are aligned in a direction that is parallel with the Galactic plane. The four subgroups (I(a)-(d)) have been found to have ages that increase in sequence from I(d), estimated to be 12 E6 years, to I(a) nearest L1641, which is only 2 E5 years (Blaauw 1964). The total mass contained in these two giant molecular clouds has been calculated to be 6 E4 (Ori A) and 1 E5 (Ori B) solar masses. It would appear that star formation started some 12 million years ago in a large molecular cloud that has fragmented and dispersed to leave the I Ori association and the two molecular cloud complexes. From the ages and separation of the four subgroups of the I association, it can be seen that star formation has not occurred at one epoch at the centre of one large cloud, but has progressed along the edge of the cloud at 10-15 km/s (Kutner et al. 1977).

Two types of mechanism to explain the progression of OB star formation in the form of a sequence of subgroups have been put forward. Elmegreen and Lada (1977) suggest a local mechanism whereby a cluster of massive OB stars forming at the edge of a molecular cloud will produce an ionization-shock front that will expand into the dense cloud creating further star formation through compression of the gas. A second category of sequential star formation can be produced by the passage of a large-scale shock wave through a molecular cloud, e.g. a radiative shock wave due to a supernova, a Galactic density wave or many stellar winds.

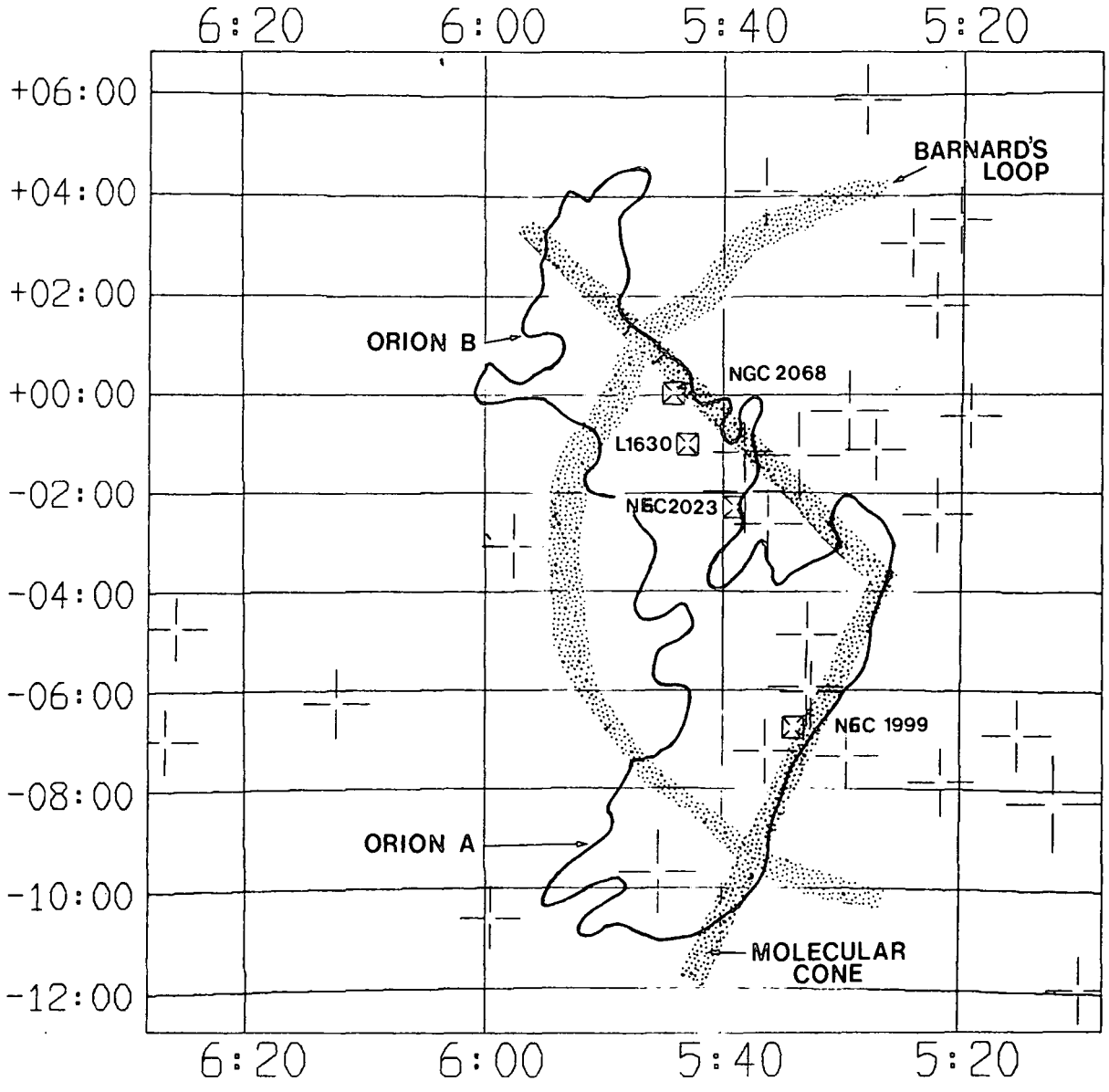

Fig. 1.1. The Orion molecular complexes.

Looking at a large-scale map of the Orion region (Fig. 1.1) one can see an apparent wedge-shape pattern of star formation (Thaddeus 1982) whose centre is concentric with the arc of Barnard's Loop. Cowie et al. (1979) have examined the gas dynamics around the newly formed stars of the Orion OB associations through ultraviolet absorption line observations. There appears to be an expanding shell of gas centred on the oldest OB subgroups and provides evidence along with the dynamical model of the region proposed by Cowie et al. (1979) that due to the combined effects of supernovae, stellar winds and ionization fronts from OB stars this outflow may have swept up the molecular gas in the two clouds and compressed it sufficiently to induce star formation. This explanation for coherent star formation in the two molecular clouds is an example of an external trigger.

The northern cloud complex, Ori B, includes the dark dust cloud L1630 (Fig. 1.2). This cloud has been investigated by Strom et al. (1975a). They showed that several stars associated with three reflection nebulae - NGC 2068, NGC 2071 and NGC 2023 in the dust cloud - have ages of order E5 years and that these reflection nebulae were sites of star formation. Star formation throughout the cloud has been occurring over several million years and manifestations of this include: Herbig-Haro objects, T Tauri stars (Herbig and Kuhi 1963), a type I OH maser (Johansson et al. 1974) and the detection of CO emission (see Fig. 1.3). Carbon monoxide

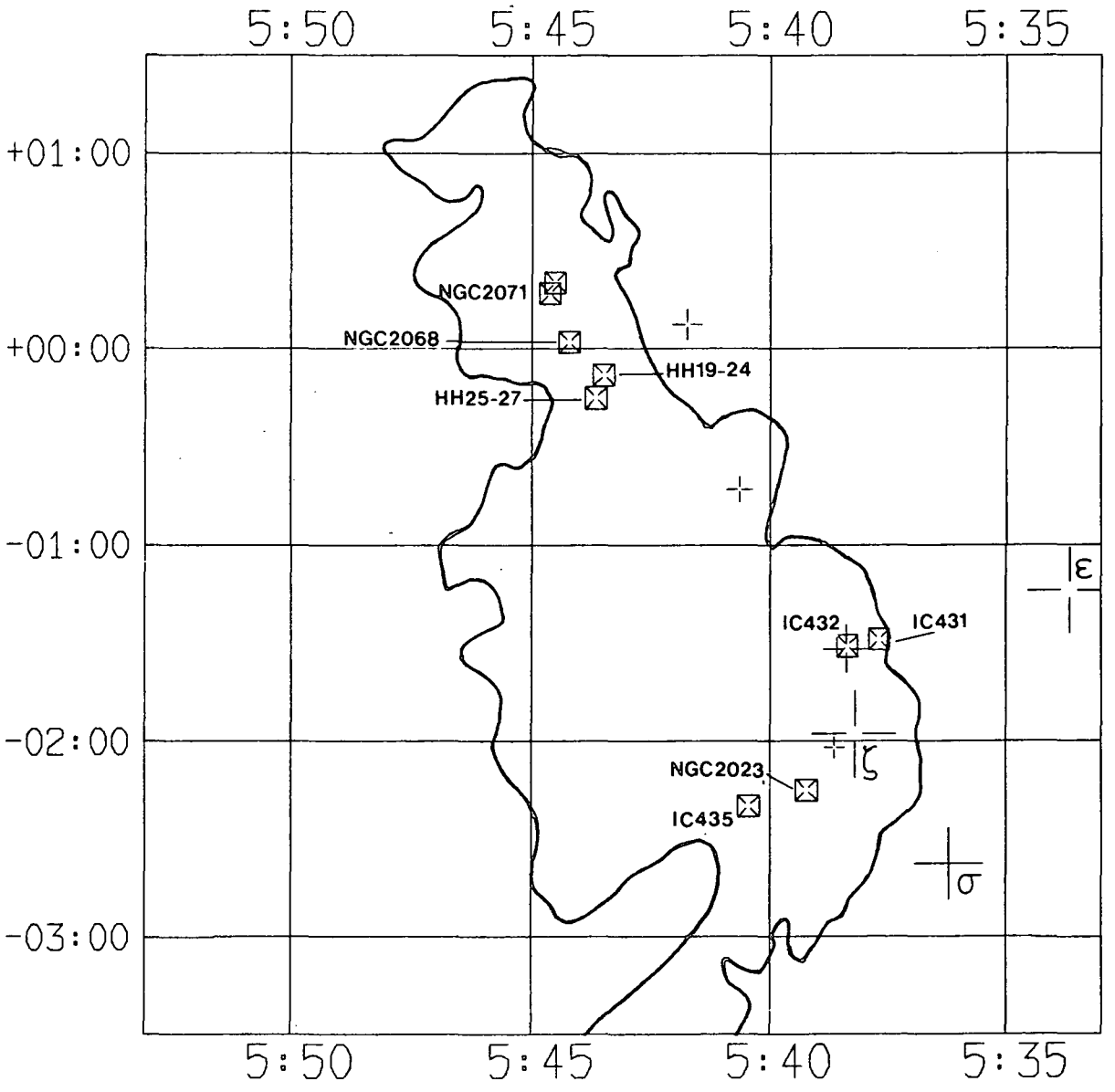

Fig. 1.2. The dark dust cloud - Lynds 1630.

M78 REGION FIG. 1.3.
CENTRE : 05 44 10 , +00 03.0 (1950.0)
EPOCH : 1950.0 EQUINOX : 1950.0

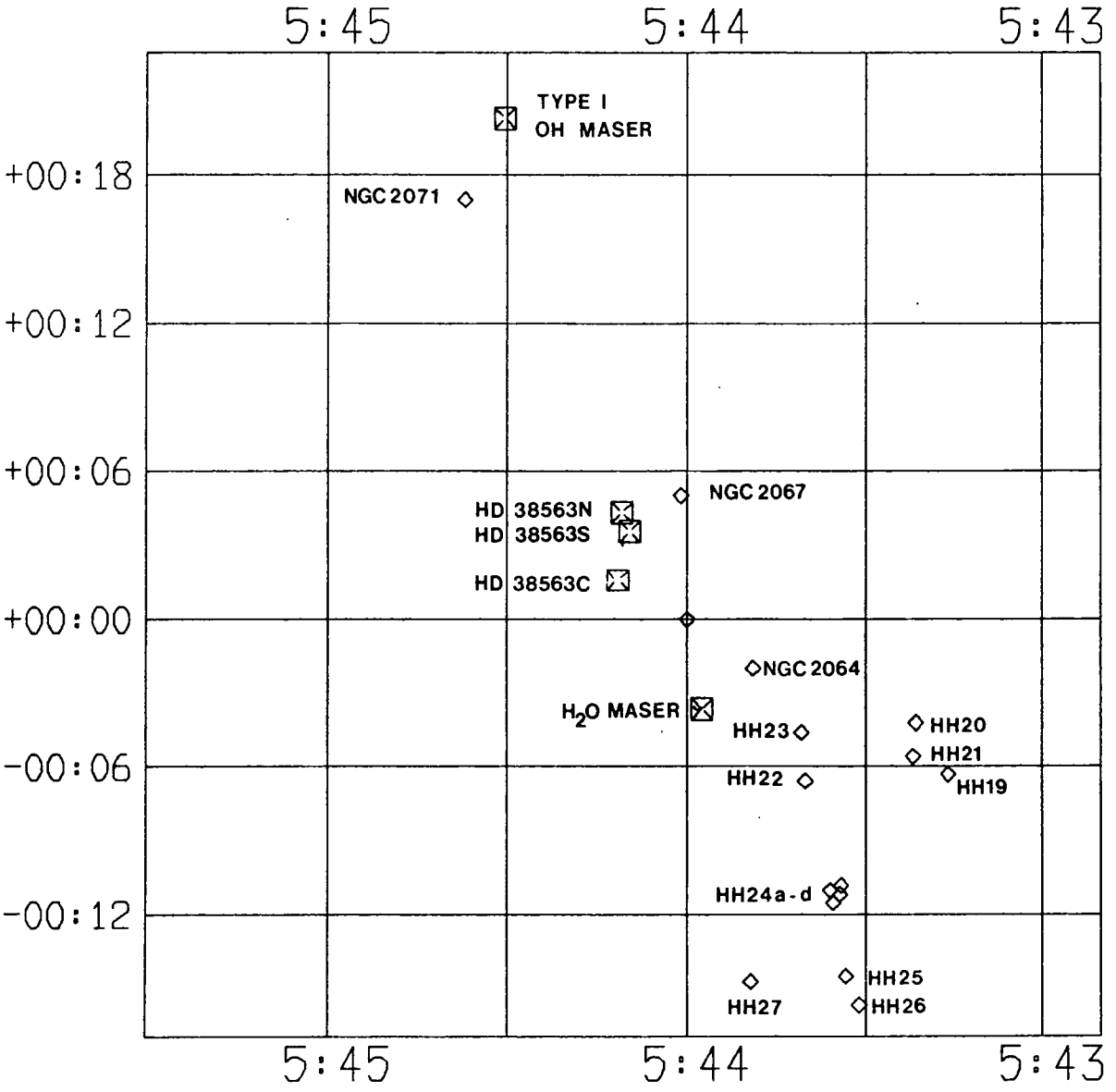

Fig. 1.3. Manifestations of star formation near the M78 complex.

emission observations by Milman et al. (1975) show the CO to be similarly distributed to the visible dust in L1630 with enhancements in the direction of the reflection nebulae, NGC 2023 and NGC 2068. Tucker et al. (1973) estimate the L1630 cloud to have a mass in the range 2.5 E4 - 1.0 E5 solar masses.

1.4 Reflection nebulae

The Sun is situated close to the Orion-Cygnus local arm. The inner edge of the local arm from l=75 deg. to l=220 deg. has been found to contain many groups of reflection nebulae or R associations (van den Bergh 1966; Racine 1968). Observations of 188 stars that illuminate reflection nebulae were made by Racine in order to determine their spatial distribution; he found that 70% of his sample could be grouped into 15 R associations and that these were similarly distributed to known OB associations as shown in Fig. 1.4. The nearest reflection nebulae are only 350 pc distant in the direction of Perseus (Racine 1968) along Gould's belt. The Ori R1 association, to which NGC 2068 and NGC 2023 belong, is at a distance of ~500 pc (Lee 1968) and is therefore a comparatively nearby region of star formation. Table 1.1 lists the members of the Orion R1 association (data from Coyne et al. 1974; Harvey and Thronson 1980; Knapp et al. 1977; Strom et al. 1975a; and Voshchinnikov and Marchenko 1982).

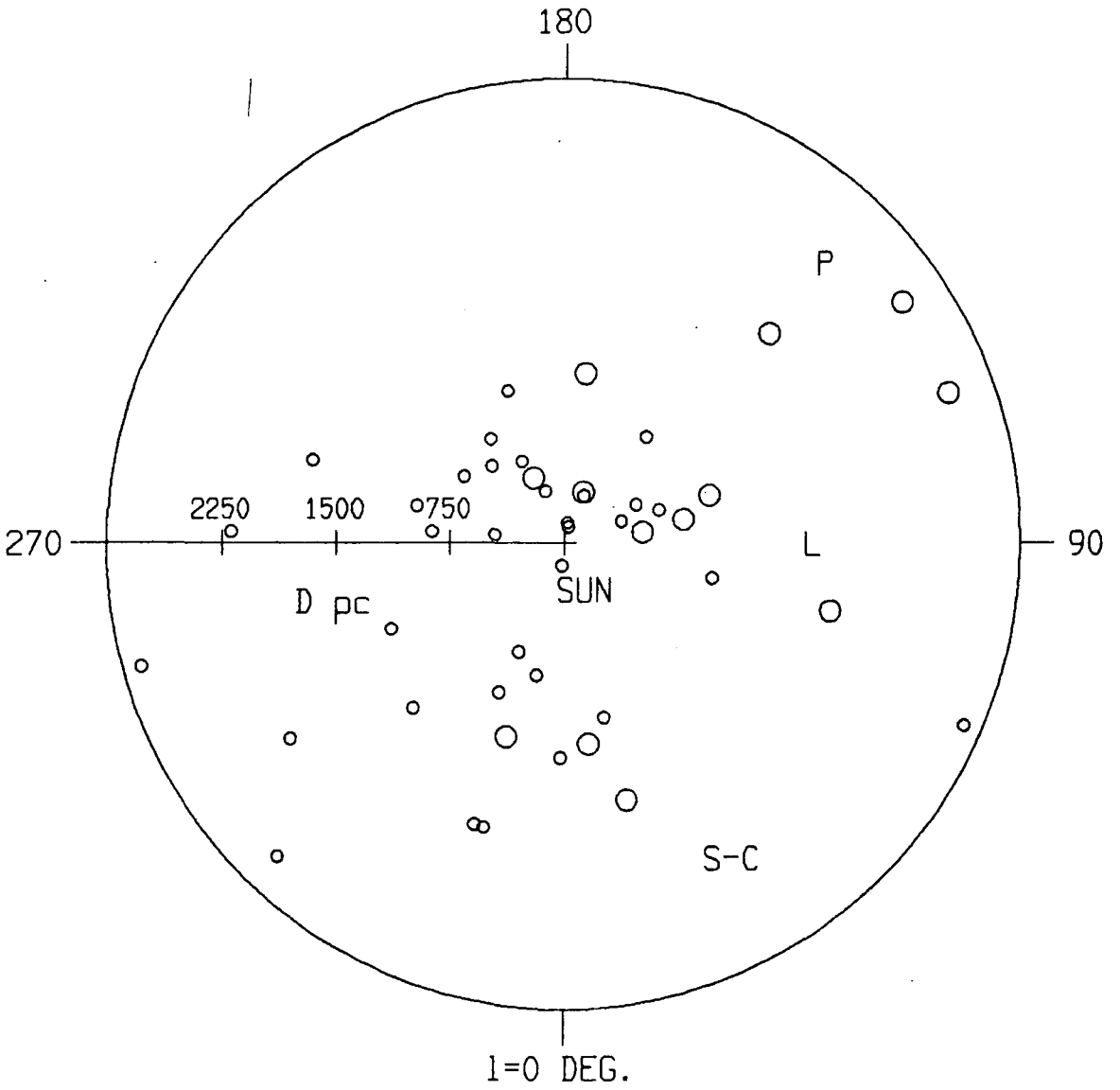

ADAPTED FROM RACINE (1968), ALLEN (1973), HERBST (1975), HUMPHREYS (1978).

KEY: R ASSOCIATIONS ○ SPIRAL ARMS: PERSEUS - P

OB ASSOCIATIONS ○ LOCAL - L

SAGITTARIUS-CARINA - S-C

Fig. 1.4. Galactic distribution of R and OB associations.

Table 1.1. The Orion R1 association.

NAME	ILLUMINATING STAR	COORDINATES R.A. (1950)			DEC (1950)			V MAG	Sp. CLASS
NGC 2068	HD 38563N	5	44	10.8	0	4	19.2	10.56	B1-B2
NGC 2023	HD 37903	5	39	7.3	-2	16	58.3	8.5	B1.5V-B3
IC 431	HD 37674	5	37	41.5	-1	29	17.4	8.3	B8
IC 432	HD 37776	5	38	24.3	-1	31	54.9	8.4	B2V-B5
IC 435	HD 38087	5	40	29.5	-2	20	5.1	8.5	B8
NGC 1999	-6 1253	5	34	5.0	-6	45	0	10.2(v)	pec.

Reflection nebulae are small (<1pc), dense regions of the interstellar medium which are illuminated by intrinsically luminous stars mostly of spectral type later than B2 and are seen by reflected light. Illuminating stars of earlier type are hot enough to produce ionization of the interstellar medium and give rise to Stromgren spheres (Lang 1978 page 245). The reflected light can be modelled by Mie scattering (Mie 1908) off spherical interstellar dust grains whose size is comparable to the wavelength of light (i.e. ~0.5 micron). The spectra of the light from reflection nebulae are therefore true copies of the spectra of the illuminating stars as was first shown by Slipher (1912) in his observations of the Pleiades. Martin (1978) describes three types of reflection nebulae:

(1). Interstellar type in which the illuminating star and the interstellar medium are not closely related, an example being the Pleiades (Arny 1977); these nebulae are described as being illumination bounded and their size is given by the Hubble

relation (Hubble 1922):

$$m + 5 \log a = K$$

where m = magnitude of the illuminating star

a = radius of nebula in arcminutes

K ~ 11.0.

(2). Compact reflection nebulae; a group which contains many early main sequence stars that are illuminating the clouds of dust and gas from which they formed. These nebulae are found to be density bounded. Most of these nebulae are amorphous in appearance but there are some which are biconical (called bipolar) or consist of a single star at the apex of a single cone (called cometary).

(3). High Galactic latitude nebulosity: that is due to clouds of gas and dust, at distances around 100 pc above the Galactic plane, being illuminated by the integrated light of the Galaxy.

Observations of compact reflection nebulae not only provide traces of Galactic spiral arm structure, but are intrinsically useful in determining the composition, density and spatial distribution of dust surrounding newly formed stars. Two examples of this class are NGC 2023 and NGC 2068, which are described as very bright in van den Bergh's (1966) catalogue of reflection nebulae.

The general optical characteristics of reflection nebulae, besides both the illuminating star and nebula having similar spectra, are: (1) the nebula is bluer than the exciting star at

small offset angles, but becomes increasingly redder at larger offset angles; (2) polarization usually increases with offset distance and wavelength, and (3) surface brightness is usually found to decrease in a power law with distance (Witt and Cottrell 1980), the extent of which is dependent on the star-nebula geometry and the wavelength dependence of scattering.

For reflection nebula modelling, the most important observational data that can be obtained from reflection nebulae are: (1) the spatial dependencies of colour, surface brightness, position angle and degree of polarization, and (2) the wavelength dependencies of surface brightness and degree of polarization.

In order to develop a numerical model of a reflection nebula, theories of light scattering have had to be developed which has involved solving Maxwell's equations using appropiate boundary conditions. (The topic of single scattering is covered by the formalism in van de Hulst's (1981) treatise.) The mathematical description of light scattering by spherical particles was first formulated independently by Mie (1908) and Debye (1909). Lindblad (1935) was the first to propose that dust grains could condense out of the interstellar medium and his work agreed with Schalen's determination of the size of grains derived from applying Mie theory to extinction in the Galactic plane. Later (see Zellner 1970 and references therein), Schalen was the first to suggest that interstellar grains were made of iron particles and to use iron grains to model the Merope nebula. Since then, many materials

have been considered (e.g. ices of water, methane and ammonia; silicates; graphite; and bacteria), however the use of reflection nebula modelling and the constraints from observations of scattering and transmission of light by dust has helped to restrict the number of possible grain materials. As well as a knowledge of grain properties, sizes, and the use of Mie theory to determine the degree of polarization of the scattered light, the geometry of the nebula should be known. The geometry can sometimes be inferred from polarimetric observations if not known a priori, but usually it is one of the unknown parameters in the reflection nebula model.

So a reflection nebula model must be able to reproduce the above observational data through a knowledge of: grain composition and shape, the size distribution of dust grains; and also the geometry of the nebula, which can then give the physical relationship between the star and its surrounding dust that may be the remnant of prestellar material. Only the brightest reflection nebulae have been modelled and include: the Merope (Hanner 1971); NGC 7023 (Moore 1982); NGC 1999 (Warren-Smith 1979); and LkHalpha 208 (Shirt 1984).

1.5 Interstellar dust grains

Observations of compact reflection nebulae only provide information on interstellar dust grains that are close to young early B stars (~1 parsec). There are many observations that can be

made of interstellar dust grains, from extinction studies of distant OB stars probing out to a few kiloparsecs in the Galactic plane and observations of the Diffuse Galactic Light over many kiloparsecs to recent IRAS data of the Galactic nucleus at 10 kpc.

Some of the questions which these observations are helping to answer are firstly: Are the local dust grain properties found around early B type stars in reflection nebulae the same as the dust in circumstellar shells that surround red giants or young protostellar objects? Secondly: Are the interplanetary dust grains involved in producing the Zodiacal light or those that make up comets similar in nature to the interstellar dust grains in molecular clouds? Finally: Are there differences in the nature of dust grains in molecular clouds that are involved in star formation and those that are not? These questions are still largely unanswered more than half a century after Trumpler's (1930) pioneering work on interstellar dust. The importance of dust in interactions both physical and chemical is beginning to be understood with the opening up of all wavelengths to astronomers, and one of the most important tools in determining the nature of interstellar dust grains is polarimetry.

1.6 Polarimetry

Astronomical polarimetric observations were pioneered in the late 1920's by Lyot and other workers, initially with observations of the bright planets and the Moon. The paper by Ohman (1939)

describes a photopolarimeter with which he obtained the first measurements of polarization in an external galaxy - the Andromeda Galaxy. This polarimeter was similar in design to that proposed by E.C. Pickering in 1885 and incorporated a grating of parallel bars, a plane-parallel plate of Iceland spar as the polarizer and a lens to image the grating onto a photographic plate. The idea of dividing the image into adjacent parallel strips of orthogonal polarization requiring two sets of exposures with the polarimeter, the grid position determining which half of the image to be analysed, was also developed in the Durham polarimeter, which is described in the paper by Scarrott et al. (1983).

Before describing different types of polarimeter and considering the efficiency and sensitivity of the Durham polarimeter used in making the observations for this thesis, it will be worthwhile looking at the nomenclature used in polarimetry and the processes involved in the production of polarized light in astronomy.

Electromagnetic waves are transverse waves which consist of two orthogonal components: an electric and a magnetic field whose vector quantities are described by Maxwell's equations:

$$\text{curl } H = \frac{dD}{dt} + J \qquad \text{div } B = 0$$

$$\text{curl } E = -\frac{dB}{dt} \qquad \text{div } D = \rho \, .$$

From these one can derive a wave equation (either for the electric field or the magnetic field, but by convention one examines the electric component):

$$\nabla^2 E - \frac{1}{C^2}\frac{d^2E}{dt^2} = 0$$

whose solution is:

$$E = \hat{a}\, Eo \exp i(k.r - wt) .$$

This solution describes a linearly polarized wave whose plane of polarization is defined by the electric vector and the propagation direction (see Rybicki and Lightman 1979). Generalising the solution for a wave of any polarization, we have the case of elliptical polarization:

$$E = (x\, E1 + y\, E2) \exp(-iwt) = Eo \exp(-iwt) .$$

For a right hand frame and using Clarke's (1974) notation, the values of the electric vector in the x and y direction are:

$$Ex = Exo \exp i\left(wt - \frac{2\pi z}{\lambda} + dx\right)$$

and

$$Ey = Eyo \exp i\left(wt - \frac{2\pi z}{\lambda} + dy\right) .$$

The Stokes parameters (I,Q,U,V), which can uniquely define the polarization state of light, are given in terms of the electric vector components Ex and Ey and their respective phases dx and dy as:

$$I = \langle Exo^2 \rangle + \langle Eyo^2 \rangle$$

$$Q = \langle Exo^2 \rangle - \langle Eyo^2 \rangle$$

$$U = \langle 2\, Exo\, Eyo \cos(dy - dx) \rangle$$

$$V = \langle 2\, Exo\, Eyo \sin(dy - dx) \rangle .$$

These parameters define the total energy of the EM wave (I); the orientation of the ellipse relative to the x and y axes (Q and U); and finally the ratio of the principal axes (V). From the Stokes parameters, one can define the degree of polarization (P) and the plane of polarization, which is given by the position angle of the electric vector (O). For astronomical measurements, the position angle is taken as the angle between the direction of the meridian at that point measured from the north direction (0 deg.) to the electric vector through east (90 deg.). The polarization P, which is usually given as a percentage is:

$$P = \frac{\sqrt{(Q^2 + U^2 + V^2)}}{I}$$

also for linear polarization one has:

$$P = \frac{Imax - Imin}{Imax + Imin}$$

where Imax and Imin are the maximium and minimum intensities measured when the analyser is either parallel or perpendicular to the E vector of the incoming radiation.

The mechanisms for producing polarized light in astronomy include:

1) Synchrotron radiation: Highly relativistic electrons in a magnetic field emit synchrotron radiation which is partially linearly polarized. For electrons with a power law spectrum of energies ($N(E)dE = E^{-p}dE$), the degree of polarization is given by: $P = (p+1)/(p+7/3)$ which can be as high as 70 - 80 % (cf. The Crab Nebula).

2) Scattering: All scattering interactions give rise to polarization. Scatttering can be from free electrons (Thomson scattering); by free atoms and molecules (Rayleigh scattering); by dust grains whose size is comparable to the wavelength of light (Mie scattering); or simply diffuse scattering from planetary surfaces.

3) Transmission: Unpolarized light that is transmitted through aligned cylindrically shaped dust grains will become linearly polarized to a small extent (few %).

4) Zeeman effect: The atomic Zeeman effect is produced when atoms undergo bound-bound transitions in a magnetic field. This has been observed in white dwarfs with surface magnetic fields of ~E6 gauss and magnetic Ap stars.

All polarimeters consist of an analyser and a detector. The simplest form of polarimeter uses a dichroic filter, e.g. a piece of polaroid, to analyse the incoming light; however, the use of polaroid is found to be too inaccurate for astronomical measurements. Most astronomical polarimeters use a birefringent prism as an analyser which splits the beam of light into two orthogonally polarized beams whose intensities are proportional to the parallel and perpendicular polarization components and are measured by a low light level detector. For a one-dimensional polarimeter, a single photomultiplier can be used as the detector, but for areal polarimetry of extended objects a two dimensional detector is required, e.g., a CCD camera, or an electronographic camera. Serkowski (1974) describes many types of polarimeter that

Table 1.2. A comparison of CCD and electronographic detectors.

PARAMETER	CCD	ELECTRONOGRAPHIC CAMERA
D.Q.E. (%)	60-70	20
RESOLUTION (MICRON)	25	5
DYNAMIC RANGE (DEX)	7	2
SPECTRAL RANGE (MICRON)	0.4 - 1.0	0.3 - 0.7
LINEARITY RANGE (DEX)	4-5	1-1.5
ADVANTAGES		
1) data digitised immediately		inexpensive
2) extremely linear response		ease of use
DISADVANTAGES		
1) cryogenic equipment needed to cool detector		developing the electronographic film
2) Hot spots, dead pixels and trails		requires a micro-densitometer to digitise data

have been used for measuring both linear and circular polarization in astronomy. He cites the main source of error in measuring polarization as photon noise. It is important then to use a detector with a high quantum efficiency. Photographic films, which have detector quantum efficiencies less than 4%, are not used in astronomical polarimetry. The accuracy to which polarimeters can measure the polarization and position angle of photometric standard stars is +/- 0.1 % and +/- 0.1 degrees (Serkowski 1974; cf. The accuracy of the Durham polarimeter: +/- 0.5% - Scarrott et

al. 1983). The differences between the two types of detector that were used with the Durham polarimeter in making the observations for this thesis are outlined in Table 1.2.

1.7 Aims

The main theme of this thesis is concerned with observations of polarization produced by the scattering of light by dust grains in two compact reflection nebulae and the aims and reasons for this research are:

1) The study of reflection nebulae which are illuminated by early B type stars is important in understanding the heating and cooling of molecular clouds.

2) The illuminating stars of the reflection nebulae, NGC 2068 and 2023, have ages of a few times E5 years, so the characteristics of young main sequence stars will be investigated.

3) Both NGC 2068 and 2023 have associated young star clusters, many of which are pre-main sequence stars (Sellgren 1983), and the distribution of these stars and their characteristics will be looked at.

4) The nature of the dust in reflection nebulae in the Orion R1 association will be determined through modelling.

5) The geometry of the dust in both reflection nebulae should be found and compared to theoretical models.

6) The properties of the R association, Orion R1, may be determined.

7) Local conditions in the dust cloud L1630 around both reflection nebulae with respect to the interaction of star and dust will be determined and compared to the modelling done by Voshchinnikov and Il'in (1983). Polarimetry may be useful in this context in studying the magnetic field in this cloud if there are aligned grains present (Vrba et al. 1976).

The thesis is divided up into 8 chapters; in chapters 2 and 3 a review is given of the nature of interstellar dust grains and recent ideas of star formation with special emphasis on the Orion star formation region. In chapter 4, broadband V polarimetry of NGC 2068 is reported and these results are compared with other workers. From the observational data detailed on NGC 2068 a numerical model is advanced in chapter 5 to explain the results. Chapter 6 accounts the extensive work done in six wavebands on NGC 2023 and these results are analysed in chapter 7. Finally, in chapter 8 a synthesis is given of all the observations reported on the reflection nebulae in the Orion R1 association and the dark dust cloud L1630.

The most important objective of this thesis is to determine to what extent limits can be placed on the parameters used in the modelling of the reflection nebulae studied and then place constraints on the nature of grains and the geometry involved in the nebulae NGC 2068 and NGC 2023.

CHAPTER 2 Interstellar Dust Grains

2.1 Introduction

The total mass of our Galaxy is estimated to be ~ 1.4 E11 Mo (Allen 1973) and this is made up as follows: stars - 1.3 E11 Mo (95%), neutral hydrogen HI - 3.5 E9 Mo (2.5%), molecular hydrogen - 3 E9 Mo (2.1%), ionized hydrogen HII - 2.6 E8 Mo (0.2%), and in the form of interstellar dust grains - 1 E8 Mo (0.07%) (Savage and Mathis 1979; Sanders et al. 1984). Although the dust contributes a negligible part to the total mass of the Galaxy, it has a crucial role in interstellar astrophysics.

It was Trumpler (1930) who showed that interstellar space was not perfectly transparent and demonstrated the existence of a 'fine cosmic dust'. These interstellar dust grains were found to scatter and absorb starlight producing both general and selective extinction: thus affecting the determination of the photometric distance of stars from a comparison of absolute and apparent magnitude using the relation:

$$m = M + 5 \text{ Log } r - 5 + A$$

where m = apparent magnitude

M = absolute magnitude

A = extinction

r = distance in parsecs.

The presence of dust is also manifest from observations of the polarization of starlight in the Galaxy. Work by Mathewson and Ford (1970); Axon and Ellis (1976) shows that light from stars near the Galactic plane is linearly polarized and the plane of polarization is parallel with the Galactic plane. The mechanism involved in producing this polarization has been attributed to the alignment of elongated grains by the Galactic magnetic field (Davis and Greenstein 1951). Another process producing polarization of starlight is found to occur in reflection nebulae. The scattering of light in reflection nebulae gives rise to linearly polarized light that is sometimes up to 60% polarized (Taylor and Scarrott 1980).

Apart from the evidence just described for elongated, aligned dust grains from polarization measurements of stars in the plane of the Galaxy and existence of interstellar grains from extinction and reflection nebulae studies, the most notable optical evidence for dust comes from observations of dark dust lanes in our Galaxy and the large dust globules first seen by Sir William Herschel. The reduction in numbers of extragalactic nebulae and globular clusters towards the Galactic plane showed that interstellar dust is concentrated towards the Galactic plane and this became known as 'the zone of avoidance'. The optical observations of dust in the Galaxy indicated that the interstellar medium was not homogeneous, but consisted of many types of clouds of various sizes. Bok Globules (Bok 1977) represent some of the smallest individual dark clouds in the interstellar medium. At the other

end of the range in cloud sizes are giant molecular clouds. The characteristics of the various components of the interstellar medium are set out in Table 2.1 below. The interstellar medium is a very complicated mixture of gas in various states and dust. In this thesis the term molecular cloud will also be used to denote dark dust clouds, which are simply molecular clouds that are seen to obscure background stars because of their comparatively near distance.

Table 2.1. The interstellar medium.

	Physical Parameters		Cloud Parameters		
Constituent	T/k	n/cm-3	Diam./pc	Av/mag	Mass/Mo
Coronal Gas	6 E5	<0.01	-	-	-
HII regions	8 E3	10 - 100	5 - 10	-	-
Compact HII	E2-E3	1 E4	0.1 - 1	> 15	~1
Masers	E2	E5-E11	< 0.01	-	-
Intercloud Med.	6 E3	0.3	-	-	-
Large Globules	10	7 E3	0.1 - 1	5 - 25	20 - 800
Diffuse Clouds	50-80	20 - 100	5	0.2	400
Molecular Clouds	10	E3-E5	1 - 5	4	E2 - E4
SFR	~30	E3-E5	0.1 - 1	> 10	E3
GMC	10-20	300	40-100	> 10	E5-E6

Evidence useful in determining some basic properties of the interstellar dust comes from deriving the Oort limit: this is the analysis of the Galactic z velocity component of stars in the

Solar neighbourhood in order to derive the local mass density. The gravitational acceleration perpendicular to the Galactic plane is given by the one dimensional form of Poisson's equation:

$$\frac{-dg(z)}{dz} = 4\pi G \rho(z).$$

Knowing the total mass density and the contributions to this from visible stars, an upper limit can be found for the interstellar density. Recent values for the various density components are taken from Allen (1973) and Spitzer (1978):

total	= 10 * E-24 g/cm3
stars	= 4 * E-24 g/cm3
gas	= 3.0 * E-24 g/cm3
dark stars	~ 3.0 * E-24 g/cm3
dust	= 1.8 * E-26 g/cm3.

From the amount of extinction observed per kiloparsec in the Galactic plane by Trumpler (1930) and the density of dust from the above analysis, this implied that grains were of micrometre size. Trumpler also showed that extinction was selective (the colour index of stars increased with distance), and it was later found that the extinction in the optical region varied proportionally to the reciprocal of wavelength. This latter observation ruled out Rayleigh scattering as the cause of extinction, but supported scattering in the Mie domain with particle size similar to the wavelength of light.

Given that there is dust in the Galaxy and the grain size has been determined to be ~0.5 micron, what is its astrophysical importance and why should it be studied? This can be answered by listing the roles that dust plays in astrophysics, which are many and diverse and are summarized below:

1) Importance in star formation as grains can provide strong radiative cooling when a protostar undergoes rapid contraction. (Both dust, and molecular hydrogen - which is formed on dust grains, can radiate away energy from the collapsing protostar.)

2) The interaction of grains with the Galactic magnetic field via the Davis-Greenstein mechanism gives rise to the phenomenon of interstellar polarization. From measurements of interstellar polarization, the Galactic magnetic field can be mapped and the properties of the grains be deduced (Johnson 1982).

3) Determination of the composition of the interstellar medium depends on knowing the amount of depletion of elements through accretion onto grains.

4) Interstellar grains can act as a catalyst in dense gas clouds in the production of interstellar molecules. (Dust catalyses the formation of molecular hydrogen and attenuates UV radiation, which can break up molecules that form in dark clouds.)

5) Grains from the placental clouds in which some stars condense may sometimes conglomerate to form planetesimals (and hence comets, asteroids and planets etc.) so are essential in the formation of solar systems and therefore a knowledge of these

grains are required in cosmogenic theories of solar systems and protostellar shell evolution.

6) It is important to know the interstellar extinction curve accurately so that the exact energy distribution of stars embedded in dust clouds may be determined.

Observations relating to the properties of the dust in our Galaxy will now be considered; data on extragalactic dust being beyond the scope of this thesis.

2.2 Data on dust grains

As well as the data obtainable from the whole of the electromagnetic spectrum on interstellar dust which is reviewed below, there is a wealth of data that can be directly found from interplanetary dust.

It is unlikely that there is a significant amount of interstellar dust mixed with the interplanetary dust in our Solar System; an upper limit of E-30 g/cm3 indicates that the Sun is in an intercloud region (Whittet 1981 and references therein). However, it is believed that some interplanetary grains, which are derived from cometary debris, represent the composition of the primitive solar nebula which may have contained interstellar grains. So even though no recent interstellar grains can be examined, the most primitive meteorites - type I carbonaceous chondrites - and the meteoritic debris from comets may comprise of

unprocessed interstellar grains from the time the solar nebula condensed. Data from micrometeoroids (interplanetary particles collected in the stratosphere) show that these grains are mostly of silicate or magnetite composition and have a heavy element distribution similar to the standard element distribution of Cameron (1973) (see Whittet 1981). The grains are found to have sizes of a few micrometres being aggregates of smaller submicrometre size grains, which in turn may be single crystals or composed of yet smaller particles (~0.01 μm). The type I carbonaceous chondrites appear to have suffered the least chemical fractionation of all meteorites (Trimble 1975) and are composed of: 55% hydrated silicates, 20% magnesium sulphate, 20% magnetite, and 5% carbon and organic compounds. These meteorites are believed to have a composition similar to micrometeoroids and thus possibly to interstellar dust grains.

Spectroscopic data on comets have shown the 9.7 μm silicate feature in emission similar to that found in such diverse objects as: meteors, circumstellar dust, and in the solar corona (Martin 1978). No other firm conclusions on cometary material can be made at present.

Summarizing this data on interplanetary dust that is found in comets, type I carbonaceous chondrites, and micrometeoroids, there is a strong similarity in size and composition of primitive interplanetary dust grains to the refractory silicate grains seen in the interstellar medium.

2.2 a Extinction

Light that is transmitted through the interstellar medium suffers extinction due mainly to the combined effects of absorption and scattering by dust grains.

If the intensity received at the Earth for a star that suffers no extinction is Io and I is the intensity when there is extinction, then the extinction is related to the optical depth (τ) by:

$$I = Io \exp(-\tau).$$

The extinction in magnitudes is simply:

$$dm = -2.5 \log (I/Io)$$

so in terms of optical depth (τ)

$$dm = 1.086 * \tau .$$

The terms used in extinction studies will now be defined:

Av The interstellar extinction in the visible band (5500 A) is measured in magnitudes. Av = -2.5 log (I/Io).

B-V This is the colour index of a star and is simply the difference in the apparent brightness of a star in the B and V wavebands.

E(b-v) The standard or intrinsic colour index is given by the difference in colour index of a reddened and unreddened star of the same spectral type and luminosity class:
= (B-V)star - (B-V)o = Ab - Av.

E(l-v) Normalised extinction - normalised to unit colour excess.

E(b-v)

Rv The ratio of total to selective extinction. Rv = Av/E(b-v).

The interstellar extinction curve shown in Fig. 2.1 is a graph of averaged normalised extinction and wavenumber taken from Savage and Mathis (1979). The range in wavelength that extinction measurements have been made now extends from 1000 A in the ultraviolet (UV) to 20 micrometres in the infrared (IR). Dividing this wavelength range into three regions, the characteristics of the extinction curve are:

1) Infrared: Observations of the extinction of starlight in the infrared, although difficult due to possible contamination by infrared emission from circumstellar dust, offers the chance to determine the composition of interstellar grains through identification of absorption features due to molecular transitions in the solid grain material. The features that have been detected include: the 3.07 μm feature attributed to ice; the 9.7 μm and 20 μm features identified with silicates or silicon monoxide; and bands at 3.3-3.4, 6.0 and 6.8 μm that are possibly due to organic compounds (Salpeter 1977).

2) Visible: Extinction in the visible band (1.2 - 3.1 μm^{-1}) follows approximately an inverse wavelength dependence except for a discontinuity or 'knee' at 2.3 micrometres^{-1}. The size of dust grains required to produce this extinction is given by:

$$a \sim \frac{\lambda}{2\pi(n-1)}$$ (Whittet 1981).

Taking two possible grain materials and their respective refractive indices the typical size of dust grains from Mie theory is: 1) Ice m = 1.33 => a ~ 0.27 micrometres

2) Silicates m = 1.6 => a ~ 0.15 micrometres.

In this wavelength region there has been found some 39 diffuse band features (Martin 1978) with the principal features being at 4430 A, 5780 A, 5797 A and 6284 A. The typical width of these features is between 1 - 20 A. Identifying these features has proved an enigma: they may be due to grains or have a molecular origin. There is also a very broadband structure (VBS) in the visible region which appears as a shallow dip (dm ~ 0.1 mag) between 1.6 - 2.0 μm-1 that may be due to magnetite (Fe_3O_4) grains (Whittet 1981).

3) Ultraviolet: The dominant feature seen in the ultraviolet region of the extinction curve is the pure absorption feature at 4.6 +/- 0.1 μm-1 which has been identified with carbon in the form of small graphite particles. The symmetry of the feature's profile, the strength of the feature, its correlation with colour excess, and its ubiquitous nature, implies small grains (< 0.02 μm) of carbon (the fourth most abundant element in the ISM) which are well mixed in the interstellar medium. The slope of the extinction curve increases rapidly beyond a shallow minimum at 5.5 - 7.5 μm-1 where the extinction has a λ^{-4} dependence due to scattering in the Rayleigh domain.

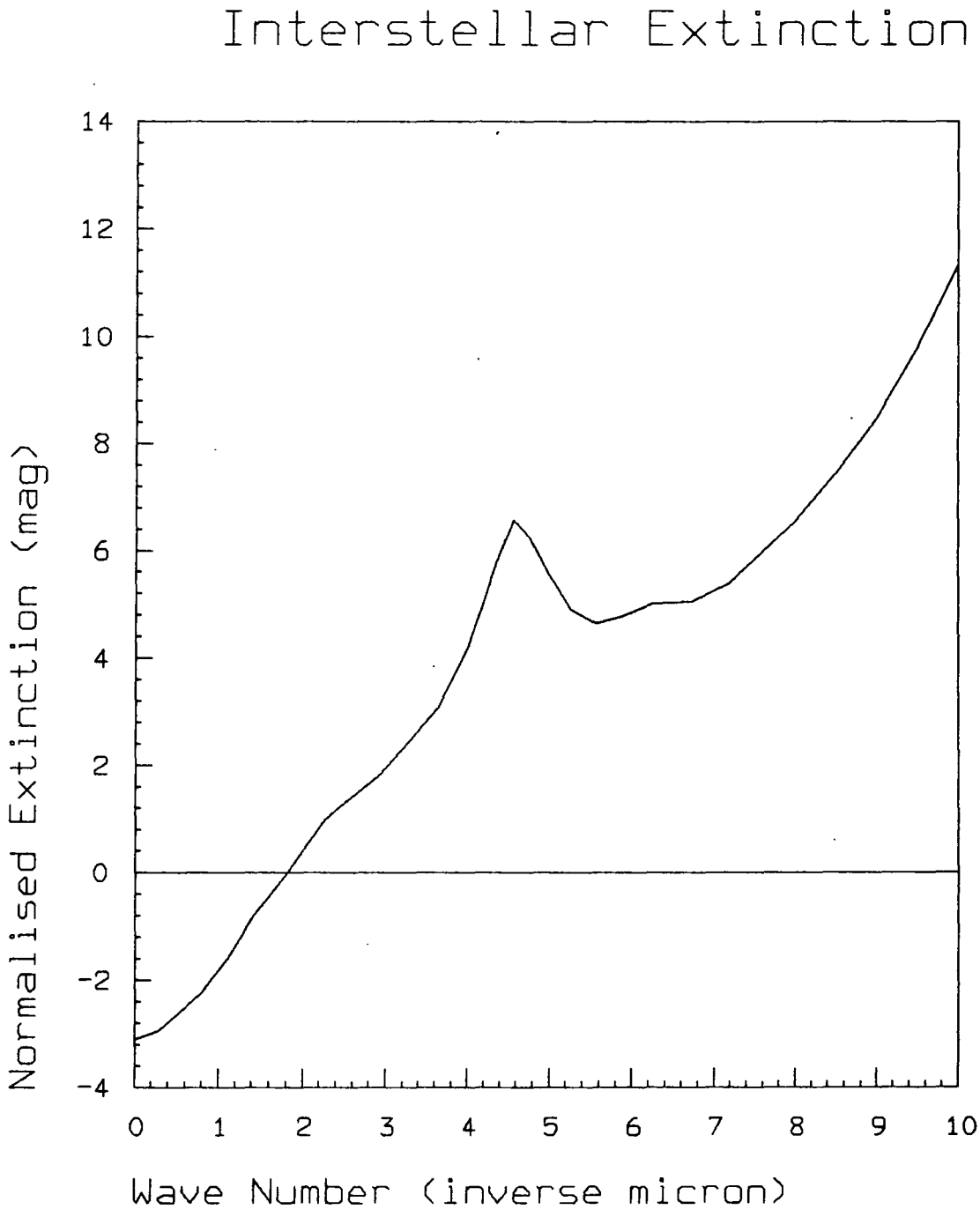

Fig. 2.1. The interstellar extinction curve.

2.2 b Polarization

Interstellar polarization was discovered independently by Hall (1949) and Hiltner (1949). Several theories have been put forward to explain this observed polarization by transmission through aligned grains, e.g. Harwit (1970); Gold (1952); Purcell (1975); and Davis and Greenstein (1951), however, the one proposed by Davis and Greenstein is the most widely accepted today. Fig. 2.2 shows the extent and distribution of the interstellar polarization, which is mostly confined to the Galactic plane and is taken from the work done by Axon and Ellis (1976), who collated measurements of 5070 stellar polarizations.

The wavelength dependence of interstellar polarization has been observed by Coyne and Gehrels (1967) and Serkowski et al. (1975). Coyne and Gehrels found that the polarization against reciprocal wavelength curve had a maximum for most stars at 5200 angstroms which decreased rapidly towards the IR and less rapidly towards the UV. It was apparent that many stars deviated from the mean polarization curve and later Coyne et al. (1974) derived a unique representation to fit the data for all stars using two parameters - lmax and pmax - the values of wavelength and polarization where maximum polarization occurs. Their empirically derived formula to fit the wavelength dependence of polarization is:

$$P/Pmax = \exp [-K \ln (l/lmax)]$$

where K = 1.15

l = wavelength in the range $0.22 < l < 2.2$ μm

lmax = " " " $0.45 < lmax < 0.8$ μm

P = polarization in the range $1\% < P < 10\%$.

A similar investigation of interstellar polarization by Serkowski et al. (1975) showed that lmax was correlated to Rv, the ratio of total to selective extinction (Rv = 5.5 lmax), and also to ratios of colour excess (e.g. Ev-k/Eb-v). The parameter lmax has been found to be larger in denser clouds (cf. Carrasco et al. 1973) and from theoretical considerations should be proportional to grain size - $lmax \propto (n-1)a$ (Whittet 1981). Thus, observations of the wavelength dependence of interstellar polarization can give indications of grain size and shape (Coyne et al. 1974), while measurements of the position angle dependence of interstellar polarization on wavelength should show how grain alignment and size changes in the interstellar medium (Coyne 1974).

Circular polarization will be produced if light which has already been linearly polarized passes through aligned dust grains as this will introduce a relative phase shift to the two orthogonal components of the electric vector of the original beam which are parallel and perpendicular to the direction of alignment. This birefrigence due to interstellar grains should show how the alignment of grains changes along a line of sight, while the wavelength dependence of circular polarization, which is

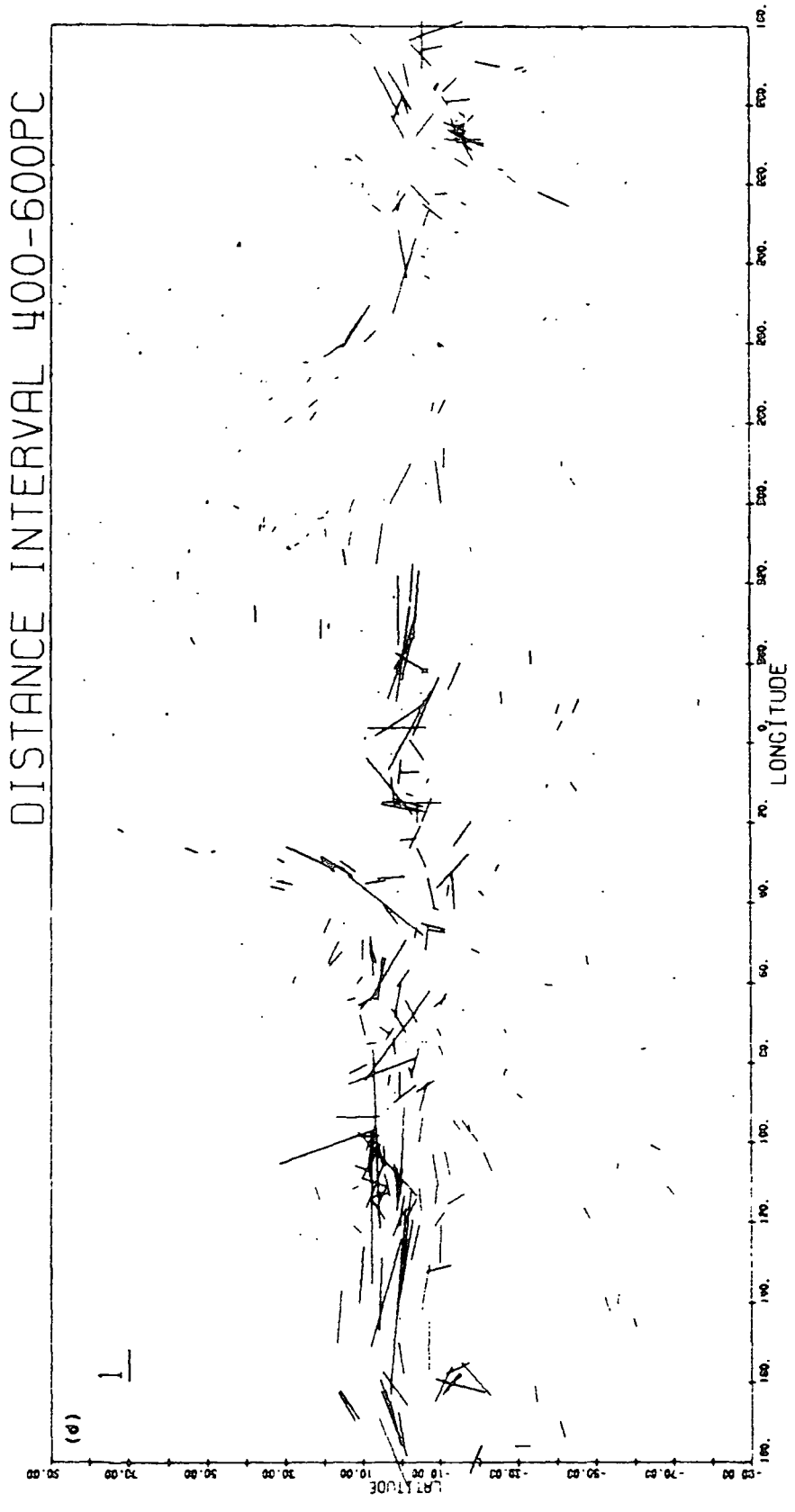

Fig. 2.2. Interstellar polarization.

dependent on grain composition, has indicated the presence of dielectric grains (Martin 1978).

In the last decade some of the brightest reflection nebulae have been observed using 2-dimensional polarimeters. These have included Eta Carinae (Warren-Smith et al. 1979), NGC 1999 (Warren-Smith et al. 1980), NGC 7023 (Moore 1982) and LkHalpha 208 (Shirt 1984) that have been observed by the University of Durham Polarimetry Group. Many reflection nebulae exhibit a centrosymmetric pattern of polarization vectors whose centre of radius is the illuminating star: for a single illuminating star, the scattering plane includes the star, dust grain and observer, and the E vector of the scattered light is either parallel with this plane (negative polarization) or perpendicular (positive polarization). Non-radial polarization is indicative of aligned non-spherical grains.

In modelling reflection nebulae, single scattering is usually assumed. This is true if the nebula is optically thin, i.e. $\tau < 0.3$, but most bright cases are optically thick ($\tau > 1$) so multiple scattering should be taken into consideration (van de Hulst 1981). The effect of multiple scattering is one of depolarization as shown by the modelling of Vanysek and Solc (1973). Data that has been modelled by Carty et al. (1979) on Eta Carinae and Moore (1982) on NGC 7023 have indicated silicate grains and a power law distribution of grain size, but interpretation of the scattering in reflection nebulae is very difficult.

2.2 c Spectroscopy

The composition of dust grains may not only be determined from extinction studies, but obtained more directly through infrared spectroscopy observations. Vibrational transitions (due to stretching or bending of molecular bonds) of many molecular species that are believed to be grain constituents can be observed in the near- and middle-infrared (2 - 40 micrometres). The 9.7 micrometre feature, either in absorption or emission, is the most universal feature known and has been attributed to the Si-O stretching vibration in either silicon monoxide or silicates. Table 2.2 lists other infrared bands that have been studied (see Aitken 1981; Savage and Mathis 1979; Whittet 1981).

Circumstellar dust, as well as producing some extinction, will, because it is hot enough (T ~100 - 1000 K), produce an infrared excess in a star's continuum. Spectroscopic studies of the infrared continua of stars with circumstellar shells have indicated that oxygen-rich stars have the 10-μm emission feature (due to SiO/Silicates) while carbon-rich stars have a continuum and emission features that have been attributed, respectively, to graphite, and acetylene and silicon carbide grains.

The broad emission features seen at 3.3, 3.4, 6.2, 7.7, 8.6 and 11.3 μm in planetary nebulae (like NGC 7027) and other objects are probably due to dust, but have not yet been identified (Aitken

1981).

Table 2.2. Infrared features of dust grains.

Wavelength of Feature/ μm	Grain composition	Region
3.07	NH3 + WATER ICE (O-H)	Taurus MC
6.0 }	HYDROCARBONS (C-H)	W33 A
6.8 }		NGC 7538 IRS 9
9.7	SILICATES (Si-O-Si)	Gal.Centr., Comets
	or SILICON MONOXIDE	O-rich stars
11.2	SiC	Circumstellar dust
18	SILICATES, MgO, FeO, NiO	HII regions
45	WATER ICE (O-H)	Orion Nebula

2.2 d Scattering

Scattering of light by dust is observed in the form of the diffuse Galactic light (DGL), in HII regions, and in reflection nebulae. The DGL is predominantly due to forward scattering of starlight by interstellar dust in the Galactic plane whose effective thickness is 200 pc. Observations of the DGL enable the albedo, a (the ratio of scattering to extinction cross-section) and phase function, g (average cosine of the scattering angle) to be estimated by modelling; however, the determination of grain composition by this method cannot be done directly (Martin 1978). Typical values obtained for the albedo and phase function of Galactic dust are a ~ 0.7 and g ~ 0.7 at B and V wavebands (Martin

1978) and a ~ 0.35, g ~ 0.9 at 2200 A (showing this extinction feature to be due to absorption). The study of the DGL is still in its infancy and present model calculations are controversial, however, this work is especially important in calculating the penetration of UV in molecular clouds (through determination of albedo and phase function; Chlewicki and Greenberg 1982).

Scattering by dust grains in HII regions and reflection nebulae has been modelled using Mie theory. For coherent, independent, single scattering as described in van de Hulst (1981), the case of Mie scattering can be characterised by four complex scattering amplitude functions S1-4 in a matrix equation:

$$(E1^{l}, E2^{l}) = [\ S2(\theta)\ ,\ S3(\theta)\ ]\ [\ E1\ ]$$
$$[\ S4(\theta)\ ,\ S1(\theta)\ ]\ [\ E2\ ]\ .$$

Assuming scattering by homogeneous spheres then S3 = S4 = 0 and S1 and S2 are only dependent on the scattering angle (S1 and S2 represent the components of the scattered wave whose E vectors are perpendicular and parallel to the scattering plane respectively.):

where
$$S1 = \sum_{n=1}^{\infty} \frac{2n+1}{n(n+1)} \{\ a_n \pi_n(\cos\theta) + b_n t_n(\cos\theta)\ \}$$
$$S2 = \sum_{n=1}^{\infty} \frac{2n+1}{n(n+1)} \{\ b_n \pi_n(\cos\theta) + a_n t_n(\cos\theta)\ \}$$
$$\pi_n(\cos\theta) = P_n^{1}(\cos\theta)/\sin\theta \quad \text{and } P_n^{1} = \text{Legendre Polynomial}$$
$$t_n(\cos\theta) = dP_n^{1}(\cos\theta)/\, d\theta\ .$$

These functions are sufficient to calculate the intensity and polarization of scattered light as well as the scattering

cross-section and phase function of the grains.

2.2 e Distribution

Galactic dust is confined to the plane of our Galaxy as shown by the Galactic latitude dependence of stellar colour excess, which crudely approximates a cosecant law with very little dust seen at high Galactic latitudes - $E_{b-v} < 0.01$ for $|b| > 50$ degrees (Martin 1978). Optical studies of dust are restricted to observations within ~ 3 kpc of the Sun due to extinction, which averages 1.8 mag/kpc (Spitzer 1978). The dust appears concentrated on a large scale in the Galactic spiral arms. Along a distant line of sight, dust can vary in density by factors of E3 showing the non-uniformity of the interstellar medium (Whittet 1981). On a small scale, dust is found to be concentrated in gas clouds and is seen in molecular clouds, HII regions, planetary nebulae, Bok globules and reflection nebulae. Most dust clouds are irregular in shape and exist in groups (Martin 1978). Spitzer (1978), from statistical modelling of interstellar extinction, calculates the average number of clouds along a line of sight as ~ 6 standard clouds/kpc with $E_{b-v} = 0.06$/kpc and 0.8 large clouds/kpc with $E_{b-v} = 0.29$/kpc.

2.2 f Dust-to-gas ratio

The dust-to-gas ratio has been measured in many regions of the Galaxy. Measurements of the HI constituent of interstellar gas

rely on 21-cm emission line observations, while molecular hydrogen is inferred from CO and other molecule density data assuming the ratio of hydrogen to the known molecular specie a constant. The density of dust is calculated from the value of extinction it produces along a line of sight to a star from colour excess measurements. The gas and dust in the interstellar medium appear closely correlated as can be seen when plotting total hydrogen column density ($N(HI + H_2)$) against colour excess (Fig. 2; Bohlin et al. 1978). The average gas-to-colour-excess ratio obtained by Bohlin et al. was 5.8 E21 cm-2 mag-1, however, this might be too low for dense clouds with larger than average grains e.g. Rho Oph (Carrasco et al. 1973) which can then result in an anomalously large ratio. Spitzer (1978) calculated the total gas-to-dust mass ratio as 1:160 from interpreting gas-to-colour excess data while studies of the scattered light from dust in HII regions indicated gas-to-dust mass ratios in the range 1:20 - 1:700 averaging 1:100 (as for HI regions).

From measurements of the local dust and total hydrogen density - dust density ~1.8 E-26 g/cm2 and gas density ~ 3 E-24 g/cm2 - the local dust-to-gas ratio is 1:166 so an average of 1:100 (the canonical value) appears typical for many regions in the Galactic plane. However, it is expected that in HII regions where sputtering of grains is important and in dense clouds where accretion is dominant that the value of the dust-to-gas ratio will be different.

2.2 g Physical properties

The physical properties of dust grains such as: shape, size distribution, electric potential, magnetic susceptiblity, and temperature, are required to determine the physical interactions of grains in the interstellar medium. Taking each property in turn, and using the observational data described in the previous sections, the following can be inferred:

Shape: The dichroism of interstellar grains, which is exhibited in linear and circular interstellar polarization, can only be explained by elongated shaped grains. Draine and Lee (1984) have modelled the polarization cross-section for silicate grains and concluded that these grains were predominately oblate spheroids.

Size distribution: To determine the size distribution of interstellar grains Mathis, Rumpl and Nordsieck (1977; hereafter MRN) modelled the interstellar extinction curve between 0.11 and 1 micrometre and derived a power law distribution with spectral index ~ -3.5. An investigation by Mathis (1979) into fitting interstellar polarization with bare infinite dielectric cylinders used a similar power law distribution and gave good agreement to the polarization data.

Electric potential: The ISM has no net electrical charge as the amount of positive charge of ions is balanced by the total charge of the electrons. However, the process of photoelectric emission (dominant in HII regions), and electron and ion adsorption on grain surfaces can lead to an electric potential

developing on a grain. This potential will be a function of: distance to the nearest star; electron and ion density; cosmic ray intensity; composition of grain; grain radius; and gas temperature. Results of calculations show for grains of radius r=0.3 μm, temperature ~100K V ~ 1e while in HII regions grains can develop a positive charge of several thousand e (Wickramasinghe and Nandy 1972). The majority of grains are likely to have an electric charge which will affect their motion in the ISM through interaction with magnetic fields. Charge is also likely to affect grain accretion and grain-gas coupling (Mitchell and Evans 1984).

Magnetic susceptibility: The Davis-Greenstein mechanism relies on paramagnetic relaxation to align the rotational angular momentum vector J with the Galactic magnetic field B. For a paramagnetic substance the magnetic susceptibility X is complex and the imaginary component is given by X" = 2.5 E-12 W/Ts, where W = angular rotational frequency and Ts is the grain temperature (K). Observations of interstellar polarization can be explained by paramagnetic relaxation if the magnetic susceptibility is enhanced by either superparamagnetism or ferromagnetism assuming the Galactic magnetic field to be < 3 microgauss (Spitzer 1978).

Temperature: The temperature of a grain which is in thermal equilibrium can be calculated by equating the gain of internal energy by photoabsorption, gas collisions, and through exothermic grain surface reactions with the loss of energy through far-infrared (FIR) emission. This energy balance requires knowledge of grain material and size, the interstellar radiation density, and distance to the nearest star. Typical values deduced

are 8-19 K in molecular clouds, 45-55 K in HII regions and 200 K near hot stars. (Spitzer 1978).

These parameters can then be used in grain modelling.

2.3 Grain Models

Grain models that have been proposed over the last fifty years have divided the numerous possible grain constituents into various categories, e.g., refractory v. organic compounds (Whittet 1981); metallic v. dielectric (Zellner 1970); homogeneous v. core-mantle grains (Voshchinnikov 1978b). However, all grain models are required to fit some aspect of the observational data on dust, but none have been able to reproduce all the observed characteristics. One explanation for this is that the property of grains will vary with the interstellar enviroment. Most models are constructed to explain one category of observation. These models can be divided into three distinct groups.

1) Models required to fit and explain observations of transmitted light including interstellar extinction and polarization; for example, such as recent work by MRN, Mathis (1979); Hoyle and Wickramasinghe (1982); Draine and Lee (1984).

2) Modelling of scattered light of the DGL, in HII regions, and in compact reflection nebulae.

3) Models that account for the depletion of elements from the gas phase in the ISM, e.g. Whittet (1984).

Table 2.3. Reflection nebula models.

MODEL REF.	DATA FITTED	GEOMETRY	PARAMETERS	NEBULA FITTED	COMMENTS
Henyey & Greenstein (1938)	Colour Difference (U-B)	Homogeneous Plane-Parallel	Albedo Grain size	Merope NGC 2068	Single scattering, failed to match colours.
Minin (1965)	Intensity Pol.	Homogeneous Sphere	Optical Depth	NGC 7023 NGC 2023	Ice grains gave best fit radius < 0.07 μm.
Greenberg & Roark (1967)	(B-V) Colour Difference	Plane-Parallel Slab	Dielectric v. Metallic	Merope	Single scattering excluded metallic grains.
Greenberg & Hanner (1970)	(B-V) (U-B) B,V Pol.	Plane-Parallel Slab	Dielectric v. Graphite	Merope	Single scattering best fit: dielectric grains.
Zellner (1970)	UBVRI Pol.	Free Parameter	Metallic v. Dielectric	IC 5076 NGC 2068 NGC 7023	Pol. decreases with wave number => dielectric grains.
Hanner (1971)	U,B,V Pol.	Plane-Parallel	Silicate Grains	Merope	Single scattering, no match to colour data.
Roark et al. (1974)	Intensity gradients	Cylinder	Optical Depth	Merope	Multiple scattering off dirty ice grains.

Table 2.3 continued. Reflection nebula models.

MODEL REF.	DATA FITTED	GEOMETRY	PARAMETERS	NEBULA FITTED	COMMENTS
Witt (1977a,b,c,d)	Surface Brightness	Plane-Parallel	Albedo Phase Func.	Merope	Multiple scattering 3D Monte Carlo model.
Voshchinnikov (1978b)	UBV UBVR pol.	Spherical Homogeneous	Silicate + Ice Mantle	-	Single scattering and core-mantle grains.
White (1979a,b)	Intensity Pol.	Thick Slab	Power Law	-	Single scattering & Multiple scattering.
White et al. (1980)	Intensity Pol.	Hemisphere Thick Slab	Optical Depth	Orion Nebula	Single scattering Model too simplistic.
Shah & Krishna Swamy (1981)	IR pol.	Homogeneous Plane-Parallel	Ice, Silicate, Graphite	Merope	1-100 μm FIR flux calculated.
Moore (1982)	BVR Pol.	Conical Cavity	Grain Size Distribution	NGC 7023	Multiple scattering Silicates & Ice best.
Warren-Smith (1983b)	Surface Brightness Pol.	Star Inside Cloud With Tilted Surf.	Grain Size Distribution	NGC 1999	Multiple scattering High albedo, low R.I. grains gave best fit.
Shirt (1984)	UBVR pol.	Bipolar + Torus	Power Law Index	LkHa208	Multiple scattering High albedo, low R.I. grains gave best fit.

The first category of models usually use several different grain components: small graphite grains; refractory dielectric grains such as silicates and metal oxides; and common to all are the elements C, N, O, Mg, Si, Al, Fe. These conclusions are similar to results of depletion studies used in models of category 3 which finds that 90-100% of heavy metals, 30% C, 40% O, and 95% Si are depleted and can be accounted for by accretion onto grains.

In the second category of models, reflection nebulae modelling can provide more information than the modelling of the DGL; this will now be considered.

The determination of grain properties through the numerical modelling of reflection nebulae by considering the Mie scattering of light has been attempted by many workers (see Table 2.3). Ideally, surface brightness, polarization, and colour of the nebula can be predicted if the geometry of the nebula, the nature of the dust grains and a rigorous radiation transfer theory is known. Unfortunately, in nearly all cases the geometry has to be assumed and the optical constants of the grains parameterised. These constants required for modelling are: albedo, complex refractive index, grain size and size distribution, and phase function. Information derived from interstellar extinction studies have suggested a power law size distribution (MRN) with a mixture of silicates, SiC, graphite, Fe, and metal oxides as the dust constituents. These data can then be used along with other

possible grain materials and size distributions as input into a grid of models.

The earliest work concerned modelling the brightness distribution of reflection nebulae. Henyey and Greenstein (1938) tried to determine the composition of grains as either dielectric or metallic by deriving the 'colour factor' or the intensity of the nebula in comparison with the intensity of the illuminating star as a function of wavelength, optical depth, grain size and geometry. Since then, models have grown in complexity and the most recent work by Warren-Smith (1983b) concludes that dust in reflection nebulae has a low refractive index and a power law size distribution. Modelling dust grains must also include processes of formation, growth and destruction.

2.4 Formation, growth and destruction

The likely places for nucleation of dust grains to occur is in the expanding envelopes of evolved stars such as: late-type giants and supergiants, planetary nebulae, novae and possibly supernovae remnants; or, in the condensing gas clouds of protostars. Theories of nucleation are dependent on knowing the temperature, pressure and chemical composition of the gas so that thermochemical reactions can be calculated in order to determine the abundances of the species that could condense. Assuming thermodynamic equilibrium, temperature-pressure phase change calculations are used to indicate which molecular/atomic species condense out of

the gas phase as the temperature of the gas decreases. The abundance of the condensing grains and grain size can then be compared to direct observational evidence of grains that are condensing in late-type stars. From spectroscopy of evolved stars the following grain materials have been identified: oxygen-rich stars - 9.7 μm silicate feature; carbon-rich stars - 11.2 μm feature attributed to silicon carbide, and a continuum due to carbon grains in the form of graphite or amorphous carbon; planetary nebulae - 9.7 and 20 μm silicate features. Polarization data of the variable star Mira, indicate grains with sizes up to 0.1 μm (Whittet 1981). The conditions of temperature and pressure in the stellar winds of cool evolved stars which give rise to nucleation of grains seem to be met in planetary nebulae and some novae, but the enviroment in supernova remnants is thought to be too extreme for nucleation to occur although the expelled material will greatly enrich the interstellar medium in heavy elements for future grain production and growth (Salpeter 1977).

Accepting that evolved stars are able to produce grain cores through nucleation and then to expel them into the interstellar medium, how do these grains then evolve? From abundance measurements of the interstellar medium it is apparent that the heavy (refractory) elements Mg, Si, Fe, Ni, Cr, Al, Ti, etc. are highly depleted from the gas phase (Zn is an exception; Whittet 1984). There is a correlation between the amount of depletion of an element in its gas phase and its condensation temperature (Field 1974) and also to the density of the interstellar medium

(Whittet 1984). All this is evidence for the growth of grains through accretion. Grain growth is also expected to occur through coagulation of small grain cores. Accretion of volatile elements (e.g. C,N,O) from the gas phase and subsequent modification by grain surface reactions into ices has been shown to occur in the densest regions of dark molecular clouds, e.g., Taurus Molecular Cloud 1 where the 3.1 μm ice band feature has been detected indicating that these grains have formed a volatile ice mantle (Jones and Williams 1984).

Several processes are thought to be responsible for the destruction of dust grains. These are evaporation, sputtering, ultraviolet photodesorption, and shattering. Evaporation or sublimation occurs in HII regions and in protostellar nebulae and are a function of grain temperature and vapour pressure of the adsorbed molecular specie. For volatile ice mantles, the critical temperature for sublimation is between 20-40 K (Spitzer 1978).

Sputtering of grains by high velocity atoms/ions will occur in the blast wave of supernova shock waves, in shock waves produced in cloud-cloud collisions, and in the stellar winds of OB stars. Shock wave velocities of ~ 200 km/s are produced by supernovae which is sufficient to cause sputtering of the most refractory grain cores (Salpeter 1977).

Ultraviolet photodesorption is most effective for photons with energy in the range 5-13 eV so consequently is an important process in HII regions (Spitzer 1978). Greenberg (1982) has modelled the effects of UV photons on dust grains and has found

that UV photoprocessing can lead to complex organic compounds being formed which may produce explosive chemical reactions that can destroy the dust grains (chemical sputtering).

Shattering through grain-grain collisions will arise if the total kinetic energy in the centre of mass frame exceeds the grain vaporization energy. This is dependent on relative velocity of the grains, grain material, shape and grain temperature. The range in relative velocities required to shatter grains is between 3 km/s for ice and 8 km/s for iron grains (Spitzer 1978).

2.5 Dust interactions in the interstellar medium

There are some sixty molecules that have been found in the ISM in the gas phase, the most abundant of which is molecular hydrogen. These molecules range in complexity from simple diatomic CO to the 13-atom $HC_{11}N$. If the chemistry networks that describe the chemical reactions which can produce all these molecules can be understood, then this will be a very useful tool in determining the chemical and physical conditions in the ISM. An important ingredient in any mathematical model describing the chemistry of the ISM is the catalytic surface of interstellar grains. The role that grains have in attenuating UV (without which most molecules would be destroyed in < E3 years), in the formation of molecular hydrogen (this is a three-body reaction requiring the dust grain to absorb the excess energy of formation), and in the production of complicated molecules (via the condensation of atoms and molecules plus grain surface reactions) are vital in understanding

interstellar chemistry. Once these complex molecules have been produced on grain surfaces, it has been proposed that they are returned to the ISM either through the action of supernova shock waves, or as a result of the explosive nature of some of the grain-surface reactions. Thus, the processing of the mantles of dust grains can greatly enrich the ISM.

Physically, dust grains are important in the heating (via photoelectric emission) and cooling (via FIR emission) of the interstellar medium so grains can modify cloud evolution both physically and chemically.

2.6 Conclusions

Restraints from the numerous observations of dust grains have restricted the possible size, composition, and shape of interstellar grains, but have not led to a simple unique solution as to the nature of dust, nor a determination of any one grain property exactly. What has been excluded as possible grain constituents are the abundant elements H and He, and grains totally made of ices. Biological material, like bacteria, seem unlikely from abundance considerations and unnecessary as inorganic material is able to fit extinction data well (Duley 1984). The constancy of Rv (3.1 +/- 0.1) in the majority of clouds in the Galaxy implies similar grain sizes, but to explain the wavelength dependence in the FUV, very small grains are required, and for dense cold molecular clouds where Rv may attain values

5-6, large grains have been invoked. There thus seems to exist a bimodal grains size distribution with the observation of interstellar extinction requiring classical size grains (a~0.15 μm) to fit the visible wavelengths and very small grains (a < 0.02 μm) to explain extinction in the FUV (Whittet 1981). Grains also appear to have a similar refractive index as deduced from the empirically derived Serkowski's Law of interstellar polarization, which is indicative of dielectric grains. Mathis (1979) has shown that cylindrical silicate grains are capable of producing the degree of interstellar polarization seen.

Theories of grain formation point to regions of high density and temperature as the conditions for grain nucleation, i.e. in the stellar winds of evolved stars, in novae and protostellar shells; the ISM being too diffuse for nucleation to occur. The diameters of the grains that are expelled from these sites will be ~0.02 μm and their composition is dependent on the C:O ratio of the star: carbon-rich stars (C/O> 1) produce SiC and C grains (graphite) while oxygen-rich stars (O/C> 1) produce SiO and silicate grains.

Once these grain cores have been expelled into the ISM, growth by accretion and coagulation will then take place in dense clouds. The exact nature of the mantle formed on grains is still largely unknown. Ice mantles are rarely seen - only occurring in dense molecular clouds where there are no OB stars present. However, some 90-100% of metals are found to be depleted from the gas phase

(Whittet 1984) and with ~50% of condensable elements in the ISM forming grains, this implies that 33% of grain material are metals. These metals must be in the form of metal silicates and oxides to meet the observational constraints that grains show mostly dielectric characteristics. The C,N,O accreted might, through UV photoprocessing, produce mantles with complex organic compounds (Greenberg 1982). The accretion of hydrogen atoms and the subsequent formation of molecular hydrogen by grain surface reactions is the only effective way of producing molecular hydrogen.

The size distribution of grains is probably of a power law form produced as a result of a steady state between the processes of accretion and destruction with shattering and sputtering being the most effective grain destruction mechanisms.

The symbiosis of dust and gas in the ISM has a direct bearing on the chemical and physical evolution of the Galaxy and in theories of star formation. Studies of reflection nebulae should elucidate some important properties of dust (size and refractive index) and also possibly the role of dust in star-forming regions.

To summarize, a list of grain properties and characteristics adapted from Hildebrand (1983) and Whittet (1981) are set out in Table 2.4 below. This data on grains will form the basis of the model in chapter 5.

Table 2.4. Interstellar dust grains.

Effective diameter	a ~ 0.2 μm
Size distribution	$n(a)da \sim a^{-3.5}$
Mass	m ~ E-15 g
Density	ρ ~ 2 g/cm3
Phase function	g ~ 0.7 +/- 0.1
Albedo	a ~ 0.7
Space density	1.8 E-26 g/cm3
Temperature	T ~ 12 K

Composition

Circumstellar shells: C-rich stars - SiC, C, C_2H_2

O-rich stars - SiO, MgO, NiO, $MgSiO_4$

Diffuse clouds: Grain core plus accretion.

Molecular clouds: Core-mantle grains including volatile mantles of ices, tarry complex organic compounds produced by UV processing of accreted C,N,H,O.

CHAPTER 3 Star Formation

3.1 Theories of star formation

This review of star formation will only be concerned with those theories and observations that pertain to star formation that is occurring in the disc of our Galaxy at the present epoch in our Galaxy's history so observations will be limited to star formation regions (SFRs) within 1 kpc from the Sun and that are not more than 20 million years old.

It is now generally believed that most stars form in molecular clouds. Evidence for this comes from the association of signposts of star formation with molecular clouds and that the theoretical conditions required for stars to form exist only in these types of cloud. Evans (1981) has classified molecular clouds into two types, not by mass or linear size, but dependent on their kinetic temperature. Type A molecular clouds have a peak gas temperature < 20 K throughout while those of type B have a temperature > 20 K. It is found that molecular clouds of type B are the ones which show signs of recent star formation: the higher temperature of these clouds being a result of heating by young stellar objects.

The first phase described by star formation models are concerned with the collapse of molecular clouds and must have as their input parameters the observed conditions of molecular clouds that are undergoing star formation. Conditions in molecular clouds

have been probed through microwave spectroscopy observations of CO and other molecules (Thaddeus 1977). The rotational transitions of CO, OH, CS, HCN etc. provide information on the radial velocity, kinetic temperature, ionization, magnetic fields and density of molecular clouds. However, it is CO, the second most abundant molecule which is the most useful, as this gives an estimate of the hydrogen molecule density and can be seen over a large range of cloud density (E3-E6 cm-3). The regions where star formation is occurring have been found to have densities of ~ E5 cm/3 and temperatures of ~ 30 K, which indicates that these are the conditions in which clouds are unstable. These results can be compared with the Jeans criterion for gravitational stability of a gas cloud: i.e. the critical mass of a cloud for which the kinetic pressure is insufficient to stop the cloud from gravitational collapse. This is called the Jeans mass (Mj):

$$Mj = \left(\frac{\pi k T}{\mu G} \right)^{1.5} \cdot \frac{1}{\rho^{0.5}}$$

or

$$Mj = 3 \left(\frac{T}{(20K)} \right)^{1.5} \left(\frac{2n(H_2)}{(E5\ cm/3)} \right)^{-0.5} Mo$$

(where k = Boltzmann constant, T = kinetic temperature of gas, n = gas density, μ = mean mol wt., G = Gravitational constant).

An analysis of the temperature, mass, and density of molecular clouds would indicate, using the Jeans criterion, that many clouds should be collapsing under gravity and forming stars. The star formation rate would, however, be many times the rate observed,

which implies that there must be mechanisms which exist in clouds preventing them from collapsing. Observations of the energetic outflow from young objects in GMCs indicate the molecular gas to be in a very turbulent state moving with supersonic velocities Vgas ~ 2 km/s (cf. Vsound ~ 0.2 km/s) (Bash et al. 1981). This observed turbulence may be an important mechanism that is required to prevent gravitational free-fall collapse in clouds that exceed the Jeans mass. Larson (1981) has looked at data on GMC dynamics and found a hierarchy of interstellar turbulent motion with the internal velocity dispersion being correlated to both size and mass of molecular cloud. Other mechanisms that will have a role in cloud support are magnetic fields and rotation (e.g., see Larson 1973).

The formation of giant molecular clouds is still not very well understood, but is generally thought to occur in the spiral arms of the Galaxy (Elmegreen 1982). The mechanism for this has been ascribed to a combination of Parker and Jeans instabilities in the ISM (Elmegreen 1982 and references therein). The distribution of GMCs in our Galaxy is not very well known; however, there does appear to be a ring of enhanced density between 4-8 kpc Galactic radial distance (Sanders et al. 1984). The spiral arms of our Galaxy have an excess star formation rate compared to the interarm regions of the disc although it is uncertain if there is a higher concentration of GMCs in these regions. This increase in star formation, especially of massive stars, is generally thought to be due to a Galactic spiral density wave (GSDW) which is a standing

shock wave that will cause compression in gas clouds enhancing their density by almost a factor of ten (Clayton 1978).

Concerning GMCs themselves, it has been observed that they have the following general characteristics: 1. masses in the range E3-E6 Mo, and a power law mass distribution m-1.5 (Dame 1983); 2. they are all inhomogeneous (average density is 300 cm-3, but there are dense core regions with density ~ E4-5 cm-3); 3. typical size is 50-100 pc with dense core regions ~ 1 pc; 4. they consist of 70% molecular hydrogen; and 5. have lifetimes that are greater than E7 years - a few free-fall times (Larson 1981). Two theories have been put forward to explain the observed energetics and dynamics of the supersonic turbulence seen in GMCs. These are by Bash et al. (1981) in which the energy input is due to collisions by small molecular clouds and the other by Norman and Silk (1980) considers continuous energy input by high velocity energetic stellar winds from T Tauri stars.

A statement of gravitational stability of a molecular cloud is given by the virial theorem:

$$\frac{1}{2}\frac{d^2 I}{dt^2} = 2K + \sum_i Fi.ri$$

(where I = generalized moment of inertia, K = kinetic energy of the cloud, Fi = force on a particle at radius ri).

If the term $d^2 I / dt^2$ is positive the cloud is unstable and will

disperse, but if negative the cloud will contract, and if equal to zero the cloud is in equilibrium and the long-term average of the kinetic energy is half the potential energy. Larson (1981) found that the virial theorem was satisfied in many regions of GMCs over a large range in mass including the smallest condensations, which have masses ~ 1 Mo and could be protostars. The condensations have velocity dispersions which follow a power law spectrum with size and were possibly formed by processes of supersonic hydrodynamics. He predicted a lower mass limit to these condensations of a few tenths of a solar mass. More work needs to be undertaken to discover what physical properties of clouds determine the characteristics of stars formed including the initial mass function.

Applying the Jeans criterion in terms of a critical molecular cloud density (ncrit) we have the following expression (Clayton 1978):

$$ncrit = \frac{E3\ T^{3}}{(M/Mo)^{2}}\ cm{-}3\ .$$

From this, one can see that the critical density is inversely proportional to the mass squared and therefore larger masses will tend to collapse first. As most molecular clouds are observed to be in approximate virial equilibrium as indicated by their long lifetimes, then there must be a triggering mechanism which can compress the gas further and initiate gravitational collapse. The proposed mechanisms for this include: 1) Strong stellar winds from OB stars. 2) Ionization fronts from OB stars. 3) Supernova remnant

shock waves. 4) Shock waves produced by cloud-cloud collisions. 5) A Galactic spiral density wave (GSDW). Observations of recently formed stars in molecular clouds suggest that low-mass stars, e.g. T Tauri stars, form throughout clouds while high-mass stars like OB stars are formed at the edges of molecular clouds. It is also thought likely that supernovae shock waves are responsible for triggering low-mass stars, and ionization fronts and the GSDW are the main triggering mechanisms for high-mass star formation (Clayton 1978; Larson 1981).

It appears from observations that all OB high-mass stars were formed in associations and never singly (Lada et al. 1978). Sequential star formation, as proposed by Elmegreen and Lada (1977), envisages high-mass star formation propagating through a GMC due to ionization fronts produced by a recently formed group of OB stars compressing the gas and triggering the formation of a contiguous group of massive stars in a timescale ~ 3 E6 years. This theory can be used to explain the observed alignment of groups of stars in OB associations, which have been found to occur in a linear sequence separated by distances of 10-20 pc and ages of 2-4 million years. This is shown schematically in Fig. 3.1 (taken from Lada et al. 1978). The initial trigger to start an OB association might be a random supernova explosion or more likely for a GMC in a Galactic spiral arm to be due to the GSDW.

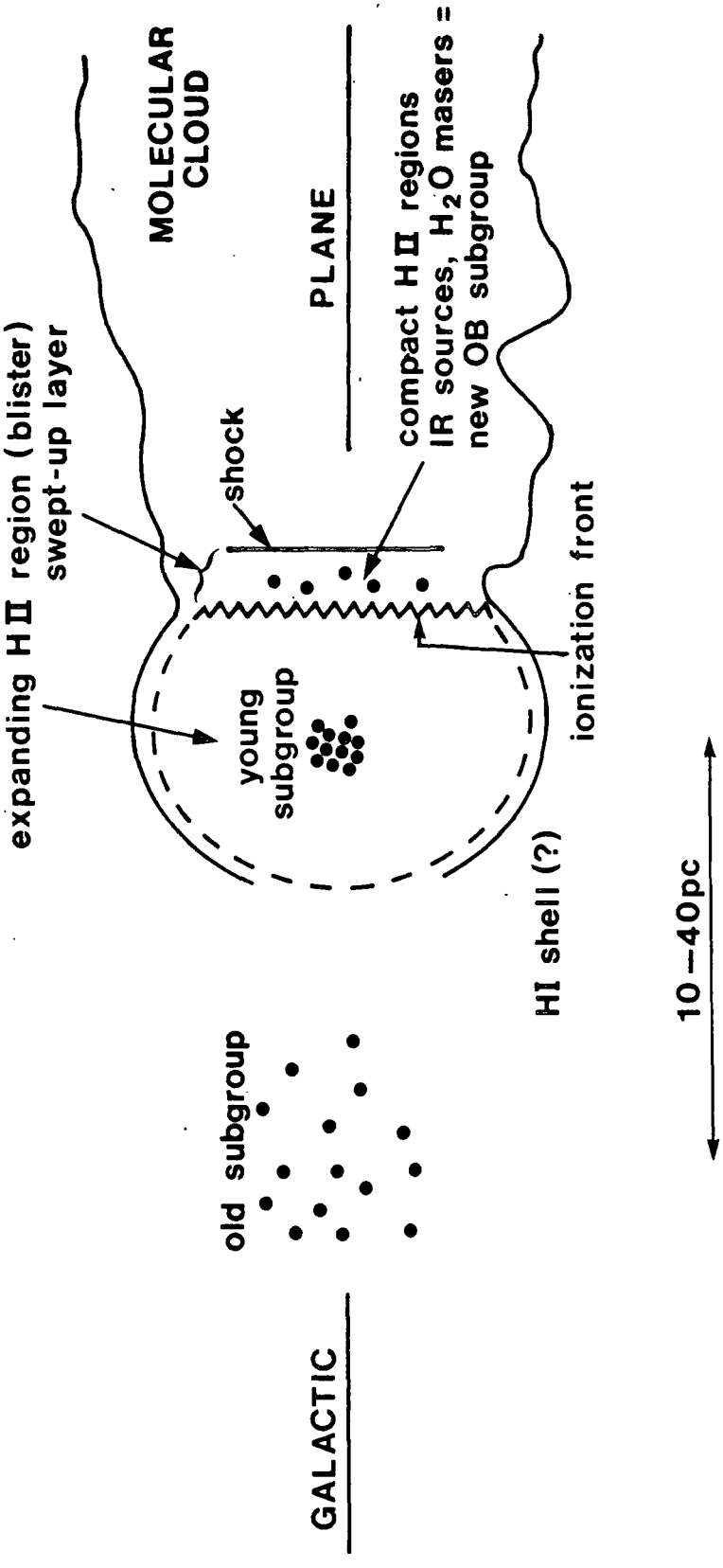

Fig. 3.1. Sequential star formation in OB associations.

Given that a part of a GMC exceeds the Jeans mass and starts to contract through gravitation (For average GMC densities and temperatures Mj ~ E3 Mo) then qualitatively one can see that if the collapse proceeds isothermally the Jeans criterion will be satisfied by smaller and smaller masses as the density increases - $Mj \sim (T^{1.5}/\rho^{0.5})$ - and that these masses will themselves collapse and form separate condensing fragments. This fragmentation will continue until some lower mass limit is reached (fragmentation stops when the fragments become opaque to their own radiation, Appenzeller 1982) thus giving rise to a cluster of stars. As observations of star clusters show little flattening, this implies that the fragmentation process starts early on before the cloud has had time to collapse to a disc. If a condensing fragment is of sufficient mass that it will gravitationally contract to a star on the main sequence, but not too massive that it will fragment further, then it is defined to be a protostar. The evolution of a collapsing protostellar cloud will be determined by gravity, magnetic fields if the cloud is partially ionized, angular momentum, and by how effectively it can radiate away the energy gained in collapsing ($Mj \sim T^{1.5}$). This in turn will be dependent on the amount of dust present, which is very effective in radiating energy in the infrared.

Numerical calculations of the dynamical collapse of a single isolated protostar were first done by Larson (1969). He found that the collapse was extremely non-homologous. These early calculations by Larson and other workers were based on the initial

conditions of a spherical non-rotating cloud of uniform density and no magnetic field. Since then, modelling of axisymmetric and 3-dimensional collapse has been performed, which is a refinement on early spherical models, but results of these models only show how protostellar clouds might collapse (Larson 1977). In the cases of spherical, axisymmetric, and 3-dimensional models, these have all resulted in non-homologous collapse and to condensates of approximately Jeans mass with little tendency for further fragmentation. However, in the more sophisticated 2- and 3-dimensional cases, the outcomes of collapse were not just single stars but either single stars / protostars + formation of rings/ accretion disc and then framentation into binary or multiple stars occurred (Larson 1977). The present picture of the collapse of a protostar can be described qualitatively as follows:

The quantitative results of calculations of the evolution of single collapsing protostars are given in terms of evolutionary tracks on a Hertzsprung-Russell diagram (see Fig. 3.2) for initial masses of 0.5, 1.0, 3, and 10 Mo and is taken from Iben (1965). The letters on the diagram refer to the various stages in the evolution of a one solar mass protostar. For a one solar mass protostellar cloud, the initial collapse is expected to proceed isothermally in gravitational free-fall with the loss of potential energy being radiated away by line emission from molecules and by dust in the infrared. This collapse continues with the result that a sharply peaked density distribution is formed in the center giving rise to a core. The core increases in density and becomes

optically thick thus trapping the infrared radiation and allowing the temperature of the core to rise (from the initial core temperature ~ 10 K). The luminosity of the star is also rising and reaches a peak at A. With the core having reached a density of ~ E11 cm-3 the core is opaque to infrared (mostly due to dust emission, Silk 1983) and its temperature increases nearly adiabatically (Larson 1973); at 1800 K molecular hydrogen will dissociate and produces a large rise in pressure thus halting the speed of collapse. The temperature of the core continues to rise so that first hydrogen and then helium is ionized giving rise to a plasma. The protostar has reached point B. Here energy is no longer transported throughout the star by radiation as convection sets in with the temperature gradient being greater than the adiabatic gradient. The track that the protostar now follows is termed a Hayashi track. At point C the protostar finally attains hydrostatic equilibrium. Transport of radiation is soley by convection, and as the radius of the protostar decreases, the luminosity thus decreases between points C -> D. The temperature of the core still increases and becomes sufficiently high for the core to become optically thin allowing radiation transport to become dominant (D). At this stage the evolving protostar is sometimes termed a pre-main sequence star. The star continues to accrete mass from the the surrounding protostellar cloud as it slowly moves to point E where the core temperature reaches the critical point when hydrogen fusion starts and the protostar has become a star on the main sequence.

This then is a qualitative description of the collapse of a low-mass star. As can be seen from Fig. 3.2, high-mass stars evolve differently with the pre-main sequence star being equilibrium radiative and moving along a radiative or Henyey track (as opposed to stars ~ 1 Mo which are in convective equilibrium and follow Hayashi tracks, Strom et al. 1975b). For stars >> 3 Mo it is expected that ignition of hydrogen will occur before mass accretion from the protostellar cloud has finished (Appenzeller 1982). The typical timescale for free-fall collapse of a star is given by Spitzer (1978, p287) as:

$$tff = \sqrt{\frac{3\pi}{32\ G\ \rho(0)}} = \frac{4.3\ E7\ years}{\sqrt{nh(0)}}$$

where nh(0) = initial hydrogen density (cm-3).
However, the theoretical times to reach each stage in the evolution of a protostar is marked in Fig. 3.2. So far this description has applied to single protostars in isolation, but one must consider whole clusters of stars forming, and as most stars (more than half) are observed to be in binary or multiple systems the evolution of these systems will have to be modelled (Larson 1977).

Other problems to be addressed in modelling star formation are the factors of how collapsing protostars are able to lose both their angular momenta and magnetic fields, which, if were conserved during collapse would be many times greater than observed. For a one solar mass protostellar cloud the initial angular momentum

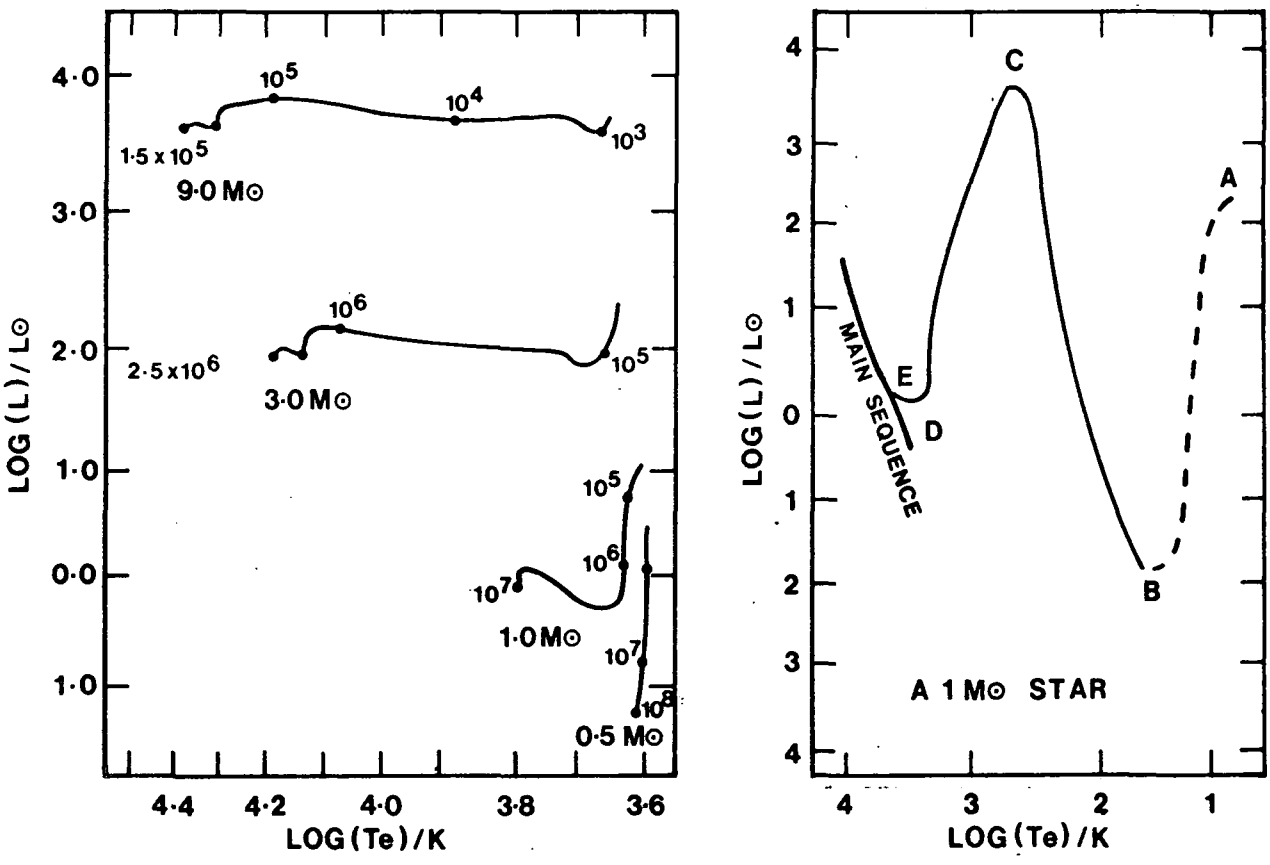

ADAPTED FROM IBEN (1965) APPROXIMATE TIMES TO REACH EACH STAGE OF EVOLUTION GIVEN ⊙

Fig. 3.2. Evolutionary tracks of collapsing protostars.

is thought to be ~ E22 cm2/s and the observed large-scale Galactic magnetic field is ~ 2.2 microgauss. However, for stars on the main sequence, the observed final states of angular momenta are ~ E15 cm2/s and their magnetic fields, which if conserved would be ~ E9 gauss, are typically ~ 1 gauss. To explain this, it is thought that the protostellar magnetic field is expected to play an important role in removing angular momentum through magnetic braking (Appenzeller 1982), while the low magnetic flux of main sequence stars might be due to the process of ambipolar diffusion. All models, however, are dependent on knowing the initial conditions of the molecular cloud before collapse and these are largely unknown (Larson 1978).

An important physical process in the evolution of the collapsing protostar is the ability of the star to radiate away the energy of collapse. A knowledge of dust density and emissivity and of the various molecular line transitions are required to determine exactly the dynamical evolution of the protostar. Another important detail in the evolution of pre-main sequence stars that is not fully understood is the phenomenon of stellar winds. Strong stellar winds have been observed in pre-main sequence stars like T Tauri stars $\langle \dot{M} \rangle$ ~ E-8 Mo/yr with 0.1 Mo being lost during collapse (Larson 1978). In early-type stars, where the stellar wind is the result of radiation pressure, mass loss is even greater ~ E-6 Mo/yr. These winds could occur in the convective phase of all pre-main sequence stars where acoustic or magnetohydrodynamic waves could heat the outer layers giving rise

to mass outflow (Appenzeller 1982). The amount of mass ejected by a star in its protostellar evolution is strongly dependent on its mass (Appenzeller 1982). The mass outflow and radiation pressure from young stellar objects, especially OB stars, will greatly affect the evolution of the molecular cloud, the protostellar cloud and possible evolution of protoplanets.

Some visual observations of processes involved in star formation provide some useful constraints to star formation theory, but because of the large amount of dust associated with protostellar clouds only details of pre-main sequence stars (PMSS) have been recorded. These observations are of: 1) Definite PMSS such as low-mass T Tauri stars, the subclasses of T Tauri stars like FU Orionis and YY Orionis stars, and Herbig emission-line stars (HES), which are high-mass (>2.5 Mo) PMSS. 2) Polarimetry of outflows from pre-main sequence stars. These outflows are driven by strong stellar winds often bipolar in nature with evidence for equatorial circumstellar disks, non-spherical reflection nebulae, CO outflow and collimation of Herbig-Haro objects (Cohen 1982). This phenomenon has been seen in both low-mass T Tauri stars and high-mass stars like Cep A (Cohen 1982). 3) Herbig-Haro objects, which are believed to be shocked interstellar gas produced by the focusing of isotropic stellar winds from PMSS and their interaction with the ISM (e.g. HH 24-27, Snell and Edwards 1982). 4) The types of compact reflection nebulae that are illuminated by pre-main sequence stars; these are often bipolar or cometary depending on their morphology (Konigl 1982). An example of a

pre-main sequence star that illuminates a bipolar nebula is LkHalpha 208 (Shirt 1984). 5) Star clusters such as recently formed OB, R and T associations. These star clusters will, through radiation pressure, ionization and stellar winds, disrupt the molecular cloud in which they formed. After the cluster has dispersed the cloud, the consequent loss of mass will then disperse the cluster giving rise to isolated field stars. Associations of OB stars, which have typical masses ~ several E3 Mo (Kerr 1977), will disrupt the molecular cloud from which they formed in ~ 4 E7 years.

Further observations of young main sequence stars can give the upper and lower mass limits to stars, which appear to lie in the range 0.1-100 Mo. The predictions of evolutionary PMSS models can be tested against the observed positions that the recently formed cluster stars occupy on the Hertzsprung-Russell diagram. Comparing the masses of GMCs and the masses of star associations forming in them, one can derive an approximate star formation efficiency. This is typically a few percent and as large as 5-10% for the Orion SFR (Shevchenko 1980) and Taurus-Auriga dark cloud (Silk 1983 and references therein). Indications on the different physical mechanisms involved in triggering and the formation of high- and low-mass stars should be revealed from seeing where different mass stars are born. One should examine how the star formation rate is dependent on gas and dust density and look at the role of dust grains in promoting star formation: Alfven and Carlqvist (1978) suggest that the sedimentation of dust grains in

a cloud could trigger the gravitational collapse of the cloud. From linear polarimetric observations of stars in star formation regions, the magnetic field geometry can be mapped which will show the roles magnetic fields have in star formation and cloud evolution (Vrba et al. 1976). It is important to determine the mass distribution of stars formed which is referred to as the initial mass function (IMF) and also the dependence of the IMF on cloud mass and the statistics of multiple stars. This can be derived from either the mass distribution in very young clusters where the stars will have lost very little mass or from field stars. Zinnecker (1984) has shown that the IMF is a function of the physical processes of star formation, and from modelling done by Zinnecker it appears a process of hierarchical fragmentation can lead to the observed log-normal IMF.

If protostellar collapse cannot be observed at visible wavelengths (PMSS are difficult to observe because of infalling dust which is opaque) then IR and molecular line observations (CO etc.) should provide the information on the physical parameters of protostellar collapse. This stage has not so far been observed; however, cloud cores, which are the regions sufficiently dense to form stars, will appear as CO hot spots with very little emission in the infrared or radio continuum (Evans 1981). For a collapsing protostar, one will see copious amounts of infrared radiation when the density of infalling matter falls and the optical depth decreases and one is then able to see the core of the protostar (Larson 1973). Possible protostars seen in the infrared are the

Becklin-Neugebauer (BN) object and the Kleinmann-Low nebula, which are compact IR objects in a molecular cloud adjoining the Orion Nebula (Thaddeus 1982). There is a rough evolutionary sequence to the observable size that a pre-main sequence star subtends as seen in first infrared and then radio wavelengths. A collapsing protostar will be first seen as a CO hot spot and then as the outer protostellar shell reaches 300 K it will be visible as a compact IR source (2-30 μm). Later, conditions in the protostellar envelopes or stellar winds of high-mass stars might be suitable for OH and H_2O maser emission, i.e. n ~ E5-E11 cm-3 and Lstar > E4 Lo (Reid and Moran 1981). For these high-mass stars, a compact HII region will be formed and start to expand. This phase lasts only ~ E5 years (Habing and Israel 1979). These young stars will then be seen in the radio continuum and from radio recombination line observations. Once an early-type star has reached the main sequence, its UV flux can create a CO hot spot as has been observed by Kutner et al. (1980) in CO observations of reflection nebulae. During the evolution to the main sequence most stars are believed to undergo a period of mass loss through stellar wind (Edwards and Snell 1984). Stellar winds and CO molecular outflows have been observed through CO line emission. These outflows from PMSS have velocities > 30 km/s, sizes ~ E18 cm, momenta ~ 200 Mo km/s, total energy ~ E46-47 erg and masses in the range 0.3-100 Mo (Bally and Lada 1983). Often associated with high velocity molecular outflows is the occurrence of maser emission and both phenomena are phases that last several E4 years. For the brightest compact HII regions, Strom et al. (1975b) has described three

stages in the early evolution of high-mass stars: 1) O star arrives on the MS. Small HII region forms. 2) Heated grains cause expansion of ISM near star. 3) Ionization front propagates towards low density regions. The blister model by Israel (1978) supposes that high-mass stars are formed at the edges of molecular clouds and through ionization of the surrounding gas and stellar winds, which cause the surface of the cloud to be disrupted, creates a cavity from which the ionized material flows away from the molecular cloud. Recently formed stars at the edges of molecular clouds could have their stellar winds focused by pressure gradients giving rise to shocked interstellar gas and Herbig-Haro objects (Canto and Rodriguez 1980). The arrival of massive OB associations leads to large HII regions forming and probably the end of star formation in the molecular cloud, but the formation of low-mass stars might promote further low-mass star formation. The molecular clouds with recently formed low-mass stars need to be probed at infrared wavelengths and IR surveys of GMCs can be used to locate and derive valuable PMSS observations.

3.2 Signposts of star formation

Discussed here are those signposts of star formation which indicate that stars have formed within the last few million years. A comparison is made of the observational evidence of the processes involved in forming stars in star formation regions with the above theoretical treatment. Strom et al. (1975b) have reviewed many of the signs of recent star formation and these are

now described in approximate chronological order both in the context of star formation theories and their relationship to one another.

1) Giant molecular clouds (GMCs) are the centres of major star formation in the Galaxy. There are over 4000 in the disc of our Galaxy and most occur in a ring between 4-9 kpc Galactocentric radius (Solomon et al. 1979). Most star formation in the Galaxy is due to the gravitational contraction of dense core regions in GMCs triggered possibly by the GSDW which results in hierarchical fragmentation, the final condensates being protostars. All star formation regions (SFRs) have been found in the densest regions of molecular cloud complexes (see the list of 49 SFRs by Shevchenko 1979). The typical timescale for the lifetime of a GMC is > few E7 years. The mechanism for forming GMCs is not understood, but is thought to rely on the GSDW. This wave rotates around the centre of the Galaxy at 13.5 km/s/kpc (or E6 yrs to cross a local GMC) and so local matter (for a two-arm spiral) passes through the wave once per solar rotation period (Lada et al. 1978). Thus, the most recent large-scale OB star formation delineates the passage of the GSDW.

2) CO hot spots and IR compact regions are signatures of recent star formation. CO emission from CO hot spots is generated either by an early-type star embedded in a molecular cloud which can warm the nearby interstellar grains and if these are thermally coupled to a dense surrounding gas will produce a molecular hot

spot, e.g. NGC 2023 (Emerson et al. 1975) or by a collapsing molecular cloud core region (Evans 1981). Protostars will emit copious amounts of radiation in the infrared so large-scale infrared surveys should help locate clusters of protostars or very young pre-main sequence stars. The heating of a region in a molecular cloud where protostellar collapse is taking place or where stars have recently formed is evident in the Orion Molecular Cloud where one can see the compact infrared objects, the Becklin-Neugebauer object and the Kleinmann-Low nebula (Larson 1973).

3) Compact HII regions and H_2O masers are usually closely associated as signposts of large-mass stars (at least 15 Mo). Compact HII regions have sizes < 0.5 pc and electron densities > E4 cm-3 and their ionization is produced by a recently formed OB star: L > E4 Lo and M > 10 Mo. As the ionized region is expected to rapidly expand, their lifetimes are only E5 years. When first produced, they will be seen as a compact IR source with no HII region, then later, high velocity water masers and a stellar wind could be associated with the object. Finally, an ultra-compact HII region (<0.1 pc) is formed which expands and usually becomes associated with an OH maser that disappears when the size of the HII region grows larger than 3 E17 cm (Reid and Moran 1981). The conditions in the circumstellar envelopes of protostars might be those that give rise to masering i.e. T ~ 500-1000 K, n ~ E7-10 cm/3, d ~ 10-100 A.U.

4) Pre-main sequence stars such as T Tauri stars of which more than 70 are known have been studied extensively in an attempt match their position on the Hertzsprung-Russell diagram with evolutionary models. It now appears that all T Tauri stars undergo directed mass loss during their evolution to the main sequence (Cohen 1982). Associated with PMSS are CO outflows. The mechanism for producing the energy and momentum of these outflows might be due to stellar winds in the form of collimated bipolar outflows which have velocities ~ 100 km/s. The archetypal CO molecular outflow is found in the molecular cloud L1551 where a collimated bipolar outflow is seen emanating from the infrared source, IRS5. The mechanism involved in these outflows is unknown, but is thought to be connected with the interaction of the stellar wind with the toroidal disc that is formed from the remnant protostellar cloud, the magnetic field, the accretion flow, and the density structure of the surrounding ISM. This outflow phase in the evolution of a pre-main sequence star might only last E3-E4 years (Cohen 1982). The more massive pre-main sequence stars are Herbig emission stars (HES) which are PMSS (B1-F8) approaching the main sequence along Henyey tracks and have masses > 2.5 Mo and ages between E5-E6 years.

5) Herbig-Haro objects are thought to be a phenomenon associated with pre-main sequence stars and have lifetimes ~ E5 years. Canto (1981) has given a recent review of observations and models of Herbig-Haro objects and concludes that they are produced by strong stellar winds (>100 km/s) from young stellar objects

interacting with the ISM. They are usually situated ~ 0.1-1 pc from the young stellar object and the stellar wind is focused by pressure gradients that might be expected to exist at the edges of molecular clouds (Canto and Rodriguez 1980), e.g. HH 28+29 in the molecular cloud L1551, which are high proper motion HH objects that are highly collimated with the molecular outflow (Cohen 1982; Cohen and Schwartz 1983).

6) HII regions are signposts of recent high-mass star formation as the stars which can extensively ionize the molecular clouds are massive OB stars. These stars have reached the main sequence and will disperse the cloud from which they formed in a period ~ 4 E7 years so HII regions are between E6-E7 years old. Over 700 are known (Clayton 1978) but are thought to be no longer active sites of star formation. Most are apparently located at the edges of molecular clouds (Israel 1978) and their study should elucidate how OB associations form.

7) Lindblad's ring is a circular structure of GMCs and OB associations in the Solar neigbourhood that surrounds the Sun. This ring is thought to be a giant star complex that is ~ 6 E7 years old and was produced by an input of energy of E51 ergs in a timescale ~ E7 years which corresponds to E3 Lo or the energy produced by the formation of a large group of OB stars (Elmegreen 1982). Here we see examples of primary and secondary star formation as well as sequential star formation of OB stars in individual GMCs. (See Elmegreen 1982 and references therein.)

Most of these signposts can be seen in individual SFRs; an example being the Rho Ophiuchi dark cloud. From examining several SFRs one can look at the factors which affect the star formation efficiency, star formation rate and IMF, like gas density, electron density, temperature, magnetic fields, chemical composition, shocks, etc. The Rho Ophiuchi cloud is an example of a molecular cloud that is probably collapsing (Martin 1978) and in it have been found some 67 IR sources at 2-micron (Strom et al. 1976). This is a recently formed cluster whose brightest members are of B3-F5 spectral type which are embedded in a dense (nH ~ E3-E5 cm-3) region of the cloud whose kinetic gas and dust temperature is ~ 30 K (Martin 1978). An important parameter that will greatly affect star formation is the magnetic field in the SFR. Are there large magnetic fields present in GMCs? To map out the magnetic field geometries of star forming molecular clouds, Vrba et al. (1976) has measured the linear polarization towards stars in five star formation regions.

Many star formation regions have been looked at to determine how star formation proceeds and these have included: NGC 2264, Mon OB1, Mon R2, Per OB2, but we will now look at observations of star formation in one particular region, the Orion Molecular Cloud Complex.

3.3 Star formation in the Orion Molecular Cloud Complex

The Orion molecular cloud complex consists of two large

molecular clouds, Orion A and B, the stellar associations Orion OB1 and R1, numerous signs of recent star formation like Herbig-Haro objects and masers etc., and the large ionized arc called Barnard's Loop. This region is the most well studied region of star formation in the Galaxy and covers an area some 10 by 15 degrees on the sky. At a distance of approximately 500 parsecs, very good resolution observations can be made of this extensive star formation region (SFR) which is the nearest part of the Orion-Cygnus local arm to the Sun. (10.5 kpc Galactocentric radius.)

Reynolds and Ogden (1979) have examined the optical evidence of the ionized gas associated with the star formation in the Orion-Eridanus region most of which is in an expanding shell-like structure: the visible ionized arc is called Barnard's Loop. The OB and R1 associations contain young O and B stars, most of which are between 1-7 million years old, and have a combined mass of 7 E3 Mo (Shevchenko 1980). The largest structure in the Solar neighbourhood is Gould's Belt, an association of B stars formed ~ 50 E6 yrs ago and 500 pc in extent (Kerr 1977).

To explain the existence of Barnard's Loop and the recently formed stars of the Orion OB1 and R1 associations, Cowie et al. (1979) has invoked a hypothesis that the observed expanding gas shells, HII region and 100 km/s radiative shock in Orion is due to both a recent supernova and a combination of supernovae, stellar winds and ionization fronts from the recently formed stars of the

Orion OB1 association. Barnard's Loop has resulted from either supernovae or OB stellar winds and radiation pressure (Clayton 1978). This area has been examined in various wavelengths such as work in:

a) the visible: Reynolds and Ogden (1979) - they looked at ionized gas through Halpha and [NII] emission lines in Orion and Eridanus. Reipurth (1985) has examined deep red United Kingdom Schmidt Telescope plates of L1630 and L1641 in order to locate Herbig-Haro objects. Herbig and Kuhi (1963) searched for stars with strong Halpha emission lines in L1630 near NGC 2068 and found 45 T Tauri stars.

b) CO emission line: Large-scale CO surveys of L1630 have been performed by Tucker et al. (1973), Milman (1975), and Kutner et al. (1977), with Kutner et al. having surveyed both Orion A and B molecular clouds. A detailed survey of CO emission of reflection nebulae by Kutner et al. (1980) included NGC 2068 and NGC 2023 in Orion. A more recent and better resolution survey of these two reflection nebulae was carried out by White et al. (1981).

c) the radio continuum: Matsakis et al. (1976) measured the radio continuum at 13, 4, and 2-cm in order to locate compact HII regions. One of the areas they looked at was NGC 2068. Werner et al. (1974) carried out measurements at 1-mm towards OMC-2.

d) the infrared: Strom et al. (1976) surveyed a region of L1630 at 2-microns and found many 2-micron sources to be clustered in the vicinity of reflection nebulae. The Orion molecular cloud OMC2 has been mapped by Gatley et al. (1974) in the infrared and from CO emission line observations.

From these observations, the mass and extent of all the star formation that has been going on in Orion has been revealed. A more detailed look at L1630 observations will be undertaken in Chapter 7.

Conclusions specific to the star formation in the Orion Molecular Cloud Complex are:

1) It is hypothesised (Elmegreen 1982) that through primary cloud formation a GMC was formed which produced a first generation OB association between 6-7 E7 years ago near the centre of the present-day Lindblad's ring (about the time that the Gould's Belt was formed).

2) From the energy deposited by the initial burst of star formation, secondary cloud formation then produced the GMCs of Lindblad's ring.

3) The collapse of regions of GMCs in this ring 20 million years ago gave birth to the Orion OB1 and Sco-Cen associations.

4) Sequential star formation in the Orion Molecular Cloud may have given rise to the present two molecular clouds, Orion A and B, through disruption of the original molecular cloud.

5) The stellar winds and ionization fronts from the Orion OB stars produce an expanding Barnard's Loop.

6) Present-day star formation appears to be centred on the Trapezium.

One must study the morphology and chemistry of molecular clouds to understand star formation (Clayton 1978) so we will now look at recent star formation regions in the cloud L1630 and

examine the local and global parameters of star formation i.e.: chemical abundance, molecular and electron densities, dust, gas and dust temperatures, masses, angular rotation, magnetic fields, cosmic ray flux, UV flux and the GSDW, and ask the questions: Is L1630 stable? How did it come into existence? How long will it last? What are the triggering mechanisms involved in star formation in L1630? especially to the question, what is the size and dust distribution around newly formed stars and how does it compare to theoretical models (Evans 1981). Polarimetry observations will be used to provide some of the answers in the following chapters.

CHAPTER 4 Polarimetry of NGC 2068

4.1 Introduction

Visually, NGC 2068 (Messier 78) is a bright reflection nebula (mv ~ 20.6 mag/sq. arcsec.) which measures 8' by 6' (Johnson 1960). It lies in the dust cloud L1630 (NGC 2068 1950.0 coords: R.A. 5h 44m 13s, Dec. 0 deg 2 min.) at a distance of ~ 500 pc (Lee 1968). Associated with the nebula are three stars: HD 38563N, S, and C with HD 38563N being a visual binary (separation 2.5") and forming a triplet system with HD 38563S; this is known as ADS 4374 (Aitken 1932). Data on these three stars are given in Table 4.1. The star HD 38563N suffers ~ 3 magnitudes more extinction than HD 38563S (Strel'nitskii 1970) so HD 38563S may be foreground to the dust (Zellner 1970). To the north of HD 38563N there is a dark lane of obscuration running east-west with a small patch of nebulosity to the north-west of the main nebula. This can be seen in Plate 1 which is a copy of the United Kingdom Schmidt Plate Unit (UKSTU) plate J8970.

In the vicinity of NGC 2068, studies of carbon recombination line spectra by Pankonin and Walmsley (1978) and observations of CO emission by White and Phillips (1981) have revealed many molecular clouds, and centred on the reflection nebula is a CO hot spot. From 2-mm H_2CO line emission observations towards NGC 2068, Lada et al. (1974) showed that the reflection nebula is embedded in a molecular cloud whose mass they estimated to be > 260 Mo.

There are many recently formed stars in this region of L1630 as has been shown by surveys of: T Tauri stars (Herbig and Kuhi 1963); 2-micron sources (Strom et al. 1975a; Strom et al. 1976); and by the most recent NIR survey of Sellgren (1983). Evidence of recent star formation is signposted by the cluster of Herbig-Haro objects HH 24-27 which are some 14' south of NGC 2068 (Snell and Edwards 1982), a water maser (Haschick et al. 1983) and a type I OH maser (Johansson 1974).

Table 4.1. Data on the stars associated with NGC 2068.

Star	R.A.	Dec	mv	Sp	Eb-v	Pv	P.A.
	h m s	o ' "	mag	class	mag	%	degrees
HD 38563N	5 44 10.8	0 4 19.2	10.56	B1-B2	1.42	2.1	15
HD 38563S	5 44 9.5	0 3 32.5	10.42	B3-B5	0.78	4.2	100
HD 38563C	5 44 11.5	0 1 38.0	13.09	A0 II	0.96	-	-

data referenced in: Strom et al. (1975a)

Strel'nitskii (1970)

AGK3.

Plate 1. A copy of UKSTU plate J8970 showing NGC 2068.

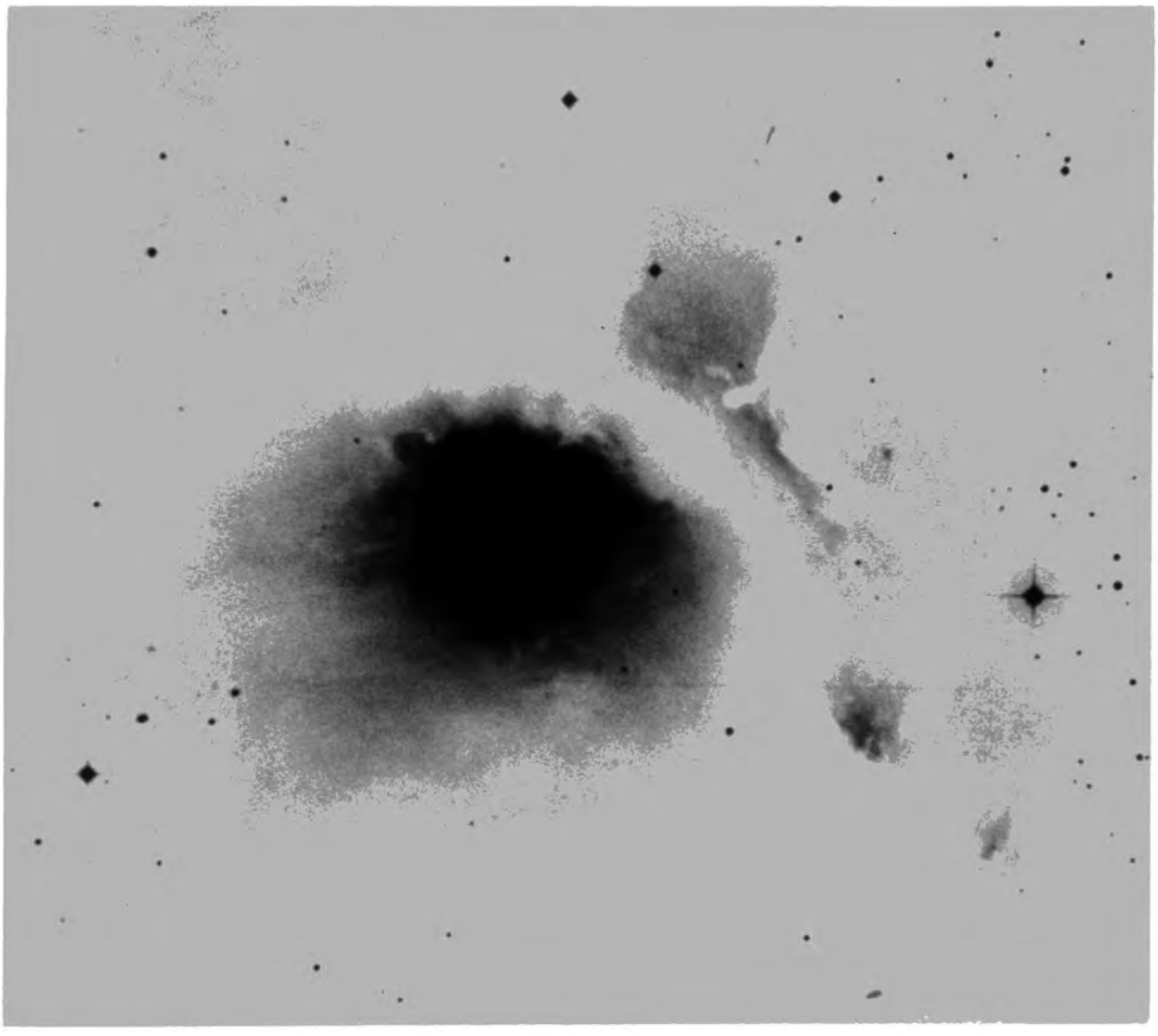

4.2 Summary of previous work

Previous optical polarimetry work on the reflection nebula NGC 2068 has been done by the following workers: Johnson (1960); Glushkov (1965); Elvius and Hall (1966); Strel'nitskii (1970); and most recently by Zellner (1970). All these workers (except Glushkov) used single aperture polarimeters so were only able to select a few small regions of the nebula for study. Measurements of polarization and colour are tabulated in Table 4.2 giving the position relative to the illuminating star HD 38563N (Elvius and Hall 1966) in arcseconds, the size of aperture, and the type of filter used.

To summarize their conclusions: it was found that the nebula polarization is positive (E vector at right angles to the scattering plane) and shows a radial symmetry about HD 38563N which is therefore the sole illuminating star. The polarization was found to increase with offset distance to a maximum of 15-20% and increased uniformly with wavelength. The strong spectral dependence of polarization is due to Mie-scattering by dust grains (Zellner 1974). Zellner (1970) observed a small but definite rotation of position angle with wavelength. From the difference in colour excess between the stars HD 38563N and S, the latter star appears to be foreground to the dust, while there appears to be a dust globule (elongated north-south) in front of HD 38563N. Colorimetry by Zellner, Johnson, and by Elvius and Hall all showed

that the nebula was extremely blue ([B-V]neb-[B-V]star ~ -1.0) and became bluer with offset distance. The total number of polarization measurements tabulated in Table 4.2 are 51 covering a range of aperture sizes between 10-40 arcseconds with the furthest regions observed being 60" W, 63.3" E, 114.5" S from HD 38653N. No measurements of polarization were made to the north of HD 37903, but Glushkov (1965) in his Fig. 1 shows the polarization up to 3.5 arcminutes south of the illuminating star; however, no values were tabulated. The errors quoted by the authors on degree of polarization and position angle were as follows: Glushkov, +/- 1.5 % polarization for bright areas and +/- 2.5 % other regions and +/- 8 deg. in position angle; Strel'nitskii, +/- 0.4 % polarization and < 5 deg. position angle; Zellner, +/- 0.4 % and 1-2 deg. position angle; while Elvius and Hall, and Johnson gave no values for errors. The wavelength dependence of polarization of HD 38563N was found by Zellner to be unusual as its differs markedly from the mean wavelength dependence of interstellar polarization as measured by Coyne and Gehrels (1967) and Coyne et al. (1974). Strel'nitskii showed that both HD 38563N and S had an anomalous wavelength dependence of polarization since the polarization was found to increase towards the red end of the spectrum.

Comparisons of this data and that taken with the Durham polarimeter will be made mostly with Zellner's observations and those of Elvius and Hall as these observations provide the most extensive and accurate polarization measurements.

Table 4.2. Previous polarimetry of NGC 2068.

Reference	Aperture position (")	Aperture size (")	Filter (UBV)	Polarization %	Position angle degrees
Johnson	HD 38563N	-	V	2.5	99
(1960)	HD 38563S		V	3.6	0
Glushkov	HD 38563N	12	V	2.2	99
(1965)	HD 38563S		V	3.6	0
Elvius &	HD 38563N	14,29	U	0.5	-
Hall (1966)			B	1.3	175
			V	2.4	179
	HD 38563S	14,29	U	3.4	92
			B	4.0	90
			V	4.3	96
	20.0 W, 20.0 S	29	V	0.2	-
	38.0 W, 28.0 S	29	U	3.5	116
			B	3.4	119
			V	4.2	118
	40.0 W, 40.0 S	29	U	3.6	129
			B	4.4	144
			V	4.9	137
	60.0 W, 60.0 S	29	U	4.6	134
			B	5.5	132
			V	8.3	133
	47.0 E, 48.0 S	29	U	2.5	76

Table 4.2. Previous polarimetry of NGC 2068 contin.

Reference	Aperture position (")	Aperture size (")	Filter (UBV)	Polarization %	Position angle degrees
Elvius & Hall (1966)	47.0 E, 48.0 S	29	B	5.5	47
			V	7.5	36
	46.6 E, 33.3 S	29	U	4.5	34
			B	4.8	11
			V	6.1	29
	46.6 E, 6.7 S	29	U	5.5	1
	23.3 E, 33.3 S	29	V	3.5	52
	23.3 E, 6.7 S	29	V	3.1	24
Strel'nitskii (1970)	HD 38563N	13	B	1.3	-
			V	2.1	-
			R	2.6	-
	HD 38563S	13	U	1.9	-
			B	2.9	-
			V	4.2	-
			R	4.2	-
	20 W, 59 S	13	~B	6.0	103
	0 S, 10 E	13	~B	4.0	8
	33 W, 46 S	13	~B	5.0	121
Zellner (1970)	HD 38563N	10	U	2.78	-
			B	2.33	13.5
			G	1.93	8.5

Table 4.2. Previous polarimetry of NGC 2068 contin.

Reference	Aperture position (")	Aperture size (")	Filter (UBV)	Polarization %	Position angle degrees
Zellner	HD 38563N	10	0	1.56	10.2
(1970)			R	1.21	15.0
Region	63.9 E, 47.2 S	30.8	U	4.9	45.6
I			B	7.2	45.4
			V	8.4	43.3
			0	9.1	42.3
			R	12.5	40.8
Region	9.9 E, 114.5 S	40.7	B	12.1	87.2
II			0	16.4	85.8

4.3 New observations

An early reduction of polarimetric data of NGC 2068 produced from data taken using a McMullan electronographic camera and the Durham polarimeter at the f/15 focus of the 1-metre S.A.A.O. telescope utilised programs developed by Drs. Warren-Smith and Pallister on the NUMAC (Northumbrian Universities Multi Acess Computer) computer. The reduction system is fully described in Warren-Smith's thesis (Warren-Smith 1979) and a paper written by Dr. Scarrott and the author based on this initial analysis can be found in Appendix A (Mannion and Scarrott 1984).

Subsequent reduction of the data on this nebula and that of NGC 2023 (chapter 6) involved using the EDRS (Electronographic Data Reduction Sytem) and DIPS (Durham Imaging Polarimetry System) packages: a suite of programs that were based on the previous package used on NUMAC and now including new software designed to reduce CCD data, but implemented on the SERC's Durham Starlink node using a Digital Equipment Corporation Vax 11/750.

A comparison will be made of the two reductions in Appendix B. The authors of the earlier observations were not able to answer the questions as to whether the polarization of the stars HD 38563 N and S is intrinsic or not and if there is a component to the nebula polarization which is due to aligned grains. The data presented here will be used to answer these questions.

4.4 The polarimetry data

The data were obtained in March 1979 at the S.A.A.O. using a 4-cm McMullan electronographic camera giving a field of view of 9.2 arcminutes. Eight plates were taken of the object NGC 2068 using a broadband visual filter (GG455 + BG38) whose effective wavelength was 0.52 micron. The exposures were for 15 minutes on Ilford L4 emulsion. These plates were digitised using a PDS microdensitometer with 25 micron resolution (which matches the resolution of the instrument) giving a 512 by 512 pixel array. The Durham polarimetry system is a seeing limited technique and errors due to variations in sky transparency, night sky brightness and

polarization are minimised and good flat fielding allows for instrumental effects, so the accuracy obtainable is close to the photon noise limit. The polarimeter and reduction technique is described in Scarrott et al. (1983).

The DIPS reduction involves using flatfield images to enable corrections to be made for point-to-point variations in detector sensitivity. Corrections are also made for unexposed film density, non-linearity in the emulsion and microdensitometer as well as the detection of blemishes such as dirt and scratches. The images are aligned using field stars and grid spots. Areas of sky are interactively chosen for the final reduction procedure which involves estimating the background night sky signal and subtracting this off the nebula plus sky signal. This procedure then gives two separate polarization maps for the two grid positions (designated 'grids in' and 'grids out'). Normalisation of the two grid maps was performed using east-west total intensity traces across the nebula.

The grids of the polarimeter were aligned north-south with the field of view centred on the reflection nebula so that the whole object could be measured. There are two positions for the polarimeter grids termed 'grids in' and 'grids out' which define the field of view of the Durham polarimeter. Plates taken in the 'grids out' position have stars HD 38563N, S and C clearly visible while 'grids in' data has only HD 38563C.

The two polarization maps representing 'grids in' and 'grids out' were joined by matching the positions of the star HD 38563C and the centres of centrosymmetry of the polarization vectors. This map is shown in Fig. 4.1. The integration bins are 5 by 5 pixels (corresponding to 6 by 6 arcseconds) at intervals of 5 pixels. Plate 2 is a photograph of the intensity image produced after reduction and alignment of the data which was displayed on the ARGS image display unit. This plate can be compared with the area around NGC 2068 on the United Kingdom Schmidt Plate Unit (UKSTU) plate J8970 that was examined by the author using a binocular microscope (see Plate 1). This examination was similar to that carried out by Reipurth (1985) who looked for nebulous objects in L1630 in an attempt to identify young stellar objects.

From the reduction of the electronographic data a 3-d image stack was produced which contained 2-d images of polarization, polarized intensity and total intensity. These images are shown in Plates 3-5. Linear traces of polarization, polarized intensity and total intensity through the illuminating star, HD 38563N in a north-south direction are shown in Figs. 4.3 - 4.5. For these traces the data was binned 3*3 in order to smooth the data.

Examining Plates 1 and 2 of the reflection nebula and the surrounding region of L1630, the nebula exhibits an inhomogeneous appearance with a sharp edge to the dust to the north of HD 38563N. Beyond this lane of obscuration to the north-west of the main nebula is a faint patch of nebulosity which extends to the

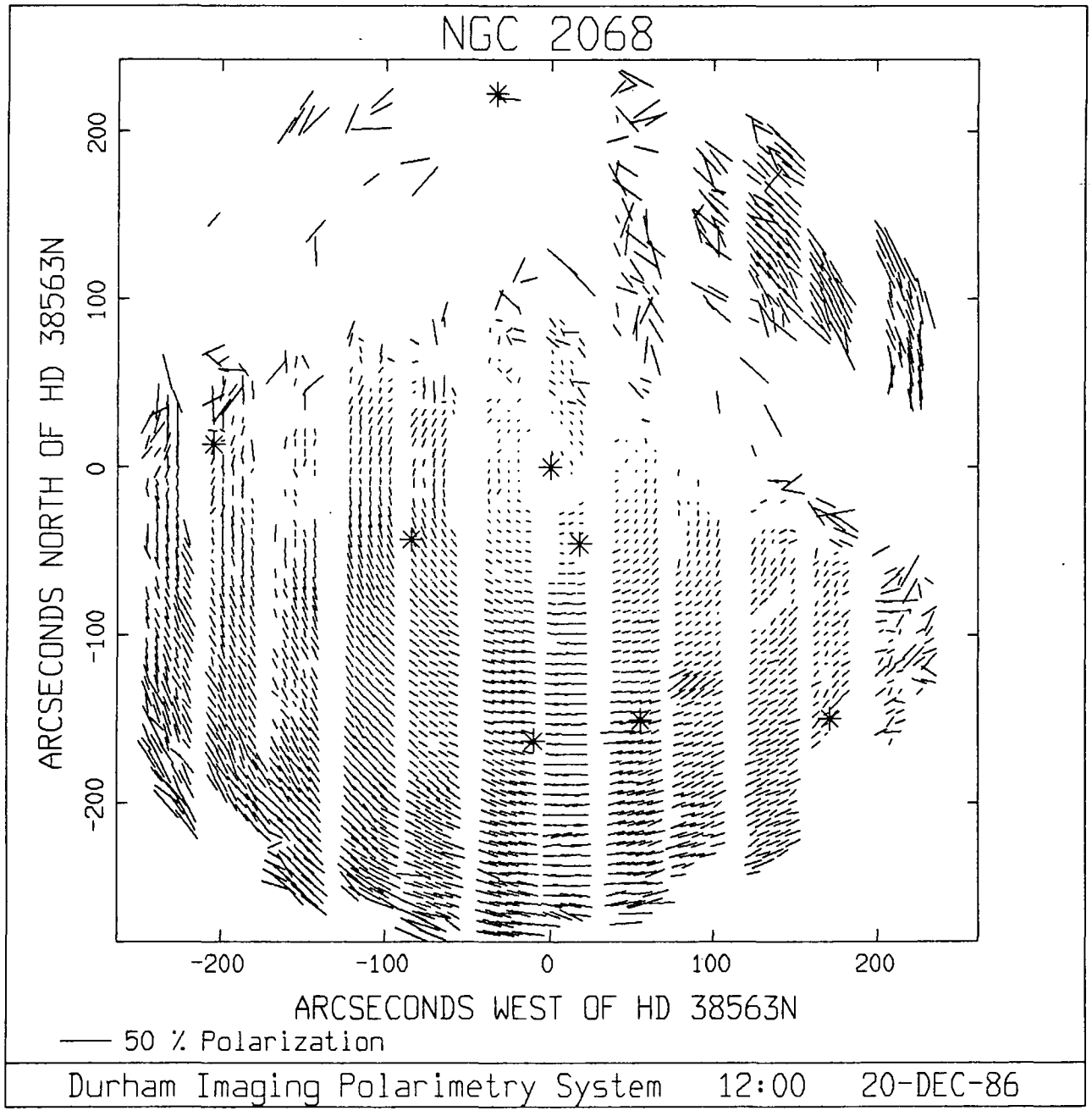

Fig. 4.1. A visual polarization map of NGC 2068.

star M78/111 (Strom et al. 1975a). This apparently marks part of the northern limit to the dust cloud L1630. Plate 2 shows the elongated globule which lies in the direction of HD 38563N (Zellner 1970) but which cannot be seen on the UKSTU plate J8970. None of the Herbig-Haro objects of Haschick et al. (1983) could be seen on the Schmidt plate.

Table 4.3 lists the infrared and visible stars that were found in the vicinity of NGC 2068 in the near-infrared surveys of Strom et al. (1975a), Strom et al. (1976) and Sellgren (1983). The star names are taken from the designations used in these surveys. These stars are plotted in Fig. 4.2. From a comparison of Fig. 4.2 and Plate 2 - the total intensity image of NGC 2068 from the electronographic data - one can see that stars HD 38563 N, S, C and M78/109 and LkHalpha 306 are visible. Using these stars and their celestial coordinates, the plate scale was calculated to be 1.20 +/- 0.02 arcseconds/pixel.

Visual inspection of the electronographic plates and the final intensity image after reduction shows three other stars visible which remain unidentified but are marked on the polarization map in Fig. 4.1. The extent of the field of view is approximately 243" N, 279" S, 248" E and 233" W offset distance from the star HD 38563N for the combined map.

Interogating the IRAS point source catalogue (IRPS) there is one source (05439+0003) which is within the boundary limit

Table 4.3. Infrared stars associated with NGC 2068.

Star	R.A.			Dec.			K	Offset from	Ref.
	h	m	s	o	'	"	mag	HD 38563N	
M78/111	5	43	44.9	-0	1	23	9.09	389 W, 342 S	3
SSV 7	5	43	56.9	0	5	47	10.6	209 W, 88 N	3,4
M78/109	5	43	58.9	0	1	47	10.0	177 W, 153 S	4
M78-4	5	44	0.4	0	5	40	9.76	156 W, 81 N	4
M78-3	5	44	0.7	0	3	16	11.2	151 W, 63 S	4
M78-5	5	44	1.9	0	5	23	9.67	133 W, 64 N	4
LkHa 304	5	44	3	0	0	17	9.8	119 W, 242 S	1,4
M78/106	5	44	6.3	0	3	47	10.15	67 W, 29 S	4
M78/107	5	44	6.4	0	4	1	10.62	66 W, 18 S	4
HD 38563S	5	44	9.5	0	3	33	8.23	20 W, 46 S	2,4
M78/104	5	44	9.7	0	4	25	8.94	17 W, 6 N	4
HD 38563N	5	44	10.8	0	4	19	6.82	0 E, 0 S	2,4
HD 38563C	5	44	11.5	0	1	38	8.66	11 E, 161 S	2,4
LkHa 306	5	44	16	0	3	36	10.3	83 E, 41 S	1,4
LkHa 309	5	44	33	-0	0	6	9.99	333 E, 265 S	1,3

References:

1) Herbig and Kuhi (1963)

2) Strom et al. (1975a)

3) Strom et al. (1976)

4) Sellgren (1983).

Notes:

Error on R.A. and Dec. ~ 2-3 arcseconds.

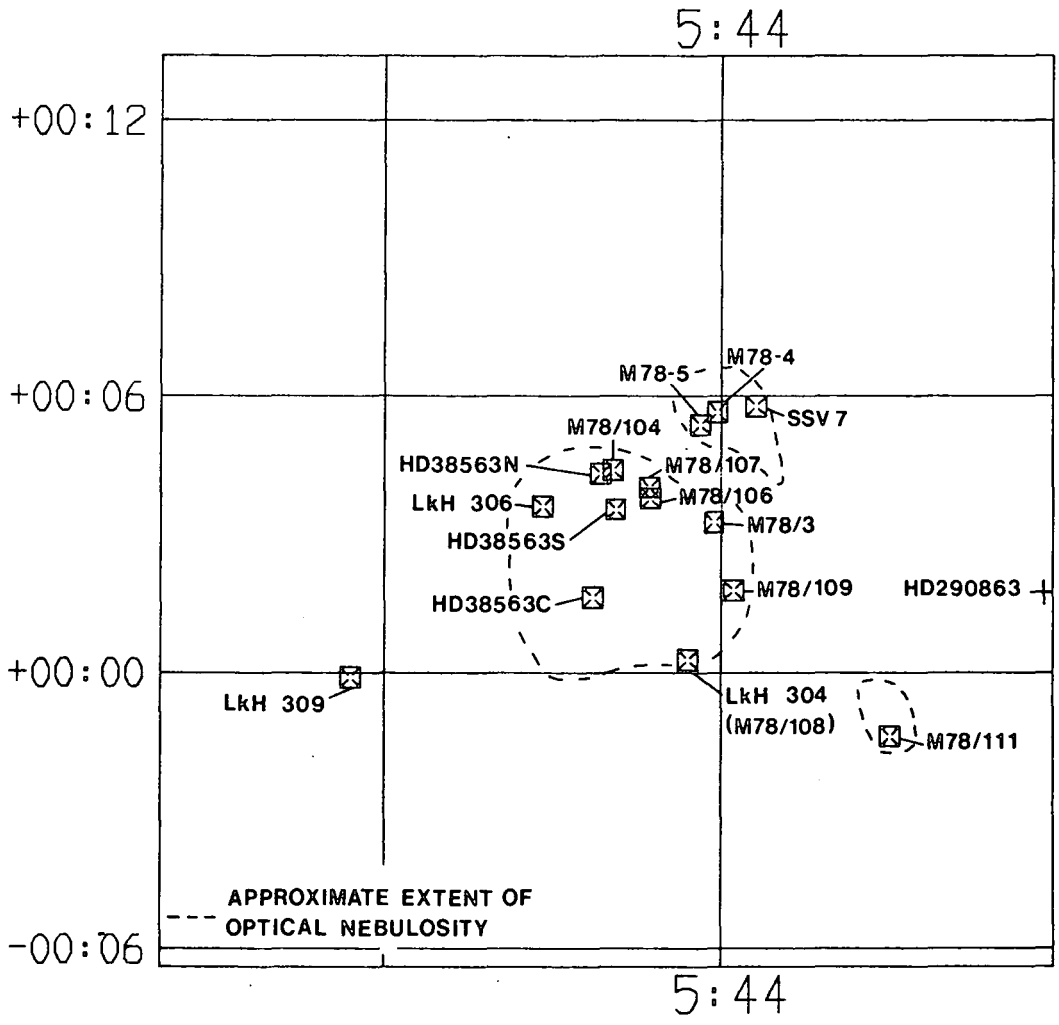

Fig. 4.2. A map of the region of NGC 2068.

Plate 2. Total intensity image of NGC 2068.

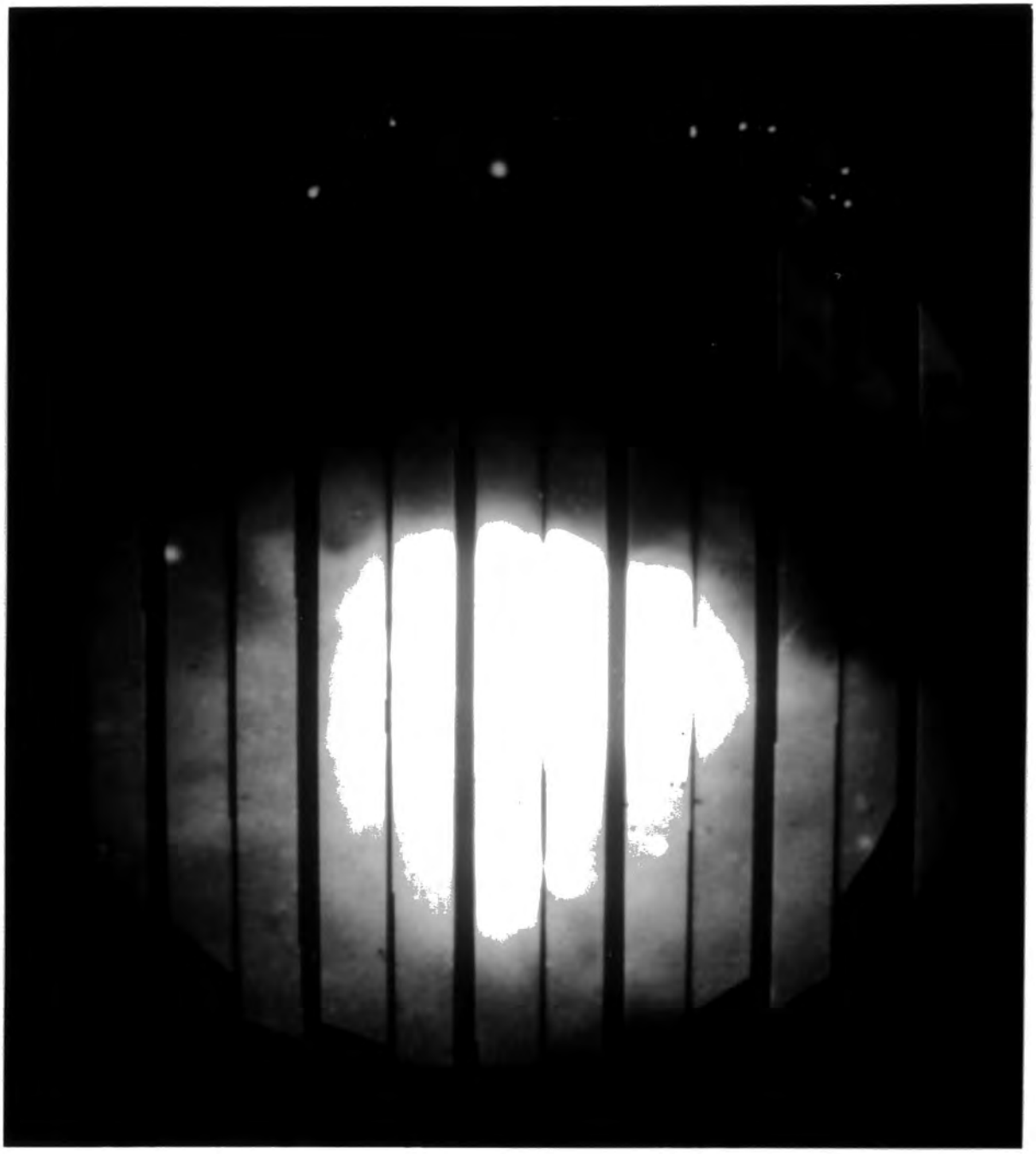

of the visible nebula and several that may be associated with the nebula and could be deeply embedded T Tauri stars. The resolution of this IRAS data is ~ 2 arcminutes.

The faintest stars visible on the electronographic data are: LkHalpha 306 r ~ 13.1 mag., M78/109 r ~ 16.1 mag. Sellgren (1983).

The visual polarization map of NGC 2068 shows a pattern of polarization vectors which are centrosymmetric about the star HD 38563N. No other star seems to affect this overall pattern of polarization vectors. The dark lane of obscuration to the north of HD 38563N is not polarized, but the small patch of nebulosity to the north-west is due to reflected light off dust grains; the source of the illumination being HD 38563N.

There is no evidence for aligned grains which would be manifest if magnetic fields were present as a region of parallel polarization vectors (e.g. NGC 6279; Ward-Thompson et al. 1985).

Looking at the polarization trace shown in Fig. 4.3, it is seen that the degree of polarization is approximately 1-2 % close to the star HD 38563N then rises monotonically to 20 +/-2 % at 4.2 arcminutes south, while to the north it increases more rapidly to greater than 15 % at 1.5 arcminute north of the illuminating star.

The trace north-south through HD 38563N for polarized intensity shows a maximum at 1.8 arcminutes south of the

illuminating star and very little polarized light coming from regions to the north. The total intensity trace shows a maximum at the position of the illuminating star which then decreases monotonically to the south but decreases rapidly towards the north.

Comparing the new observations with those of Zellner (1970) and Elvius and Hall (1966) of their selected regions I and II (Table 4.4), one sees general agreement on the degree of polarization and position angle within the quoted errors.

Table 4.4. Polarization of selected regions of NGC 2068.

Region	New Observations		Zellner (1970)		Elvius and Hall	
	Pol.	P.A.	Pol.	P.A.	Pol.	P.A.
63.9 E, 47.2 S	8.0	37.3	8.4	43.3	-	-
I						
9.9 E, 114.5 S	11.6	81.5	16.4	85.8	-	-
II	+/- 1.7	4.0	0.4	1-2		
47.0 E, 48.0 S	6.4	47.6	-	-	7.5	37.6
I	+/- 1.6	9.7				

For Zellner's region I, the polarization was calculated for a 19 arcsecond circular aperture, however for region II this could not be performed and an average polarization was found for a 42 arcsecond square aperture. This procedure was also carried out for Zellner's region I (Pol. = 8.6 +/- 1.2; P.A. = 34.1 +/- 9.3) and region I of Elvius and Hall (29.9 arcsecond square aperture).

Plate 3. Visual polarization of NGC 2068.

Plate 4. Polarized intensity of NGC 2068.

Plate 5. Total intensity of NGC 2068.

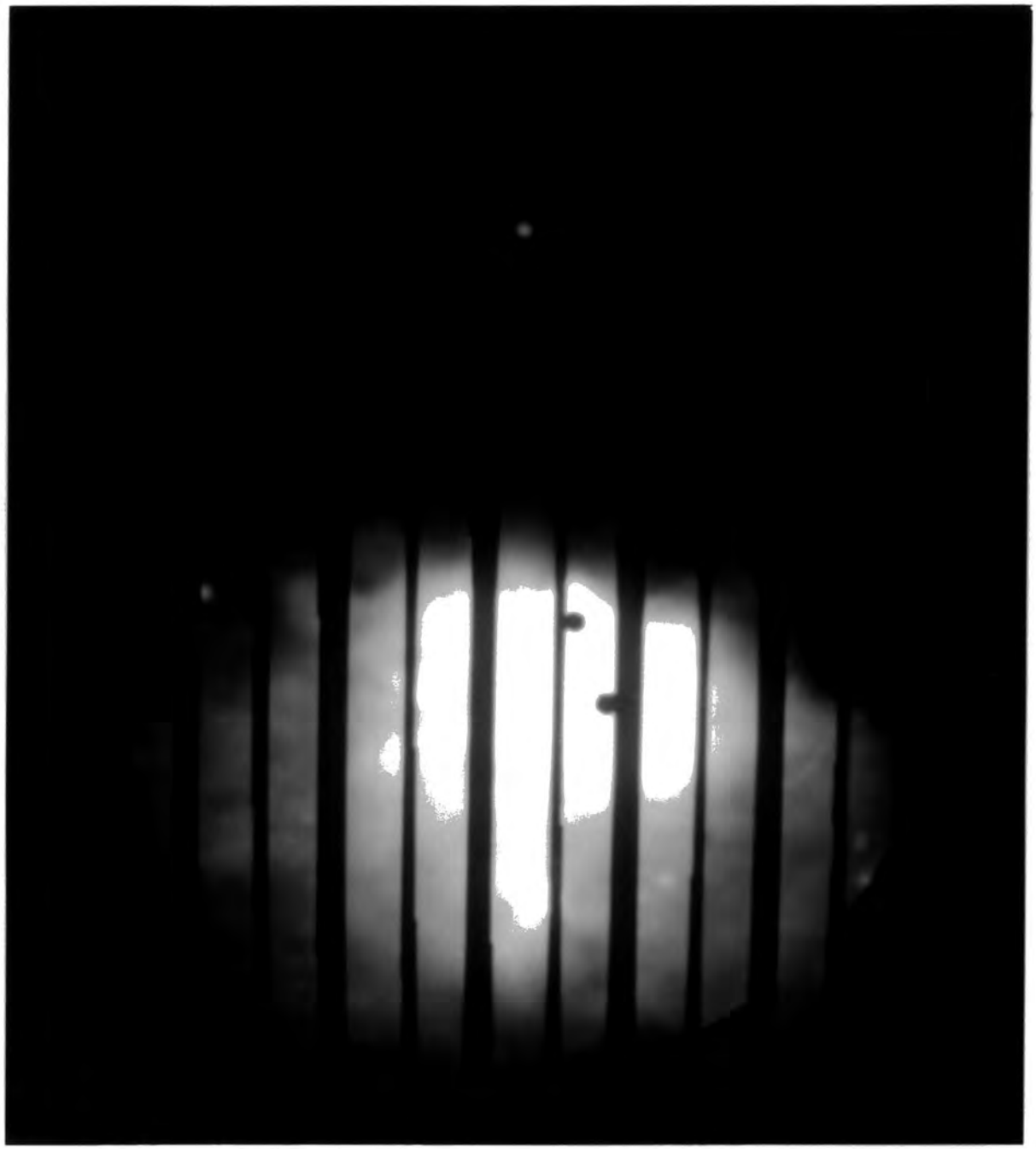

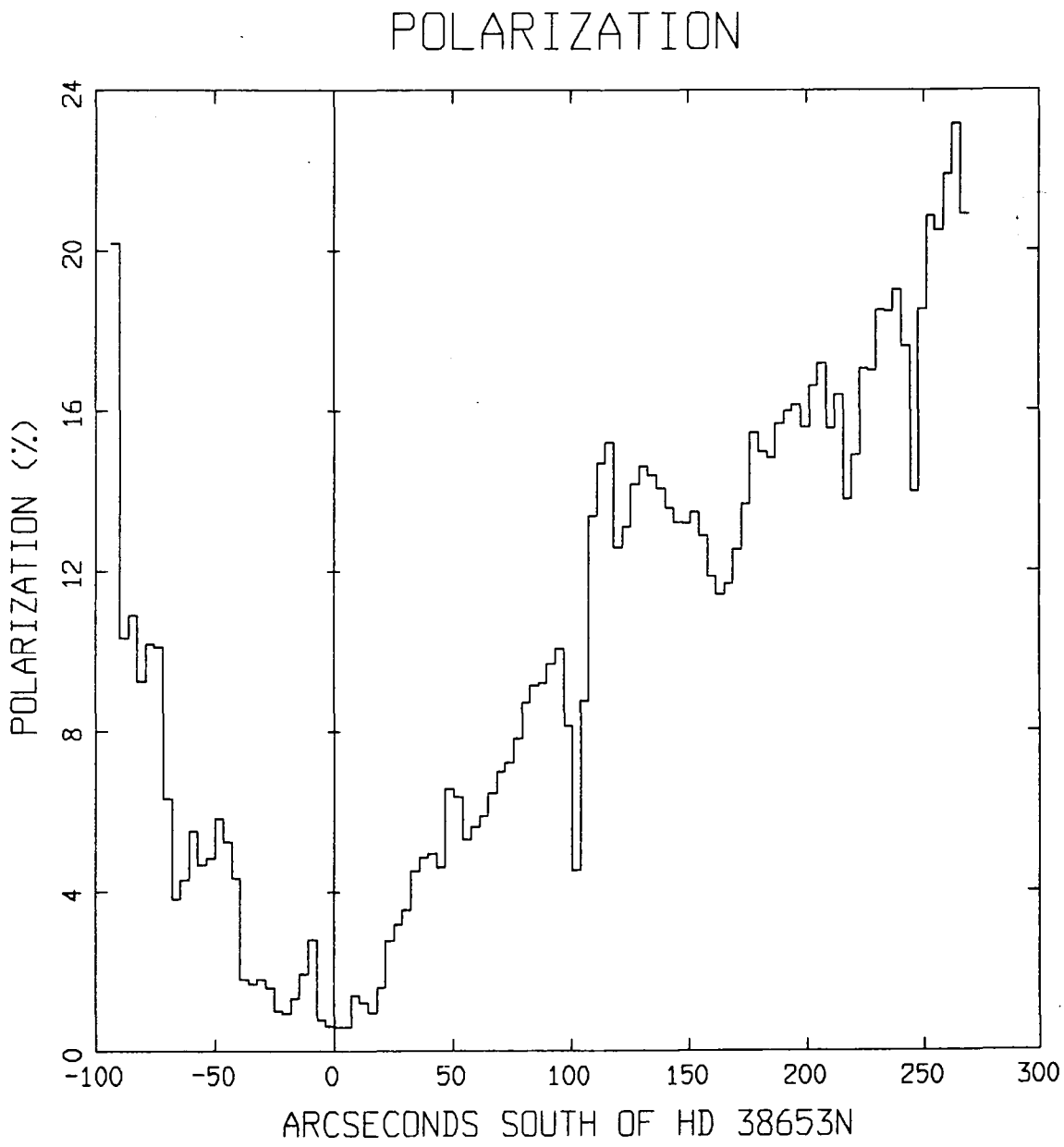

Fig. 4.3. Polarization trace through HD 38563N in a north-south direction.

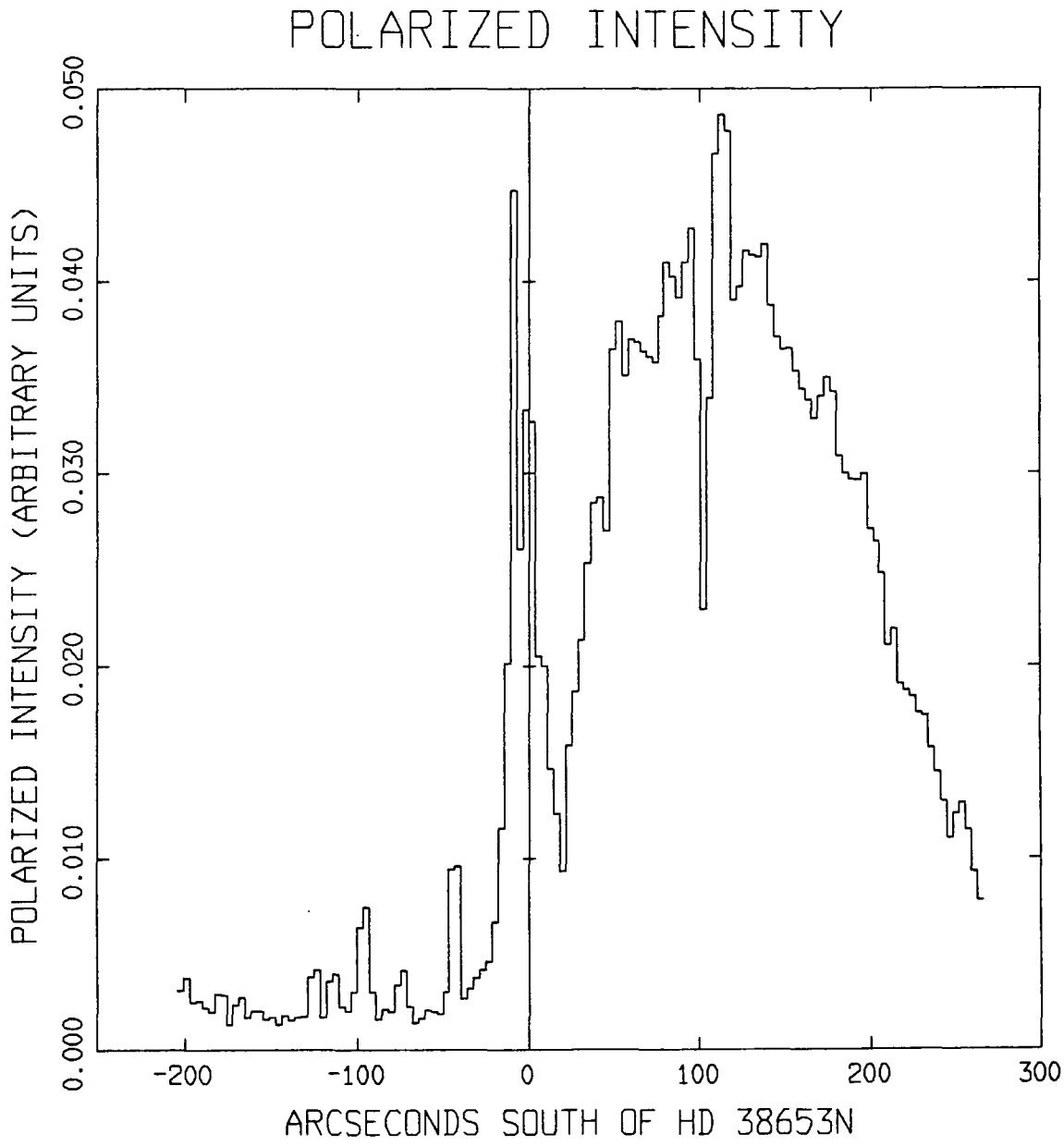

Fig. 4.4. Polarized intensity trace through HD 38563N in a north-south direction.

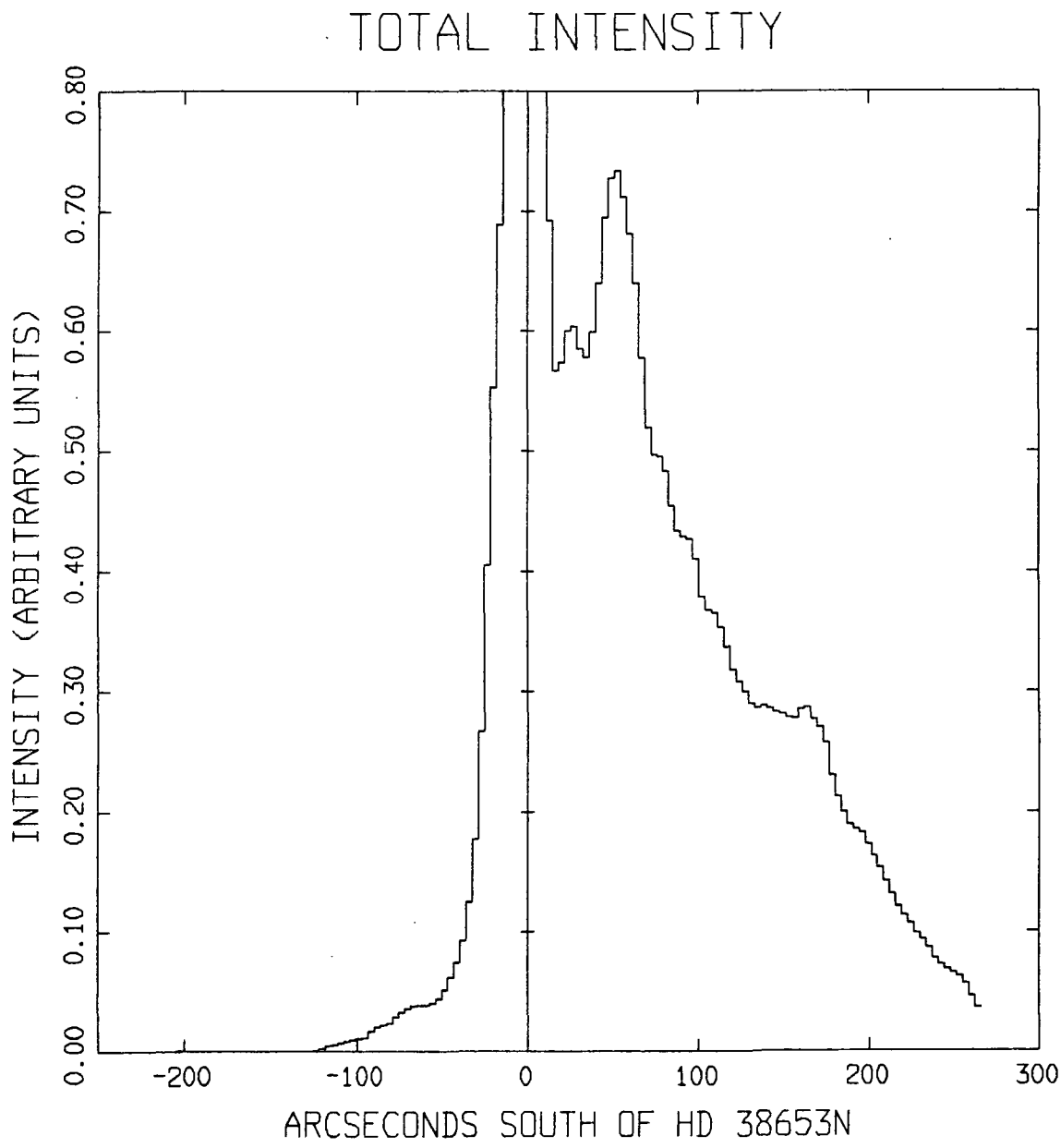

Fig. 4.5. Total intensity trace through HD 38563N in a north-south direction.

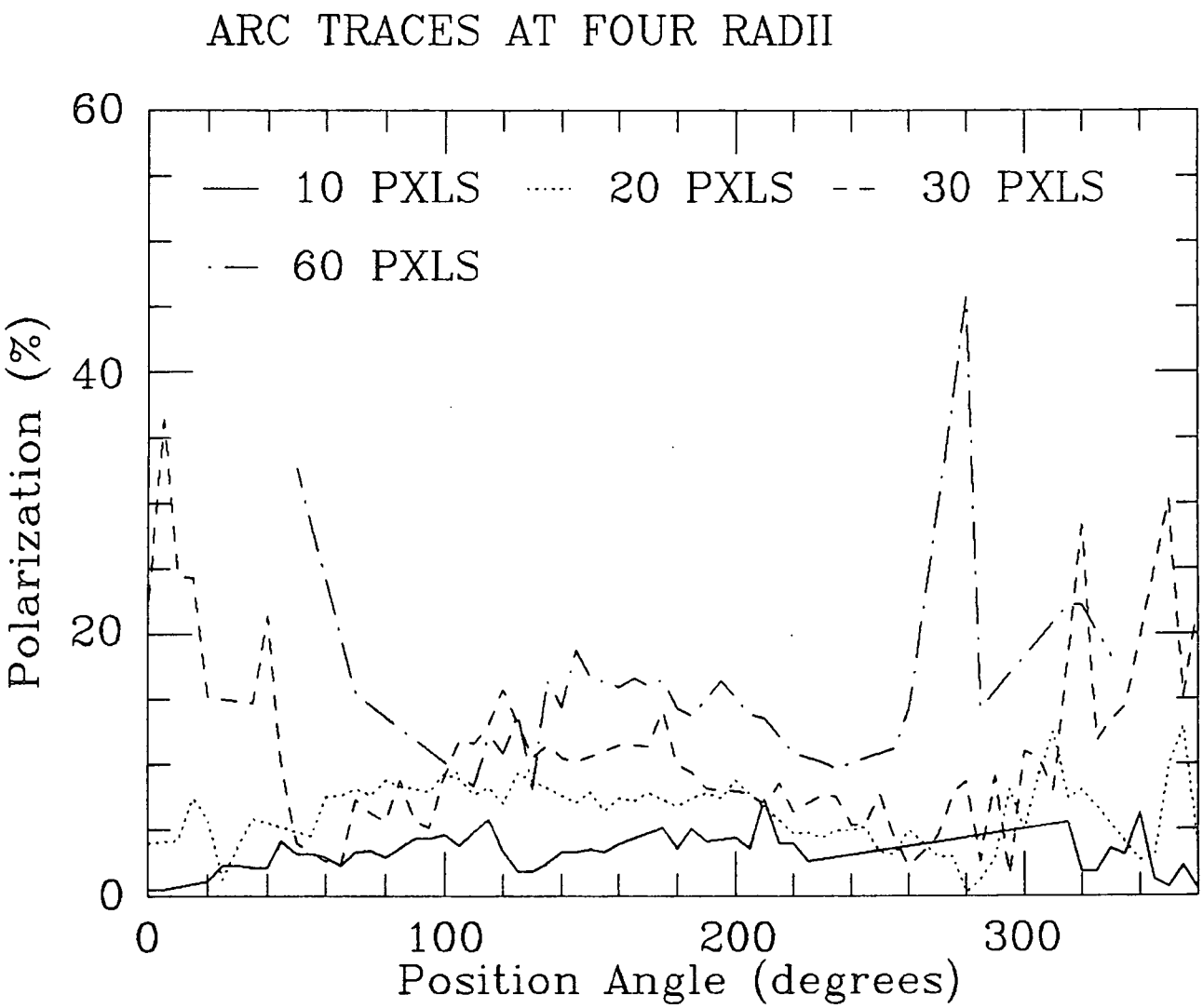

Fig. 4.6. Arc traces about HD 38563N.

As well as linear traces through the illuminating star, plots were drawn of arc traces centred on the illuminating star at different radii. This was to show the uniformity or otherwise of the degree of polarization at a specified radius from the illuminating star.

Arc traces in Fig. 4.6 show the polarization over radii of 10-60 pixels radius about HD 38563N as a function of position angle. If the slab of dust is tilted in an east-west direction this would be manifest from the degree of polarization being different over position angle 90-180 degrees compared to 270-180 degrees. For position angles between 60-260 degrees the degree of polarization is fairly uniform suggesting that the slab is not tilted out the plane of the sky in an east-west direction.

4.5 Discussion

The sole illuminating star of NGC 2068 is HD 38563N as can be readily seen by the centrosymmetric pattern of polarization vectors which extends over a region 248" E to 220" W and 280" S to 90 arcseconds north of HD 38563N. The traces of polarization, polarized intensity and total intensity are non-symmetric about the illuminating star in a north-south direction. The asymmetry of these traces cannot be explained by a spherically symmetric dust cloud about HD 38563N, e.g. Voschinnikov (1978a and b). It could, however, be ascribed to a tilted slab: In the case of a foreground tilted slab (see Fig. 4.7) the relative brightness of the slab can

be explained by forward scattered light: interstellar grains have a high value for the Heyney-Greenstein asymmetry function g of 0.7 (Allen 1973). For Mie scattering, the maximum degree of polarization occurs for scattering angles close to 90 degrees. The linear traces can thus be explained by a foreground tilted slab with varying dust density: for forward scattered rays (A) the brightness will be a maximum but the degree of polarization a minimum; for rays further north there is an increase in dust density causing the intensity to fall rapidly, but with increasing scattering angle the polarization will rise (B). Considering rays (C) and (D) to the south of the illuminating star: the intensity will continue to fall the further south one looks at from HD 38563N, and as the scattering angle is increased the polarization will increase to a maximum at approximately 90 degrees. As the polarized intensity is a product of polarization and total intensity there should be a maximum in this value at some offset distance. This is indeed observed at 105 arcseconds south of HD 38563N (Fig. 4.4).

The small patch of nebulosity north-west of the illuminating star is denoted in Fig. 4.7 as due to rays along path E where large scattering angles are involved at a large distance from HD 38563N thus giving rise to large polarization but low intensity. The extinction towards HD 38563N and S has been measured to be between 5.0-6.0 and 2.5-3.0 magnitudes respectively (Strel'nitskii 1970; Sharpless 1952) assuming the authors' values of the star's colour excess and a range in value of Rv of 3-4. Thus the

illuminating star experiences approximately 2-3 magnitudes more extinction than HD 38563S. A comparison with other reflection nebulae, e.g. NGC 7023, Moore (1982); NGC 1999, Warren-Smith (1980), shows that NGC 2068 is similar to other reflection nebulae in that it has a single illuminating star, the maximum polarization in the visual waveband of 20 % is at the low end of the 20-30 % found for other reflection nebulae, and NGC 2068 is associated with a young cluster of stars (Sellgren 1983).

To determine the extent and contribution of emission in the reflection nebula, one can calculate the approximate size of the HII region produced by HD 38563N. Assuming values of hydrogen density as measured by Tucker et al. (1973) and Brown et al. (1975) of between 500 - 1000 cm-3 and the spectral type of HD 38563N as B2-B5 (Strom et al. 1975a; Lee 1968), then the Stromgren sphere radius (Rs) is given by the formula by Allen (1973):

$$Rs = So\ N^{-2/3}$$

where Rs = Stromgren radius in parsecs

So = 15 pc for a B2 star and 3 pc for a B5 star

N = hydrogen density cm-3.

For a B2 star; N = 500 : R = 0.24 pc/ 1.66 arcmin.

N = 1000 : R = 0.15 pc/ 1.04 arcmin.

For a B5 star; N = 500 : R = 0.05 pc/ 0.35 arcmin.

N = 1000 : R = 0.03 pc/ 0.21 arcmin.

The Stromgren radius for these examples is in the range 13-100 arcseconds assuming a distance of 500 pc for NGC 2068; however, this calculation has not taken into account the absorption of UV

photons by dust grains, and looking at the polarization map in Fig. 4.1 there is very little evidence of emission making a significant contribution to the nebula light.

Recently, observations in the near-infrared (2-5 micron) by Sellgren et al. (1983), Sellgren (1984) and Witt et al. (1984) have shown that certain reflection nebulae (including NGC 2068) have unusually large continuum emission between 1-5 microns. The mechanism for this is not understood, but is not thought to be responsible for emission at visual wavelengths, which can readily be explained by scattering from dust grains. It would be useful to obtain polarimetry observations in the R, I and Z bands to measure the extent of dust scattering at these longer wavelengths.

The new observations total more than 3000 polarization measurements with an accuracy comparable to previous workers as was shown in comparing selected regions of the reflection nebula. These comparisons indicate that the new observations in the visual band have a precision of +/- 2% polarization and +/- 10 degrees in position angle.

These new observations have shown that the light from the nebula is polarized up to 20% and is due to forward scattered light from a foreground illuminated slab. There is little or no emission due to the B2 illuminating star. The proposed geometry for NGC 2068 of a tilted slab apparently makes it the only known case of this particular geometry. Given the geometry, one also

needs to know the density of dust and the nature of the material to specify the polarization and intensity of nebula light, and for this a numerical model was devised (see chapter 5).

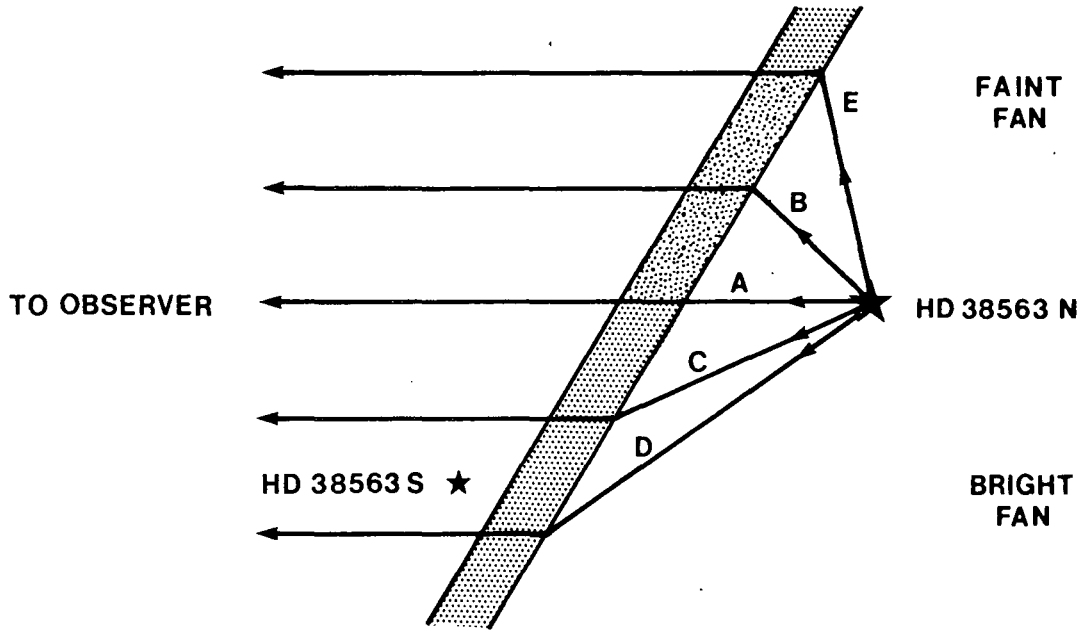

Fig. 4.7. Tilted slab model.

CHAPTER 5 A Model of NGC 2068

5.1 Tilted slab

An infinitely thin tilted slab model was initially tried to fit profiles of polarization, polarized intensity and total intensity in a direction north-south through the illuminating star HD 38563N. The parameters of this model are: 1) The grain material's complex refractive index: $m = n - in'$. 2) A power law size distribution of dust grains: $n(a)=a^{-Q}$ where n(a) is the number of grains in the range a to a+da and Q is the power law index. 3) Limits to the particle size in a power law size distribution designated Amin and Amax. 4) The geometrical parameters - scattering angle (Theta), angle that the slab is tilted to the line of sight (Phi), and the distance that the slab is from the illuminating star (XO). Amin and Amax were set to 0.02 and 1.0 micron respectively.

The range in values for the parameters chosen for this model are drawn from the conclusions of chapter 2 where a power law size distribution was assumed and values of Q between $-2.5 < Q < -5.5$ were indicated (Mathis 1979; Moore 1982). The grain materials chosen were ices, graphite, silicates, silicon carbide, iron, organic material and the biological dust grains proposed by Hoyle and Wickramasinghe (1982 and references therein).

The refractive indices of grain materials for visual

wavelengths are given in Table 5.1. Eight materials have been selected from the many possible grain constituents, but of these, it has been concluded that silicates and graphite are the most important. Grains composed totally of ices are not expected to exist in NGC 2068 as the temperature of the dust (20-40 K) is too warm. Bacterial grains are not thought likely (Duley 1984), but are an example of low refractive index grains. The conditions for the nucleation and expulsion of carbon grains have been shown to occur in late-type stars by Tabak et al. (1975). Silicates, graphite and silicon carbide (SiC) were the main constituents of the grain mixture proposed by Mathis, Rumpl and Nordseik (1977). SiC grains were used by Mathis (1979) to model interstellar polarization assuming a power law distribution Q=-2.5, and a refractive index, n=2.5. Lewis and Ney (1979) noted that many astrophysical objects (Wolf Rayet stars, novae etc.) formed dust grains at temperatures between 900-1100 K and that the condensation temperature of iron for many enviroments is ~ 1000 K, so concluded that iron (or iron carbide cohenite) is the universal condensate at 1000 K.

The geometry of the initial numerical model is shown in Fig. 5.1 and it was assumed that the slab was infinitely thin so that only single scattering was considered (i.e. small optical depth).

The distance to NGC 2068 was taken to be 500 parsecs (Lee 1968) so that 1 parsec corresponds to 6.9 arcmin. on the plane

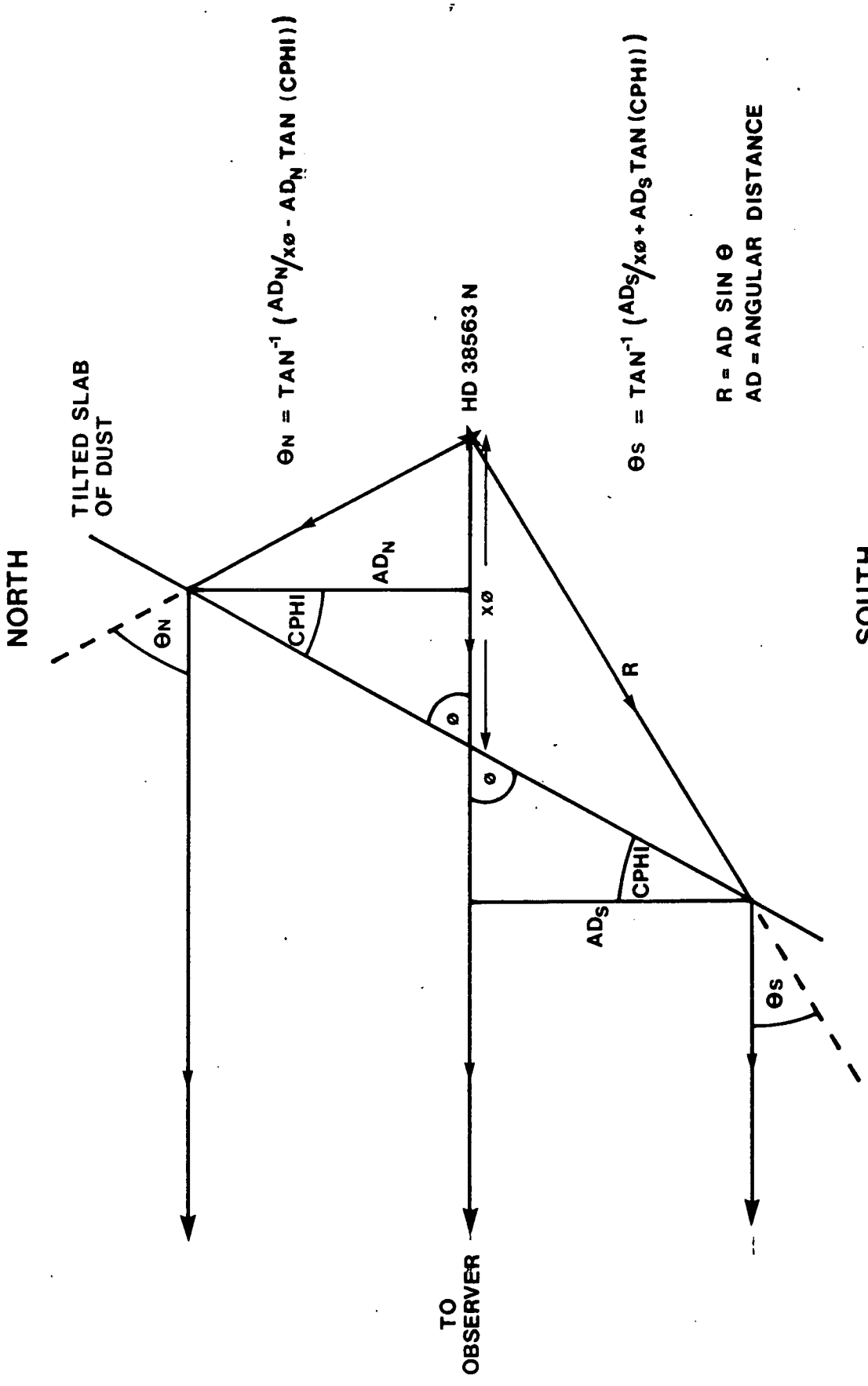

Fig. 5.1. Geometry of the tilted slab model.

Table 5.1. Grain materials.

Material	Refractive Index	Reference
Ice	1.33	Wickramasinghe (1973)
Dirty ice	1.33 - 0.05i	Greenberg (1978)
Organic	1.16	Hoyle and Wickramasinghe (1982)
Silicates	1.63 - 0.05i	Hanner (1971)
Graphite	2.5 - 1.3i	Wickramasinghe (1973)
SiC	2.5	Mathis (1979)
Iron	3.55 - 3.0i	Wickramasinghe (1973)
Bacteria	1.2 - 0.05i	Hoyle and Wickramasinghe (1982)

of the sky.

The numerical model utilised Mie scattering subroutines written by Dr. Warren-Smith which normalised the power law distribution and calculated the degree of polarization and intensity due to single scattering from a homogenous spherical grain for light at a particular wavelength; in this case 0.52 micron.

To calculate the scattering angle for the end north and south points of the polarization trace, limits were set for the maximum and minimum polarization at these points which gave the corresponding range in scattering angles Theta north and south. From the range in scattering angle the parameters XO and Phi were derived and the model then calculated the polarization, polarized

intensity and total intensity for the north-south trace.

The line of sight distance through the cloud to HD 38563N has been calculated to be ~ 0.4 parsecs (Sellgren 1983) from measurements of the CO column density and the H_2 gas density assuming the ratio of CO to H_2 a constant. XO was varied between 0.1 to 1.5 parsec in steps of 0.1 parsecs and Phi took values between 20-85 degrees in steps of 5 degrees in the model.

A chi squared test was used to measure the goodness of fit of the model predicted polarizations compared to the observations,

i.e. $\chi^2 = \sum_i 1/\sigma_i^2 [P_{observed} - P_{predicted}]^2$

and values of chi squared are given in Table 5.2. Normalisation of polarized intensity and total intensity of the model prediction with observation was done at 1.5 arcminute south of HD 38563N, at the peak of polarized emission. The model was tried for eight materials each with seven power law distributions from Q=-2.5 - Q=-5.5. Results are shown in Fig. 5.3. of graphs of polarization, polarized intensity and total intensity v. distance north-south (arcmin) from HD 38563N.

Mie scattering curves showing degree of polarization against scattering angle for various grain materials and power law size distributions are shown in Fig. 5.2. From looking at the various curves presented in Fig. 5.2 a-d, one can see how the parameters Pmax - the maximum degree of polarization, Theta max - the scattering angle at which Pmax occurs, and the shape of the

polarization profile varies with the complex refractive index and the power law index Q. Also presented is the intensity of the scattered light as a ratio of the maximum scattered radiation or I/Imax.

In Fig. 5.2 a, one can compare ice and dirty ice, with dirty ice having a small imaginary part (-0.05i). Figs. 5.2 b, c and d respectively compares organic v. bacteria, silicates v. SiC, and the metallic grains, iron v. graphite. The trends are: 1) Pmax decreases with increasing real part of the complex refractive index. 2) Pmax increases with increasing imaginary part. 3) As Q the power law index is increased then Pmax increases and the polarization scattering profile becomes more symmetrical with Theta max tending to 90 degrees. Comparing the scattering properties of dielectric v. metallic grains it can be seen that negative polarization is never produced by a power law distribution of metallic grains. Metallic grains back scatter light to a far greater extent than do dielectric grains. Amin in Fig. 5.2 was set to 0.02 micron as varying Amin between 0.002 and 0.02 microns had little effect on the polarization; very small particles affect extinction more than polarization. Amax was varied between 0.6 - 1.0 micron, but there was little difference in polarization between 0 - 90 degrees as there are few large grains and so Amax was set to 1.0 micron. The range in particle size chosen of 0.02 - 1.0 micron is similar to that expected by Voshchinnikov and Il'in (1983) for dust grains around a B5 star due to the fact that small grains (< 0.01 micron) will be

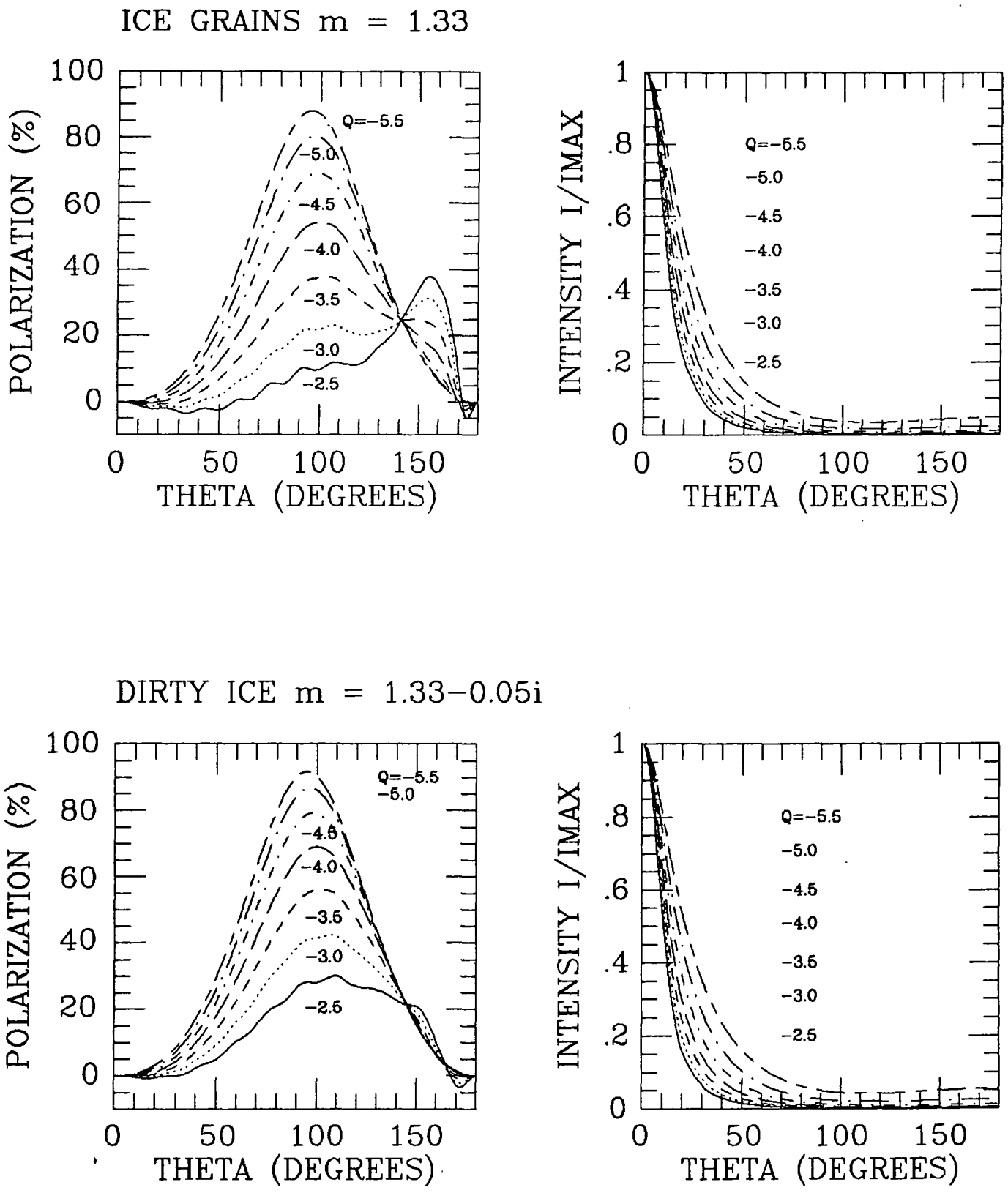

Fig. 5.2 a. Mie scattering curves.

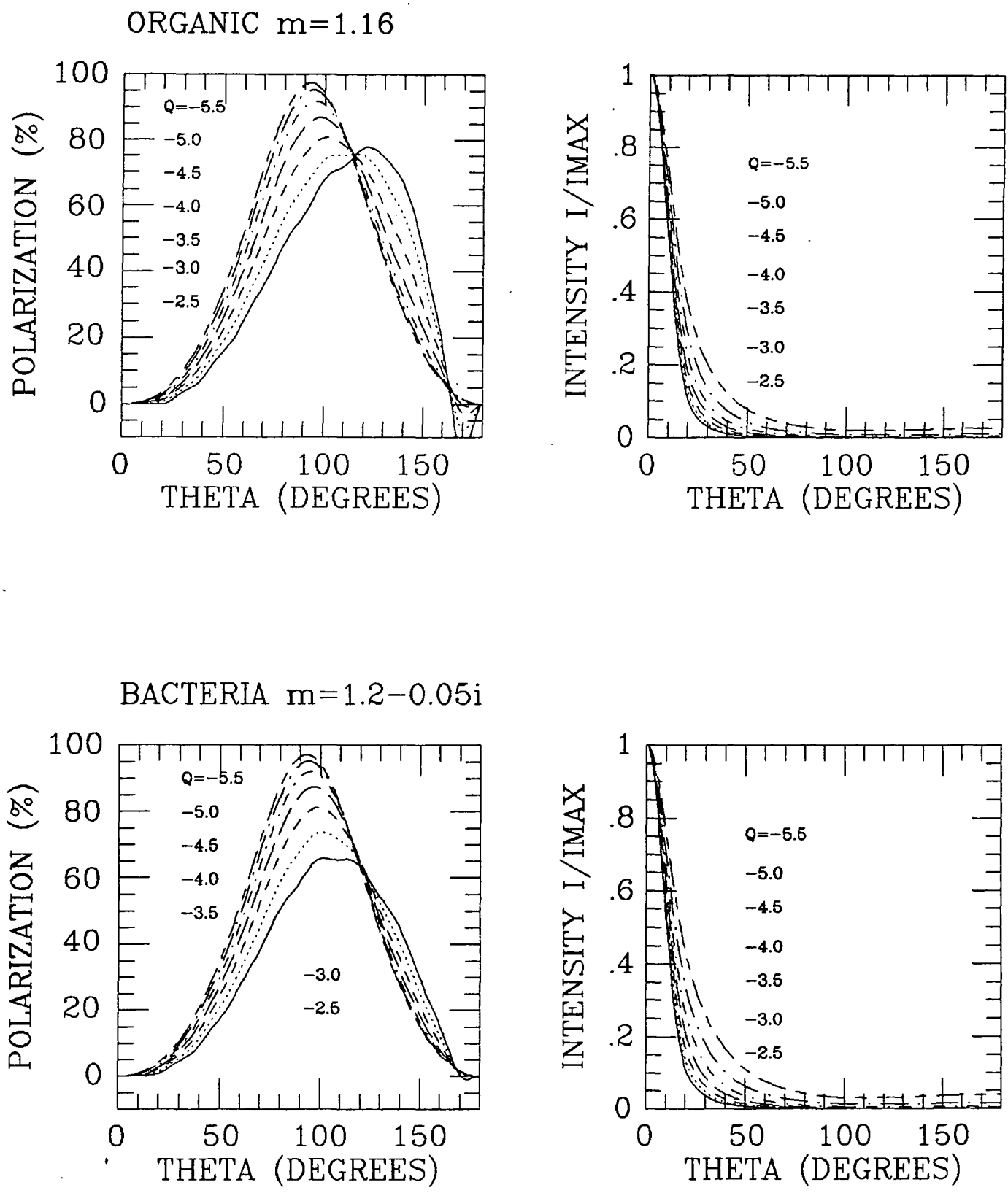

Fig. 5.2 b. Mie scattering curves.

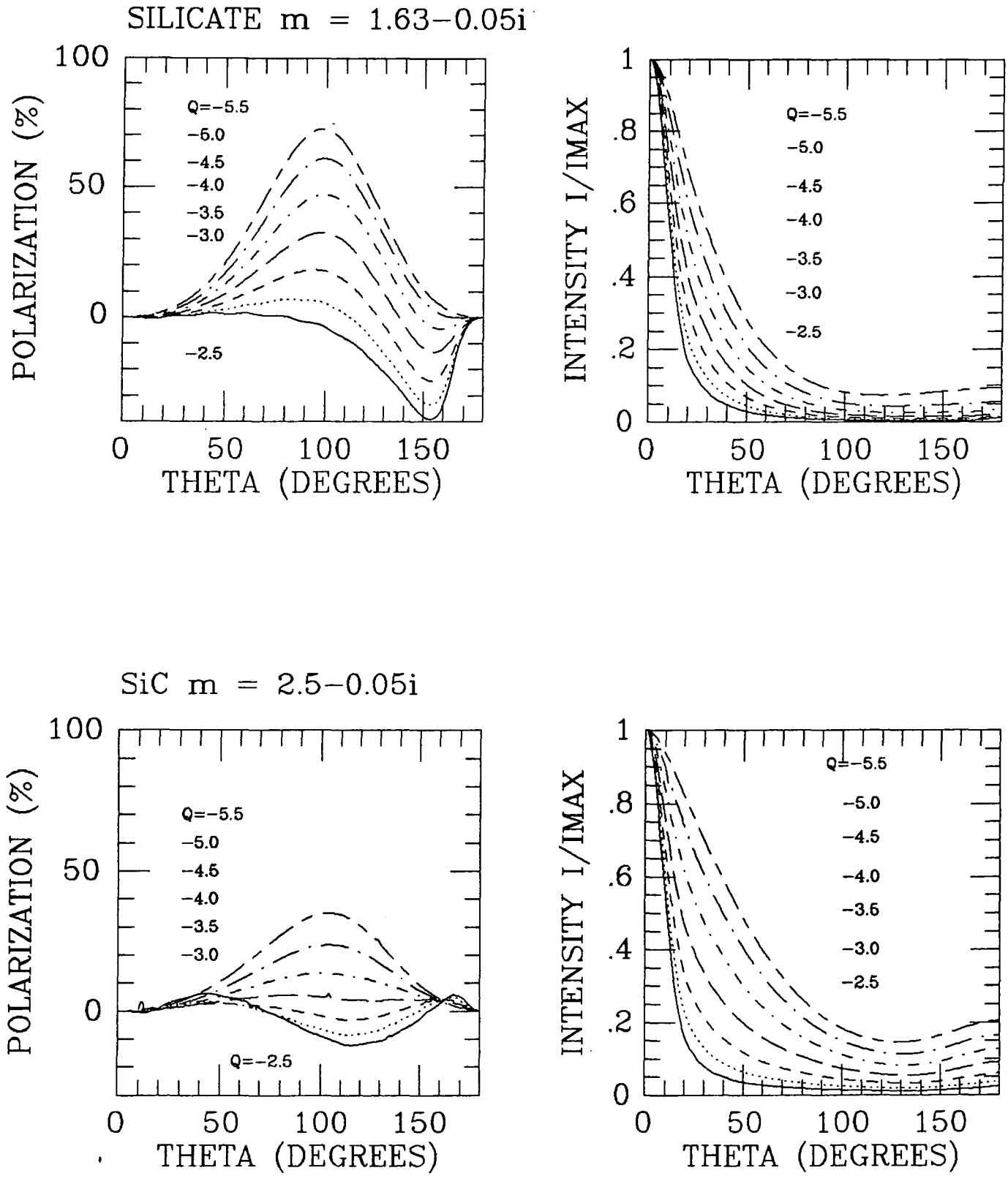

Fig. 5.2 c. Mie scattering curves.

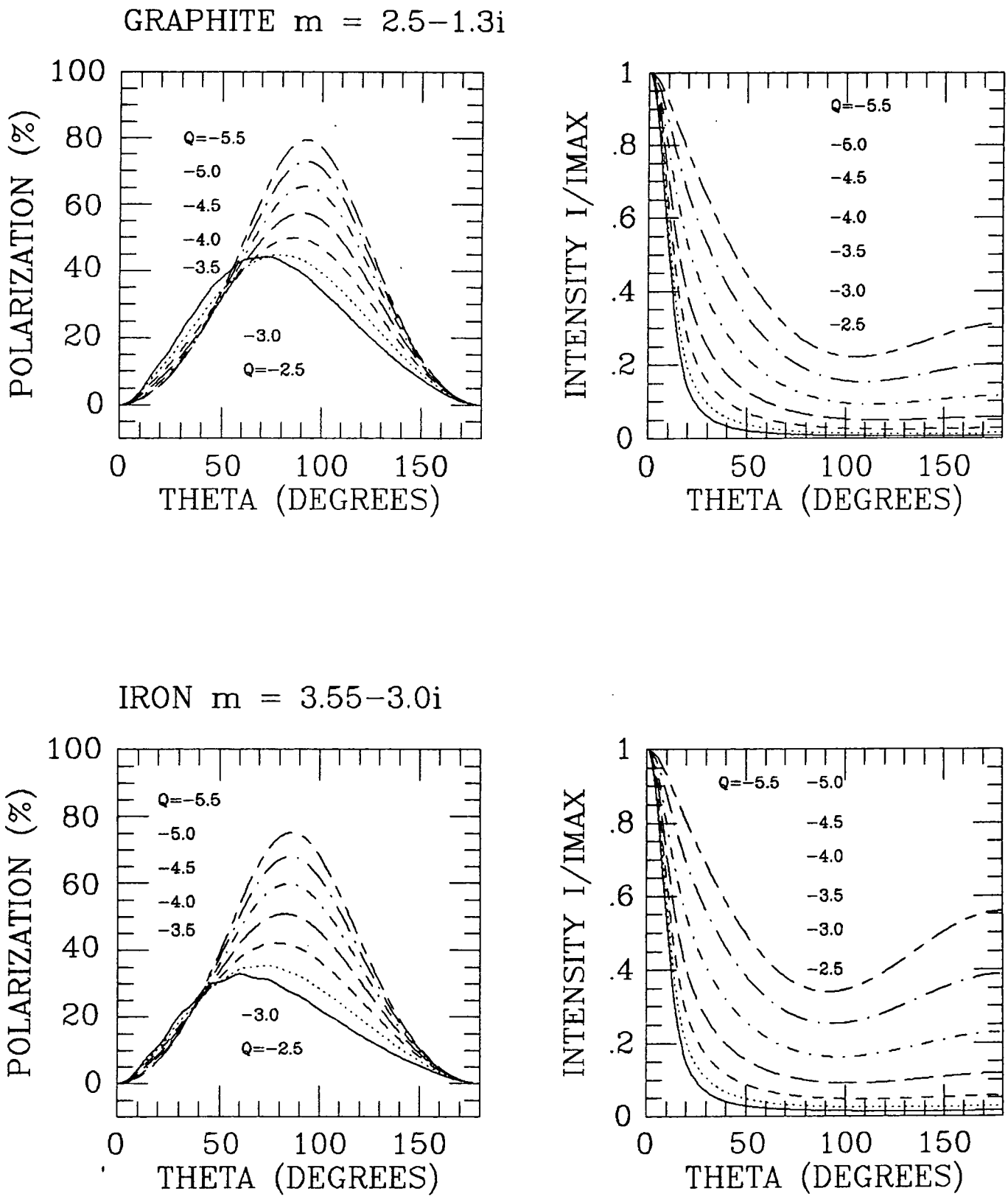

Fig. 5.2 d. Mie scattering curves.

Table 5.2. Grid of models.

Values of Chi squared

	Power Law index Q						
Material	-5.5	-5.0	-4.5	-4.0	-3.5	-3.0	-2.5
Ice	2848.3	1811.7	2491.2	1187.7	*	*	*
Dirty Ice	2175.7	2641.9	1445.4	2028.3	861.0	2214.9	377.6
Organic	3995.4	2102.5	2367.0	4082.4	1807.9	2319.9	*
Silicates	1190.2	1798.4	681.3	2186.7	*	*	*
Graphite	1328.8	1065.7	616.4	410.7	292.5	330.8	374.7
SiC	903.1	285.7	-	*	*	*	*
Iron	897.0	711.3	490.8	364.3	310.9	333.8	297.8
Bacteria	3332.8	1549.2	2104.2	2297.6	3917.2	1765.7	2333.0

vapourized and/or swept out and that particles in this size range contribute most to the scattering of light. SiC was given a small negative imaginary part so that the Mie-scattering calculations were not inordinately long. It can also be seen that forward scattering produces the highest intensities and gives rise to the steepest gradient in intensity as a function of scattering angle.

There was no negative polarization observed (i.e. the polarization E vector was not parallel with the radius vector from the illuminating star) which rules out certain power law distributions of e.g. Ices Q=-2.5, -3.0 and Organic material

Q=-2.5 etc.

One can also rule out immediately certain materials and power law indices from the contraint that the degree of polarization at maximum north and south points of the trace must lie between the errors of the observed polarization. At a scattering angle of zero degrees the polarization will be 0% and then should rise to 19 % +3,-5 at 4.2' south and 21 % + 6 at 1.5' north. This will exclude from inspecting Figs. 5.2a-d those materials and power law indexes marked with an asterisk in Table 5.2.

The best fits to the data were for the metallic materials graphite and iron with iron grains producing better fits to the observed polarized intensity and total intensity data. A power law size distribution of iron grains index Q=-4.0 is shown in Fig. 5.3 with geometric parameters given: XO=0.5 parsec, Phi=55 degrees.

A model could have been tried with varying dust density with the optical depth a function of distance north-south from the illuminating star, i.e. Tau fn(AD); the intensity being reduced by a factor I = Io exp(-tau), but it was not thought that this refinement would be worthwhile and a more complicated multi-scattering model is obviously required in the future.

5.2 Immediate enviroment in NGC 2068

As well as trying to determine the nebula geometry one can

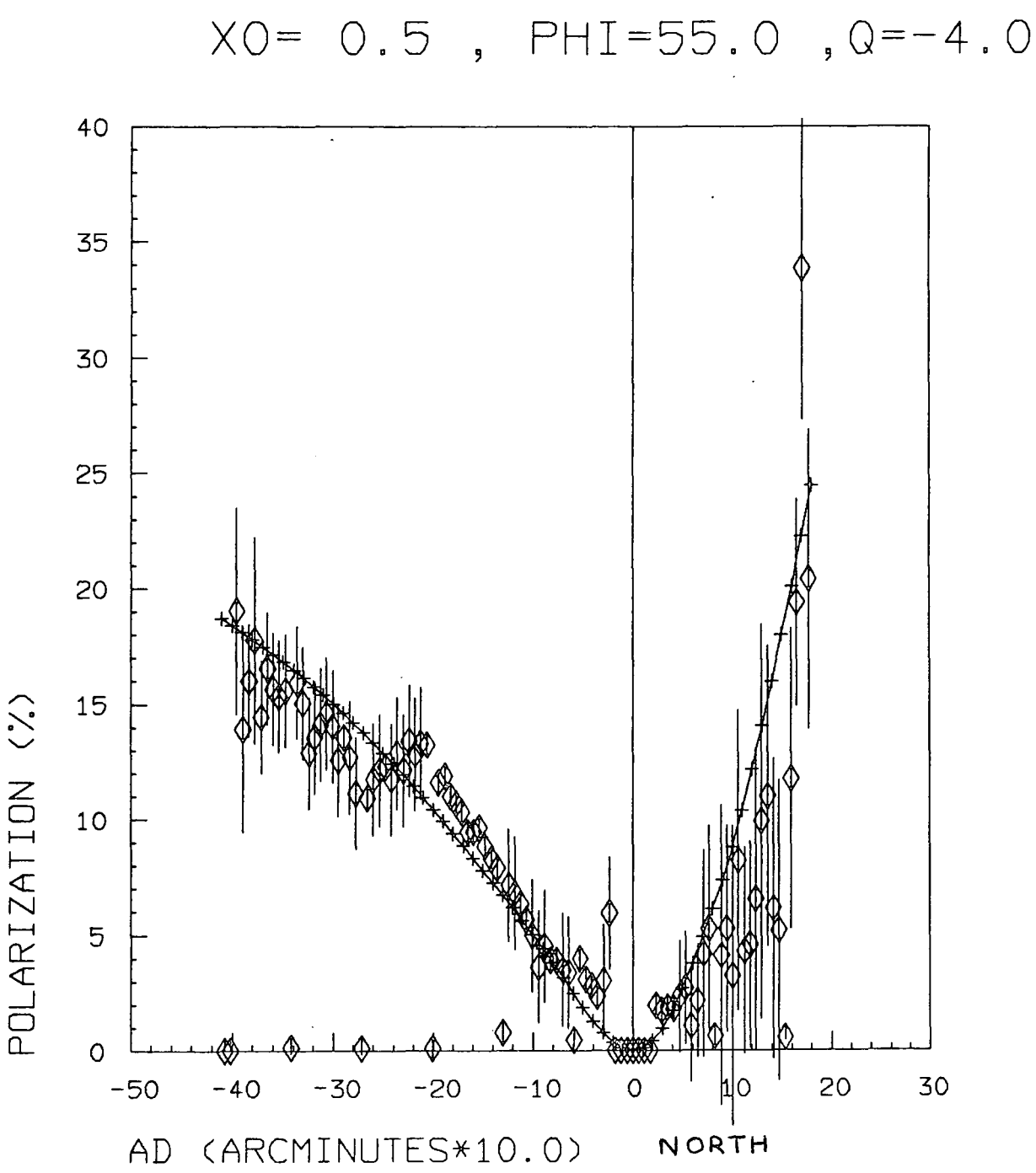

Fig. 5.3 a. Model fits to the data - Polarization.

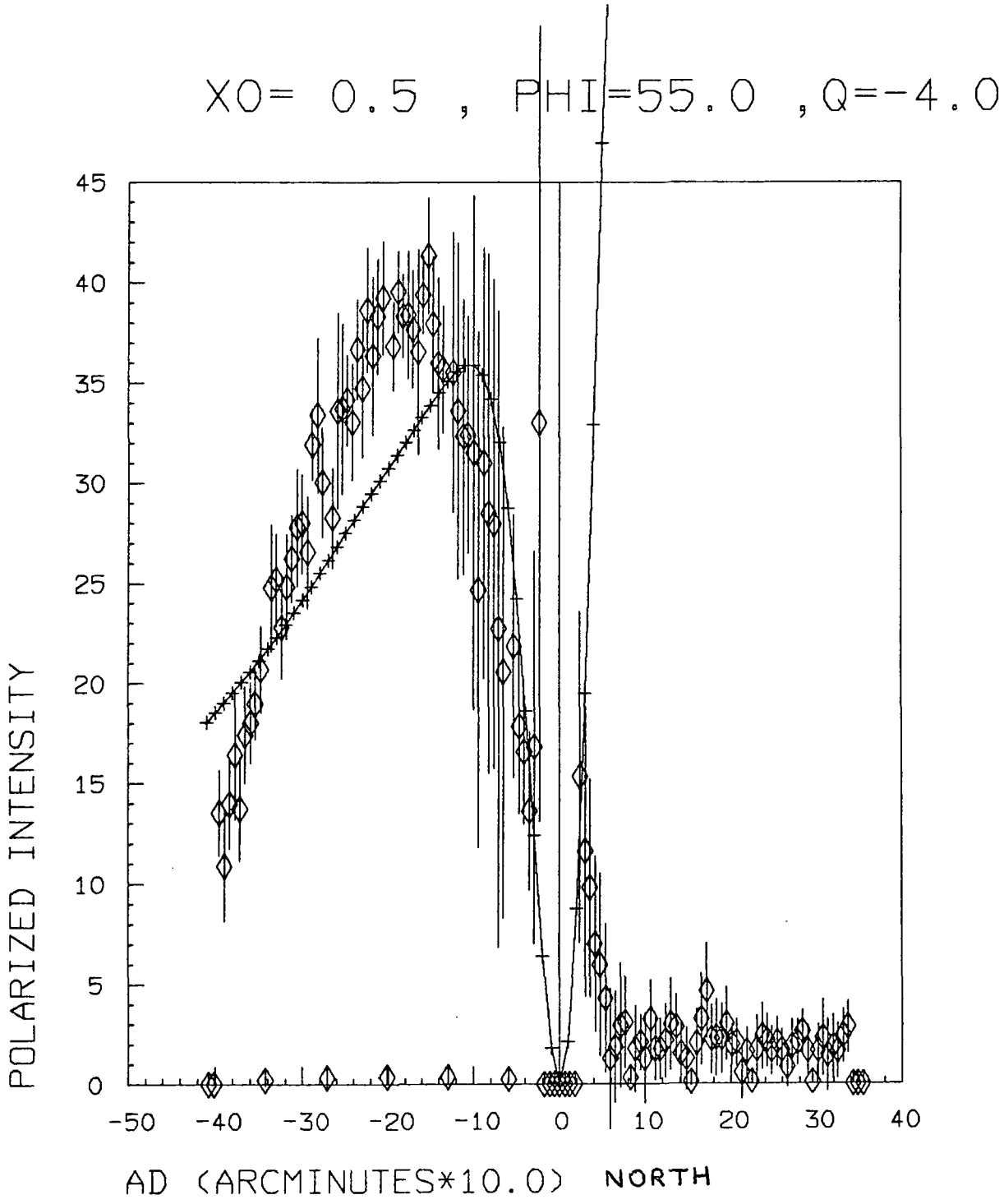

Fig. 5.3 b. Model fits to the data - Polarized intensity.

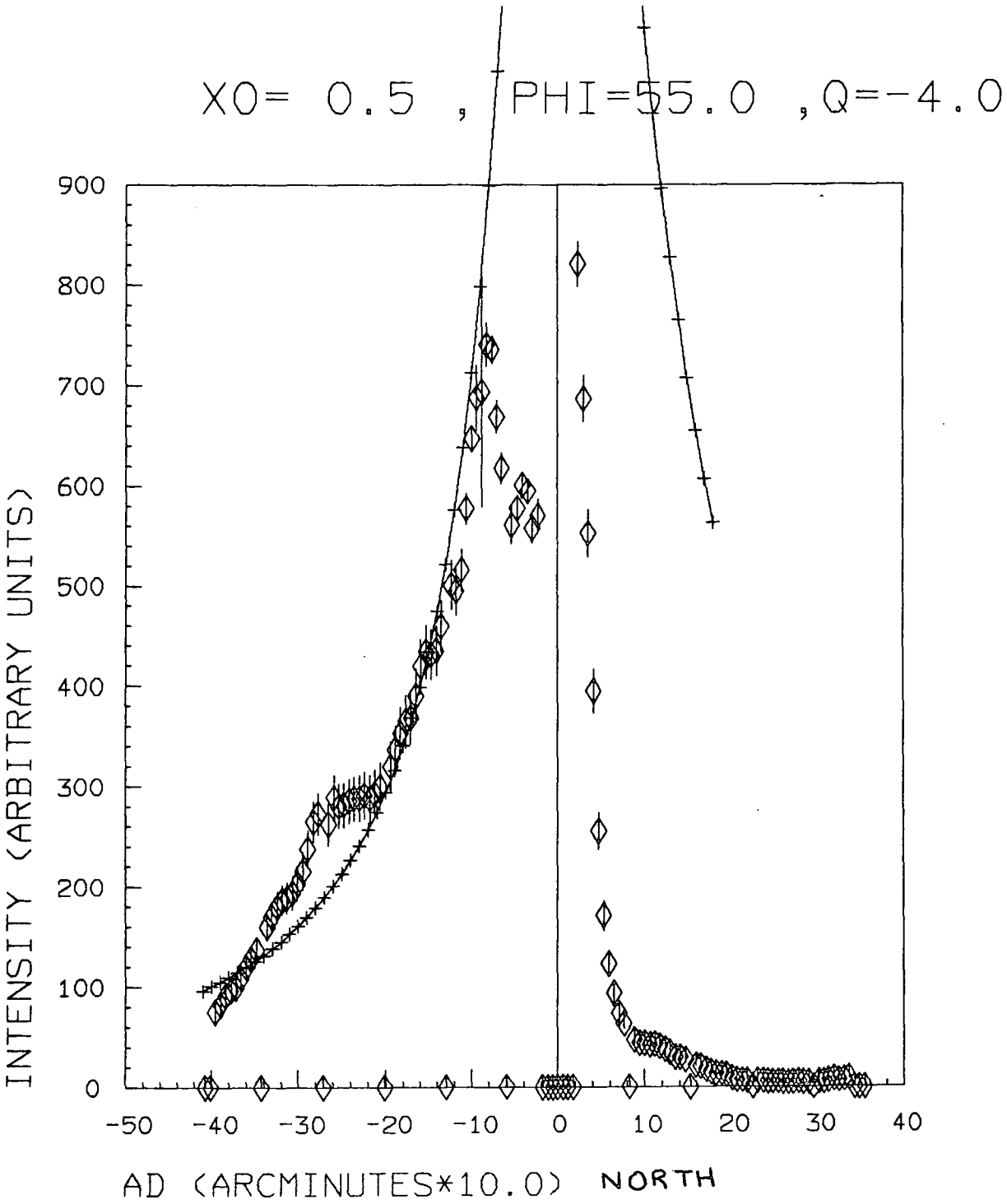

Fig. 5.3 c. Model fits to the data - Total intensity.

model the effect of radiation from HD 38653N on the surrounding dust in NGC 2068 and gain an insight into the star-cloud interactions.

Grain interactions are due to: 1) The dynamical effects of grain potential, which is dependent on photoelectric emission, sticking of electrons and sticking of ions, and include: a) strong coupling of the translational velocity of the grain to the magnetic field; b) increased drag from the plasma through which the grain may be moving; c) precession of the angular momentum vector of the grain around the interstellar magnetic field (see Martin 1978). 2) Radiation pressure on grains: Voshchinnikov and Il'in (1983) wanted to calculate the effect of radiation pressure on dust grains around (amongst other objects) B stars that illuminate reflection nebulae. They defined a parameter, beta - the grain sweeping efficiency, as the ratio of the radiation-pressure force (Fpr) to the gravitational attractive force on a grain (Fg).

$$Fg = \frac{G.M^*.\rho d.Vd}{R^2} \quad , \qquad Fpr = \frac{1}{C}\frac{R^{*2}}{R^2} Sd.\bar{Q}pr.\sigma.T^{*4}$$

where c = speed of light, G = Gravitational constant, σ = Stefan-Boltzmann constant, R* and T* are the radius and effective temperature of the star, R is the distance of the grain from the star (R>>R*), Sd is the geometrical cross-section of the grain, $\bar{Q}pr$ is the mean Planck radiation-pressure efficiency factor, M* is the mass of the star, ρd and Vd are the density and volume of the

dust grain, a_s is the radius of a spherical grain.

For spherical grains:

$$\text{Beta} = \text{Fpr/Fg} = \frac{R^{*2}\, T^{*4}\, Sd\, \bar{Q}pr}{c\, G\, M^*\, \rho d\, Vd} \sim 2.12\ \text{E-8}\ \frac{R^{*2}\, T^{*4}\, \bar{Q}pr(a_s, T^*)}{M^*\, a_s\, \rho d}$$

The grain sweeping efficiency was computed for seven different grain materials, which included dirty ice, graphite, iron, silicates and silicon carbide, for the case of a B5 star in a reflection nebula. They found: (1) 'a zone around the star to be swept clear of dust'. (2) The illuminating star would be surrounded by a zone deficient of small-sized grains so expected depolarization to be observed in regions close to the illuminating star in the red waveband. (3) There would be an increase in Rv with the removal of small grains. (4) Beta was not sensitive to either grain shape and orientation or composition (although SiC and Graphite grains were expelled the most rapidly).

Conditions in NGC 2068 have been examined by Strom et al. (1975a), White and Phillips (1981), and Pankonin and Walmsley (1978). They have reported on near-infrared star surveys, CO molecular-line observations and carbon recombination line observations respectively. Strom et al. (1975a) pointed out that the radiation pressure due to HD 38563N could be effective over a large region of the dark cloud as the radius at which radiation pressure balances gas pressure (Rrp) is:

Rrp = 2.0 E2 (L/Tn)1/2

where L = Luminosity of star (Lo), T = temperature, n = molecular density. The radius of the dust-free zone around HD 38563N was calculated to be approximately 0.1 pc by Strom et al. (1975a) assuming a typical Herbig Ae/Be star whose stellar wind velocities are of order 200 km/s. This would indicate that there are physical reasons why a slab of dust could be found in front of HD 38563N. White and Phillips (1981) measured the distribution of CO in NGC 2068 and showed that there is a compact core 5 by 8 arcmin surrounded by a diffuse cloud < 25 K. White et al. (1981) from high-resolution (55 arcsec beamwidth) CO observations detected two molecular hot spots: one, NGC 2068S centred on NGC 2068 and the other NGC 2068N at 7 arcmin north-west. There is also a cold CII Stromgren sphere, T ~ 20 K, centred on NGC 2068 (Brown et al. 1975) and modelling this localized region of ionized carbon they inferred a density of 700 cm-3. The temperature of the dust (Td) is between 20-50 K (White et al. 1981).

Table 5.3. Physical parameters of NGC 2068.

Density:	ne	1 cm-3	Pankonin and Walmsley (1978)
	nH	E3 cm-3	Brown et al. (1975)
Temperature:	Td	20-50 K	White et al. (1981)
	Te	20-40 K	White and Phillips (1981)
Size:	HII	~ 4.5 arcmin. /0.65 pc	Matsakis et al. (1976)
	CII	20 arcmin./ ~ 3 pc	Pankonin and Walmsley (1978)

5.3 Discussion

An attempt was made to model the observed polarization, polarized intensity and total intensity in the V waveband as a function of offset distance north-south from HD 38563N. A tilted slab of dust in front of the illuminating star and single scattering from homogenous spherical grains was assumed. The closest fit to the data was for a power law size distribution index Q=-4.0 of iron grains. Only the metallic grains were found capable of fitting the data and it would appear that dielectric grains are inappropiate.

As Zellner (1970,1973) modelled the wavelength dependence of polarization for regions of NGC 2068 and concluded that only forward throwing dielectric grains were responsible for the reflection nebulosity and this model agrees with many other workers then the model put forward in chapter 5 is probably too simplistic. It does, however, seem that a tilted slab of dust can qualitatively describe the asymmetries in the traces through HD 38563N. It would be worthwhile obtaining polarization versus wavelength data between 0.4 - 1.0 micron for regions close to HD 38563N (< 40 arcsec) for further modelling, which is the region around the star where depolarization effects may be present and the geometry of a foreground slab is likely.

CHAPTER 6 Polarimetry of NGC 2023

6.1 Optical and near-infrared polarimetry of NGC 2023

The only polarimetric study of NGC 2023 that the author has found in the literature was work by E.E. Khachikyan which was briefly described by Minin (1965). Measurements made by Khachikyan showed that the degree of polarization did not vary significantly over the visible nebula and had a mean value of 13 %. The nebula has extensively been studied in the millimetre, FIR and NIR, and these observations along with the Durham polarimetry observations are analysed in chapter 7.

Described below is the data reduction done on two sets of polarimetry data of the reflection nebula, NGC 2023 (1950 coords: R.A. 5h 39m 7s, Dec. -2 deg. 16' 58").

The two sets of data were obtained as follows: first, using an electronographic camera and filters B, V and R, and the second with a CCD detector and filters R, I and Z. The filter characteristics are given in Table 6.1. The first set of data was centred on the illuminating star HD 37903, while the second set was positioned south of the illuminating star; neither set of data recorded the star itself as it is too bright - V=7.83 mag; Witt et al. (1984).

The observations in B,V,R,I, and Z will enable the wavelength

dependence of polarization and also position angle to be determined for many areas of NGC 2023 from 440 - 930 nm in order to determine grain characteristics. Sellgren (1983) has observed a young cluster of stars associated with this reflection nebula in the J and K infrared bands. Table 6.2 tabulates the stars found in surveys by Strom et al. (1975a) and Sellgren (1983) which are in the region of sky that is covered either by the electronographic or the CCD data. These stars are plotted in Fig. 6.1.

Plate 6 is part of UKSTU plate R3816 showing NGC 2023 and some of the associated stars found by Sellgren (1983). Sellgren estimated that between 30-60% of stars in the reflection nebulae NGC 2023, NGC 2068 and NGC 7023 are pre-main sequence stars.

Table 6.1. Filter characteristics.

Data	Filter	Peak Wavelength (nm)	Mean Wavelength (nm)	F.W.H.M. (nm)
Electronograph	B	443.0	439.9	87.0
	V	480.0	521.4	117.0
	R	620.0	653.8	105.0
CCD	R	646.7	668.9	172.2
	I	744.5	783.8	125.7
	Z	928.0	932.8	64.5

Plate 6. A copy of UKSTU plate R3816 showing NGC 2023.

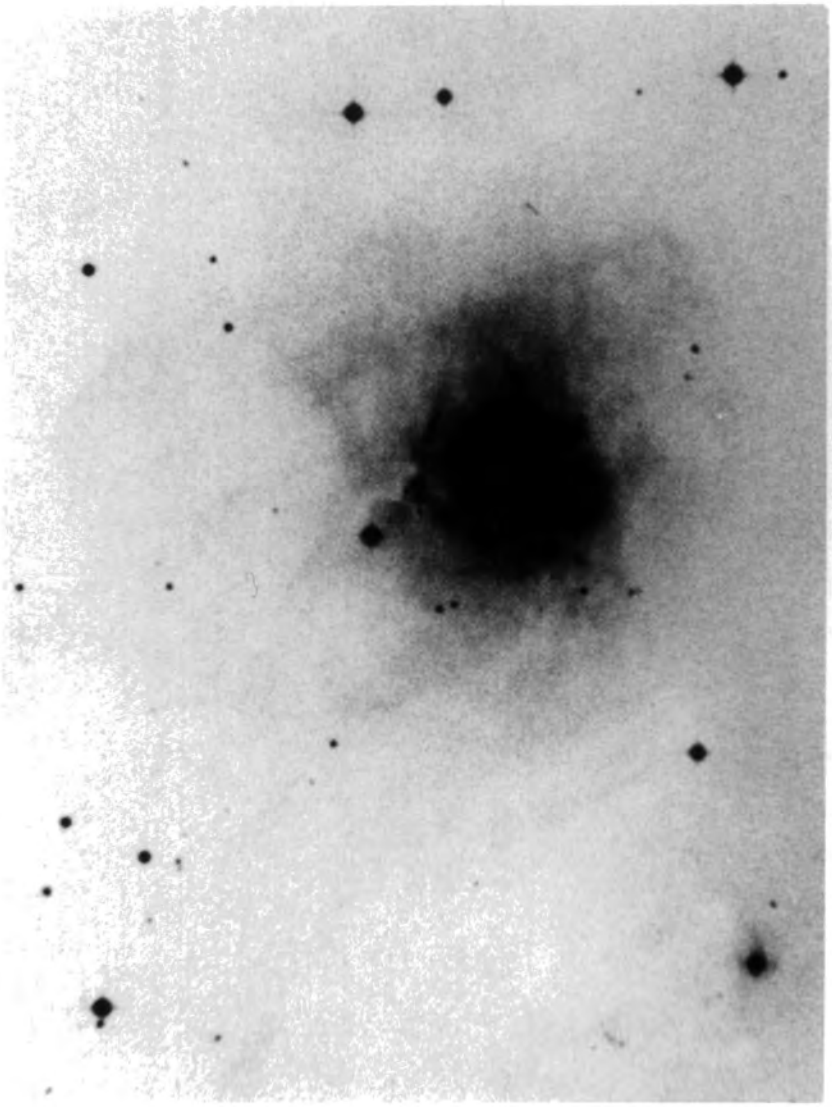

Examination of UKSTU plates J3828 and R3816 of the region close to NGC 2023 was done using a binocular microscope in order to look for Herbig-Haro objects. The Herbig-Haro objects designated HH1-3 associated with NGC 2023 had their positions measured using the Royal Observatory Edinburgh (ROE) Packman XY measuring machine and UKSTU plate R3816. These were recently discovered by Malin et al. (1986) and their measured coordinates and offsets from HD 37903 are tabled below; the accuracy is better than 1 arcsecond after using a 6-parameter empirical fit.

	R.A.	Dec.	Mean Offset (Arcsec)	
HH-1 a	5 39 0.40	-2 18 49.6	99.3 W	112.6 S
b	5 39 0.89	-2 18 52.2		
HH-2 a	5 38 55.69	-2 24 30.3	168.6 W	454.4 S
b	5 38 56.36	-2 24 35.0		
HH-3 a	5 39 1.30	-2 25 11.5	81.6 W	489.8 S
b	5 39 1.93	-2 25 8.7		
c	5 39 2.24	-2 25 4.0		

The HH objects HH1-3 consist of 2, 2, and 3 knots respectively and are labelled a-c in order of increasing R.A. These HH objects are probably collisionally excited material that has been shock heated through the interaction of a strong stellar wind with its ambient medium (Canto 1981). No other HH objects were found in the search, but subsequent to the initial discovery of three HH object two more suspected HH objects have been found (Malin et al. 1986):

HH-4	5 39 03.9	-2 18 24	50.5 W	85.7 S
HH-5	5 39 02.85	-2 18 43.6	66.2 W	105.3 S

Table 6.2. Data on the stars associated with NGC 2023.

Star		R.A.	Dec.	Offset from	K
Strom	Sellgren	h m s	o ' "	HD 37903	mag
	M	5 38 56.9	-2 21 9	156 W, 251 S	10.86
	J	5 38 57.2	-2 15 24	151 W, 94 N	10.70
S112	E	5 39 3.6	-2 18 50	56 W, 112 S	10.60
S108	C	5 39 5.3	-2 18 14	30 W, 76 S	8.42
	D	5 39 6.0	-2 18 43	20 W, 105 S	10.32
HD 37903	A	5 39 7.3	-2 16 58	0 E, 0 S	7.32
S101	B	5 39 9.2	-2 17 26	29 E, 28 S	9.92
LkHa 287	-	5 39 10.0	-2 16 42	41 E, 16 N	
	G	5 39 11.4	-2 19 3	62 E, 125 S	10.83
S106	205	5 39 12.2	-2 19 4	74 E, 126 S	>10.1
	217	5 39 13.2	-2 17 42	89 E, 44 S	
S110	218	5 39 13.3	-2 17 32	90 E, 34 S	9.40
	219	5 39 13.6	-2 17 30	94 E, 32 S	
	211	5 39 13.8	-2 18 19	98 E, 81 S	
S104	220	5 39 14.0	-2 17 24	101 E, 26 S	
S105	H	5 39 16.2	-2 18 3	133 E, 65 S	7.43

References:

Strom et al. (1975a)

Sellgren (1983).

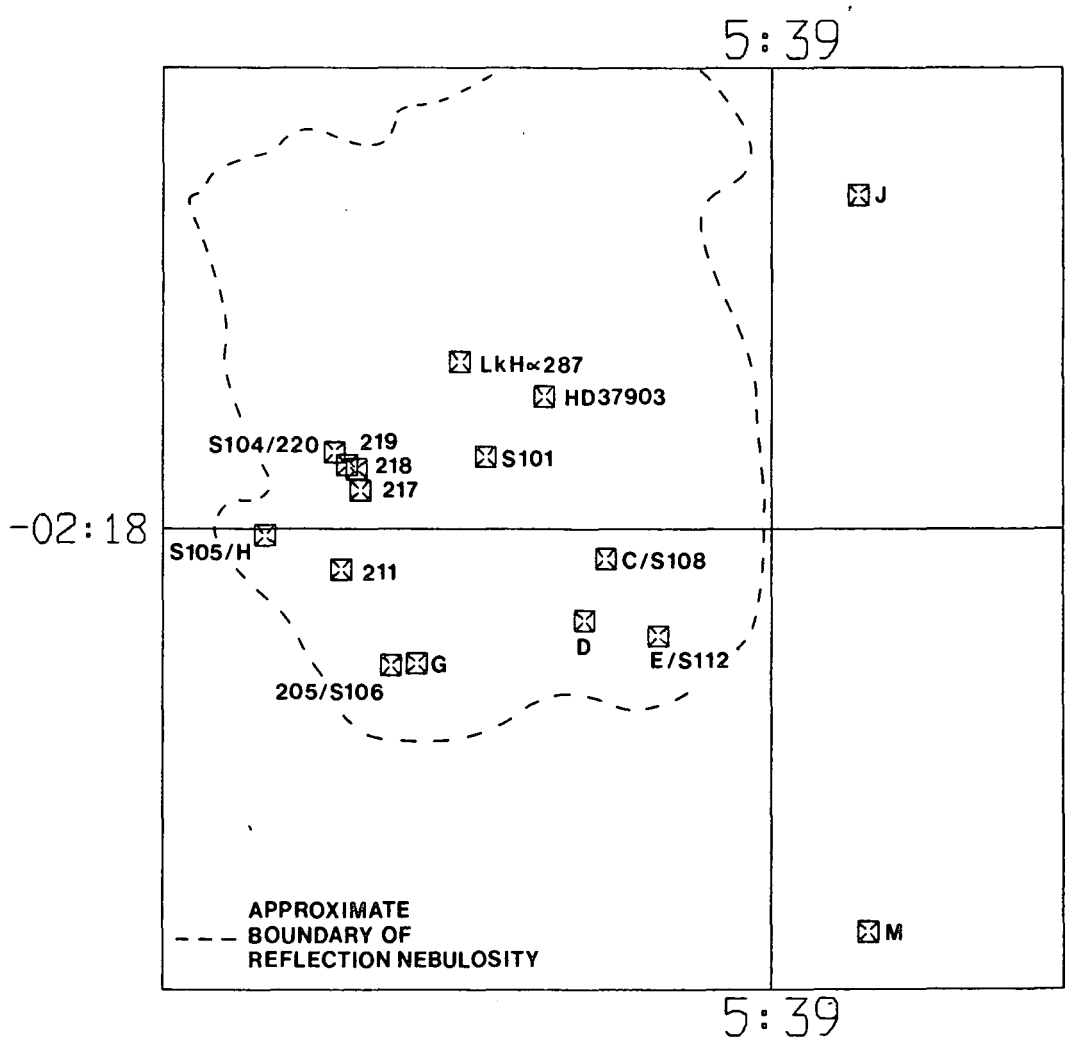

Fig. 6.1. A map of the stars in the region of NGC 2023.

6.1 a Electronographic data

The data were obtained in March 1980 at the f/13.5 focus of the 1-m telescope at the Wise observatory, which gave a field of view of 10.2 arcminutes. The grids of the polarimeter were aligned east-west and a baffle was used to block the light of HD 37903 for all the data taken. For filters B and R, electronographs were taken in the 'grids in' position only, while for the visual measurements, electronographs were exposed in the 'grids in' position and a further series taken after moving the field of the polarimeter in order to cover the whole of the nebula. These last electronographs will be termed 'grids out'. Using the filters B, V and R, the exposure times for the electronographs were respectively in the range 30-35 minutes, 12-20 minutes, and 15-20 minutes for short red and 30-35 minutes for long red. A total of nine stars have been found in the electronographic data, with six being located in 'grids in' data and three in the visual 'grids out' data. Plate 7 shows the combined visual intensity image after reduction; the translation for combining the visual polarization maps and intensity images having been calculated from matching the centres of centrosymmetry of the polarization vectors and the position of the star S105, which was common to both data. The eight stars visible on Plate 7 are marked E1-8. One of the stars, S105, was originally identified from comparison of Plate 7 with Fig. 1b of Strom et al. (1975a).

Use was made of the Packman XY measuring machine at the Royal

Observatory Edinburgh to measure accurately the position of stars on the UKSTU plates J8970 and I1963. From these positions, identification of the stars recorded in the electronographic data were made through comparison with the measured star positions tabled in Sellgren's (1983) survey of NGC 2023. Measurement of the XY position on these stars and their celestial coordinates then enabled the plate scale to be calculated, which was 1.48 +/- 0.01 arcseconds/pixel.

All eight stars in the electronographic data are listed in Table 6.3 with their measured offset distance from HD 37903 in arcseconds.

In the reduction procedure, the 'grids in' data were aligned to the visual polarization map using the most prominent stars common to the B, V and R electronographs. The alignment error for all the maps produced is approximately +/- one arcsecond. The field of view of 'grids in' is 306" N, 198" S, 282" E and 320" W offset distance from HD 37903.

Figs. 6.2 and 6.4 are polarization maps of NGC 2023 using blue and red filters respectively, while Fig. 6.3 is the combined visual polarization map of NGC 2023. The field of view of the combined map is 308" N, 252" S, 286" E and 340" W offset from HD 37903.

Table 6.3. Identification of stars in Electronographic data.

Star name	Sellgren (1983)	Strom et al. (1975a)	Offset from HD 37903 R.A.	Dec.
E1	M	-	158 W	252 S
E2	J	-	152 W	95 N
E3	-	S108	33 W	75 S
E4	-	-	71 E	304 N
E5	205	S106	71 E	130 S
E6	H	S105	130 E	65 S
E7	-	-	146 E	289 N
E8	-	-	253 E	112 N

Looking at Fig. 6.3, the combined visual polarization map of NGC 2023, this shows that there is no deviation in centrosymmetry of the polarization vectors about HD 37903. The size of the region of visual polarization is 200" N, 200" S, 200 " E to 185" W with a maximum polarization of V = 28 + 3 % at 185" W. None of the stars E1-8 affect the centrosymmetric pattern of polarization so do not illuminate the dust in NGC 2023.

Of the Herbig-Haro objects HH1-5 tabled in Malin et al. (1986) only HH-4 is in the field of view of the electronographic data; however, it was not detected in the B, V or R data and it has not affected the pattern of polarization in B, V or R.

Plate 7. Combined visual total intensity image of NGC 2023.

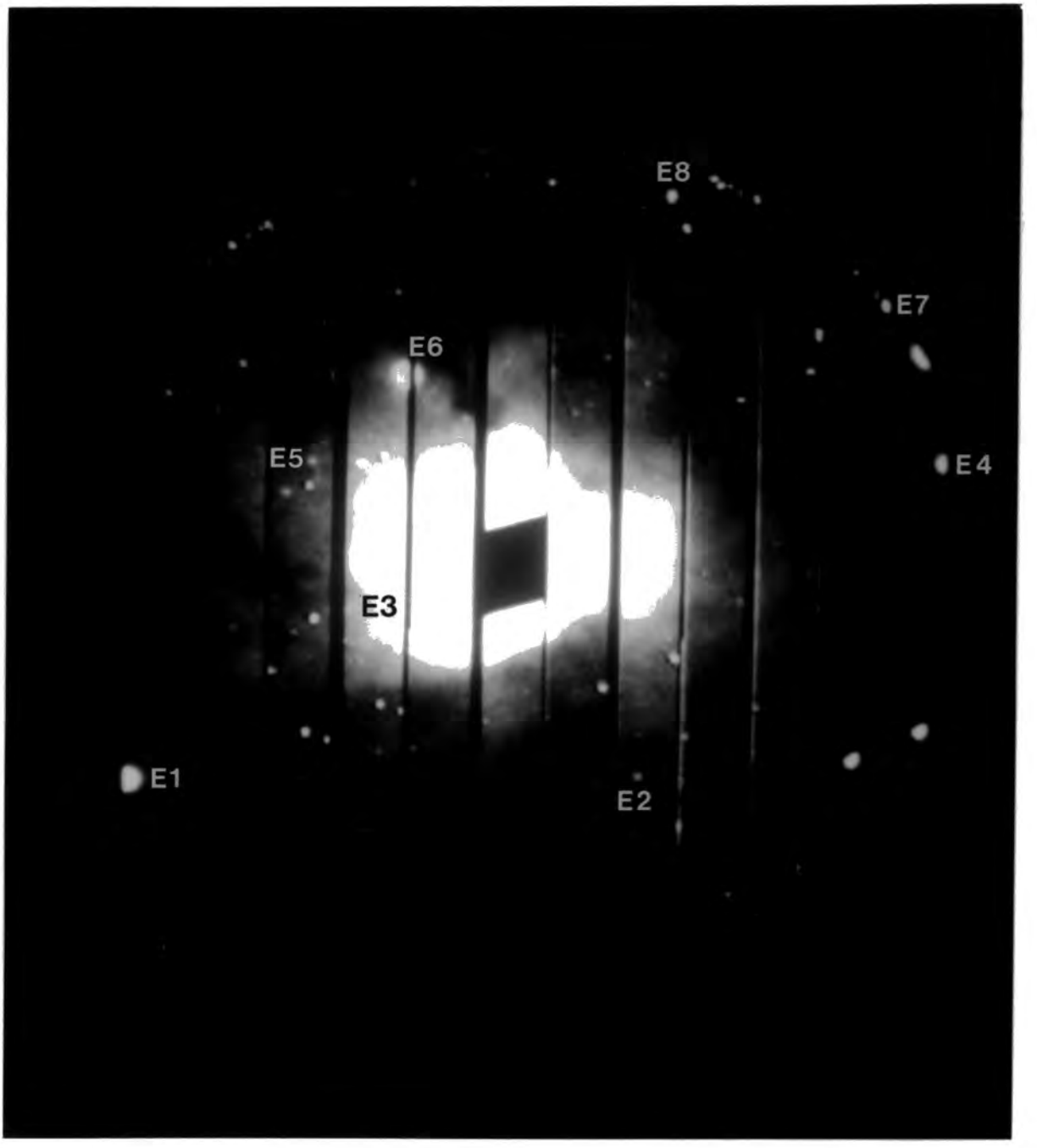
E8
E7
E6
E5
E4
E3
E1
E2

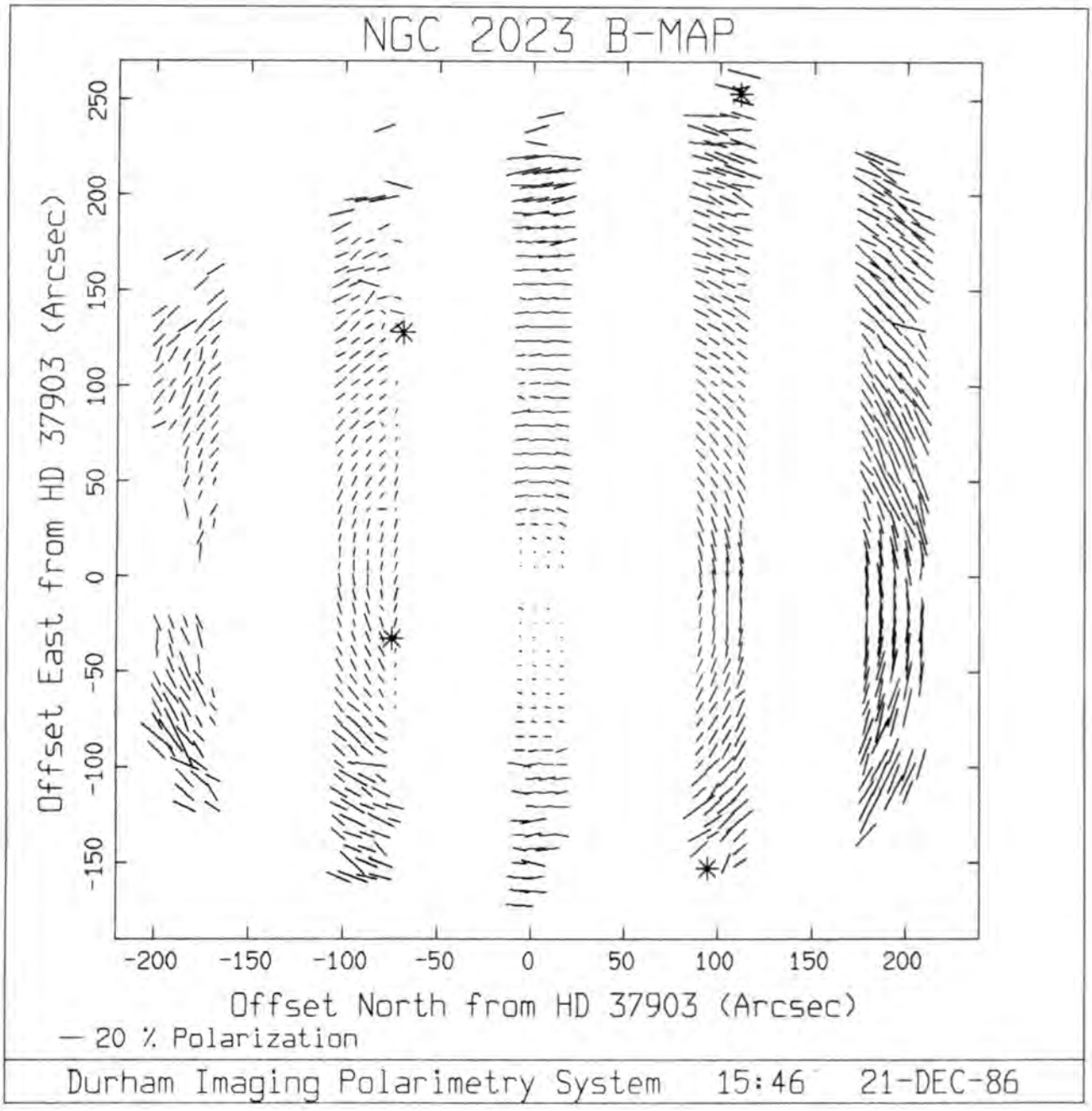

Fig. 6.2. Polarization of NGC 2023 using a B filter.

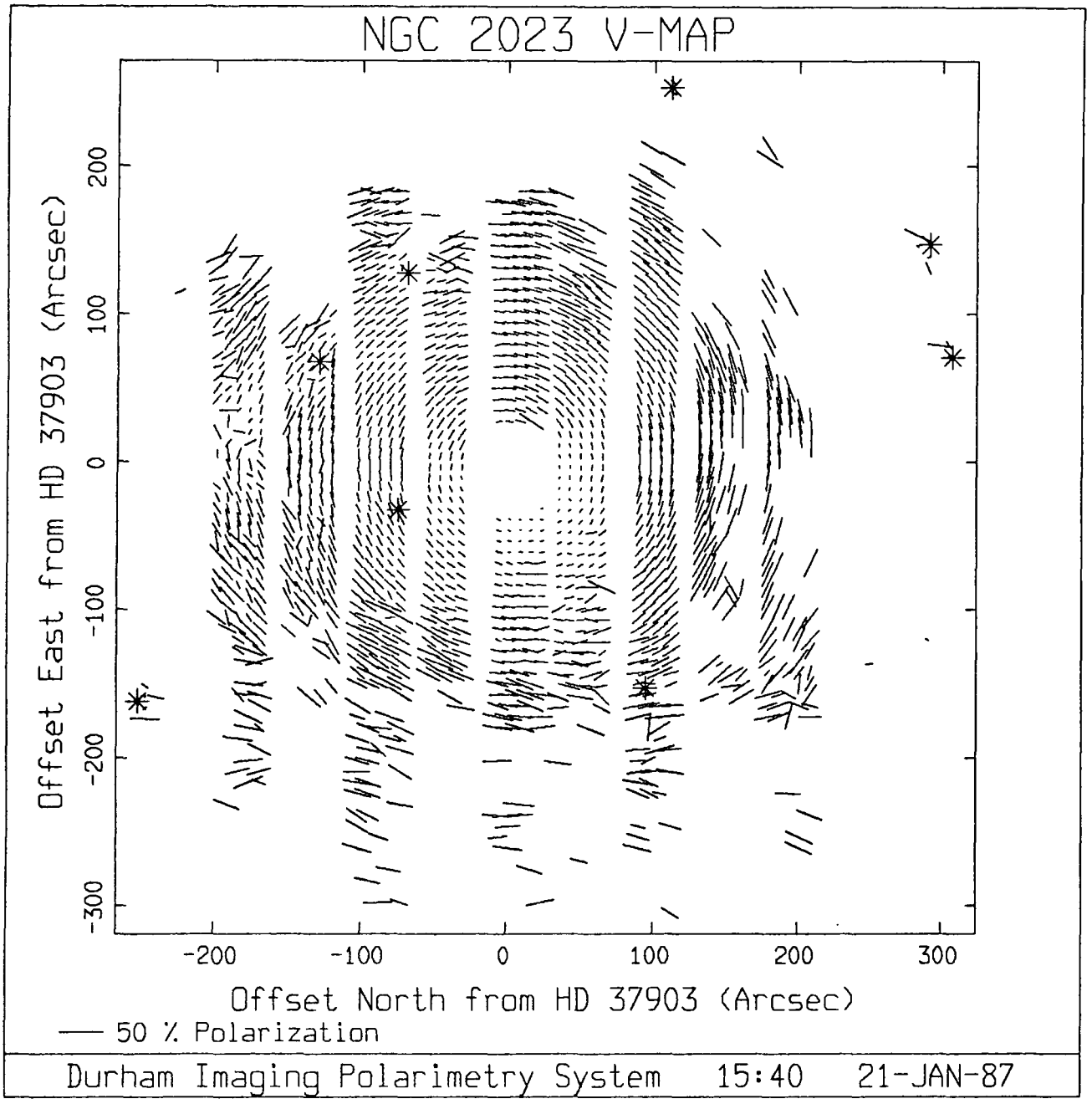

Fig. 6.3. Polarization of NGC 2023 using a V filter.

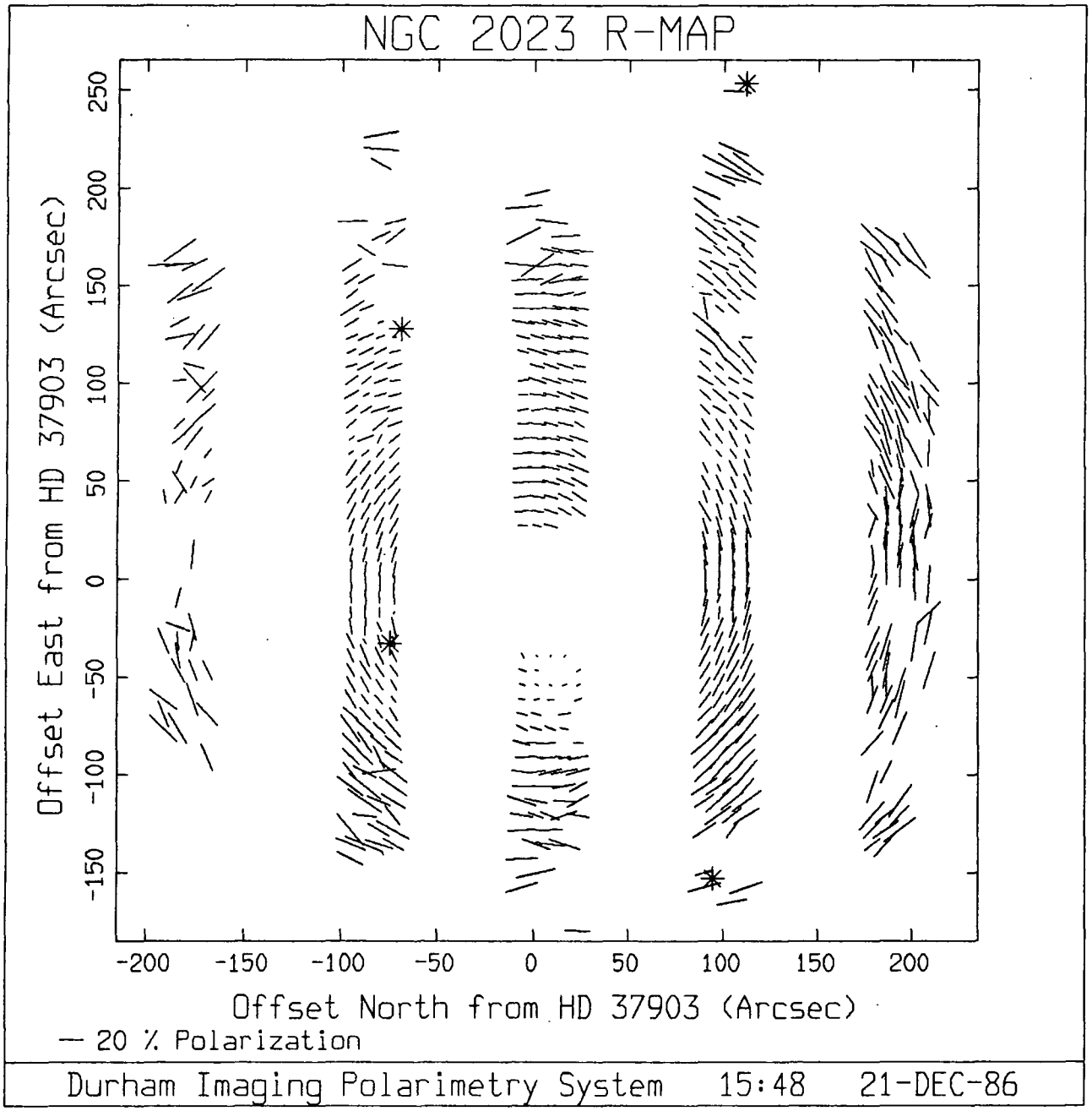

Fig. 6.4. Polarization of NGC 2023 using an R filter.

The B map shows the largest extent of polarized light emission from NGC 2023 extending from 250" E to 180" W and 220" N to 200" S with a maximum degree of polarization of 25 + 3% at 180 arcseconds W of HD 37903. Comparing the three colour maps shows that B > V > R in size of polarized emission so the extent of the nebula is seen to decrease with increasing wavelength, which may simply be due to an exposure effect.

Traces through HD 37903 in a east-west direction are given in Appendix C for filters B, V and R. All three polarization traces are asymmetric rising sharply and monotonically to the west and less steeply to the east. The degree of polarization increases with wavelength and offset distance: at 180" W of HD 37903 the nebula polarization is 25 + 3 (B), 28 + 2 % (V) and 40 + 5 (R). Arctraces of degree of visual polarization are plotted in Appendix C showing that the degree of polarization is not a constant with position angle for various radii from HD 37903. The polarized intensity traces are similar in profile with the highest intensity recorded between 40-50" E, a sharp fall off from maximum to 100" E, and low polarized intensity recorded to the west of HD 37903. The total intensity traces are also asymmetric about HD 37903 with the highest intensity recorded to the east of the baffle used to block the light of the illuminating star and a smaller maximum to the west followed by a sharp decline in intensity.

6.1 b CCD data

The data were obtained at the f/13.5 focus of the 1-m telescope at the Wise observatory, Israel during the nights of the 26th and 27th of November 1984. The grids were aligned north-south with the bright star HD 37903 placed outside the field of view. The region covered by the data was south of HD 37903; the approximate extent of which was 16" S to 412" S and 181" E to 318" W offset distance from the illuminating star. Eight stars were common to all the CCD data and these are labelled C1-8 in Plate 8. These stars were used to align all the data by matching their positions in the reduction with the stars in the red data as reference. A comparison of Plate 8 with Fig. 2 of Witt et al. (1984) led originally to the following stars - C, G, and 205 (Sellgren 1983) being identified. Again, from the measured positions of stars on UKSTU plates J8970 and I1963 and the centroid X,Y positions of the same stars on the CCD plates, the remaining stars had their celestial coordinates measured and this enabled the plate scale to be calculated, which was 1.21 +/- 0.01 arcseconds/pixel.

Table 6.4 lists the eight stars that are visible in the CCD data as marked on Plate 8. The reduced polarization maps in R, I and Z are shown in Figs. 6.5-6.7 (the reduction procedure and CCD system used to obtain this data is described in: Draper 1987; Wright and MacKay 1981).

All three polarization maps show positive polarization (E vector perpendicular to the radius vector from the illuminating

Table 6.4. Identification of stars from CCD data.

Star name	Sellgren (1983)	Strom et al. (1975a)	Offset from HD 37903 R.A.	Dec.
C1	-	-	179 E	272 S
C2	-	-	161 E	240 S
C3	205	S106	70 E	126 S
C4	G	-	58 E	122 S
C5	217	-	86 E	43 S
C6	218	S110?	87 E	33 S
C7	C	S108	30 W	74 S
C8	-	-	222 W	376 S

star) and a centrosymmetric pattern about HD 37903. There is an additional source of polarization that surrounds star C8, but which is illuminated by a source outside the field of view of this data. V615 Ori, an embedded star (Mannino 1959) and IRPS (05388-0224), is the most likely illuminating star. The extent of this reflection nebulosity around C8 is approximately 35 by 30 arcsec in the red plate, 40 by 45 arcsec in the I and 30 by 25 arcsec in Z. The data is generally smooth however there are three lines of insensitive pixels at 71" S, 119" S and 318" S of HD 37903 which can be seen in Plate 8.

The red map of NGC 2023 shows the largest extent of nebula polarized emission from 185" E to 220" W and from 16" S to 220" S

of HD 37903. The size of the I polarized emission is similar to R but not as smooth and there is a perturbed region of polarization around star S108. The Z data shows polarized emission out to 100" E, 100" W and 120" S from HD 37903, an increase in degree of polarization and a perturbed region around S108. All three reduced images show an additional source of reflection nebulosity around star C8, but only the R and I maps show the polarized emission due to an illuminating source outside the view of the polarimeter. The position of the source was calculated to be: (1950) R.A. 5h 38m 53.4s, Dec. -2 deg. 23' 58" using a program by P.W. Draper.

Of the three knots of Herbig-Haro object HH-1 only HH-1a and HH-1b can be seen and only in the R and I data; none of the knots are visible in the Z data. HH-1 has not affected the pattern of polarization in any of the polarization maps.

The visual appearance of NGC 2023 as shown in Plate 6 is of a nearly spherical reflection nebula with wispy filamentary structure. The angular size of the optical nebula is in agreement with the Hubble (1922) relationship: $m + 5 \log a = 11.02$ as its optical radius of ~ 4.3 arcmin is close to the implied radius of 4.5 arcmin given V=7.83 mag for HD 37903.

Plate 8 is the red CCD image of NGC 2023 after reduction. As well as seeing the reflection nebulosity due to NGC 2023 one can see the additional reflection nebulosity around star C8. The whole of this region south of HD 37903 has been mapped by White (1986)

Plate 8. A red CCD image of NGC 2023.

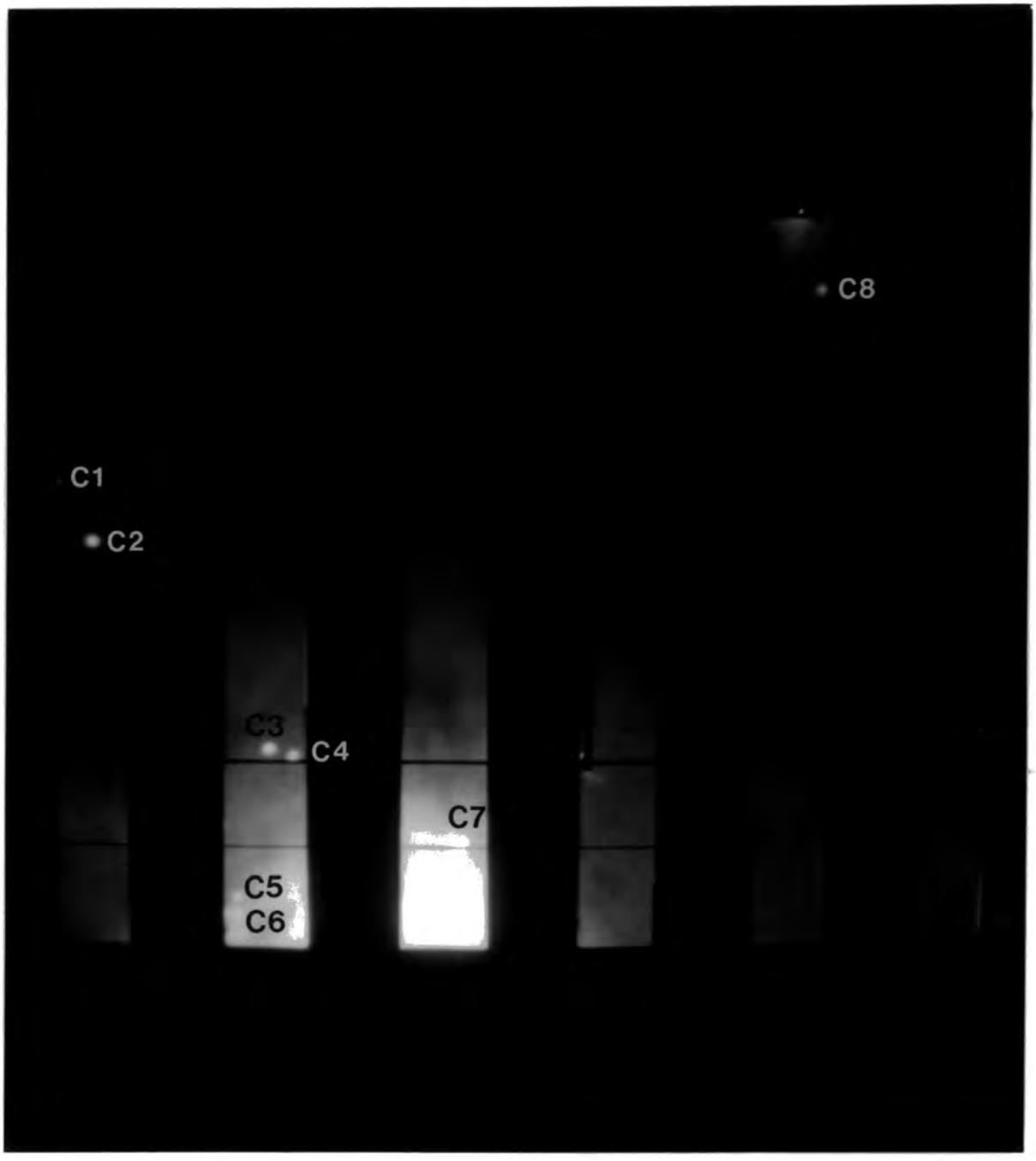
C8
C1
C2
C3
C4
C7
C5
C6

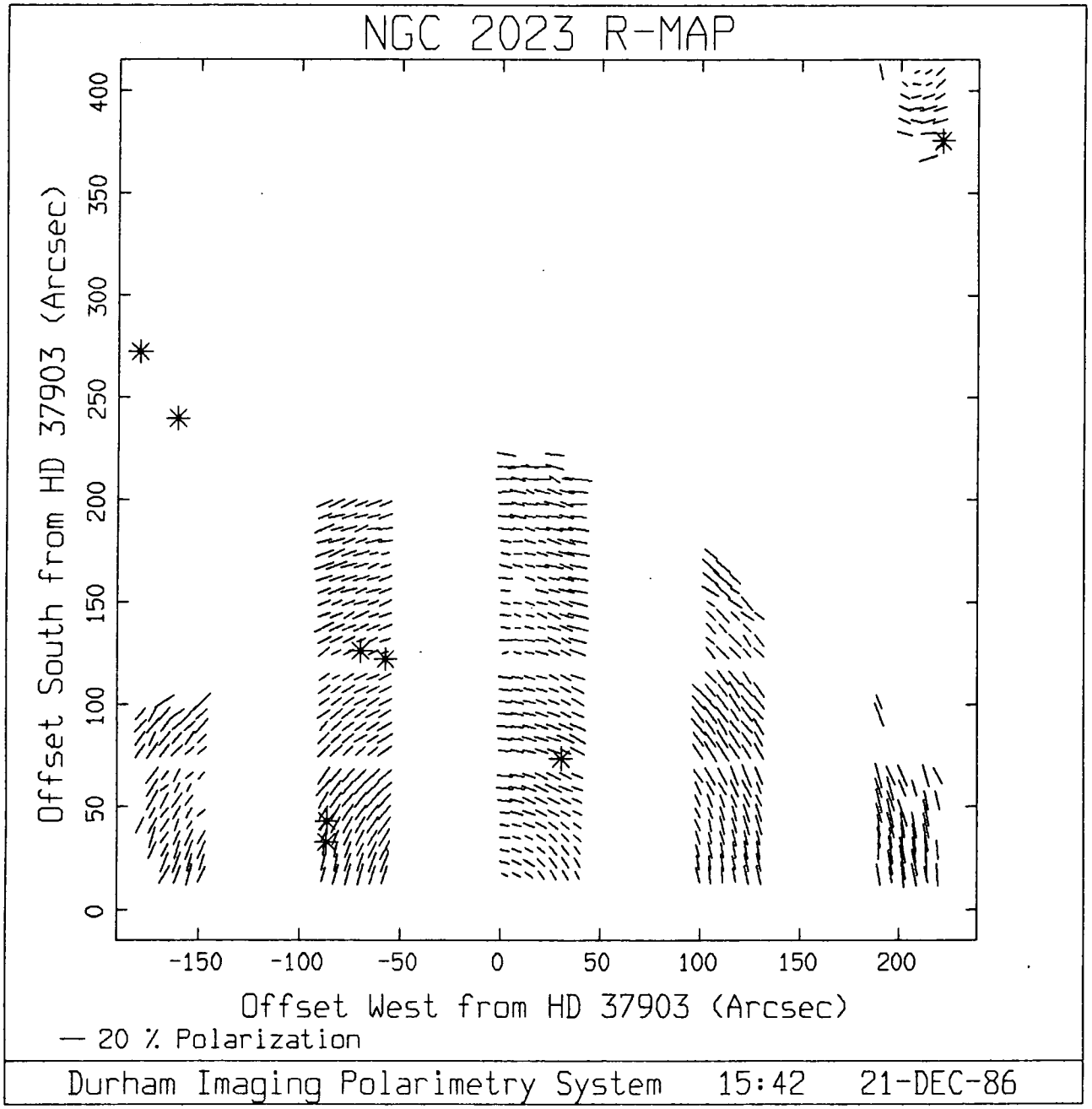

Fig. 6.5. Polarization of NGC 2023 using an R filter.

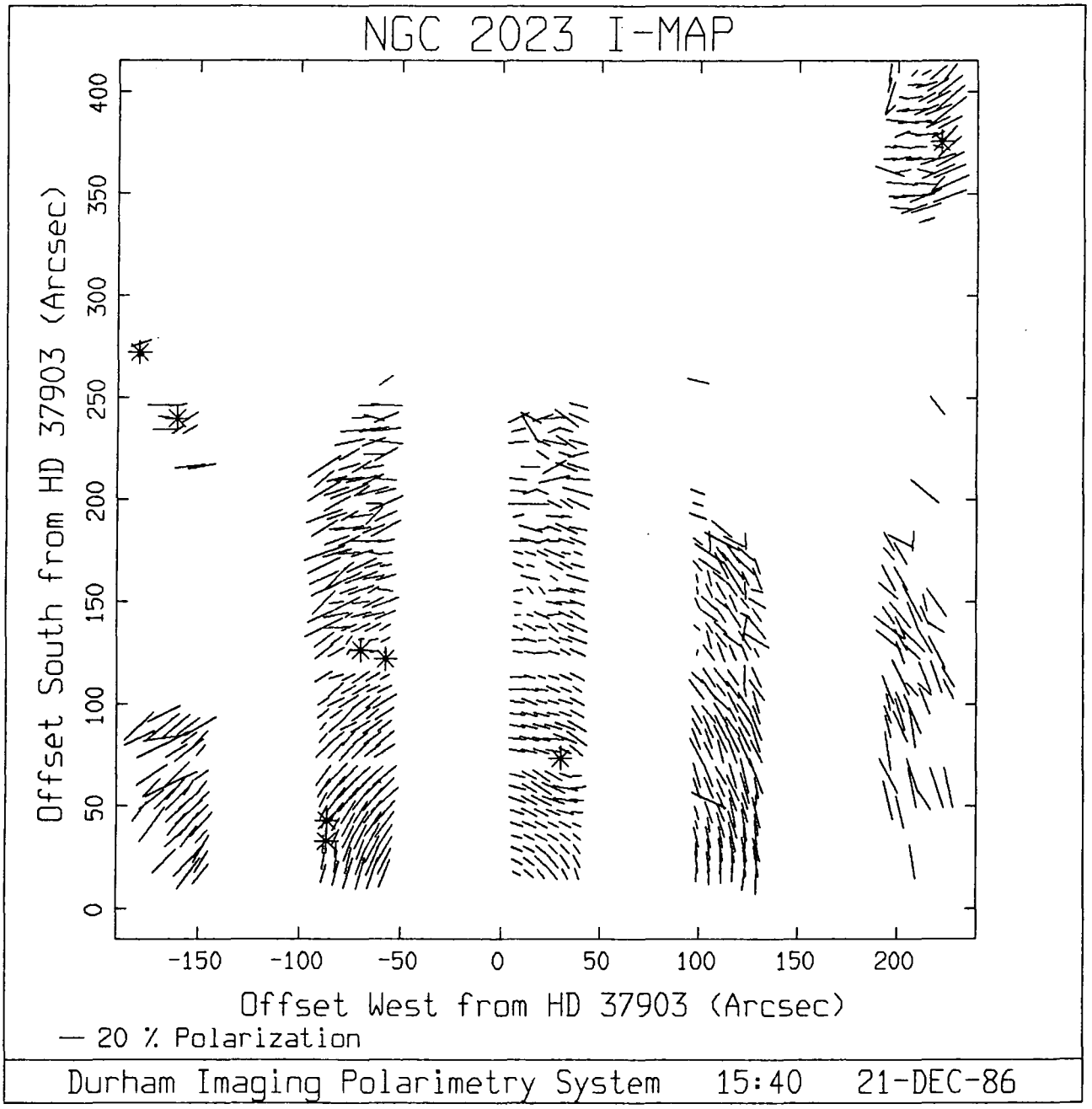

Fig. 6.6. Polarization of NGC 2023 using an I filter.

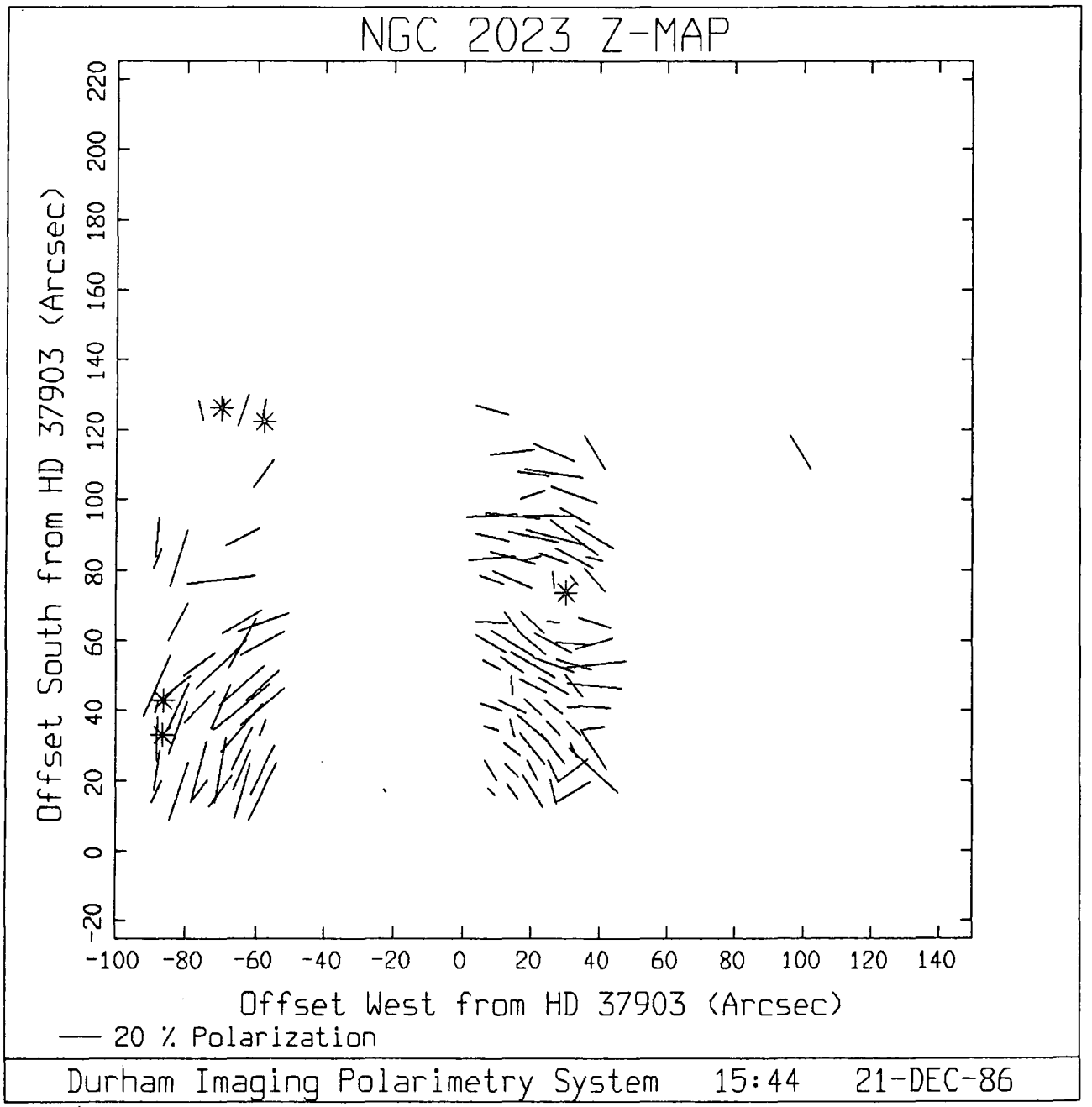

Fig. 6.7. Polarization of NGC 2023 using a Z filter.

in CO and his results of the dynamics of the area will be examined in chapter 7. A jet-like filament was found when changing the dynamic range of the image in order to enhance low intensity detail; this is shown in Plate 9. This possible polarized jet-like filament is seen near S108; the extent of the jet is between 30-35 arcseconds.

Traces through the R, I and Z data in a north-south direction are produced in Appendix C. The degree of polarization is seen to increase with offset distance and wavelength; in the Z data, the profile shows a sharp increase from 10-50 % between 6" S - 100" S while in the same interval R and I increase from 5-10 % and 8-12 % respectively. Polarized intensity falls sharply in R and I but there is a peak at 60" S while in the Z data polarized intensity is fairly constant over the 6 - 100" S range. In all three wavebands the total intensity decreases sharply between 16-50" S, then there is a small decrease from 50-70" S followed by a gradual fall off in intensity between 80-150" S and a plateau region > 150" S.

6.2 Comparison of CCD and Electronographic data on NGC 2023

A comparison of electronographic and CCD data on NGC 2023 can only be made for regions south of HD 37903. The differences in the two sets of polarimetry data on NGC 2023 can be most readily seen by examining the two sets of red images in which the star S108 is

seen in both and shows the CCD data goes to a fainter magnitude limit.

Areas common to both the electronographic and CCD data are given in Table 6.5. Listed in the table is the mean polarization for each region (calculated from sampling the areas using 6 by 6 arcsecond pixels) after polarizations greater than two standard deviations were rejected and a new mean and r.m.s. error was calculated. Table 6.5 a lists the polarization for those areas that are common to the 'grids in' electronographic data and the CCD data, while in 6.5 b, the data is for regions common to the visual 'grids out' electronographic data and the CCD data. The wavelength dependence of polarization is plotted in Fig. 6.8; the plot number referring to the region number with the mean position of the region given in arcseconds offset from HD 37903.

No evidence for aligned grains can be found from either set of data as there are no parallel polarization vectors seen in any of the data except possibly for the region surrounding the star S108 in I and Z. However, there is no perturbation around S108 in the B, V and R data. The position angle of the jet-like filament is approximately 125 + 5 degrees, and this jet is seen in the R and I data only and is not visible in the electronographic B, V, or R data.

For regions close to HD 37903, there is agreement between the CCD and electronographic red data, e.g. regions 1, 2, 3 and 6 in

Table 6.5 a. Multicolour polarimetry of NGC 2023.

Region No.	Offset in arcseconds from HD 37903	Electronographic data B %	V %	R %	CCD data R %	I %	Z %
1	92 W - 132 W	14.3	24.7	31.8	14.5	19.6	53.9
	68 S - 105 S	+/-6.5	4.9	5.9	1.6	3.1	15.7
2	1 E - 42 W	8.9	11.0	13.1	11.0	13.0	18.3
	68 S - 105 S	+/-1.8	1.4	1.8	1.1	2.3	9.9
3	52 E - 93 E	7.2	10.8	9.7	11.5	16.1	37.1
	68 S - 105 S	+/-2.1	1.4	2.1	1.2	3.2	20.5
4	181 E - 144 E	10.1	20.1	6.1	13.0	38.6	-
	161 S - 203 S	+/-3.5	4.7	3.6	2.2	16.7	-
5	92 W - 132 W	19.5	21.2	47.4	15.0	20.0	-
	161 S - 203 S	+/-9.3	10.1	11.4	3.6	10.2	-
6	1 E - 42 W	7.6	12.8	18.1	11.2	11.3	46.6
	161 S - 203 S	+/-4.3	3.7	5.3	2.9	4.7	20.1
7	52 E - 93 E	9.4	14.5	8.1	12.1	18.9	-
	161 S - 203 S	+/-2.2	4.8	3.5	1.8	7.2	-
8	181 E - 144 E	10.6	57.3	18.0	21.5	55.4	-
	161 S - 203 S	+/-4.7	13.8	10.3	4.7	11.7	-

Table 6.5 a whose radial distance is less than 200 arcsec from the illuminating star. The polarization measurements in the furthest regions suffer large errors due to the very low signal observed.

Table 6.5 b. Multicolour polarimetry of NGC 2023.

Region No.	Offset in arcseconds from HD 37903	Electronographic data B %	V %	R %	CCD data R %	I %	Z %
1	181 E - 144 E	-	37.7	-	11.7	29.2	-
	24 S - 64 S		+/-12.7	-	3.6	10.2	-
2	93 E - 52 E	-	13.6	-	14.2	21.2	31.3
	24 S - 64 S		+/- 1.6	-	1.5	4.4	16.1
3	1 E - 42 W	-	6.9	-	9.2	12.3	14.2
	24 S - 64 S		+/- 1.5	-	1.7	3.2	6.1
4	92 W - 132 W	-	19.8	-	11.9	18.7	57.5
	24 S - 64 S		+/- 3.3	-	2.1	4.9	22.3
5	93 E - 52 E	-	11.7	-	10.5	14.5	50.9
	118 S - 157 S		+/- 5.7	-	1.8	7.1	19.1
6	1 E - 42 W	-	16.2	-	9.2	10.0	49.5
	118 S - 157 S		+/- 5.5	-	3.0	3.4	22.5
7	92 W - 132 W	-	38.9	-	11.8	14.2	57.3
	118 S - 157 S		+/-21.2	-	3.4	6.5	7.9

Table 6.6 lists all the stars found in the NGC 2023 data internal accuracy is $\overset{+}{-}$ 2 arcsec cf. Sellgren (1983) whose stellar positions were accurate to between 3-4 arcsec.

Table 6.6. Stars common to CCD and Electronographic data.

Sellgren (1983)	Strom et al. (1975a)	CCD name	Electron name	CCD Offset (")	Electronographic In (")	Out (")
-	-	-	E8	-	254 E 112 N	-
-	-	C1	-	179 E 272 S	-	-
-	-	C2	-	161 E 240 S	-	-
-	-	-	E7	-	146 E 291 N	-
H	S105	-	E6	-	128 E 68 S	132 E 62 S
218	S110	C6	-	87 E 33 S	-	-
217	-	C5	-	86 E 43 S	-	-
-	-	-	E4	-	72 E 308 N	-
205	S106	C3	E5	70 E 126 S	-	71 E 130 S
G	-	C4	-	58 E 122 S	-	-
C	S108	C7	E3	30 W 74 S	33 W 75 S	-
J	-	-	E2	-	153 W 95 N	-
M	-	-	E1	-	-	158 W 252 S
-	-	C8	-	222 W 376 S	-	-

6.3 Wavelength dependence of polarization

The degree of polarization increases with wavelength in the range 440-930 nm for all the fifteen regions examined with the exception of region 1 in Table 6.5 b where the V polarization is spuriously large. Indeed, looking at Figs. 6.8 a and b which show the wavelength dependence of polarization for the closest regions

to HD 37903, i.e. regions 1, 2, 3 and 6 for 'grids in' and 2, 3, 5 and 6 for 'grids out', the underlying trend is for the degree of polarization to increase with wavelength.

Using a least-squares fitting program to fit a line (Y=mx+c) to the three closest regions to HD 37903 gave the following parameters:

Region No.	Table	Radial Distance (")	c	m
2	6.5a	89.5	1.33 +/- 2.44	1.68 E-2 +/- 3.55 E-3
2	6.5b	85.2	-12.15 +/- 8.47	4.43 E-2 +/- 1.14 E-2
3	6.5b	48.8	-2.65 +/- 1.25	1.83 E-2 +/- 1.68 E-2

This spectral dependence of polarization will be modelled in chapter 7 by considering Mie scattering from dust grains. This was done by Zellner (1970) for regions of NGC 7023 and NGC 2068 in which the models rejected graphite and metallic grains and favoured dielectric grains.

No statement can be made on how the spectral dependence of polarization varies with radial distance from HD 37903 as beyond 100" radial distance the errors on polarization become increasingly large.

Fig. 6.9 shows the constancy of polarization position angle with wavelength within the error bars (+/- 10 degrees).

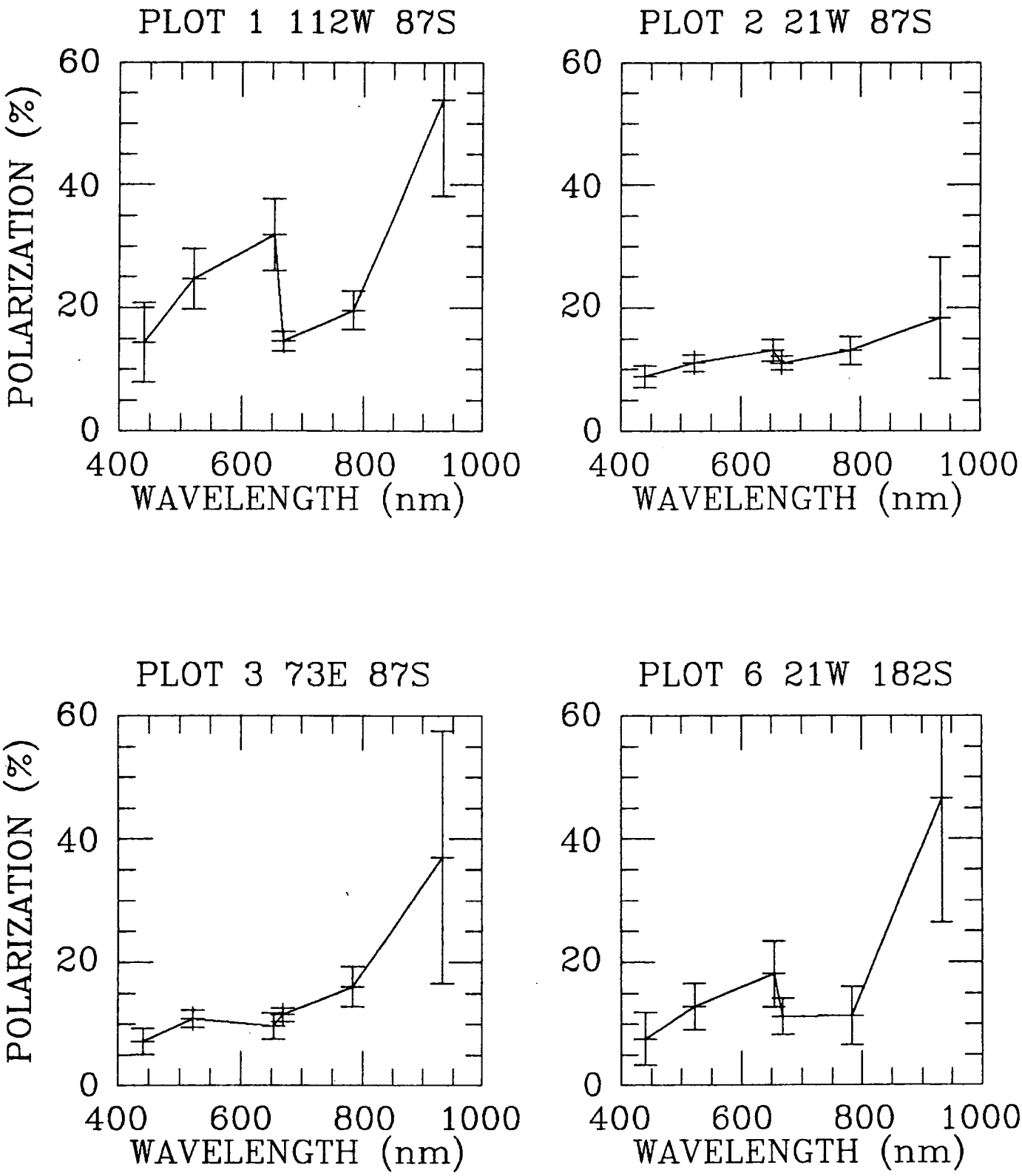

Fig. 6.8 a. Wavelength dependence of polarization.

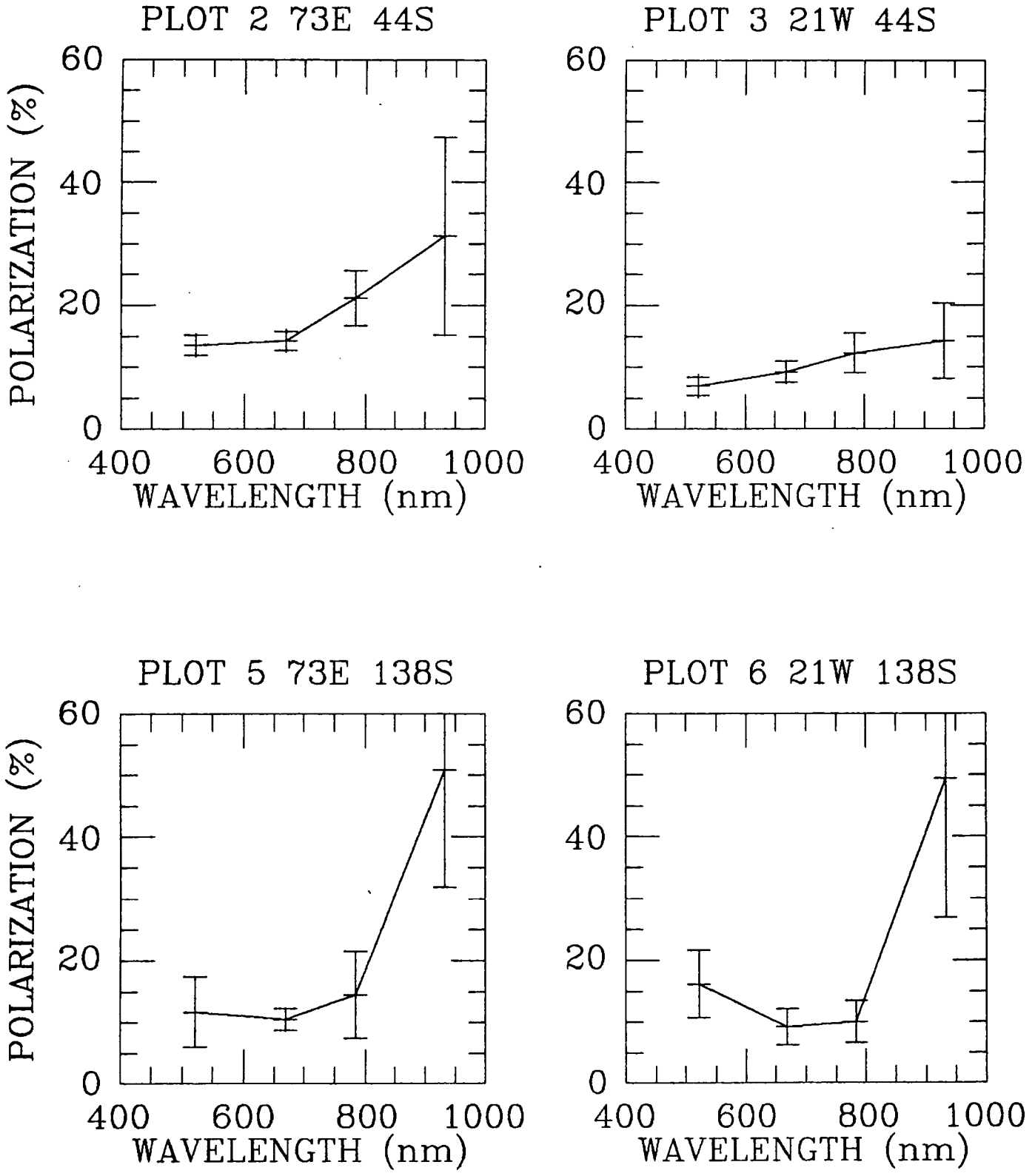

Fig. 6.8 b. Wavelength dependence of polarization.

Measurements of the wavelength dependence of polarization position angle for those regions common to the electronographic and CCD data are tabulated in Table 6.7 a and b.

Table 6.7 a. Multicolour polarimetry of NGC 2023.

Region No.	Offset in arcseconds from HD 37903	Electronographic data B deg	V deg	R deg	CCD data R deg	I deg	Z deg
1	92 W - 132 W	152.1	151.0	137.2	144.3	152.1	127.4
	68 S - 105 S	+/-2.4	5.4	9.1	3.8	6.8	43.9
2	1 E - 42 W	106.2	101.0	109.0	106.2	106.0	110.1
	68 S - 105 S	+/-1.8	9.6	9.6	7.1	8.4	30.5
3	52 E - 93 E	46.2	43.7	49.9	52.8	51.4	95.1
	68 S - 105 S	+/-1.6	6.0	10.3	1.0	6.7	20.5
4	181 E - 144 E	26.3	17.1	12.8	41.5	55.9	-
	68 S - 105 S	+/-10.6	9.9	24.0	7.1	7.1	-
5	92 W - 132 W	143.2	138.9	132.4	123.7	137.3	-
	161 S - 203 S	+/-3.7	11.9	12.5	13.4	21.1	-
6	1 E - 42 W	106.2	113.7	112.3	101.0	104.9	138.8
	161 S - 203 S	+/-12.8	14.0	2.4	5.3	15.6	47.5
7	52 E - 93 E	57.1	47.4	65.9	72.0	76.9	-
	161 S - 203 S	+/-16.1	3.3	19.5	4.8	7.2	-
8	181 E - 144 E	31.9	25.6	72.7	59.4	113.4	-
	161 S - 203 S	+/-17.0	4.8	54.7	5.8	11.7	-

Table 6.7 b. Multicolour polarimetry of NGC 2023.

Region No.	Offset in arcseconds from HD 37903	Electronographic data B deg	V deg	R deg	CCD data R deg	I deg	Z deg
1	181 E - 144 E	-	0.0	-	30.4	36.5	-
	24 S - 64 S		+/-17.1	-	8.5	26.8	-
2	93 E - 52 E	-	24.9	-	33.7	33.0	13.0
	24 S - 64 S		+/- 8.6	-	7.7	9.0	52.4
3	1 E - 42 W	-	111.5	-	115.6	114.6	122.4
	24 S - 64 S		+/-17.7	-	11.9	12.1	21.9
4	92 W - 132 W	-	156.9	-	160.7	164.4	140.4
	24 S - 64 S		+/- 5.5	-	6.0	10.9	46.3
5	93 E - 52 E	-	61.7	-	66.9	66.2	65.2
	118 S - 157 S		+/-29.7	-	5.0	13.6	23.7
6	1 E - 42 W	-	99.1	-	106.2	107.1	125.4
	118 S - 157 S		+/-12.4	-	19.1	15.7	40.2
7	92 W - 132 W	-	129.2	-	127.3	143.9	115.3
	118 S - 157 S		+/-19.9	-	12.5	22.0	26.6

Sellgren (1984a,b) has found that some reflection nebulae are significantly brighter at 2-microns than would be expected from scattering so it is important to obtain colour and polarization data in the near-infrared to understand what the emission mechanism is. As well as trying to get information on the

scattering properties of nebula dust, one can study the population of young stellar objects embedded in NGC 2023 and examine the cloud geometry, including the spatial distribution of stars and dust etc. This is in order to: 1. look at the IMF of the stars in the reflection nebula, 2. see if there are any stellar alignments (has any one star triggered a sequence of star formation?), and 3. test hypotheses on star-cloud interactions. The young stellar populations of reflection nebula can be better studied in the far-red to near-infrared (see Witt et al. 1984) as in this wavelength region the optical depth is small. The stars in the NGC 2023 cluster are on the nearside of the dust cloud and from infrared energy distribution measurements it is likely that there are inhomogeneities in NGC 2023's dust distribution (Evans 1981). Witt et al. (1984) concludes that there is considerable non-scattering emission in R and I in NGC 2023 (known as extended red emission, ERE). The evidence of ERE and the results of the wavelength dependence of polarization from this data and possible emission mechanisms will be discussed in the analysis of NGC 2023 in chapter 7.

6.4 IRAS data

Apart from the infrared stars seen (faintest star seen in the red CCD data is 218 at r=17.19 mag - Witt et al. 1984) there may be deeply embedded T Tauri stars, which may be the sources of Herbig-Haro objects HH1-5.

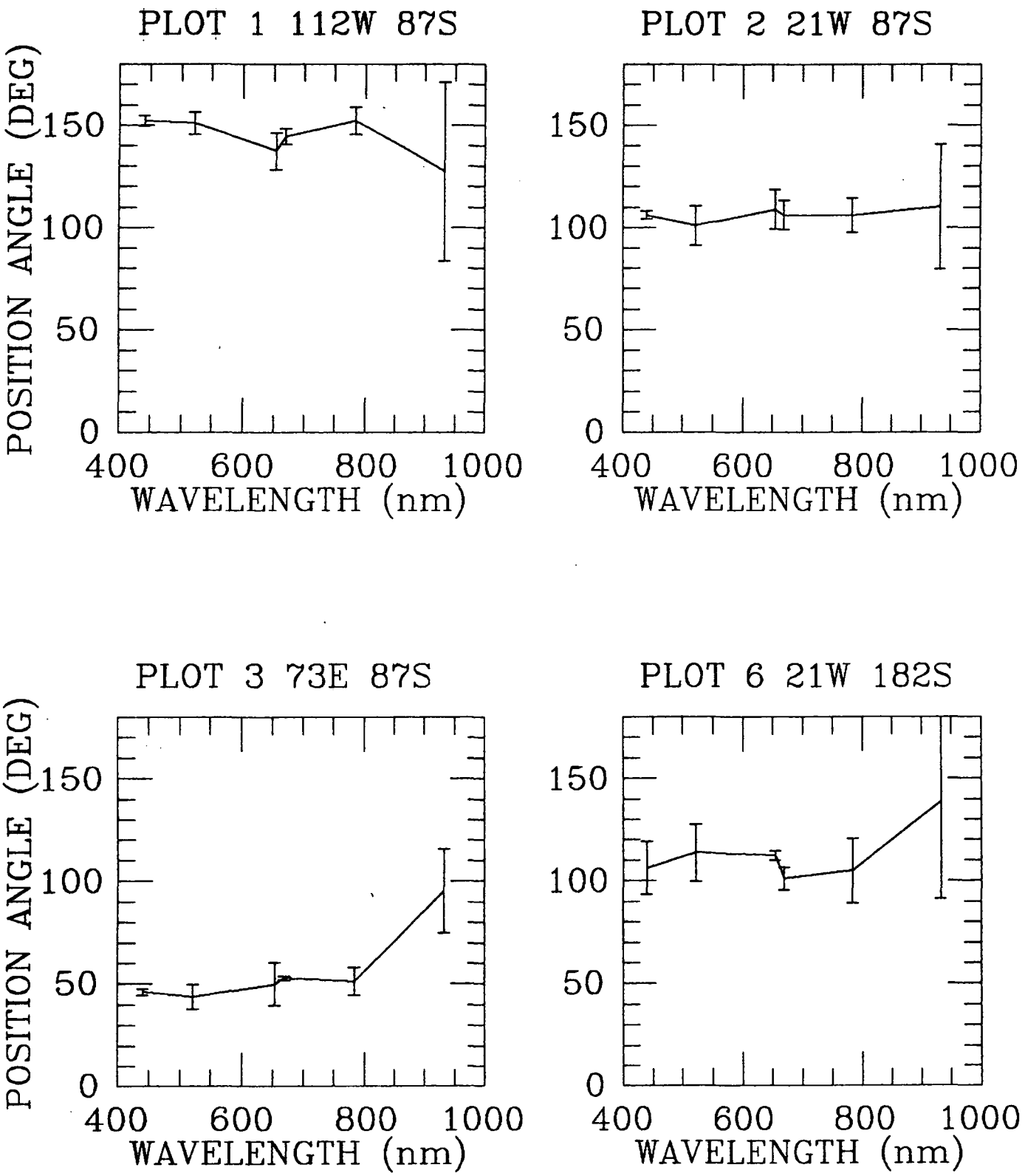

Fig. 6.9 a. Wavelength dependence of position angle.

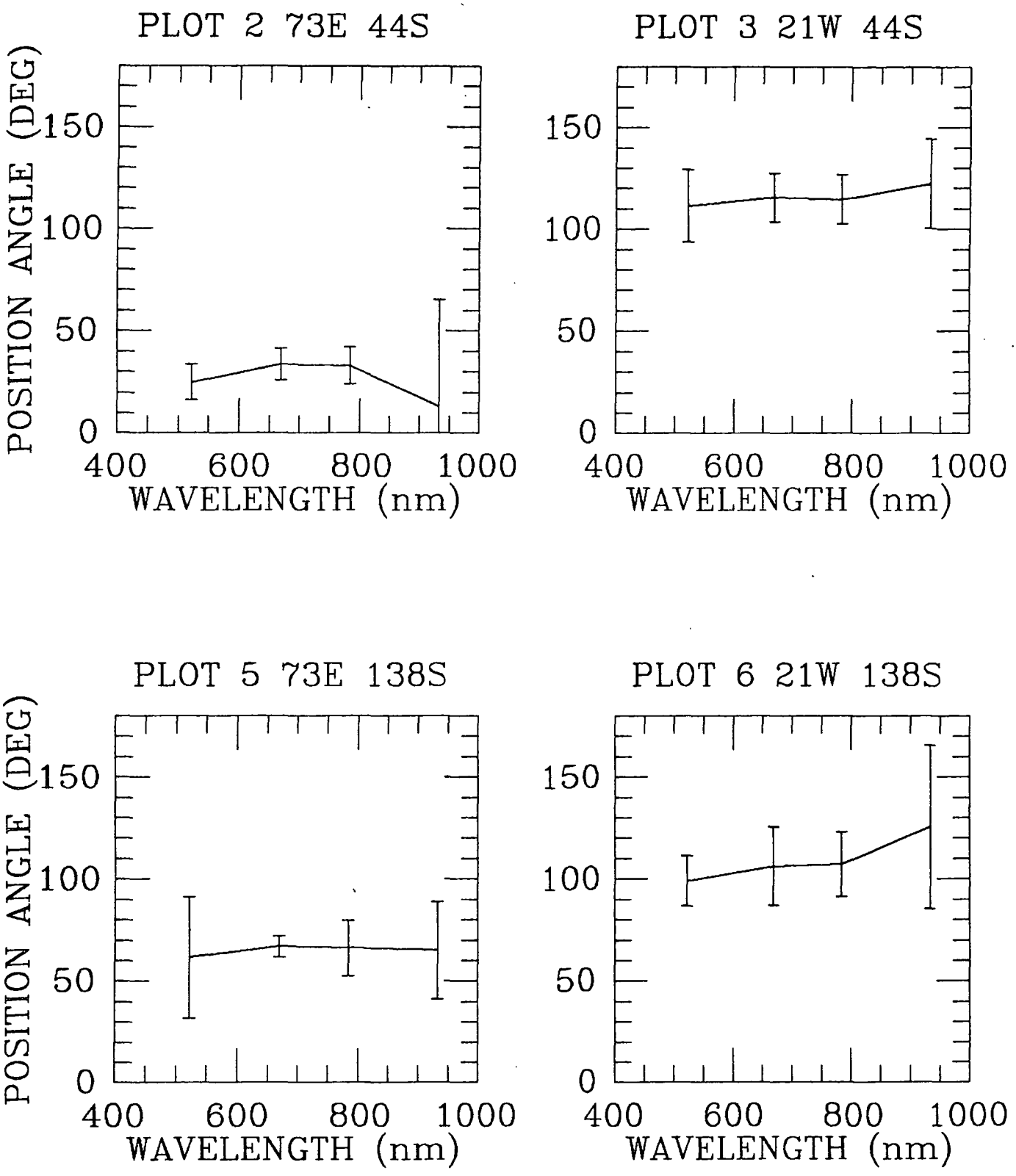

Fig. 6.9 b. Wavelength dependence of position angle.

The IRAS point source catalogue data was interogated and a source (05391-0217) was found close to the centre of NGC 2023 at 21.4 arcseconds radial distance from HD 37903. There are 12 IRPS within 15 arcminutes square centred on HD 37903, but none could be matched with the visible stars of Table 6.2. Some could be deeply embedded T Tauri stars; however, none with the exception of HD 37903, could satisfy the empirical criterion of being located in the region of known T Tauri stars in the IRAS colour-colour diagram given by: $0.0 < \mathrm{Log}(S(25\ \mu m)/S(12\ \mu m)) < 0.6$ and $-0.3 < \mathrm{Log}(S(60\ \mu m/S(25\ \mu m)) < 0.5$ (see Michael Rowan-Robinson 1986).

6.5 The optical filament and HH-1

The Herbig-Haro object HH-1 recently discovered by Malin et al. (1986) has 1950 co-ordinates: R.A. 5h 39min 00.7s, Dec. -2 deg. 18' 50" or an offset from HD 37903 = 98.5" W, 111.7" S. Optical evidence could be found for this object in the CCD data (R and I), but the object was not in the field of view of the electronographic data. As well as detecting HH-1 in the polarimetry data there was evidence of a possible cometary nebula in the CCD data. The optical filament SE from S108 has an appearance of a cometary nebula emanating from star S108. This jet-like filament is apparently not bipolar but extends in one direction 35 arcseconds = 0.08 pc if at 500 pc at a position angle of 125 degrees, i.e. nearly perpendicular to the the direction of HH-1 from S108. There is an intermediate molecular flow in NGC 2023 that was recorded in the survey of Bally and Lada (1983) and

whose coordinates are: 5h 39m 6s, Dec -2 deg. 17' 24". or 19.0" W, 25.7" S of HD 37903. This flow is only 117.1 arcseconds from HH-1 and less than 55 arcseconds from S108 and the associated optical filament. HH-1 in turn is 77.8 arcseconds from S108 and the filament. Which star is the source of HH-1 and how are these objects related? We will return to these questions in chapter 7.

In order to test whether aligned grains are responsible for the unusual polarization seen around the star S108 one can look at the wavelength dependence of polarization for this region. The wavelength dependence can fall into one of two regimes: either due to transmission through aligned grains in which the degree of polarization follows the Serkowski law and is typically a few percent, or due to scattering in which a high degree of polarization can be produced and polarization usually increases with wavelength (Zellner 1973). Aperture polarimetry was carried out using a 10 pixel circular aperture (12.1 arcsec.) on five areas close to the star S108; the results are given in Table 6.8. The degree of polarization is seen to increase with wavelength in the range 0.6 - 0.93 micron so must be due to scattering and not due to transmission through aligned grains.

Table 6.8. Polarimetry of regions close to S108.

Offset from star S108 (arcseconds)	Degree of Polarization R (%)	I (%)	Z (%)
0 E, 9 N	11.7	12.9	28.9
0 E, 8 S	12.8	16.5	11.9
18 E, 8 S	10.9	14.7	21.8
9 E, 8 S	11.4	14.1	5.5
18 E 17 S	10.7	12.9	12.9

Plate 9 shows part of an AAT plate (see Malin et al. 1986) and the CCD red plate showing the optical jet-like filament emanating from star S108. Fig. 6.10 presents a polarization map of the S108 region using an I filter adjacent to a contour map using an R filter showing the optical filament.

CO J=2-1 observations of this region one arcminute south of HD 37903 have been made (White 1986) and have indicated a CO bipolar outflow and molecular hot spot close to star S108.

6.6 Discussion

The illuminating star of NGC 2023 is HD 37903; as can be seen from the single centre of centrosymmetry displayed by the set of polarization vectors in the B,V,R,I and Z data. The exception to the generally smooth pattern of polarization about HD 37903 is the polarized region seen in I and Z that surrounds the star S108.

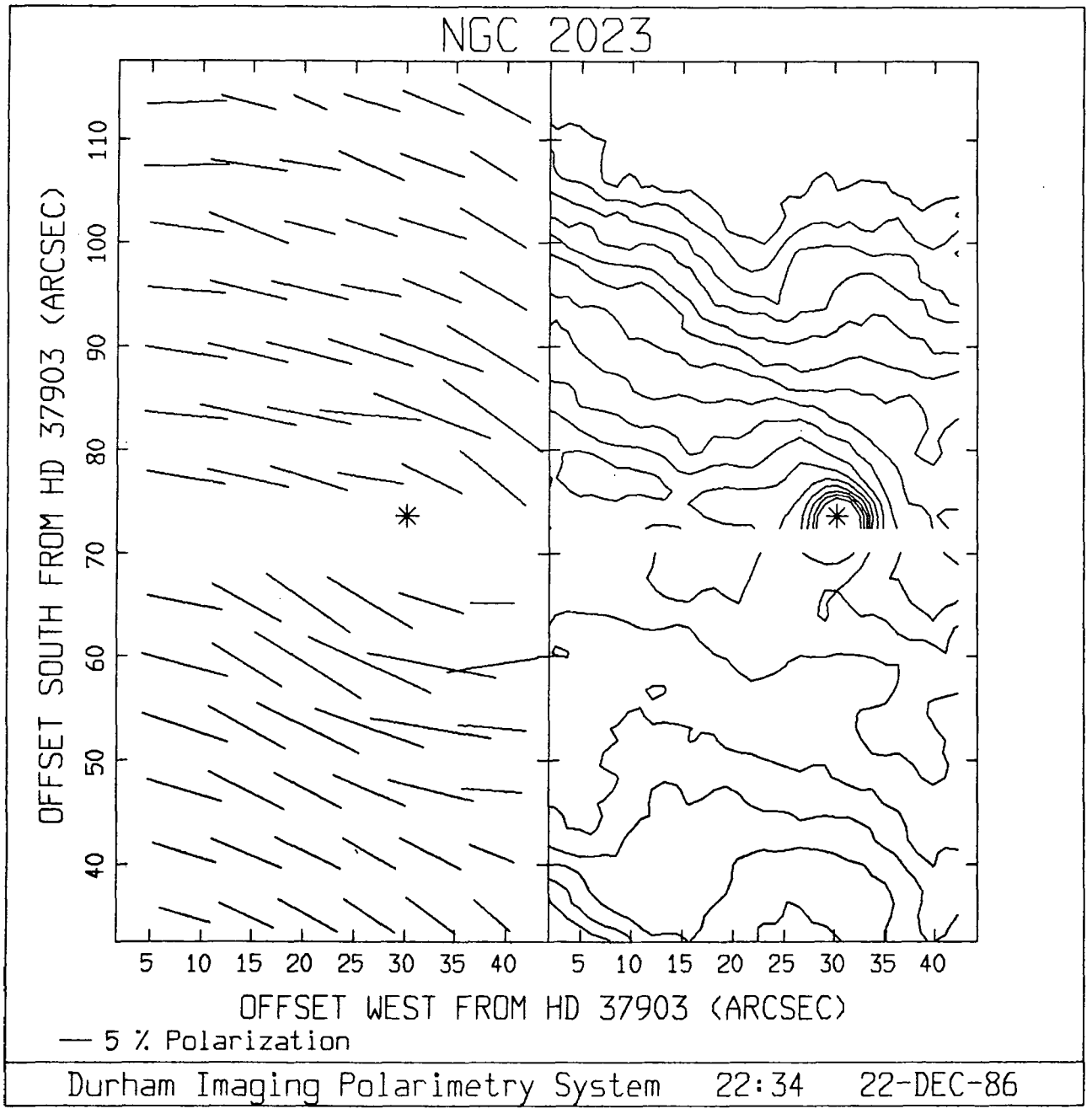

Fig. 6.10. A polarization and contour map of the S108 region.

Plate 9. The optical filament associated with S108.

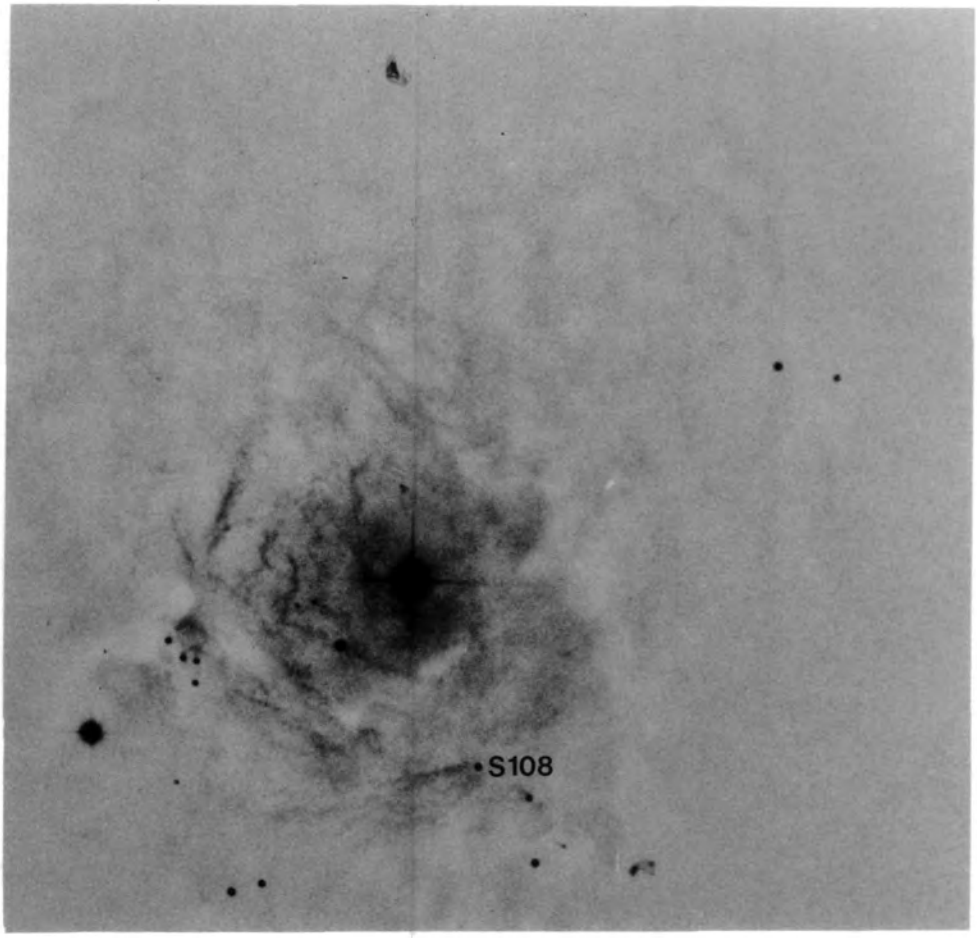
S108

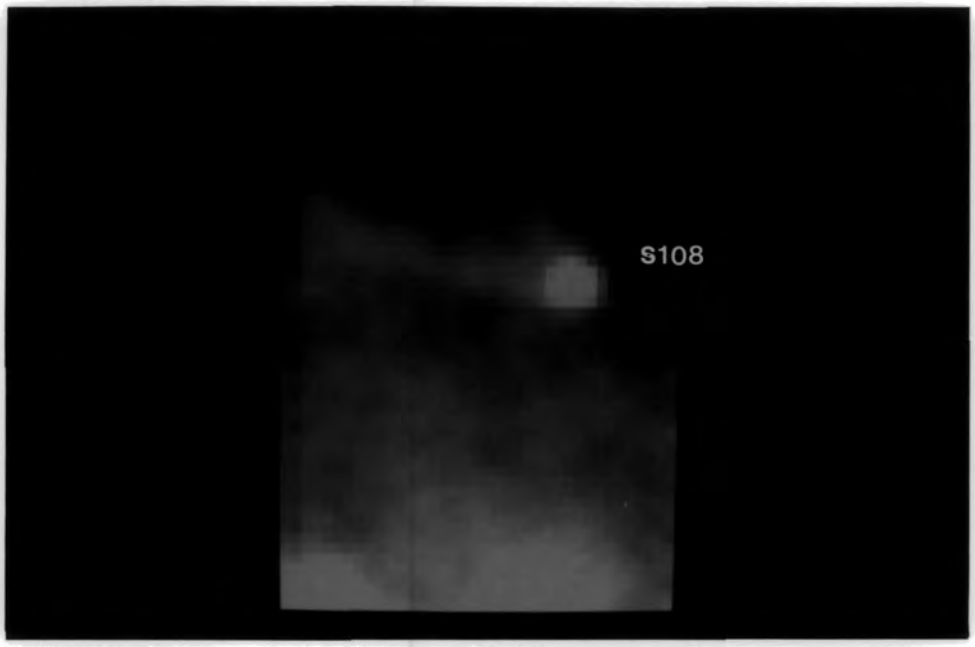
S108

It has been shown that the degree of nebula polarization increases with wavelength for regions south of HD 37903. A linear least-squares fit showed that polarization increases with wavelength uniformly as was found by Zellner (1970) for NGC 2068. However, the position angle dependence is constant with wavelength for the regions studied in NGC 2023 unlike the observation by Zellner (1970) of NGC 2068.

There is a spatial coincidence of the star S108, the unusual polarized region in I and Z that deviates from the nebula's centrosymmetric pattern, the jet-like filament seen in the red and I data, the increase in dust density and the peaks in CO, CII and FIR emissions at 1 arcminute south of HD 37903. There is also a CO bipolar outflow (White 1986) centred on this region.

The fact that the small near-centrosymmetric region that surrounds the star S108 is visible in only the I and Z wavebands but not in B, V or R is indicative of S108 being embedded in dense nebula dust and producing a reflection nebula in the near-infrared as at these wavelengths the optical depth is small enough for the polarized light - due to Mie-scattering from dust grains surrounding S108 - to escape.

Polarization is seen over a region approximately 200" N to 210" S and 220" E to 185" W of HD 37903 in R, and from the observed strong spectral dependence of polarization this implies Mie-scattering off dust grains (Zellner 1974). The nebula is very blue as is indicated by the extent of polarized emission in B

although the relative size of the nebula in polarized light may simple be due to an exposure effect.

There has been a significant increase in data on NGC 2023: this is the first multicolour polarimetry study of NGC 2023.

For regions close to the illuminating star (<100 arcsec) there is good agreement between the measured degree and position angle of polarization in R in both sets of data. Only one star was common to both sets of data, i.e. S108 and clearly the CCD data is deeper.

Zellner (1973) reported the observation of polarization decreasing with increasing wavenumber from IR to UV which is a characteristic of forward scattering dielectric grains and this was found to be the case in NGC 2023: the degree of polarization measured in Region 2 (table 6.5 a) was 8.9 % (B), 11.0 % (V), 12.0 % (R), 13.0 % (I) and 18.3 % (Z) cf. Zellner's (1970) Region 1 using 6 filters between 0.33 - 0.83 micron the degree of polarization increased with wavelength as: 4.9 % (U), 7.2 % (B), 8.4 % (V), 9.1 % (O), 12.5 % (R).

The reflection nebula is similar to NGC 1999 (see Warren-Smith et al. 1980), which is also embedded on the nearside of a dust cloud (L1641); however, in the case of NGC 2023 there is no obvious geometry, but some modelling of the spectral dependence of polarization is presented in chapter 7.

CHAPTER 7 Analysis of NGC 2023

7.1 Physical conditions in NGC 2023

The physical conditions in NGC 2023 and the surrounding molecular cloud, which are embedded in L1630, have been probed through observations in various regions of the EM spectrum (from radio to UV) and the important results are now listed below:

Radio: At cm wavelengths there will be free-free emission and recombination line emission due to ionized atoms in NGC 2023 produced by early-type stars; surrounding which will be the ionized regions known as Stromgren spheres. The size of any HII region produced is dependent on the flux of UV photons and thus the spectral type of the illuminating star as well as the density of the surrounding medium. Knapp et al. (1975) looked for H109alpha and H76alpha towards NGC 2023, but failed to detect any recombination lines unlike in the case of NGC 2068 in which a compact HII region was found (Matsakis et al. 1976). Knapp et al. estimated the size of the NGC 2023 HII region to be between 5-25 arcseconds while Pankonin and Walmsley (1976) expected a 0.015 pc (6.2 arcsec.) diameter region, but calculated that the H recombination line flux would be too weak to detect, although they did detect a point source of radio continuum centred on HD 37903.

HD 37903, although not hot enough to produce a sizeable HII region, has given rise to an extended CII region and to carbon

recombination line emission that has been detected by: Brown et al. (1975); Knapp et al. (1975); Pankonin and Walmsley (1976); Pankonin and Walmsley (1978); and Gorkom et al. (1979). Pankonin and Walmsley (1978) reported that the peak CII emission is close to where there is a peak in the CO emission, i.e. one arcminute south of HD 37903. The single source for both emissions is HD 37903, which is hot enough (B1.5V) to supply all the carbon ionizing photons, but there could be a contribution from the star S108 (Pankonin and Walmsley 1978). It appears that the illuminating star imparts no expansion or turbulent motion to the surrounding gas from examining the width of the emission lines from different parts of NGC 2023 (Knapp et al. 1975). Summarizing the physical parameters from this data: the size of the CII region is ~0.3 pc; the electron density is in the range 10-25 cm-3; the molecular density nH > E4 cm-3; and Te ~ 20-50 K.

CO line emission has been detected by Tucker et al. (1973) and by Milman et al. (1975) who found enhanced CO emission towards NGC 2023 with a peak gas temperature of 34 K centred on HD 37903. Other rotational molecular lines observed in NGC 2023 include: observations by Pankonin and Walmsley (1978) of OH and H CO (which also peak 1' to the south), and HCN detected by Morris et al. (1974) at ~ 1 arcmin SE of HD 37903. The detection of HCN implies high molecular density ~ E5 cm-3. White et al. (1981) made high resolution J=3-2 CO measurements of NGC 2023 and found an isolated symmetrical cloud with a peak excitation temperature Tex = 39 K. The CO excitation temperatures for three CO transitions are: J=1-0

51 K, J=2-1 40 K, and J=3-2 39 K (White et al. 1981 and references therein). The nebula is near the front edge of the cloud (Milman 1975) and has a size (from CO observations) of 2 pc (White et al. 1981).

FIR: Early FIR observations of NGC 2023 in the range 40-350 micron by Emerson, Furniss and Jennings (1975; hereafter EFJ) showed HD 37903 to be the source of the UV photons that are absorbed by the surrounding dust and reemitted in the FIR; this emission was found to peak at the position of HD 37903. The temperature of the dust was assumed to be equal to the CO excitation temperature that was measured by Tucker et al. (1973), i.e. Td ~ 43 K. The FIR emission was modelled to obtain the mass of dust and it was found that the dust temperature was roughly proportional to the gas temperature over the range 40-80 K; the total FIR luminosity being 2.3 E Lo. IRAS data at 12, 25, 60 and 100 micron on the FIR source of NGC 2023 (05391-0217) gives a dust temperature assuming either a 1/lambda or a 1/lambda squared emissivity law of 38 K and 31 K respectively (using a program by Chris Hirst). Harvey and Thronson (1980) made observations between 40-160 micron which show that there are two peaks in the FIR emission; at the shorter wavelength, the FIR emission peaks on or close to HD 37903, while the longer wavelength emission peaks one arcminute south of HD 37903 coincident with the CII recombination line peak. The size of the FIR emission is 5' similar to the optical size indicating the extent of dust in the nebula. The dust density increases by a factor of 4 one arcminute south of HD 37903

(Harvey and Thronson 1980). The exciting star HD 37903 appears to be on the near-side of a dense molecular cloud.

NIR: Sellgren et al. (1983) and Sellgren (1984a,b) have discovered an extended 2-5 micron continuum emission and emission lines at 3.3, 3.4 microns in NGC 2023 (and in NGC 7023 and NGC 2068). This emission apparently cannot be explained by scattered light from dust grains. Explanations put forward include thermal fluctuations in small (~10 Angstrom) grains, continuum fluorescence, and thermal emission in grains with extremely low ratios of IR to UV emissivites (Sellgren et al. 1983).

Sellgren (1983), Strom et al. (1975a) and Strom et al. (1976) carried out NIR surveys of selected regions of L1630 and discovered a significant number of heavily obscured stars (Av > 10 mag.). Many of the most luminous stars associated with the reflection nebulae NGC 2023, NGC 2068 and NGC 2071 are believed to be very young, e.g. HD 37903 appears to have a minimum age of 1.5 E5 yrs (Strom et al. 1975a). In the vicinity of NGC 2023 a cluster of ten 2-micron sources were identified, which are probably late B or early A type stars. Spectrophotometry on stars C and H by Sellgren (1983) showed that these particular stars have Halpha emission lines due to either a circumstellar shell or a stellar wind. The ratio of total to selective extinction was measured for several stars in L1630 and found to be in the range 3.6-5.8, characteristic of large grains.

Optical data: Witt et al. (1984) reported photometry of the reflection nebula NGC 2023 and various probable pre-main sequence stars in the range 350-1000 nm. They found: 1) The radiation in the 350-500 nm is due to dust scattered starlight from HD 37903; the dust having an albedo a~0.65 and phase function g=0.6-0.7. 2) The stars found associated with NGC 2023, which are most likely PMSS, are not major contributers to the illumination of the reflection nebula. 3) An R and I excess in the nebula emission which requires a non-scattering mechanism. 4) An explanation of the extended red emission (ERE) in terms of a possible high-frequency extension of the 2-5 micron emission observed by Sellgren et al. (1983). Witt and Schild (1985) did B, V and I photometry on four reflection nebulae which were found to exhibit an R and I excess. In NGC 2023, this emission correlated with the bluest nebula regions and the NIR emission of Sellgren et al. (1983). This demonstrates the common nature and origin of the I excess and ERE. A UV excitation mechanism for extended NIR emission has been put forward by Witt and Schild (1985). The optical size of NGC 2023 is in agreement with the Hubble relation so that the nebula might be luminosity bounded.

Reynolds and Ogden (1979) studied the gas structure and dynamics in the Orion region through observations of optical emission lines of ionized gas. They showed that there is an expanding shell of optically emitting gas whose diameter is 280 pc and which has an expansion velocity of 15-23 km/s. The source of ionization is believed to be the Orion OB1 association. A less

dense high-velocity radiative shock outside this visible HII region discovered by Cowie et al. (1979) is described below. Gaylard (1984) presented 13-cm H142alpha recombination-line observations of Barnard's Loop which supports the optical work of Reynolds and Ogden (1979) that BL is expanding and rotating.

UV: Witt and Lillie (1978) looked at UV photometry observations of the Orion Reflection Nebulosity; they found the extent of the dust in this region to be 250 parsecs with the scattering properties of the dust similar to those of interstellar grains. However, from ANS data of the reflection nebulosity produced by Zeta Orionis, de Boer (1983) showed that there is anomalous visual extinction towards HD 37903 with Rv ~ 4.1, which implies large grains present. The amount of reddening towards HD 37903 has been measured by Lee (1968) to be Eb-v = 0.36 mag. which implies an interstellar extinction of 1.3 mag. and this amount of visual extinction has been ascribed to nebula dust: the star being embedded in the front of L1630 (de Boer 1983).

Apart from the peculiar wavelength dependence of the dust, de Boer showed that the region of L1630 1 degree SSE of Zeta Orionis, which includes NGC 2023, has a complicated geometry from UV surface brightness measurements.

Cowie et al. (1979), from UV absorption-line measurements of stars in the Orion OB1 association, discovered a high-velocity ionization feature ascribed to a radiative shock, and a

low-velocity dense expanding shell. Part of this latter shell is the visible HII region called Barnard's Loop and the gas is believed to be photoionized due to the UV flux from the stars in the Orion OB associations. The feature is indicative of explosive events in Orion which occurred 2 E6 years ago; with the high-velocity radiative shock being the remnant of the last type II supernova event 3 E5 years ago. Knowledge of the large-scale dynamics of the Orion region is required to understand its effect on the small-scale region of NGC 2023.

Table 7.1. Physical parameters of NGC 2023.

Density:	Dust	increases by a factor of 4 between HD 37903 and 1 arcminute south of HD 37903	
	ne	10-25 cm-3	
	nH	> E3 cm-3	
Temperature:	Td	30-50 K	
	Te	20-50 K	
Size:	optical	1.2 pc	480 arcseconds
	HII	< 0.01 pc	< 4 arcseconds
	CII	0.3 pc	120 arcseconds

Knowing the temperature of the dust around the illuminating star in NGC 2023 to be between 20-45 K, this will rule out ices as a possible grain constituent as at these warm temperatures the grains would soon sublime.

The polarimetry data presented in this thesis provides constraints to models of NGC 2023 and 2068 as it gives information on grain size, grain material and the spatial density of dust grains in these reflection nebulae. The morphology of NGC 2023 will now be discussed.

7.2 Morphology and structure of NGC 2023

The polarimetric data that has been presented in Chapter 6 has a resolution of between 6-7.4 arcseconds, which corresponds to 0.015-0.018 parsecs at the assumed distance of 500 parsecs for L1630. This resolution of a few arcseconds can be used to investigate how stars form in a molecular cloud - L1630, the geometry of the cloud, star density and whether any magnetic fields are observable. A hypothesis put forward to explain the observation that OB associations were always found on the nearside of molecular clouds was Israel's (1978) blister model. There are similarities between the conditions observed in NGC 2023 and those described by Israel in his blister model for HII regions and also the conditions in which OB star formation might propagate (Elmegreen and Lada 1977). The extent of illuminated dust in the reflection nebula is ~ 8 arcmin/1.2 parsec and the reflection nebula lies on the nearside of the molecular cloud like an apparent blister. This geometry is also similar to NGC 2068 so we might be seeing in both cases a type B star analogue to Israel's OB blister model. Detailed knowledge of gas and dust density in this region is required to indicate where future star formation

might occur.

From section 7.1 it appears that the dust density increases towards the south in NGC 2023 where coincidentally a cluster of young stars has been found centred 67" south and 60" east of HD 37903 by Sellgren (1983). CO observations (Pankonin and Walmsley 1976) indicate the gas density in NGC 2023 reaches a maximum at 1-2 arcmin. south of HD 37903 so there is a correlation between an increase in gas and dust density and stellar density in NGC 2023. Apparently from CO observations there are no large-scale systematic motions present (White et al. 1981 and refs. therein).

The geometry of NGC 2023 is too difficult to infer from profiles of polarization, polarized intensity and total intensity as shown in Appendix C. However, for regions close to HD 37903, one could be seeing forward scattering from an irregular tilted slab of dust. This is reasoned from the FIR observation of Harvey, Thronson and Gatley (1980) who observed that most of the infrared emitting dust was more than 0.1 pc from HD 37903, and that HD 37903 has possibly burned a hole in the dust cloud ~ 0.04-0.08 pc or 17-34 arcsec in radius; thus there apparently is a dust free zone around HD 37903. Again, from the analysis of Strom et al. (1975a), HD 37903 could be expected to produce a dust free zone ~ 0.1 parsecs in radius and affect the dark cloud enviroment out to 1.0 parsec as discussed in Chapter 5 for NGC 2068. This geometry will be assumed in section 7.5.

The structure and evolution of NGC 2023 will be strongly determined by the low- to medium-mass star formation taking place, which will have have supplied a large energy input into the molecular cloud mainly through the action of PMSS stellar winds. There is evidence that all stars of ~ 1 Mo will undergo a period of mass loss ~ E-7 Mo/yr for E4 years (Edwards and Snell 1984). HD 37903 is the most luminous star (~ 2300 Lo) and will have affected NGC 2023 the greatest. There are no massive stars (> 15 Mo) from the lack of HII regions, compact IR sources and H 0 masers. Thus the region will not be disrupted by strong ionization fronts, but will be affected by stellar winds from T Tauri type stars. There is no evidence from the polarimetry data of magnetic fields in NGC 2023 aligning the dust grains and producing linear polarization (cf. survey by Vrba et al. 1976).

Silk (1983) has argued for a bimodal theory of star formation with low-medium mass stars appearing first and being formed over E8 years, and massive stars being formed later over a short period (E7 yrs). Once low-mass star formation has been triggered it can continue through the mechanism proposed by Norman and Silk (1980) in which the strong stellar winds from T Tauri stars provide the input energy which can trigger further star formation. Evidence of the turbulent dynamics of low-mass star formation regions are the CO bipolar outflows (e.g. close to HH24-27; Snell and Edwards 1982). There is no direct evidence of a supernova trigger for recent Orion star formation as the lifetime of a supernova is 2 E5 years while Barnards Loop is a few E6 years old so there is no

observable relic except for the high-velocity radiative shock seen by Cowie et al. (1979). It might be that this shock triggered the formation of HD 37903 and thus NGC 2023.(see Fig. 1.1)

Is the reason why we see an obscured cluster of young stars near reflection nebulae because: 1) they represent centres of SF or 2) because the illuminating star has blown away dust to reveal other stars? These were questions posed by Strom et al. (1975a) and it seems in NGC 2023 that the high stellar density of 10 pc-3, which is the critical density referred to by Norman and Silk (1980) in their model, are the conditions for continuing low-mass star formation with the B1.5 star HD 37903 possibly being the initial trigger for this region. An interesting chain of stars seen in this cluster are 217, 218, 219, 220 (Sellgren 1983), which may all have been triggered by the same mechanism. One PMSS in this cluster is S108 (Sellgren 1983).

7.3 The star S108 and HH-1

The centrosymmetric pattern of polarization vectors in I and Z breaks down near the star S108 with the vectors running approximately parallel with the optical jet-like filament that can be clearly seen in Plate 9. This was thought to be evidence for a collimated outflow from the PMSS star S108 due possibly to a non-isotropic stellar wind. The length of this jet-like filament is ~ 0.1 parsecs at the assumed distance of 500 pc, which is typical for a PMSS outflow (Bally and Lada 1983). However, as the

polarization seen in I and Z is nearly centrosymmetric about the star S108, this observation is likely to be due to the increase in dust density in this region limiting the polarization due to Mie-scattering of light from S108 to the near-infrared wavelengths where the optical depth is sufficiently small to enable the light to escape. The filament is, however, showing something of the structure of dust in NGC 2023 and possibly the interaction of S108 with the nebula dust (cf. Arny 1977).

There is mounting evidence that Herbig-Haro objects are shock excited material produced by the action of a stellar wind from a low-mass PMSS on the surrounding ISM. Usually the Herbig-Haro object is seen close to the boundary of the dust cloud (as it may not be seen otherwise due to extinction) and within 0.1 pc from the energy source. With regard to the observations given in Chapter 6 of HH-1 and HH-4, there was no evidence for polarization in HH-1a,b,c in R,I,Z or in HH-4 in R unlike in the case of HH-24 (Strom et al. 1974c) which was measured to be 24% polarized in R. This rules out a reflection nebula explanation for HH-1 and HH-4 (see Strom et al. 1974a,b,c).

HH-1a's proper motion is directed at a PA of 247 degrees at 58 km/s (assuming a distance of 450 pc) while it is noted that HH-1a is at a PA of 242.4 degrees from S108 (Proper motions and position angles of HH-1,2,3 are in Malin et al. 1986.). The intermediate velocity molecular outflow in NGC 2023 tabled in Bally and Lada's (1983) survey is possibly connected with HH-1, 4 or 5.

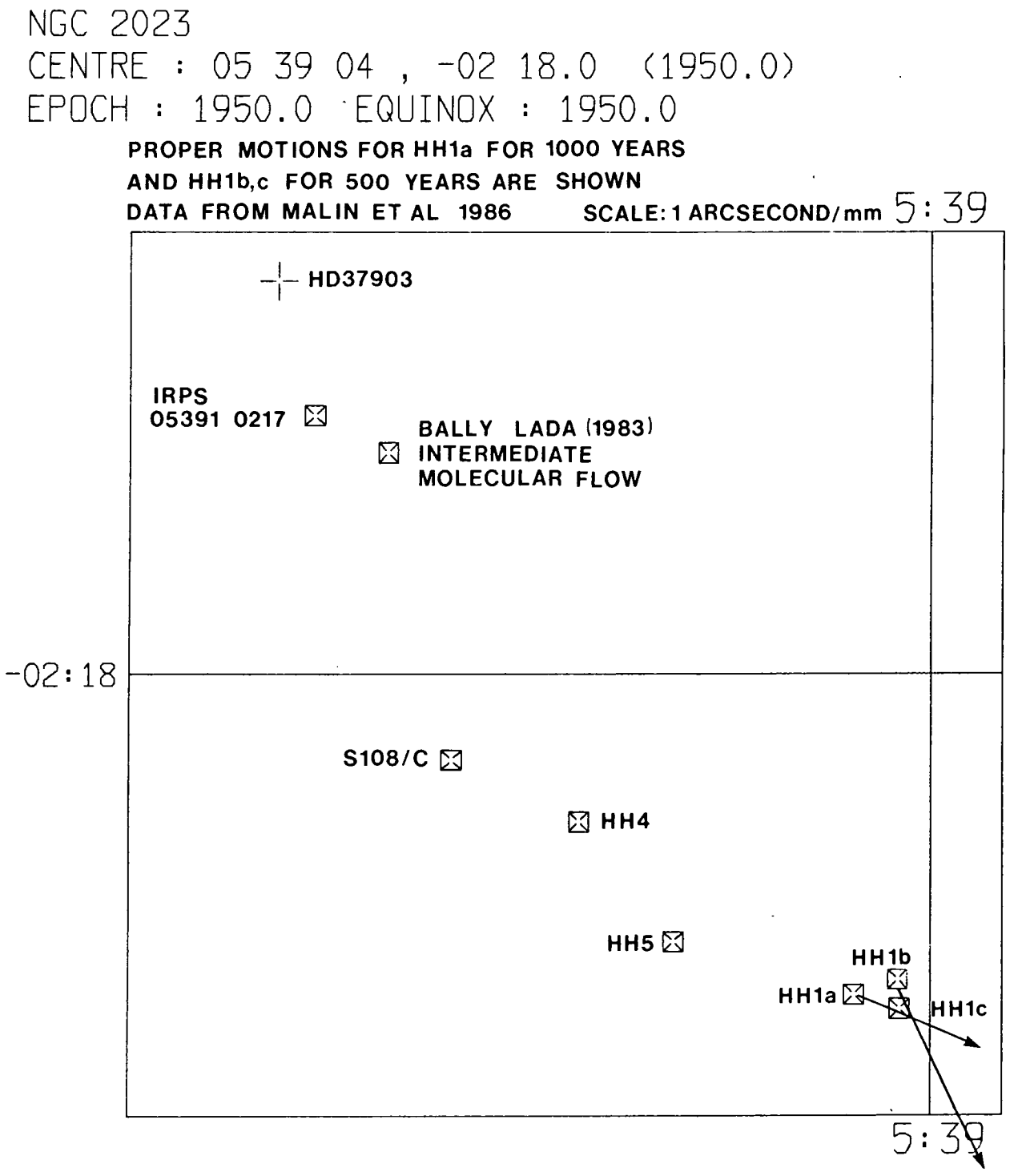

Fig. 7.1. A chart of the region around the star S108.

These objects are marked on a chart of the region and shown in Fig. 7.1, and from the proper motion studies of Malin et al. (1986) vectors are drawn in representing the proper motions of HH-1b,c over 500 years and HH-1a over 1000 years. Also included are HH-4,5 and IRPS (05391-0217); no other IRPS are in this field. It can be seen that S108 is likely to be the source of HH-1a; there being no other object in alignment with the proper motion of HH-1a within 15 arcminutes. The dynamical age of HH-1a is 3650 years assuming S108 is the energy source.

A model of the interaction of the stellar winds from PMSS in the ISM by Canto and Rodriguez (1980) provides an explanation for Herbig-Haro objects and their coincidence with PMSS and molecular outflows. This 'focused stellar wind model' explains how Herbig-Haro objects are formed in the conditions near the surface of molecular clouds where pressure gradients are expected. This seems to be the case in NGC 2023 for S108/HH-1a which are close to the surface of the molecular cloud Orion B and where pressure gradients are likely.

The heating of the ISM and the observed CO emission (see White et al. 1987) at one arcminute south of HD 37903 is probably due to S108. Fig. 7.2 shows J=2-1 CO emission observed by White (1986) with a hot spot (Ta=36 K) at RA 5h 39m 10s, Dec -2 deg 18 min. There is also evidence for a CO bipolar outflow at RA 5h 39m 6s, Dec -2 deg 18 min 30 s.

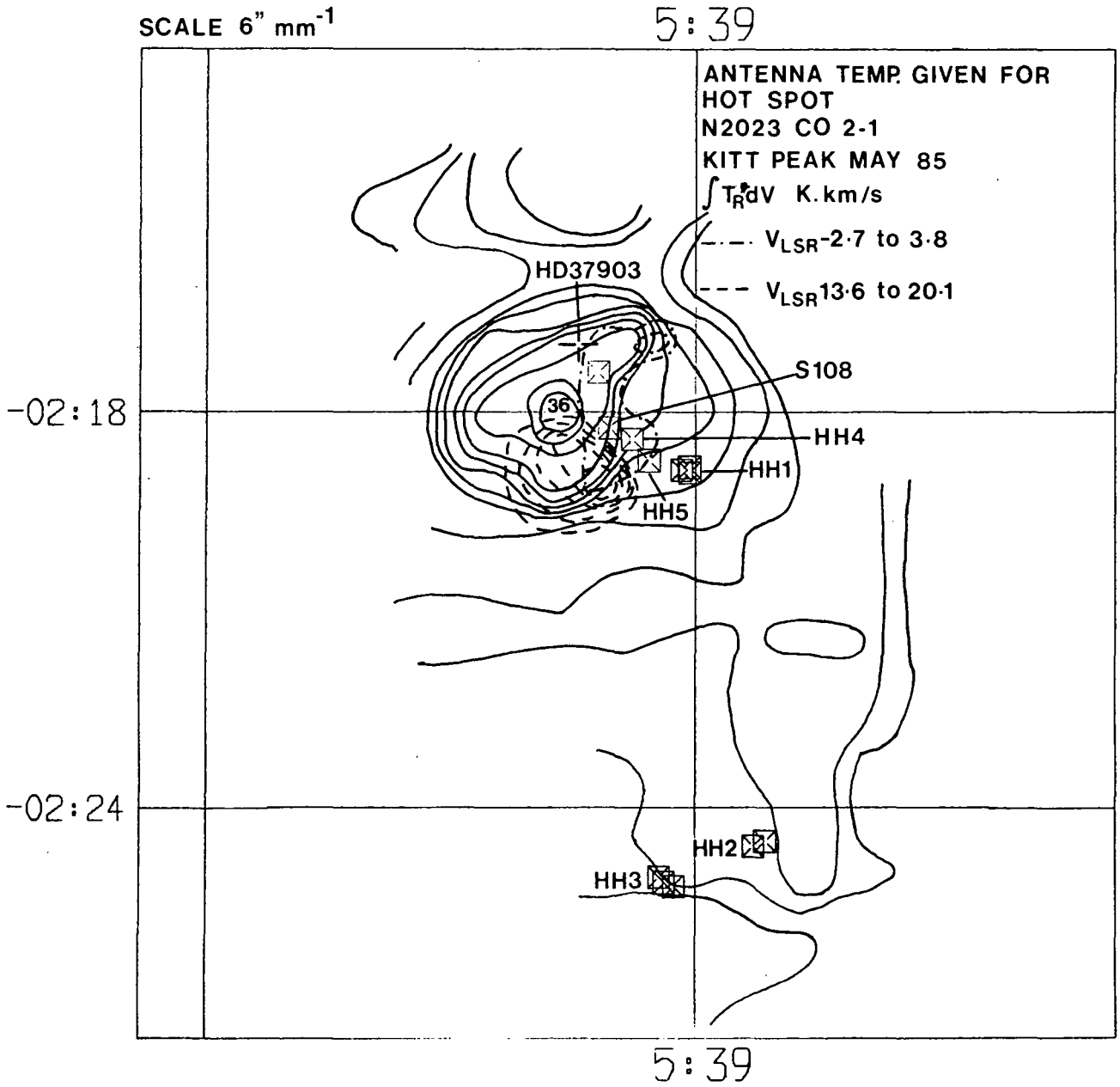

Fig. 7.2. CO observations of NGC 2023.

7.4 Extended emission

Witt and Schild (1985) expected that regions of extended I emission in NGC 2023 would not be polarized to any great extent. Supporting this idea is evidence of small linear polarization at 2.2 micron (K) Sellgren (1984a) in NGC 7023 - although no figure was given. The results presented in Chapter 6 for regions south of HD 37903 show that there is considerable scattering in I and Z wavebands and that the degree of polarization increases with wavelength in the range 440-930 nm. No statement can be made on whether the increase in polarization v. wavelength shows a spatial variation. Depolarization in reflection nebulae has been predicted by Voshchinnikov and Il'in (1983) who expect dust sweeping by B stars to produce a zone ~ 0.1 pc radius absent of small grains and therefore corresponding large Rv and depolarization in R. However, there does not seem to be a drop in polarization in R in the Durham data for the closest regions to the illuminating star. Apparently no work has been done to measure the polarization between 900-2200 nm; this should be done for NGC 2023 to find out the extent of nir extended emission in the far-red wavelengths.

7.5 Inferences on dust

The observed wavelength dependence of polarization for most reflection nebulae (Zellner 1973) is that polarization increases with wavelength, but this will depend on the grain material, size distribution, and geometry of the nebula. Given that there should

be a zone swept clear of dust in NGC 2023 around the illuminating star and that the extinction towards HD 37903 is relatively small (1.3 mag.), one could assume the small layer of dust in front of HD 37903 acts as an irregular shaped foreground slab of dust illuminated from the rear by HD 37903. For small regions of NGC 2023 the dust, to a first approximation, would scatter at one scattering angle along a short line of sight to the observer. Zellner (1973) modelled the spectral dependence of polarization and assumed wavelength independent refractive indices and single scattering, which will be the case adopted here. Calculations were made for single Mie scattering assuming a slab of dust in front of HD 37903 for one scattering angle (Theta = 40 degrees) for different power law size distributions and grain refractive indices to show the spectral dependence of polarization for various materials. The results are shown in Figs. 7.3 a and b in which are presented graphs of the spectral dependence of degree of polarization from 440 - 930 nm for seven power law size distributions of grains and eight materials. Amin and Amax was set to 0.02 and 1.0 micron respectively and the scattering angle (Th) was varied between 10-50 degrees. Fig. 7.3 a compares the dielectric grains ice v. dirty ice and organic material v. bacterial grains. Fig. 7.3 b compares SiC with silicates and the metallic grains graphite v. iron. Thus we see: 1) Grains made of iron or graphite should show polarization decreasing with wavelength for low power law indices and a nearly constant polarization for high indices. 2) SiC and silicates should also show a similar wavelength dependence of polarization. 3) In the

case of organic v. bacteria, one should see the observed wavelength dependence from 440-930 nm. Therefore, it is evident from this model that low refractive index, dielectric grains are favoured. One must exclude metallic grains, SiC, and silicate grains if the assumptions in this model are correct.

From the above data, a model was used to fit the wavelength dependence of NGC 2023 for the three regions common to the electronographic and CCD data closest to HD 37903 (Section 6.3) and the results are shown in Fig. 7.4 and Table 7.2.

Table 7.2. Best fits to the wavelength dependence of polarization.

Region	Table	Material	R.I.	Power Law Index	Theta
2	6.5 a	Organic	1.16,0.0	-3.0	40
2	6.5 b	Organic	1.16,0.0	-2.5	50
3	6.5 b	Organic	1.16,0.0	-2.5	40

Only the dielectric grains bacteria and organic material fitted the polarimetry data well.

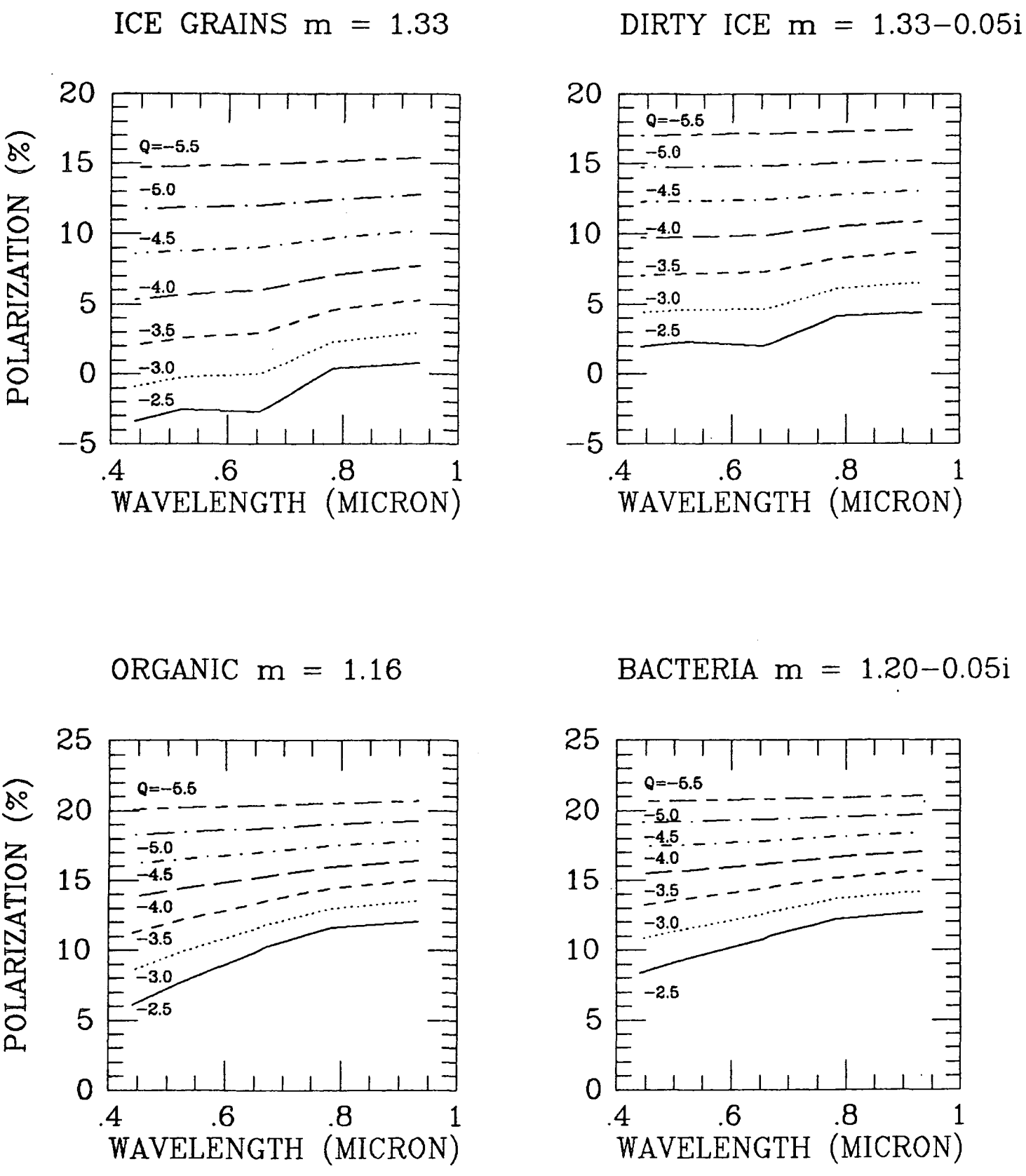

Fig. 7.3 a. Wavelength dependence of Mie scattering.

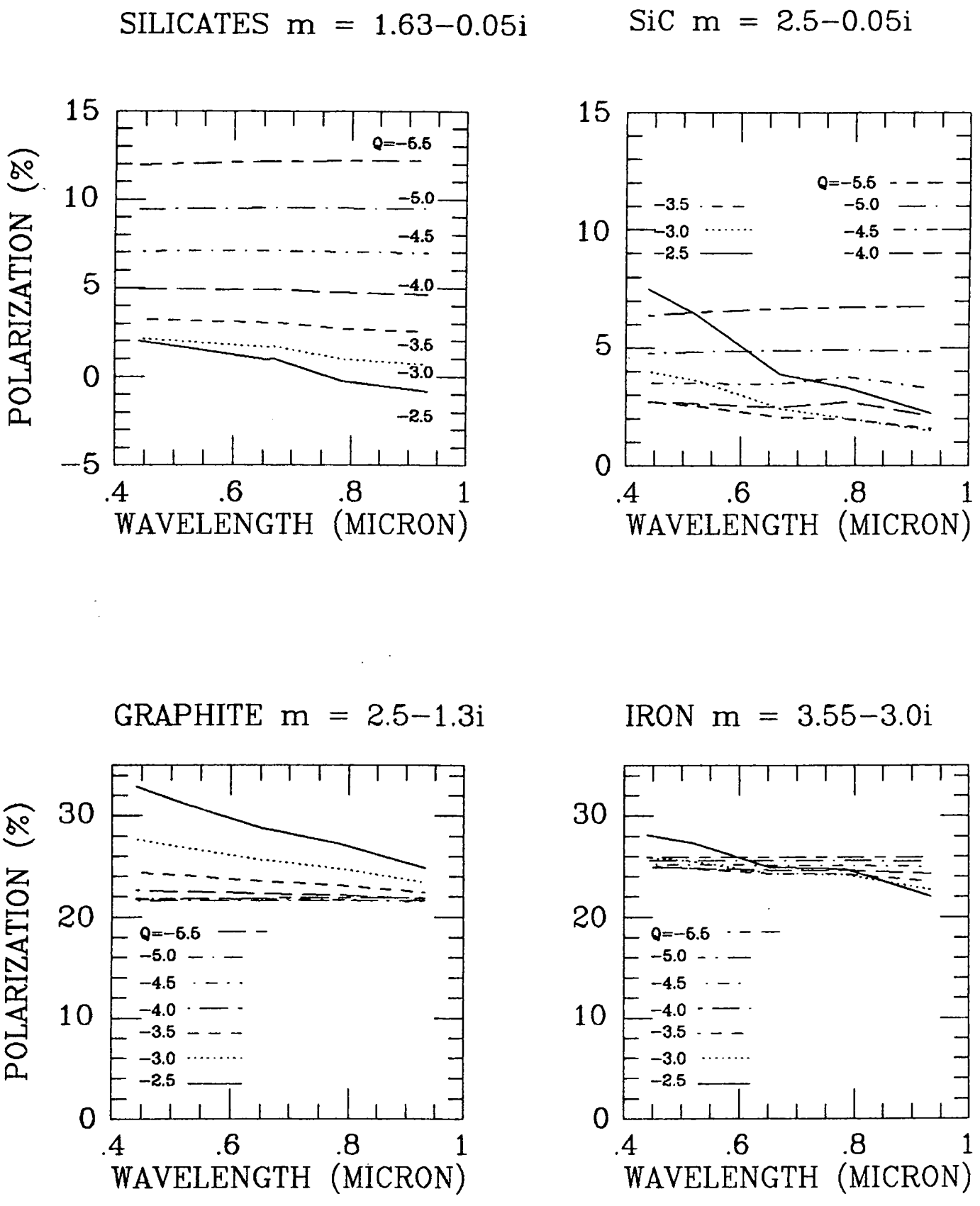

Fig. 7.3 b. Wavelength dependence of Mie scattering.

There is evidence for a bimodal grain size distribution in NGC 2023 and in the Orion Reflection Nebula (Witt 1985; Witt and Lillie 1978) as opposed to a continuous power law grain size distribution which was used to model extinction in the ISM by Mathis, Rumpl and Nordsiek (1977). This bimodal dust distribution in NGC 2023 manifests itself in:

a) An increase in Rv (~4) which is a characteristic of large grains and may be due to: 1) The high gas density of L1630 (nH2 > E3 cm-3) promoting grain growth (Strom et al. 1975a). 2) HD 37903 selectively evaporating and sweeping out the smallest grains (Voschinnikov and Il'in 1983).

b) Observations of ERE in NGC 2023 which have been explained by Sellgren et al. (1983) as evidence of very small (0.001 micron) grains.

The nearest region to HD 37903 observed was region 3 (Tables 6.5b and 6.7b), which has a mean distance of 48.8 arcsec or 0.12 parsec. Therefore, to test whether there is any unusual polarization from the dust close to the illuminating star where there may be this dust free zone further polarimetry data is required. Careful modelling of this and other reflection nebulae exhibiting ERE is needed to confirm whether there is evidence for very small or large grains in reflection nebulae and determine the exact form of the size distribution. The power law indices returned by the model are too low compared to recent workers, e.g. Moore (1982).

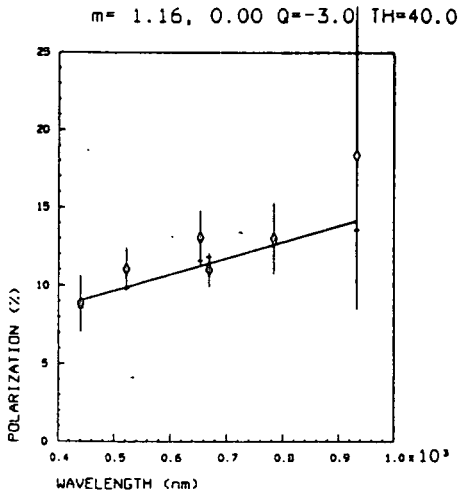

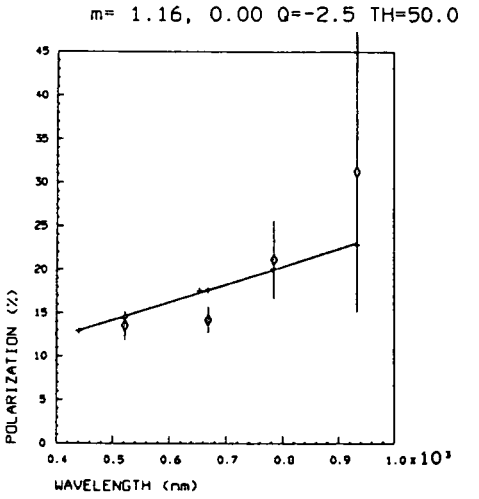

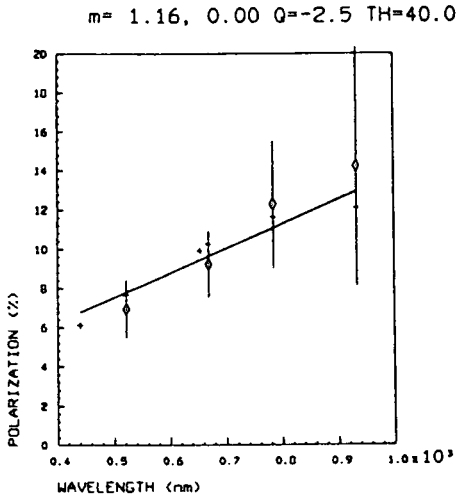

Fig. 7.4. Model fits to the spectral dependence of polarization.

CHAPTER 8 Conclusions

8.1 Interpreting the main observations of NGC 2068 and NGC 2023

The study of two reflection nebulae in the Orion R1 association which are embedded in L1630 has revealed many differences and similarities between these two reflection nebulae and some characteristics of dust grains in sites of star formation.

The differences and similarities of NGC 2068 and 2023 are: 1) Neither have a significant HII region. 2) Both have populations of young, low-mass stars with number densities of 30 and 10 pc-3 for NGC 2068 and NGC 2023 respectively (Sellgren 1983). 3) Both are excited by only one illuminating star: HD 38563N in the case of NGC 2068 and HD 37903 in the case of NGC 2023. 4) The degree of polarization has been found to increase with wavelength from 440-930 nm in NGC 2023, which is similar to the result of Zellner (1973) for NGC 2068 of a linear increase between 330-826 nm. 5) Both show asymmetric profiles of polarization v. offset distance from the illuminating star, but in NGC 2023 this is more pronounced and variable. 6) From the extent of polarized emission in the V waveband, the reflection nebulae appear to be illumination bounded in the dust cloud L1630 rather than density bounded. 7) The geometry proposed for both reflection nebulae is a star illuminating a foreground slab of dust from the rear which seems compatible with the observations of high surface brightness

and low (~20-30% V band) degree of polarization at the periphery of either nebula. As both nebulae are nearside of the L1630 molecular cloud and have similar enviroments they might be expected to have similar dust grains.

By analogy to Israel's (1980) model for formation of HII regions by OB stars we seem to see in the regions about these two reflection nebulae an enviroment dominated by an early B-type star which may have produced a dust-free zone approximately 0.1 parsecs radius and triggered the formation of a cluster of low-mass stars.

The polarimetry observations, which cover the whole of each respective nebula, did not show any signs of aligned grain induced polarization as a consequence of strong magnetic fields. However, they do show that the reflection nebulae are due to scattered light from the sole illuminating star with scattering in the Mie-domain. There is no evidence of depolarization close to the illuminating star due to either HII emission or the depolarization effects mentioned by Voshchinnikov and Il'in (1983). Also, there is no evidence for high-mass star formation; neither reflection nebula has HII regions or high-surface brightness IR sources so it is not likely that there are any stars > 15 Mo.

Molecular line observations of L1630 show there are sharp boundaries to the cloud south of NGC 2023 and north-west of NGC 2068 (Thaddeus 1982; White et al. 1981) agreeing with the visible observations of the dust boundary. An explanation for the

morphology of L1630 with regard to these two reflection nebulae appears to be that the event that produced Barnard's Loop and star formation along the edges of the two molecular clouds in Orion (A and B) triggered the formation of HD 38563N and HD 37903 which in turn have triggered low-mass star formation in regions ~ 1 parsec in extent. Indeed, the latest star formation following the progression of star formation in Orion through the subgroups of Orion OB1 might be the low-mass star formation in L1630 (Shevchenko 1979;1980). Physical conditions in the two nebulae are: Td is between 20-50 K from the center of the reflection nebula to its periphery, nH is at least E3-4 cm-3, and no obvious strong magnetic field; these are the conditions in which star formation is occurring now.

In NGC 2023 star formation is definitely occurring at present with the observation of HH-1a and the PMSS star S108. This star is immersed in dense dust and has produced a small reflection nebula in the I and Z wavebands where the optical depth is small. An optical filament is seen in R and I close to this star delineating a region of enhanced dust density. The Herbig-Haro object designated HH-1a by Malin et al. (1986) is not polarized (B,V,R,I,Z) and from its proper motion is likely to have been produce E3-E4 years ago by star S108. L1630 is a type B molecular cloud (Evans 1981) that is heated by young stellar objects of predominantly low mass like S108, which is associated with a CO hot spot (White 1986). There is very little evidence of high-mass star formation which is believed to disrupt a molecular cloud over

a short period of time ~ E7 yr (Silk 1983). An H20 maser near NGC 2071/2068 Lekht et al. 1982 is thought to be associated with a young low mass star rather than the normal high-mass star. Norman and Silk's (1980) model of low-mass star formation is possibly operating in these conditions with further low-mass star formation being triggered through the interaction of strong stellar winds with the ambient medium. In the S108 region there are the well known signs of star formation with HH-1, 4 and 5, a molecular outflow, and a PMSS in very close proximity (< 10 arcmin); the exact relationship has still to be found.

In the vicinity of NGC 2068 there are many Herbig-Haro objects (Harvey et al. 1982), but none have been located as close to the young cluster as in the case of the centre of low-mass star formation that is signposted by HH-1,4 and 5 (Malin et al. 1986). The HH objects are usually associated with high molecular density E4 - E5 cm-3 (Loren et al. 1979) and coincident with star S108 is enhanced molecular and dust density, and peaks in FIR, CO and CII emission.

With regard to the dust in these two reflection nebulae: Is the high surface brightness in R and I (ERE) due to an unusual emission mechanism only found in reflection nebulae? The data presented shows the I and Z emission to be appreciably polarized. This suggests that scattering is an important emission mechanism, which must be modelled to account for the total fluxes seen in the far-red to NIR wavebands in reflection nebulae. Therefore, more

data is required of bright reflection nebula; an obvious candidate is NGC 1999 which is associated with Herbig-Haro objects and is similar to NGC 7023 (Cardelli and Bohm 1984) which also shows ERE.

Polarimetry is useful in the study of reflection nebulae as it deals with the scattering of light from possible young stellar objects that have recently formed from a condensation in a dust cloud but the difficulties in assuming the geometry and grain parameters are enormous. The models presented here are too simplistic - only dealing with single scattering from homogeneous spherical grains. The results of these two models are totally at variance with one another, but show to serve the difficulty of trying to model Mie scattering. The number of possible grain models is very large as it is a product of: the number of grain size distributions, the number of grain size parameters e.g. Amin and Amax, the number of grain materials and their different refractive indices, the number of wavebands etc.

Work in the future should include: B, V, R, I and Z polarimetry observations of other reflection nebulae in Ori R1 including NGC 2068 and NGC 1999; and follow up with more detailed multiple scattering models like Warren-Smith (1983a).

SUMMARY

There has been a tremendous increase in polarimetry data on these two reflection nebulae with upwards of 3000 polarization

measurements being made in each waveband with an accuracy comparable to the observations of previous workers using single aperture techniques cf. Zellner (1974) who required 50 hours at a 1.5 m telescope to obtain polarimetry and colorimetry data for one region!

Table 8.1. Summary of reflection nebula observations.

	NGC 2068	NGC 2023
Observation		
Illuminating star	HD 38563 N	HD 37903
Extinction Av	5.1 mag	1.3 mag
Nebula brightness	20.6 mag/sq. arcsec.	?
Polarization	- Is due to Mie scattering -	
Offset	Both show asymmetric profiles in polarization	
Pmaximum		
V	21+/-6	28+/-3
Wavelength dep.	Both show polarization increases linearly	
Polarization	330-826 nm	440-930 nm
Position Angle	Small increase of 4.8 ° (Zellner 1970)	a constant within errors
stellar pop	30 pc-3	10 pc-3
CO outflows	5h 44m 58s (Lada 1985) -0 4'	5h 39m 6s -2 17 24s

ACKNOWLEDGEMENTS

I am grateful for the help and encouragement given to me by my colleagues in the Durham Polarimetry Group and others in the Department of Physics in Durham. This especially includes the guidance of my supervisor, Dr. S. M. Scarrott, and the following members of staff and research students at Durham: Drs. Warren-Smith, King, Berry, Ermolaev and Houston, and Messrs. Myers, Ward-Thompson, Draper, Gledhill and MacLaren.

From the Royal Observatory Edinburgh I would like to express appreciation to the staff of the library and the UKSTU and to Drs. Palmer and Beard. I would also like to acknowledge Dr. White at Queen Mary College, and Mark Ashfield, Chris Hirst and Murray Cameron from University College London, and to Jeremy Walsh and David Malin from the AAT who kindly gave me permission to use their data on NGC 2023.

My thanks also go to Karen Gittins for work on the diagrams in this thesis, to Mike Lee for the photographic plates, to Mrs. Miller for the loan of her printer, and to Mr. Lotts who helped on problems with computing.

The digitization of electronographic plates was carried out at the Royal Greenwich Observatory with the measuring of star and nebulae positions being carried out using the Packman XY measuring machine at the Royal Observatory Edinburgh.

This research would not have been possible without the studentship provided by the University of Durham.

LIST OF SYMBOLS

Av	Interstellar extinction
c	Velocity of electromagnetic radiation in vacuo.
G	Gravitational constant
Lo	Solar Luminosity
m	Complex refractive index (n - in')
Mo	Solar Mass
ne	Electron density cm-3
nH	Hydrogen number density cm-3
N	Column density cm-2
PA	Position angle (degrees)
Td	Dust grain temperature (K)
Te	Electron temperature (K)
Q	Power law size index

REFERENCES

Aitken, R.G., (1932) 'New General Catalogue of Double Stars'
Carnegie Institution of Washington.

Aitken, D.K., (1981) in: IAU Symposium 96, 'Infrared Astronomy', p207.
eds. Wynn-Williams, C.G., Cruikshank, D.P., D.Reidel, Dordrecht.

Alfven, H., Per Carlqvist, (1978) Astrophys. Sp.Sci. 55, 487.
'Interstellar clouds and the formation of stars'

Allen, C.W., (1973) 'Astrophysical Quantities' 3rd Edn.,
Athlone Press, London.

Appenzeller, I., (1982) Fund. of Cosmic Phys. 7, 313.
'Star formation and pre-main-sequence stellar evolution'

Arny, T., (1977) Ap.J. 217, 83.
'A model for the filamentary structure in the
Pleiades reflection nebulosity'

Axon, D.J., Ellis, R.S., (1976) M.N.R.A.S. 177, 499.
'A catalogue of linear polarization measurements for 5070 stars'

Bally, J., Lada, C.J., (1983) Ap.J. 265, 824.
'The high-velocity molecular flows near young stellar objects'

Bash, F., Hausman, M., Papaloizou, J., (1981) Ap.J. 245, 92.
'A turbulent model for giant molecular clouds'

Blaauw, A., (1964) Ann. Rev. Astron. Astrophys. 2, 213.
'The O associations in the solar neighbourhood'

Blitz, L., (1980) in: 'Giant Molecular Clouds in the Galaxy', p1,
Eds. Solomon, P.M., Edmunds, M.G., Pergamon Press, Oxford.
'Large scale mapping of local molecular cloud complexes'

Blitz, L., Shu, F.H., (1980) Ap.J. 238, 148.
'The origin and lifetime of giant molecular cloud complexes'

Boer de, K.S., (1983) Astron. Astrophys. 125, 258.
'Diffuse light near zeta Orionis and the Horsehead nebula, and anomalous extinction of HD 37903, as measured with the ANS'

Bohlin, R.C., Savage, B.D., Drake, J.F., (1978) Ap.J. 224, 132.
'A survey of interstellar HI and Lyman alpha absorption measurements. II.'

Bok, B.J., (1977) P.A.S.P. 89, 597.
'Dark nebulae, globules and protostars'

Brown, R.L., Knapp, G.R., Kuiper, T.B.H., Kuiper, Eva N. Rodriguez, (1975) Ap.J. Lett. 195, L23.
'Observations of carbon recombination-line emission in the reflection nebula M78'

Cameron, A.G.W. (1973) Sp.Sci.Rev. 15, 121.
'Abundances of the elements in the Solar System'

Canto, J., (1981) in: 'Investigating the Universe', p95, Ed. Kahn, F.D., D. Reidel, Dordrecht.
'Herbig-Haro objects: recent observational and theoretical developments'

Canto, J., Rodriguez, L.F., (1980) Ap.J. 239, 982.
'A stellar-wind focusing mechanism as an explanation for Herbig-Haro objects'

Cardelli, J.A., Bohm, K.H., (1984) Ap.J. 285, 613.
'The reflection nebula NGC 1999'

Carrasco, L., Strom, S.E., Strom, K.M., (1973) Ap.J. 182, 95.
'Interstellar dust in the Rho Ophiuchi dark cloud'

Carty, T.F., Perkins, H.G., Warren-Smith, R.F., Scarrott, S.M., (1979) M.N.R.A.S. 189, 299.

'A size distribution of silicate grains in Eta Carinae'

Chlewicki, G., Greenberg, J.M., (1984) M.N.R.A.S. 210, 791.

'General constraints on the average scattering characteristics of interstellar grains in the ultraviolet'

Clarke, D., (1974) in: 'Planets, Stars and Nebulae Studied with Photopolarimetry' T. Gehrels Editor., p45.

'Polarimetric definitions'

Clayton, D.D., (1978) in: 'Protostars and Planets' Ed. Gehrels, T., The University of Arizona Press, p13.

'The cloudy state of interstellar matter'

Cohen, J.G., (1977) Ap.J. 214, 86.

'The interstellar medium near stars with peculiar interstellar polarizations'

Cohen, M., (1982) P.A.S.P. 94, 266.

'The case for anisotropic mass loss from T Tauri stars'

Cohen, M., Schwartz, R.D., (1983) Ap.J. 265, 877.

'The exciting stars of Herbig-Haro objects'

Cowie, L.L., Songaila, A., York, D.G., (1979) Ap.J. 230, 469.

'Orion's Cloak: A rapidly expanding shell of gas centred on the Orion OB1 association'

Coyne, G.V., (1974) A.J. 79, 565.

'Wavelength dependence of polarization. XXV. Rotation of the position angle by the interstellar medium'

Coyne, G.V., Gehrels, T., (1967) A.J. 72, 887.

'Wavelength dependence of polarization. X. Interstellar polarization.'

Coyne, G.V., Gehrels, T., Serkowski, K., (1974) A.J. 79, 581.

'Wavelength dependence of polarization. XXVI.
The wavelength of maximum polarization as a characteristic parameter of interstellar grains'

Dame, T.M., (1983) Ph.D. Thesis, Columbia University.

Davis, L. Jr., Greenstein, J.L., (1951) Ap.J. 114, 206.
'The polarization of starlight by aligned dust grains'

Debye, P., (1909) Ann. Phys. Lpz. 30, 57.
'Der Lichtdruck auf Kugeln von beliebigem Material'

Draine, B.T., Lee, H.M., (1984) Ap.J. 285, 89.
'Optical properties of interstellar graphite and silicate grains'

Duley, W.W., (1984) Q.J.R.A.S. 25, 109.
'Evidence against biological grains in the interstellar medium'

Duley, W.W., Williams, D.A., (1984) M.N.R.A.S. 211, 97.
'Interstellar polyynes from the disruption of carbon grains'

Edwards, S., Snell, R.L., (1984) Ap.J. 281, 237.
'A survey of high-velocity molecular gas near Herbig-Haro objects. II.'

Elmegreen, B.G., (1982) in: 'Submillimetre Wave Astronomy'
Eds. Beckman, J.E., Phillips, J.P., p3,
Cambridge University Press, Cambridge.
'The formation of giant cloud complexes'

Elmegreen, B.G., Lada, C.J., (1977) Ap.J. 214, 725.
'Sequential formation of subgroups in OB associations'

Elvius, A., Hall, J.S., (1966) Lowell Obs. Bull. 6, #135, 257.
'Observations of the colour and polarization of the reflection nebulae NGC 2068, NGC 7023 and the Merope nebula obtained in three spectral regions'

Emerson, J.P., Furniss, I., Jennings, R.E., (1975)
M.N.R.A.S. 172, 411.
'40-350 micron emission from NGC 2023'

Evans, N.J., (1981) IAU Symposium 96, 'Infrared Astronomy', p107,
eds. Wynn-Williams, C.G., Cruikshank, D.P., D.Reidel, Dordrecht.
'Infrared sources in dense molecular clouds'

Gatley, I., Becklin, E.E., Matthews, K., Neugebauer, G.,
Penston, M.V., Scoville, N., (1974) Ap.J. Lett. 191, L121.
'A new infrared complex and molecular cloud in Orion'

Gaylard, M.J., (1984) M.N.R.A.S. 211, 149.
'Detection of the H142alpha line from the Barnard Loop'

Glushkov, Yu.I., (1965) Trud. Astrophiz. Inst. Akad. Nauk.
Kazakh.S.S.R. 5, 277.
'On the polarization and continuous spectrum of NGC 2068'

Gold, T., (1952) M.N.R.A.S. 112, 215.
'The alignment of Galactic dust'

Gorkom, J.H. van, Shaver, P.A., Goss, W.M., (1979)
Astron. Astrophys. 76, 1.
'Studies of ionized carbon regions in dark clouds'

Grasdalen, G.L., Strom, K.M., Strom, S.E., (1973)
Ap.J. Lett. 184, L53.
'A 2 micron map of the Ophiuchus dark-cloud region'

Greenberg, J.M., (1978) in: 'Cosmic Dust' Ed. McDonnell, J.A.M.,
'Interstellar Dust', Ch. 4., J. Wiley.

Greenberg, J.M., Hanner, M.S., (1970) Ap.J. 161, 947.
'Light from reflection nebulae. II. Colours and polarization'

Greenberg, J.M., Roark, T.P., (1967) Ap.J. 147, 917.

'Light from reflection nebulae.I.
Dielectric versus metallic particles'

Habing, H.J., Israel, F.P., (1979) Ann. Rev. Astron. Astrophys.
17, 345.
'Compact HII regions and OB star formation'

Hall, J.S., (1949) Science 109, 166.
'Observations of the polarized light from stars'

Hanner, M.S., (1971) Ap.J. 164, 425.
'Light from reflection nebulae. IV.
Scattering by silicate grains'

Hanner, M.S., Greenberg, J.M., (1970) Ap.J. 161, 961.
'Light from reflection nebulae. III.
Colour at zero degree offset'

Harvey, P.M., Thronson Jr., H.A., Gatley, I., (1980) Ap.J. 235, 894.
'A far-infrared study of the reflection nebula NGC 2023'

Harvey, P.M., Wilking, B.A., Cohen, M., (1982)
Annals of the New York Acad. Sci. 395, 199.
'Infrared observations of low-mass star formation in Orion:
HH objects'

Harwit, M., (1970) Nature 226, 61.
'Is magnetic alignment of interstellar dust
really necessary?'

Haschick, A.D., Moran, J.M., Rodriguez, L.F., Ho, P.T.P.,
(1983) Ap.J. 265, 281.
'Water-vapor masers located near Herbig-Haro objects'

Henyey, L.G., Greenstein, J.L., (1938) Ap.J. 88, 580.
'The theory of the colours of reflection nebulae'

Herbig, G.H., (1960) Ap.J. Suppl. 4, 337.
'The spectra of Be- and Ae-Type stars associated with nebulosity'
Herbig, G.H., Kuhi, L.V., (1963) Ap.J. 137, 398.
'Emission-line stars in the region of NGC 2068'
Herbst, W., (1975) A.J. 80, 503.
'R-associations III. Local optical spiral structure'
Hildebrand, R.H., (1983) Q.J.R.A.S. 24, 267.
'The determination of cloud masses and dust characteristics'
from submillimetre thermal emission'
Hiltner, W.A., (1949) Science 109, 165.
'Polarization of light from distant stars by interstellar medium'
Hoyle, F., Wickramasinghe, N.C., (1982) Ap. Sp. Sci. 86, 321.
'A model for interstellar extinction'
Hubble, E., (1922) Ap.J. 56, 400.
'The source of luminosity in galactic nebula'
Humphreys, R.M., (1978) Ap.J. Suppl. 38, 309.
'Studies of luminous stars in nearby galaxies.I.
Supergiants and O stars in the Milky Way'
Hyland, A.R., (1981) IAU Symposium 96, 'Infrared Astronomy', p125.
eds. Wynn-Williams, C.G., Cruikshank, D.P., D.Reidel, Dordrecht.
'Globules, dark clouds, and low mass pre-main sequence stars'
Iben I., Jr., (1965) Ap.J. 141, 993.
'Stellar evolution. I. The approach to the Main Sequence'
Israel, F.P., (1978) Astron. Astrophys. 70, 769.
'HII regions and CO clouds: The blister model'
Johansson, L.E.B., Hoglund, B., Winnberg, A., Nguyen-Q-Rieu,
Goss, W.M., (1974) Ap.J. 189, 455.

'OH observations near the reflection nebulae NGC 2068 and NGC 2071'

Johnson, H.M., (1960) P.A.S.P. 72, 10.

'Photoelectric photometry of diffuse Galactic nebulae and comet Arend-Roland'

Johnson, P.E., (1982) Nature 295, 371.

'Grain alignment in the Galactic magnetic field'

Jones, A.P., Williams, D.A, (1984) M.N.R.A.S. 209, 955.

'The 3 micron ice band in Taurus: implications for interstellar chemistry'

Kerr, F.J., (1977) in: 'Star Formation', IAU Symposium 75, Eds. Jong, T. de, Maeder, A., p3.

'Star formation and the Galaxy'

Knapp, G.R., Brown, R.L., Kuiper, T.B.H., (1975) Ap.J. 196, 167.

'Radio recombination line observations of the CII Region NGC 2023'

Knapp, G.R., Kuiper, T.B.H., Knapp, S.L., Brown, R.L., (1977) Ap.J. 214, 78.

'CO observations of Galactic reflection nebulae'

Konigl, A., (1982) Ap.J. 261, 115.

'On the nature of bipolar sources in dense molecular clouds'

Kutner, M.L., Tucker, K.D., Chin, G., Thaddeus, P., (1977) Ap.J. 215, 521.

'The molecular complexes in Orion'

Kutner, M.L., Machnik, D.E., Tucker, K.D., Dickman, R.L., (1980) Ap.J. 237, 734.

'Molecular clouds associated with reflection nebulae. I. A

survey of carbon monoxide emission'

Lada, C.J., (1985) Ann. Rev. Astron. Astrophys. 23, 267.
'Cold outflows, energetic winds, and enigmatic jets around young stellar objects'

Lada, C.J., Gottlieb, C.A., Litvak, M.M., Lilley, A.E., (1974) Ap.J. 194, 609.
'Molecular studies of two dark nebulae associated with Herbig-Haro objects'

Lada, C.J., Blitz, L., Elmegreen, B.G., (1978)
in: 'Protostars and Planets' Ed. Gehrels, T., p341.
'Star formation in OB associations'

Lang, K.R., (1978) 'Astrophysical Formulae',
Springer-Verlag, Berlin.

Larson, R.B., (1969) M.N.R.A.S. 145, 271.
'Numerical calculations of the dynamics of a collapsing protostar'

Larson, R.B., (1973) Ann. Rev. Astron. Astrophys. 11, 219.
'Processes in collapsing interstellar clouds'

Larson, R.B., (1977) in: IAU Symposium 75, 249.
Eds. de Jong, T, Maeder, A., D. Reidel, Dordrecht.
'Collapse dynamics and collapse models'

Larson, R.B., (1981) M.N.R.A.S. 194, 809.
'Turbulence and star formation in molecular clouds'

Larson, R.B., (1982) M.N.R.A.S. 200, 159.
'Mass spectra of young stars'

Larson, R.B., (1984) M.N.R.A.S. 206, 197.
'Gravitational torques and star formation'

Larson, R.B., (1985) M.N.R.A.S. 214, 379.
'Cloud fragmentation and stellar masses'

Lee, T.A., (1968) Ap.J. 152, 913.
'Interstellar extinction in the Orion Association'

Lekht, E.E., Pashchenko, M.I., Rudnitskii, G.M., Sorochenko, R.L., (1982) Astron. Zh. 59, 276. [(1982) Sov. Astron. 26, 168.]
'Observations of variable water maser sources associated with star formation regions'

Lewis, J.S., Ney, E.P., (1979) Ap.J. 234, 154.
'Iron and the formation of astrophysical dust grains'

Lindblad, B., (1935) Nature 135, 133.
'A condensation theory of meteoritic matter and its cosmological significance'

Loren, R.B., Evans, N.J., Knapp, G.R., (1979) Ap.J. 234, 932.
'Properties of molecular clouds containing Herbig-Haro objects'

Lynds, B.T., (1962) Ap.J. Suppl. 7, 1.
'Catalogue of dark nebulae'

Malin, D.F., Ogura, K., Walsh, J.R., (1986) M.N.R.A.S. submitted.
'Herbig-Haro objects in the vicinity of NGC 2023'

Mannino, G., (1959) Publ. Obs. Astron. Univ. Bologna, 7, #10.

Mannion, M.D., Scarrott, S.M., (1984) Mon. Not. R. astr. 208, 905.
'An optical polarization study of NGC 2068'

Margulis, M., Lada, C.J., (1984) Occ. Rep. R.O.E. 13, 41.
'Open cluster formation'

Martin, P.G., (1978) 'Cosmic Dust'
Oxford University Press, Oxford.

Mathewson, D.S., Ford, V.L., (1970) Mem. R.A.S. 74, 139.
'Polarization observations of 1800 stars'

Mathis, J.S., Rumpl, W., Nordsieck, K.H., (1977) Ap.J. 217, 425.
'The size distribution of interstellar grains'

Mathis, J.S., (1979) Ap.J. 232, 747.
'The size distribution of interstellar particles.
II. Polarization'

Matsakis, D.N., Evans, N.J., Sato, T., Zuckerman, B.,
(1976) Astron. J. 81, 172.
'Radio continuum measurements of compact H II regions
and other sources'

Mie, G., (1908) Ann. Physik. 25, 377.
'Beitrage zur Optik truber Medien, speizell
kolloidaler Metallosungen'

Milman, A.S., Knapp, G.R., Kerr, F.J., Knapp, S.L., Wilson, W.J.,
(1975) Astron. J. 80, 93.
'Carbon monoxide observations of a dust cloud in
the Orion region: L1630'

Minin, I.N., (1965) Sov. Astron. 8, 528.
'Light scattering in dust nebulae'

Mitchell, R.M., Evans, A., (1984) M.N.R.A.S. 209, 945.
'Grain growth and destruction in novae'

Moore, P.J.R.McDonald, (1982) Ph.D. Thesis, University of Durham.
'A detailed study of the reflection nebula, NGC 7023'

Norman, C., Silk, J., (1980) Ap.J. 238, 158.
'Clumpy molecular clouds: A dynamic model self-consistently
regulated by T Tauri star formation'

Ohman, Y., (1939) M.N.R.A.S. 99, 624.
'On some observations made with a modified Pickering Polarigraph'

Pankonin, V., Walmsley, C.M., (1976) Astron. Astrophys. 48, 341.
'Radio spectroscopy of the NGC 2023 CII regions'

Pankonin, V., Walmsley, C.M., (1978) Astron. Astrophys. 67, 129.
'Radio spectroscopy of C II regions associated with reflection nebulae: NGC 2023, M78, and others'

Purcell, E.M., (1975) in: 'The Dusty Universe'
Ed. Field, G.B., Cameron, A.G.W., p155.
Neale Watson Academic Publications, New York.
'Interstellar grains as pinwheels'

Racine, R., (1968) A.J. 73, 233.
'Stars in reflection nebulae'

Reid, M.J., Moran, J.M., (1981) Ann. Rev. Astron. Astrophys. 19, 231.
'Masers'

Reipurth, B., (1985) Astron. Astrophys. Suppl. 61, 319.
'Small nebulae and Herbig-Haro objects. II. The Orion region'

Rengarajan, T.N., (1984) Ap.J. 287, 671.
'An estimate of stars formation efficiency in molecular clouds'

Reynolds, R.J., Ogden, P.M., (1979) Ap.J. 229, 942.
'Optical evidence for a very large, expanding shell associated with the I Orion OB association, Barnard's Loop, and the high Galactic latitude Halpha filaments in Eridanus'

Roark, T., Roark, B., Collins, G.W., (1974) Ap.J. 190, 67.
'Monte Carlo model of reflection nebulae: intensity gradients'

Rowan-Robinson, M., (1986) Crafoord Symposium on

'Astrophysical Aspects of the Interstellar Medium
and Star Formation'
Physica Scripta, in press.

Rush, W.F., Witt, A.N., (1975) Astron. J. 80, 31.
'Search for continuous fluorescence in reflection nebulae'

Saltpeter, E.E., (1977) Ann. Rev. Astron. Astrophys. 15, 267.
'Formation and destruction of dust grains'

Sanders, D.B., Solomon, P.M., Scoville, N.Z., (1984) Ap.J. 276, 182.
'Giant molecular clouds in the Galaxy. I. The axisymmetric
distribution of molecular hydrogen'

Savage, B.D., Mathis, J.S., (1979) Ann. Rev. Astron. Astrophys.
17, 73.
'Observed properties of interstellar dust'

Scarrott, S.M., Warren-Smith, R.F., Pallister, W.S., Axon, D.J.,
Bingham, R.G., (1983) M.N.R.A.S. 204, 1163.
'Electronographic polarimetry: the Durham polarimeter'

Schwartz, R.D., (1983) Ann. Rev. Astron. Astrophys. 21, 209.
'Herbig-Haro objects'

Sellgren, K., (1983) A.J. 88, 985.
'Properties of young clusters near reflection nebulae'

Sellgren, K., (1984a) Ap.J. 277, 623.
'The near-infrared continuum emission of visual reflection nebulae'

Sellgren, K., (1984b) Occas. Rep. R.O.E., #12, 96.
'Near infrared observations of the visual reflection nebulae
NGC 7023, NGC 2023, and NGC 2068'

Sellgren, K., Werner, M.W., Dinerstein, H.L.,
(1983) Ap.J.Lett. 271, L13.

'Extended near-infrared emission from visual reflection nebulae'

Serkowski, (1974) in: 'Planets, Stars and Nebulae Studied with Photopolarimetry' ed. Gehrels, T., p135, University of Arizona Press, Tucson, Arizona.

Serkowski, K., Mathewson, D.S., Ford, V.L., (1975) Ap.J. 196, 261.

'Wavelength dependence of interstellar polarization and ratio of total to selective extinction'

Shah, G.A., Krishna Swamy, K.S., (1981) Ap.J. 243, 175.

'A model reflection nebula in the far-infrared'

Sharpless, S., (1952) Ap.J. 116, 251.

'A study of the Orion aggregate of early-type stars'

Shevchenko, V.S., (1979) Astron. Zh. 56, 297.

[(1979) Sov. Astron. 23, 163.]

'The structure of star formation regions I. Population categories and the evolution of molecular clouds'

Shevchenko, V.S., (1980) Astron. Zh. 57, 1162.

[(1980) Sov. Astron. 24, 670.]

'The structure of star formation regions. II Individual regions: spatial extent, mass, and age of SFR 1 Orionis'

Shirt, J.V.S., (1984) Ph.D. Thesis, University of Durham.

'A study of the bipolar nebula associated with LkHalpha 208'

Silk, J., (1983) 'Birth and Infancy of Stars', p349 Eds. Lucas, R., Omont, A., Stora, R., North-Holland.

'Molecular cloud evolution and star formation'

Slipher, V.M., (1912) Lowell Obs. Bull. 2, #55, 26.

'On the spectrum of the nebula in the Pleiades'

Snell, R.L., Edwards, S., (1982) Ap.J. 259, 668.

'Observations of high-velocity molecular gas near Herbig-Haro objects: HH 24-27 and HH 1-2'

Solomon, P.M., Sanders, D.B., Scoville, N.Z., (1979) in: IAU Symposium 84, 'The Large-scale Characteristics of the Galaxy' Ed. Burton, W.B, Reidel, Dordrecht. 'Giant molecular clouds in the Galaxy: distribution, mass, size and age', p35.

Spitzer, L., Jr., (1978) 'Physical Processes in the Interstellar Medium' Wiley and Sons, New York.

Strel'nitskii, V.S., (1970) Astrofizika 6, #4, 625. 'Polarimetric study of the multiple system ADS 4374'

Strom, K.M., Strom, S.E., Grasdalen, G.L., (1974a) Ap.J. 187, 83. 'An infrared source associated with a Herbig-Haro object'

Strom, S.E., Grasdalen, G.L., Strom, K.M., (1974b) Ap.J. 191, 111. 'Infrared and optical observations of Herbig-Haro objects'

Strom, K.M., Strom, S.E., Kinman, T.D., (1974c) Ap.J. 191, L93. 'Optical polarization of selected Herbig-Haro objects'

Strom, K.M., Strom, S.E., Carrasco, L., Vrba, F.J., (1975a) Ap.J. 196, 489. 'M78: An active region of star formation in the dark cloud Lynds 1630'

Strom, S.E., Strom, K.M., Grasdalen, G.L., (1975b) Ann. Rev. Astron. & Astrophys. 13, 187. 'Young stellar objects and dark interstellar clouds'

Strom, K.M., Strom, S.E., Vrba, F.J., (1976) A.J. 81, 308. 'Infrared surveys of dark-cloud complexes. I. The Lynds 1630 dark cloud'

Tabak, R.G., Hirth, J.P., Meyrick, G., Roark, T.P.,
(1975) Ap.J. 196, 457. 'The nucleation and expulsion of carbon particles formed in stellar atmospheres'

Taylor, K.N.R., Scarrott, S.M., (1980) M.N.R.A.S. 193, 321.
'The Boomerang Nebula: A highly polarized bipolar'

Thaddeus, P., (1977) in: Star Formation, IAU Symposium 75
Eds. Jong, T. de, Maeder, A., p37.
'Molecular Clouds'

Thaddeus, P., (1982) Annals of the New York Acad. Sci. 395, 9.
'Molecular clouds in Orion and Monoceros'

Trimble, V., (1975) Rev. Mod. Phys. 47, 877.
'The origin and abundances of the chemical elements'

Trumpler, R.J., (1930) P.A.S.P. 42, 214.
'Absorption of light in the Galactic system'

Tucker, K.D., Kutner, M.L., Thaddeus, P., (1973)
Ap.J. Lett. 186, L13.
'A large carbon monoxide cloud in Orion'

van den Bergh, S., (1966) A.J. 71, 990.
'A study of reflection nebulae'

van de Hulst, H.C., (1981) 'Light scattering by small particles'
Dover Publications Inc.

Vanysek, V., Solc, M., (1973) in: IAU Symposium 52, p127.
'Interstellar Dust and Related Topics', Ed. Greenberg, J.M., van de Hulst, H.C., D.Reidel, Dordrecht.
'Depolarization effect in reflection nebulae'

Voshchinnikov, N.V., (1977) Astron. Zh. 54, 1221.
[(1977) Sov. Astron. 21, 693.]

'Simplified models of reflection nebulae'

Voshchinnikov, N.V., (1978a) Astron. Zh. 55, 322.

[(1978) Sov. Astron. 22, 188.]

'Scattering in an inhomogeneous reflection nebula'

Voshchinnikov, N.V., (1978b) Astron. Zh. 55, 983.

[(1978) Sov. Astron. 22, 561.]

'Dust grains in reflection nebulae:

Spherical core-mantle grains'

Voshchinnikov, N.V., Marchenko, P.E., (1982) Astron. Zh. 59, 1115.

'Polarization of stars in R-associations: observational data'

Voshchinnikov, N.V., Il'in, V.B., (1983) Astron. Zh. 60, 1120.

[(1983) Sov. Astron. 27, 650.]

'Dust sweeping by the radiation of different types of stars'

Vrba, F.J., Strom, S.E., Strom, K.M., (1976) A.J. 81, 958.

'Magnetic field structure in the vicinity

of five dark cloud complexes'

Ward-Thompson, D., Warren-Smith, R.F., Scarrott, S.M.,

Wolstencroft, R.D., (1985) M.N.R.A.S. 215, 537.

'Evidence for discs and jets associated with R and T CRa'

Warren-Smith, R.F., (1979) Ph.D. Thesis, Univ. of Durham.

'Electronographic polarimetry of reflection nebulae'

Warren-Smith, R.F., (1983a) M.N.R.A.S. 205, 337.

'Monte Carlo estimation of polarization in reflection nebulae'

Warren-Smith, R.F., (1983b) M.N.R.A.S. 205, 349.

'Multiple scattering in the reflection nebula NGC 1999

and the nature of interstellar dust'

Warren-Smith, R.F., Scarrott, S.M., Murdin, P., Bingham, R.G.,

(1979) M.N.R.A.S. 187, 761.
'Optical polarization map of Eta Carinae and the nature of its outburst'

Warren-Smith, R.F., Scarrott, S.M., King, D.J., Taylor, K.N.R., Bingham, R.G., Murdin, P., (1980) M.N.R.A.S. 192, 339.
'The structure of NGC 1999'

Werner, M.W., Elias, J.H., Gezari, D.Y., Westbrook, W.E., (1974) Ap.J. Lett. 192, L31.
'One millimeter continuum radiation from Orion molecular cloud 2'

White, R.L., (1979a) Ap.J. 229, 954.
'Polarization in reflection nebulae. I. Scattering properties of interstellar grains'

White, R.L., (1979b) Ap.J. 230, 116.
'Polarization in reflection nebulae. II. Reflection of light from thick slabs'

White, G.J., Phillips, J.P., (1981) M.N.R.A.S. 194, 947.
'Molecular line observations of the I Ori OB association including NGC 2068, NGC 2071 and the HH-24 region'

White, R.L., Schiffer, F.H., Mathis, J.S, (1980) Ap.J. 241, 208.
'Polarization in reflection nebulae. III. How good a grain diagnostic?'

White, G.J., Phillips, J.P., Watt, G.D., (1981) M.N.R.A.S. 197, 745.
'Observations of CO J=3->2 emission from molecular clouds'

White, G.J., (1986) Private communication.

White, G.J., Sanderson, C.A., Hayashi, S.S., Kaifu, N., (1987) to be submitted to Astron. Astrophys.

Whittet, D.C.B., (1981) Q.J.R.A.S. 22, 3.
'The composition of interstellar grains'

Whittet, D.C.B., (1984) M.N.R.A.S. 210, 479.
'Interstellar grain composition:
a model based on elemental depletions'

Wickramasinghe, N.C., Nandy, K., (1972) Rep. Prog. Phys. 35, 157.
'Recent work on interstellar grains'

Wickramasinghe, N.C., (1973) 'Light Scattering Functions for
Small Particles with Application in Astronomy',
Adam Hilger, London.

Witt, A.N., (1977a) Ap.J. Suppl. 35, 1.
'Multiple scattering in reflection nebulae. I.
A Monte Carlo approach'

Witt, A.N., (1977b) Ap.J. Suppl. 35, 7.
'Multiple scattering in reflection nebulae. II.
Uniform plane-parallel nebulae with foreground stars'

Witt, A.N., (1977c) Ap.J. Suppl. 35, 21.
'Multiple scattering in reflection nebulae. III.
Nebulae with embedded illuminating stars'

Witt, A.N., Oshel, E.R., (1977d) Ap.J. Suppl. 35, 31.
'Multiple scattering in reflection nebulae. IV.
The multiplicity of scattering'

Witt, A.N., (1985) Ap.J. 294, 216.
'Colours of reflection nebulae. I.
Phase function effects in the Merope nebula'

Witt, A.N., Lillie, C.F., (1978) Ap.J. 222, 909.
'Ultraviolet photometry from the Orbiting Astronomical

Observatory. XXX. The Orion reflection nebulosity'

Witt, A.N., Cottrell, M.J., (1980) Ap.J. 235, 899.
'The HD 20075/NGC 7023 complex: a question of reddening'

Witt, A.N., Schild, R.E., (1985) Ap.J. 294, 225.
'Colours of reflection nebulae. II. The excitation of extended red emission'

Witt, A.N., Schild, R.E., Kraiman, J.B., (1984) Ap.J. 281, 708.
'Photometric study of NGC 2023 in the 3500 Angstrom to 10000 A region: confirmation of a near-infrared emission process in reflection nebulae'

Wright, J.S., MacKay, C.D., (1981) Proc. Soc. Phot. Instr. Eng. 290, 160.
'The Cambridge charge-coupled device (CCD) system'

Zellner, B.H., (1970) Ph.D. Thesis Univ. Arizona order no 70-22018.
'Polarization in reflection nebulae'

Zellner, B.H., (1973) in: IAU Symposium 52, p109,
'Interstellar Dust and Related Topics', Ed. Greenberg, J.M., van de Hulst, H.C., D.Reidel, Dordrecht.
'Dust grains in reflection nebulae'

Zellner, B.H., (1974) in: 'Planets, Stars and Nebulae Studied with Photopolarimetry' Gehrels, T., Editor., p867.
University of Arizona Press, Tucson.
'Polarization studies of reflection nebulae'

Zinnecker, H., (1984) M.N.R.A.S. 210, 43.
'Star formation from hierarchical cloud fragmentation: a statistical theory of the log-normal initial mass function'

APPENDIX A

An optical polarization study of NGC 2068

M. D. Mannion and S. M. Scarrott

Summary.

An optical linear polarization map of the reflection nebula NGC 2068 (Messier 78) is presented. A geometry is proposed to explain the pattern of polarization in terms of a single star (HD 38563N) illuminating a foreground slab of dust of varying density.

1 Introduction

The whole Orion region is a conglomeration of molecular clouds within which are found the typical indicators of recent and continuing star formation - T Tauri stars, Herbig-Haro objects, and infrared sources. To the north of the dominant molecular clouds OMC1 and OMC2 is found the dark dust cloud Lynds 1630 in which are located the reflection nebulae NGC 2068 and NGC 2071. Lynds 1630 (Lynds 1962) is approximately 20 pc in extent at a distance of 500 pc (Strel'nitskii 1970) and is composed mainly of molecular hydrogen (Tucker, Kutner & Thaddeus 1973). It is a copious source of molecular emission from various species, in particular CO, which peaks in the vicinity of M78 (Pankonin & Walmsley 1978) indicating the cloud is substantially neutral material.

NGC 2068 is a reflection nebula within which three relatively bright stars are visible - HD 38563N, HD 38563S, and HD 38563C, the first being the illuminating star for the nebula (Elvius & Hall 1966). The various parameters for these stars are summarized in Table 1. The nebula also contains several objects seen at 2 micron interpreted as highly reddened late B and early A stars (Strom et al. 1975). The area is a region of star formation as recent as E5 yr.

The visual structure of NGC 2068 is dominated by a band of dark obscuration that delineates the northern edge of the nebula. To the south of the obscuration is the bright fan shaped nebulosity containing the visble stars, to the north-west there is a much fainter patch of nebulosity.

In this paper we present an optical polarization map of the reflection nebula NGC 2068 and discuss the role of the various stars illuminating the nebula and propose a geometry for the object.

2 Experimental procedure

The observations were made at the f/15 focus of the SAAO 1-m telescope in March 1979 using the Durham electronographic polarimeter described by Scarrott et al. (1983). A broad band V filter (GG455 + BG38) was used with an effective wavelength of 0.52 micron. The linear polarization map is shown in Fig. 1 where

each measurement is represented by a line, the length of which is proportional to the degree of polarization, orientated parallel to the E-vector. The position of the stars HD 38563N, S, and C are indicated. The integration bins are 6 by 6 arcsec.

In Plate 1(a,b) we present pictures of the nebula derived from the reduced data in total and polarized intensity.

3 Discussion

The regular pattern of the centro-symmetric arrangement of polarization vectors in Fig. 1 confirms that NGC 2068 is a reflection nebula with a single source of illumination - HD 38563N. There is no evidence from our data that the other stars within the nebula HD 38563S and C illuminate the nebula in any manner. The portion of the nebulosity to the north-west of the band of dust is also illuminated by HD 38563N. Inspection of Fig. 1 indicates that the degree of polarization is small close to the illuminating star (2 per cent) and that it rises monotonically with distance from this source. Fig. 2 presents traces of the degree of polarization, polarized intensity and intensity along a line through HD 38563N in a north-south direction. With regard to the polarization trace it can be seen that the maximum polarization is 20 per cent, quite low for a reflection nebula and this feature will be discussed later. The polarized intensity trace also shows an unusual feature in that it reaches a maximum 95 arcsec south of the illuminating star. In previous measurements

of a variety of reflection nebulae we have normally found that although the degree of polarization decreases as one approaches the source of illumination due in part to line-of-sight effects, it is normal for the polarized intensity to continue to rise with decreasing distance to the central source. NGC 2068 is unusual in this respect. The total intensity trace of the nebulosity falls monotonically with distance.

Before interpreting the above features it is necessary to consider the possible involvement of aligned grain induced polarization. Previous measurements of the linear polarization of the stars HD 38563N, S, C have been ascribed to the effects of aligned grains by Coyne, Gehrels and Serkowski (1974). However the polarization map displayed in Fig. 1 shows no significant deviation from centro-symmetry suggesting the absence of aligned grains. This conclusion is compatible with the stellar measurements if one assumes that these arise from the polarized reflection nebulosity against which the stars are observed.

4 The structure of NGC 2068

In suggesting a geometrical model for NGC 2068 we recall that it is the general property of grains found in reflection nebulae and the ISM that the scattering cross-section is very forward throwing but high polarizations occur at scattering angles close to 90 degrees.

With regard to our observations of low polarizations even at the periphery of the nebula and the high surface brightness of the nebula relative to the central star we suggest that we see NGC 2068 by forward scattered light, and a simple geometry of the nebula is a star (HD 38563N) illuminating a foreground assembly of grains possibly in the form of a tilted slab. Fig. 3 illustrates such a geometry.

Such an idealized model explains our observations in a simple manner. Close to the central star the nebula is seen by very forward scattered light giving high surface brightness but low polarization (ray A), at an intermediate position (ray B) the scattering angle has increased, reducing the brightness but allowing the polarization to increase. At the periphery of the nebula (ray C) the scattering angle has increased further so we have a higher polarization but not the maximum that could rise from scattering that involves angles around 90 degrees. As the polarized intensity is the product of intensity and degree of polarization then in the geometry proposed here one can expect a maximum in this quantity at some offset distance from the central star as observed. This would not be the case for a geometry involving large scattering angles, or long lines of sight within the nebula.

Obviously the number density of grains in the proposed slab would vary with position; to give NGC 2068 its optical image the density would have to be maximum in a position corresponding to

the dark band of obscuration and presumably decrease to the north and south of this position. Strom et al. (1975) assuming a value of 3.6 for R, the ratio of total to selective extinction, estimated that the visual extinction (Av) of HD 38563N is approximately 2 mag in excess of that to HD 38563S. This latter star is foreground to the tilted slab in our model and, accepting our geometry, this gives the optical depth of the slab at the position of the illuminating star HD 38563N. The faint fan of nebulosity to the north-west of HD 38563N is also accounted for as the model predicts (ray D) the highest scattering angles for this region which as a consequence will be faint and highly polarized as observed.

Clearly modelling of this geometry is necessary to explain in numerical detail our observations and this is in progress. This procedure was followed quite successfully for NGC 1999 where the geometry proposed by Warren-Smith et al. (1980) was used by one of the authors to determine the nebula parameters (Warren-Smith 1983)

5 Conclusions

The optical polarization map presented in this paper shows that the reflection nebula NGC 2068 is illuminated solely by the star HD 38563N and the other apparently nearby stars HD 38563S and C play no role in illuminating the nebula. The distribution of polarization and polarized intensity in the nebula suggest that the nebula is seen by forward scattered light and we propose a

simple geometry for the system in the form of a foreground tilted slab illuminated from the rear by HD 38563N

Acknowledgments

We acknowledge SAAO for the use of their facilities and SERC for continuing financial support. MDM was in receipt of a University of Durham studentship while the analysis of this work was carried out.

References

Coyne, G.V., 1974. Astr.J., 79, 565.

Coyne, G.V., Gehrels, T. & Serkowski, K., 1974. Astr.J. 79, 581.

Elvius, A. & Hall, J.S., 1966. Lowell Obs.Bull., 6, 257.

Lynds, B.T., 1962. Astrophys.J.Suppl., 7, 1.

Pankonin, V. & Walmsley, C.M., 1978. Astr.Astrophys., 67, 129.

Scarrott, S.M., Warren-Smith, R.F., Pallister, W.S., Axon, D.J., & Bingham, R.G., 1983. Mon.Not.R.astr.Soc., 204, 1163.

Strel'nitskii, V.S., 1970. Astrofizika, Vol.6, No.4, 625.

Strom, K.M., Strom, S.E., Carrasco,L. & Vrba, F.J., 1975. Astrophys.J., 196, 489.

Tucker, K.D., Kutner, M.L. & Thaddeus, P., 1973. Astrophys.J., 186, L13.

Warren-Smith, R.F., 1983. Mon.Not.R.astr.Soc., 205, 349.

Warren-Smith, R.F., Scarrott, S.M., King, D.J., Taylor, K.N.R., Bingham, R.G., Murdin, P., (1980) Mon.Not.R.astr.Soc., 192,339.

Table 1. Data on the visible stars in NGC 2068.

Star	RA	Dec	M_V (a)	B-V (a)	Sp. (a)	E_{b-v} (a)	P (b)	PA (b)	P (c)	PA (c)	P (d)	PA (d)
	h min s	° ′ ″	mag	mag	type	mag	(per cent)	(°)	(per cent)	(°)	(per cent)	(°)
HD 38563N	5 44 10.8	0 4 19.2	10.56	1.18	B1–B2	1.42	2.1	15	2.4	179	–	–
HD 38563S	5 44 9.5	0 3 32.5	10.42	0.60	B3–B5	0.78	4.2	100	4.3	96	4.06	97.9
HD 38563C	5 44 11.5	0 1 38.0	13.09	0.96	A0 II	0.96	–	–	–	–	–	–

Key: P, degree of polarization.
PA, position angle of polarization.

These values are taken from the following references:
(a) Strom *et al.* (1975). (c) Elvius & Hall (1966).
(b) Strel'nitskii (1970). (d) Coyne (1974).

Table 1. Data on the visible stars in NGC 2068.

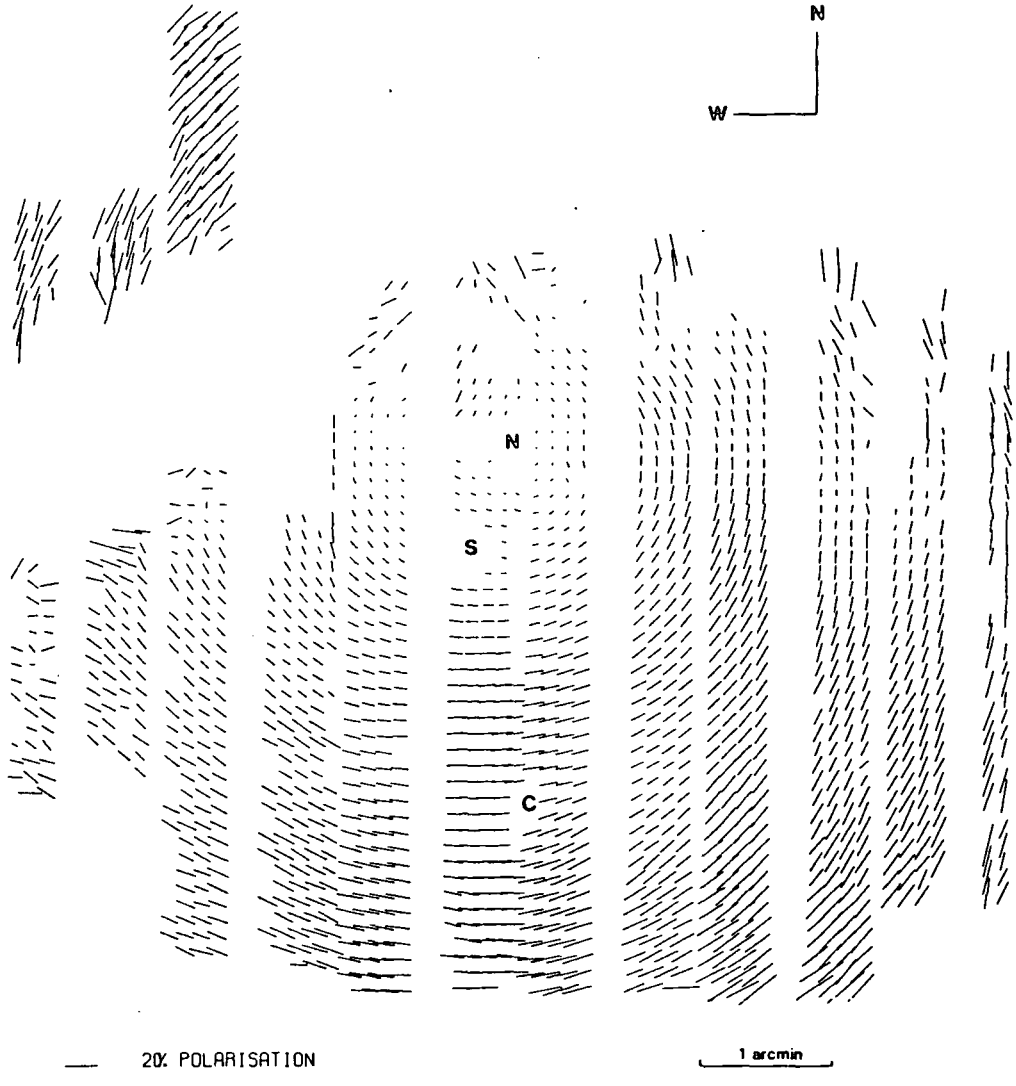

Figure 1. An optical linear polarization map of the reflection nebula NGC 2068.

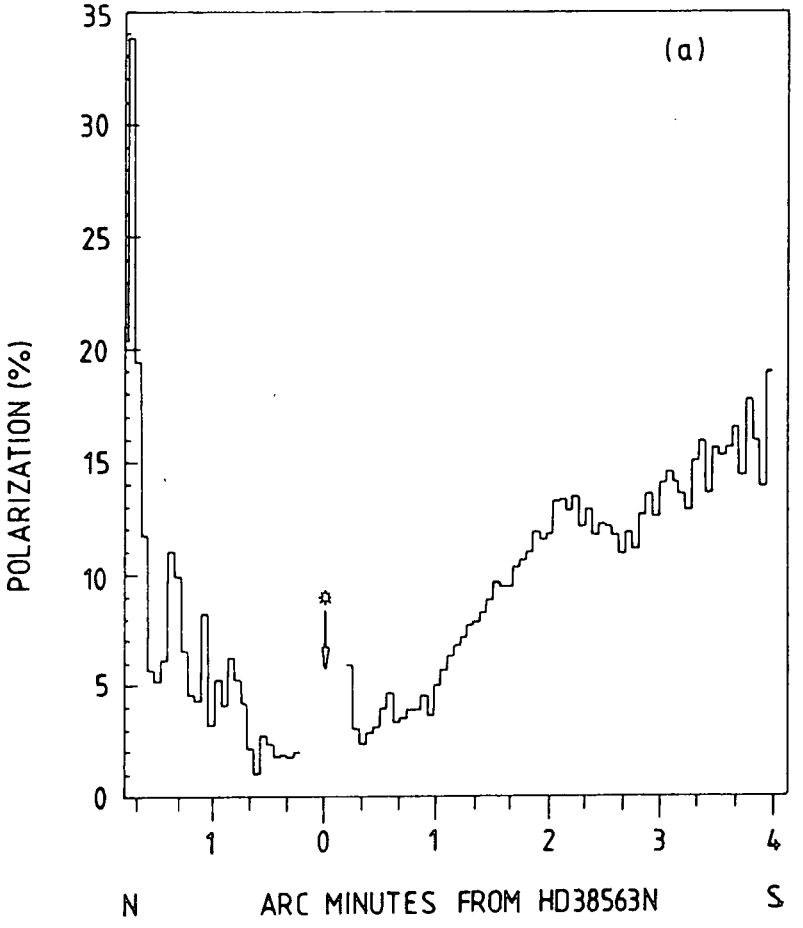

Fig. 2. Traces in a north-south direction through the illuminating star HD 38563N showing degree of polarization (a), polarized intensity (b), and total intensity (c).

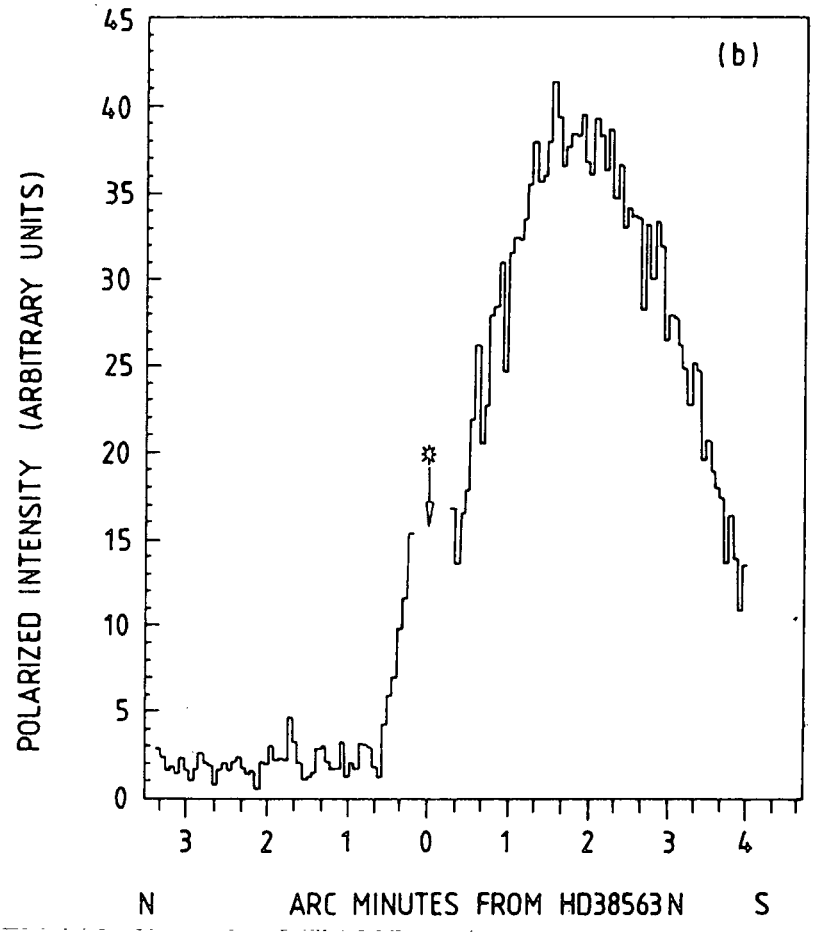

Fig. 2 - contin. (b)

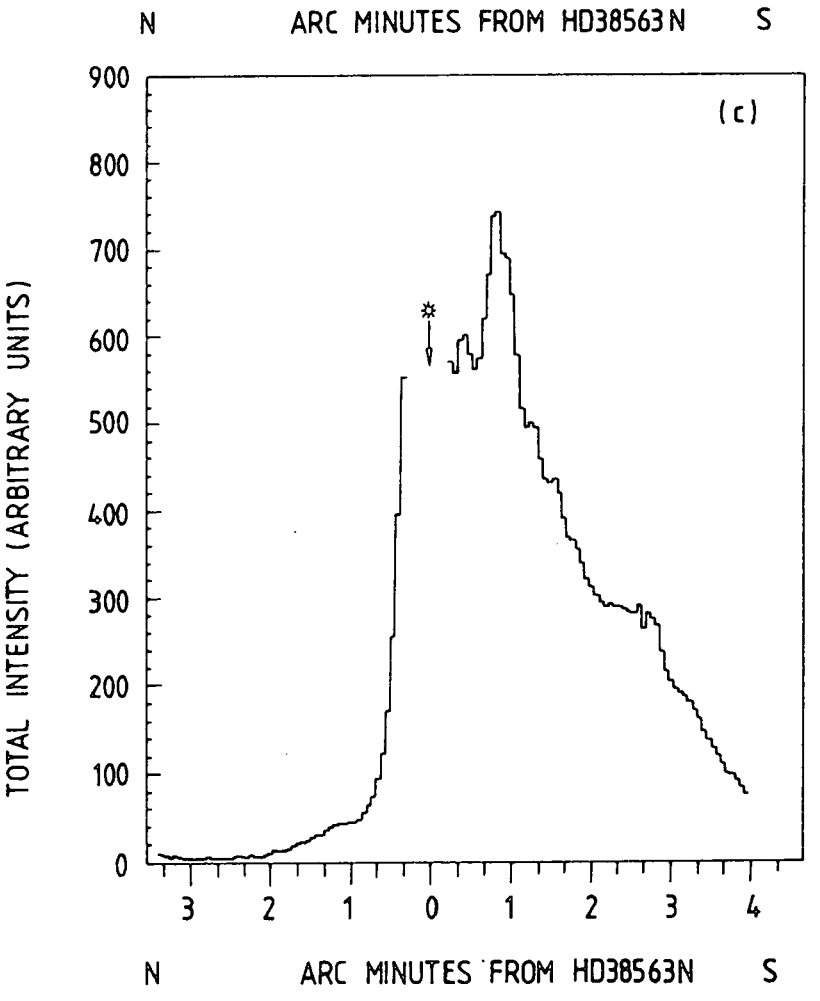

Figure 2 – *continued*

Fig. 2 - contin. (c)

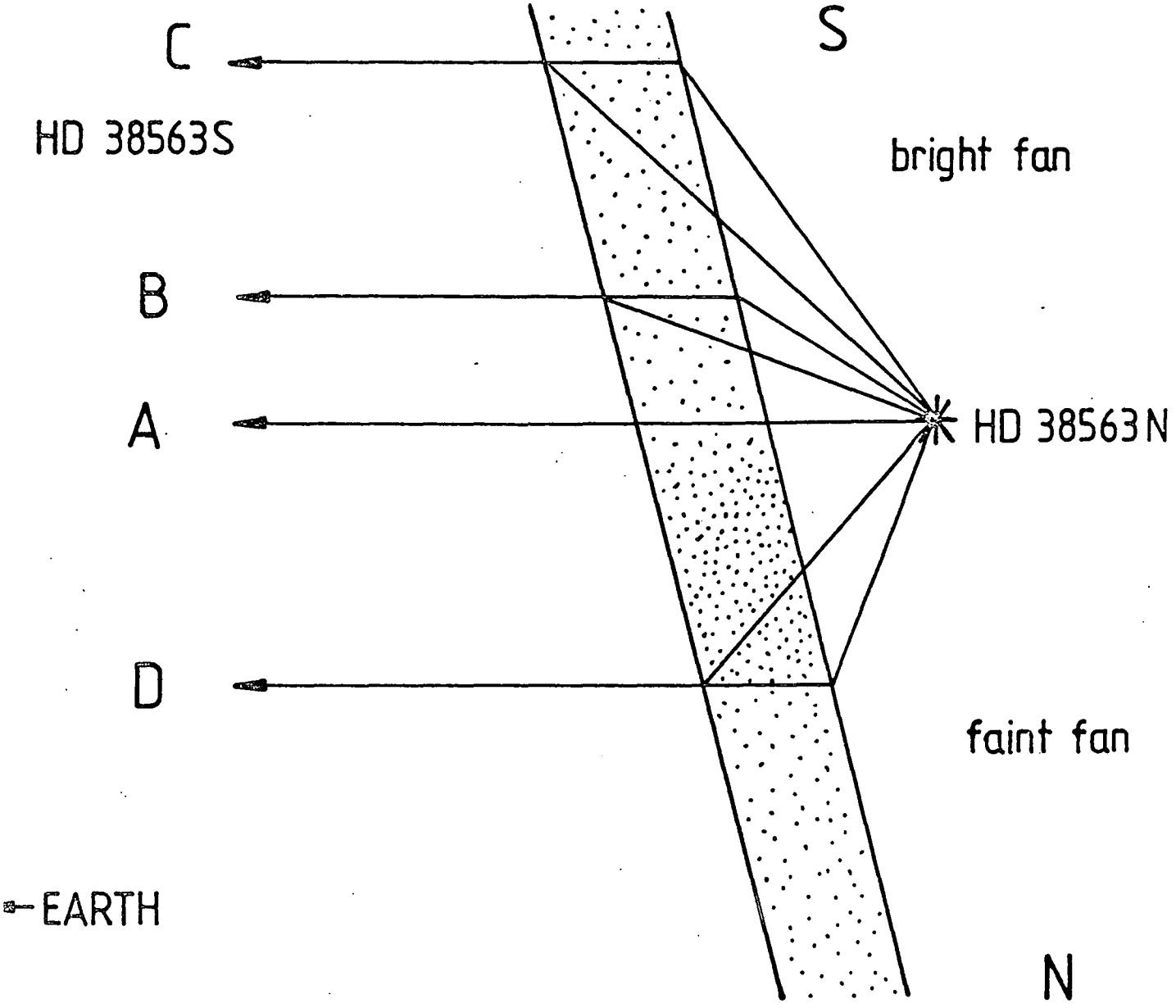

Fig. 3. The proposed geometry of the reflection nebula NGC 2068.

Plate 1. Pictures of NGC 2068 in total intensity (a)

and polarized intensity (b).


N
S
C

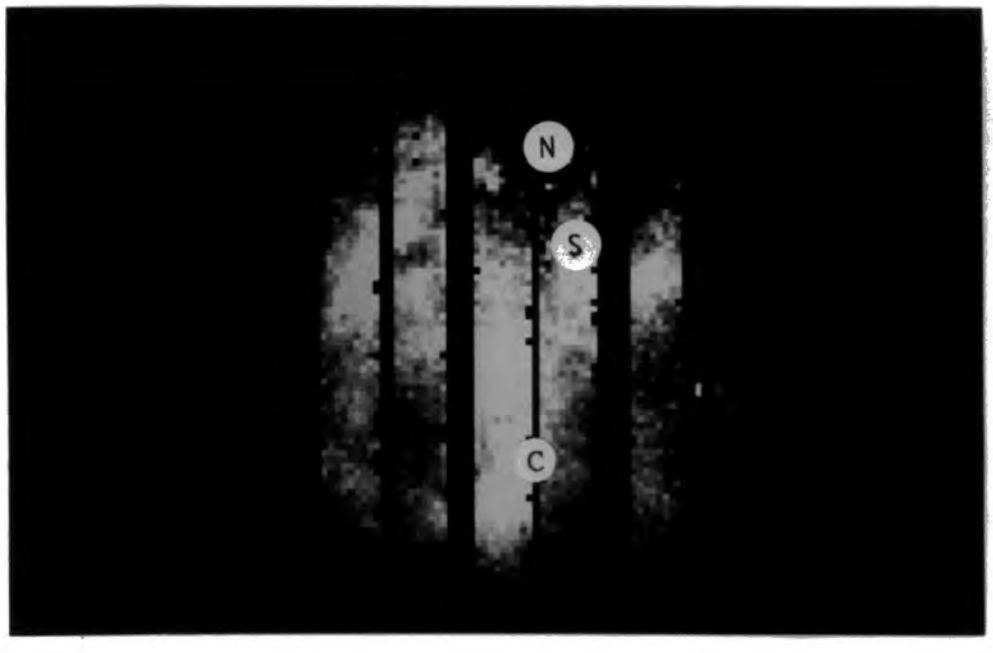
N
S
C

APPENDIX B

A comparison of data reductions of NGC 2068

The two data reductions done on the electronographic data of NGC 2068 using the original programs on NUMAC and the revised programs on the STARLINK VAX have produced similar data as can be seen by comparing the combined visual total intensity maps and traces in a north-south direction of polarization, polarized intensity and total intensity. However, there are one or two differences, for example:

a) The polarization both monotonically increases for the two data sets, but in the case of the VAX reduction there is a sharp dip in polarization at ~ 100 arcseconds south of HD 38563N which is not seen in the case of the NUMAC reduction. Both sets of data record the shallow dip in polarization at ~ 2.6 arcminutes south of HD 38563N.

b) Polarized intensity reaches a maximum at 95 arcseconds in the case of the NUMAC reduction and 105 arcseconds when the data was reduced on the VAX.

Comparing the two combined visual polarization maps one sees the same centrosymmetric pattern about HD 38563N but the pattern of vectors in the NUMAC case is much smoother. This might be because of the program 'Filter' which was not rewritten for the VAX reduction procedures. The original trace data (NUMAC reduction) was used as input in the model in chapter 5 as it is smoother.

APPENDIX C

Traces of Polarization, polarized intensity and total intensity

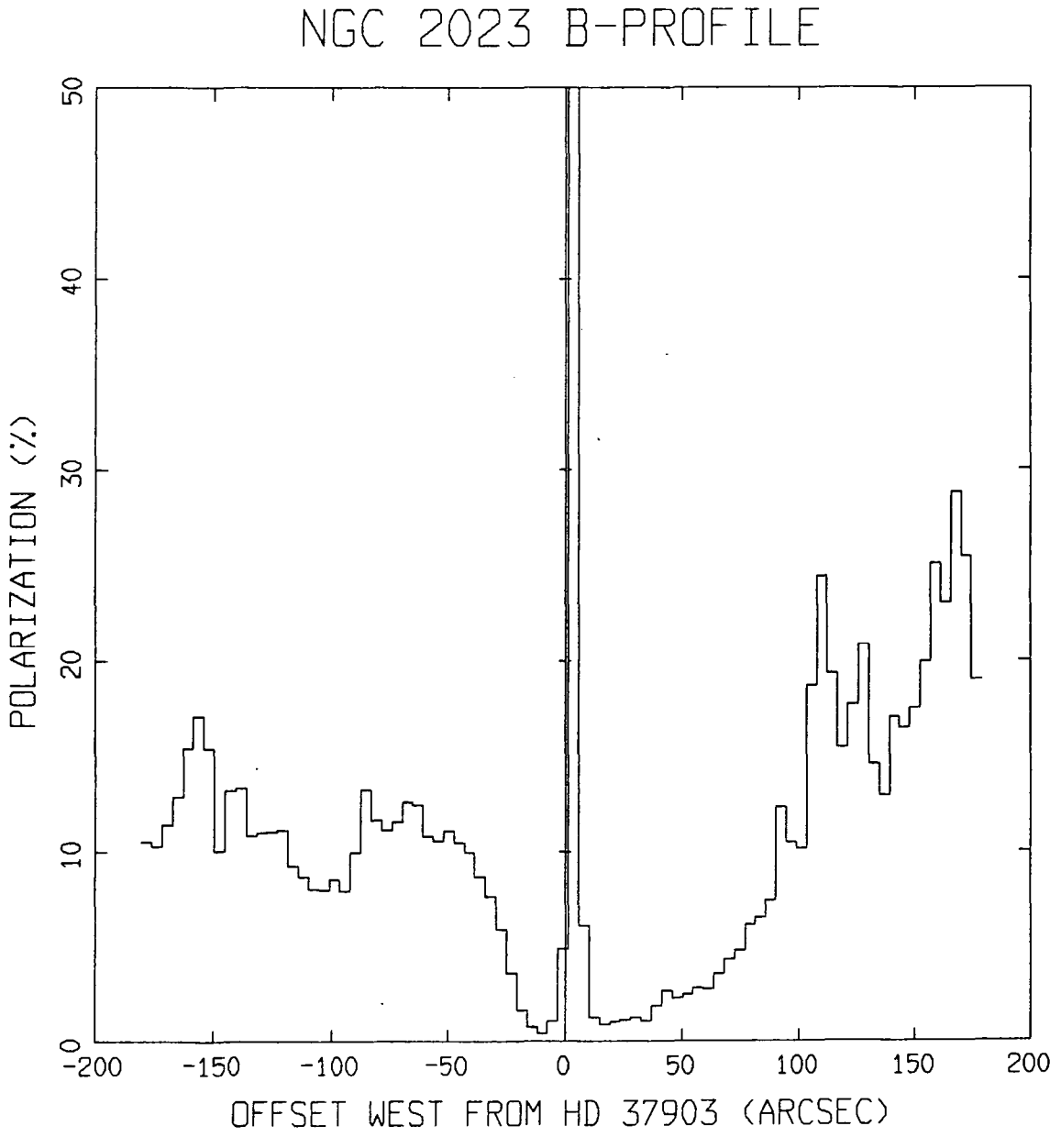

Fig. C1. Polarization (B) trace through HD 37903 in an east-west direction.

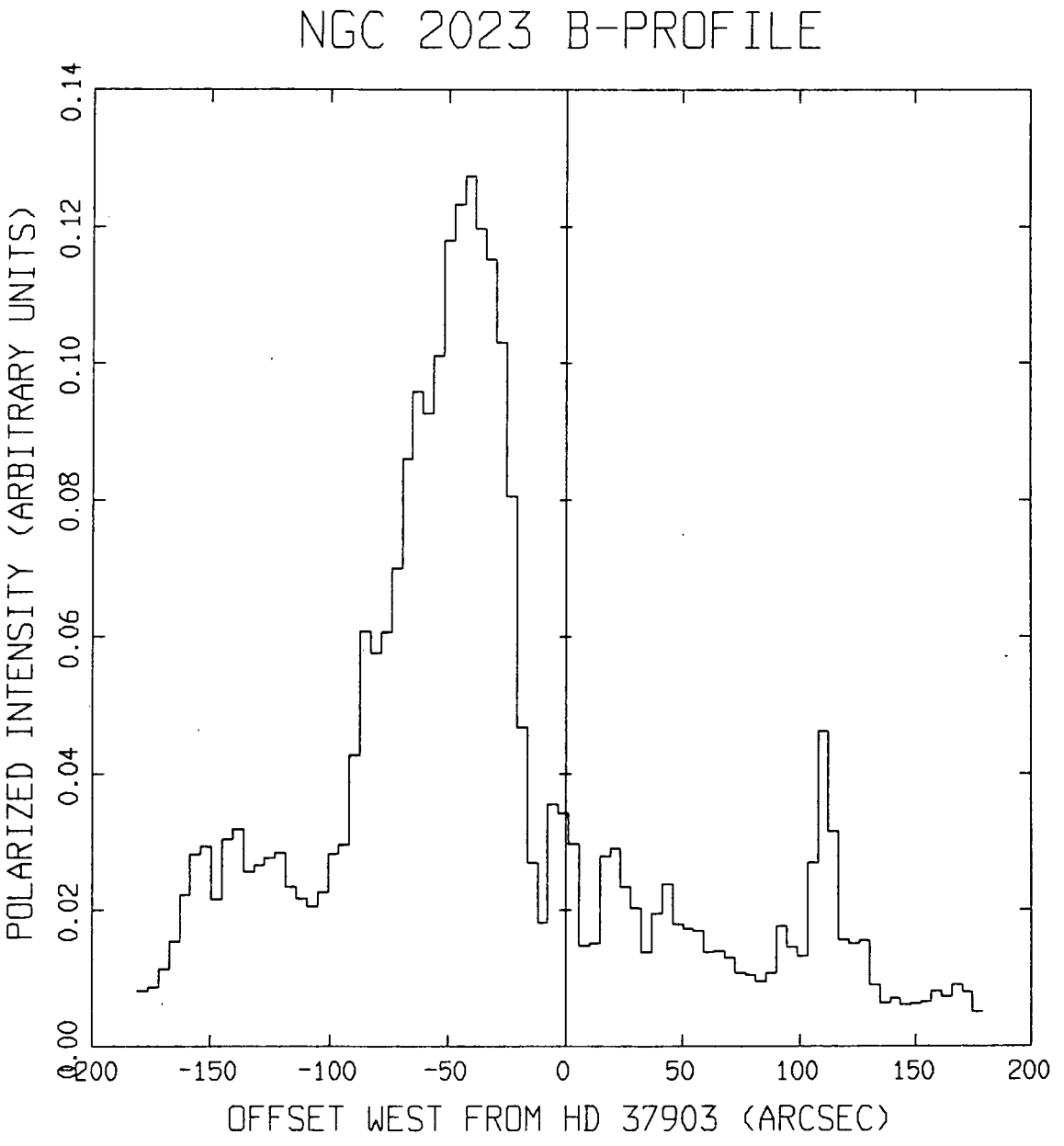

Fig. C2. Polarized intensity (B) trace through HD 37903 in an east-west direction.

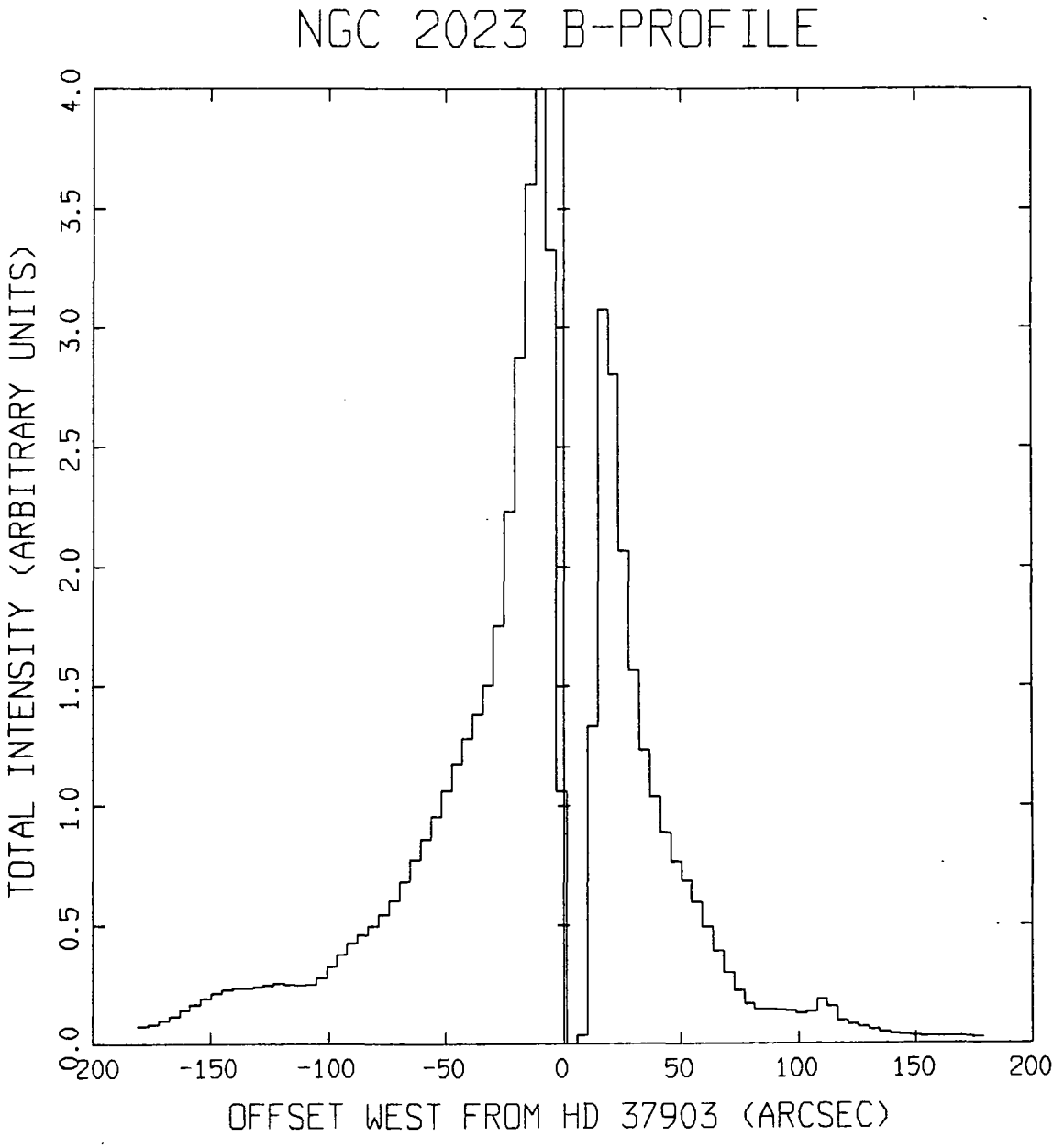

Fig. C3. Total intensity (B) trace through HD 37903 in an east-west direction.

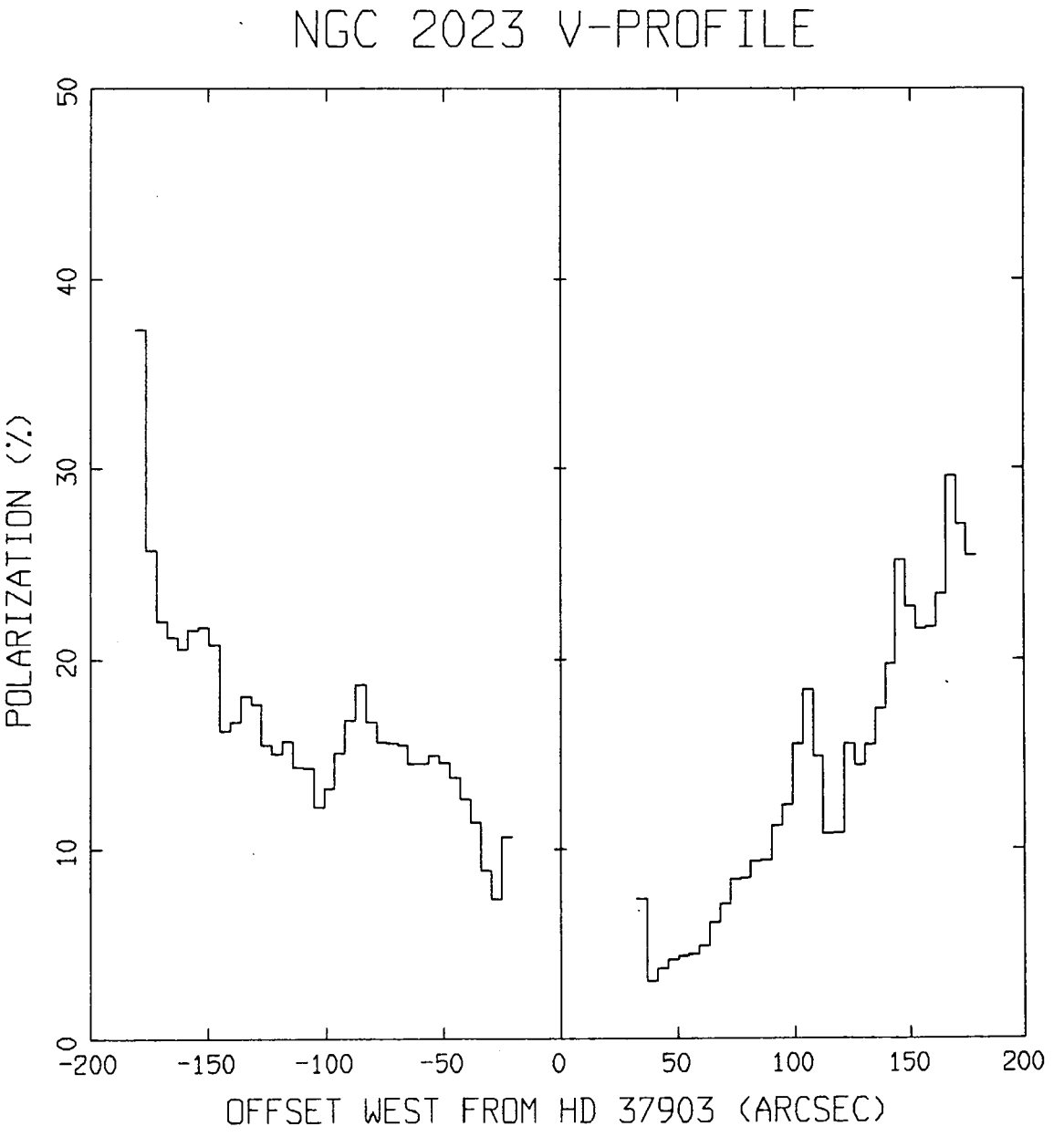

Fig. C4. Polarization (V) trace through HD 37903 in an east-west direction.

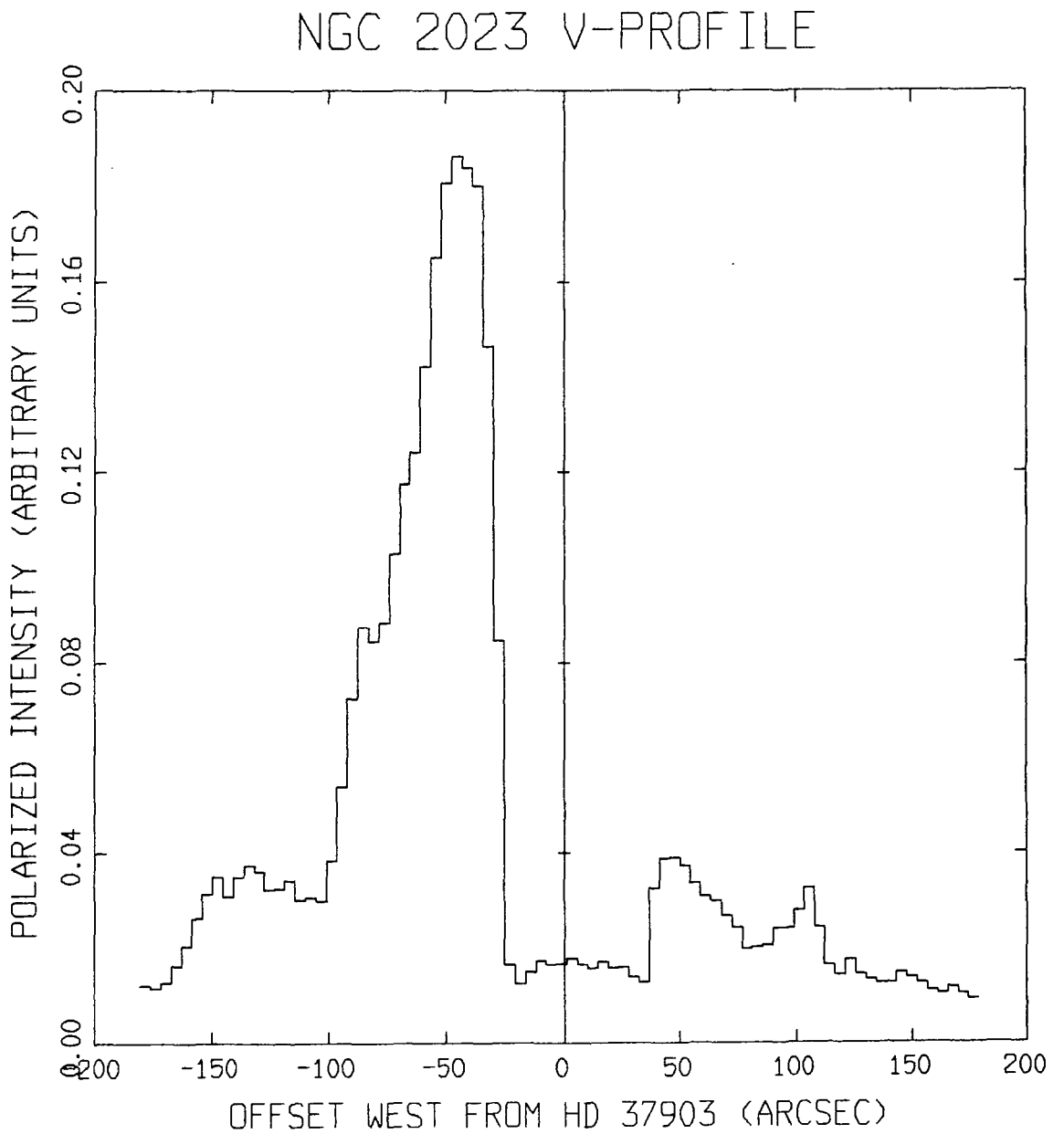

Fig. C5. Polarized intensity (V) trace through HD 37903 in an east-west direction.

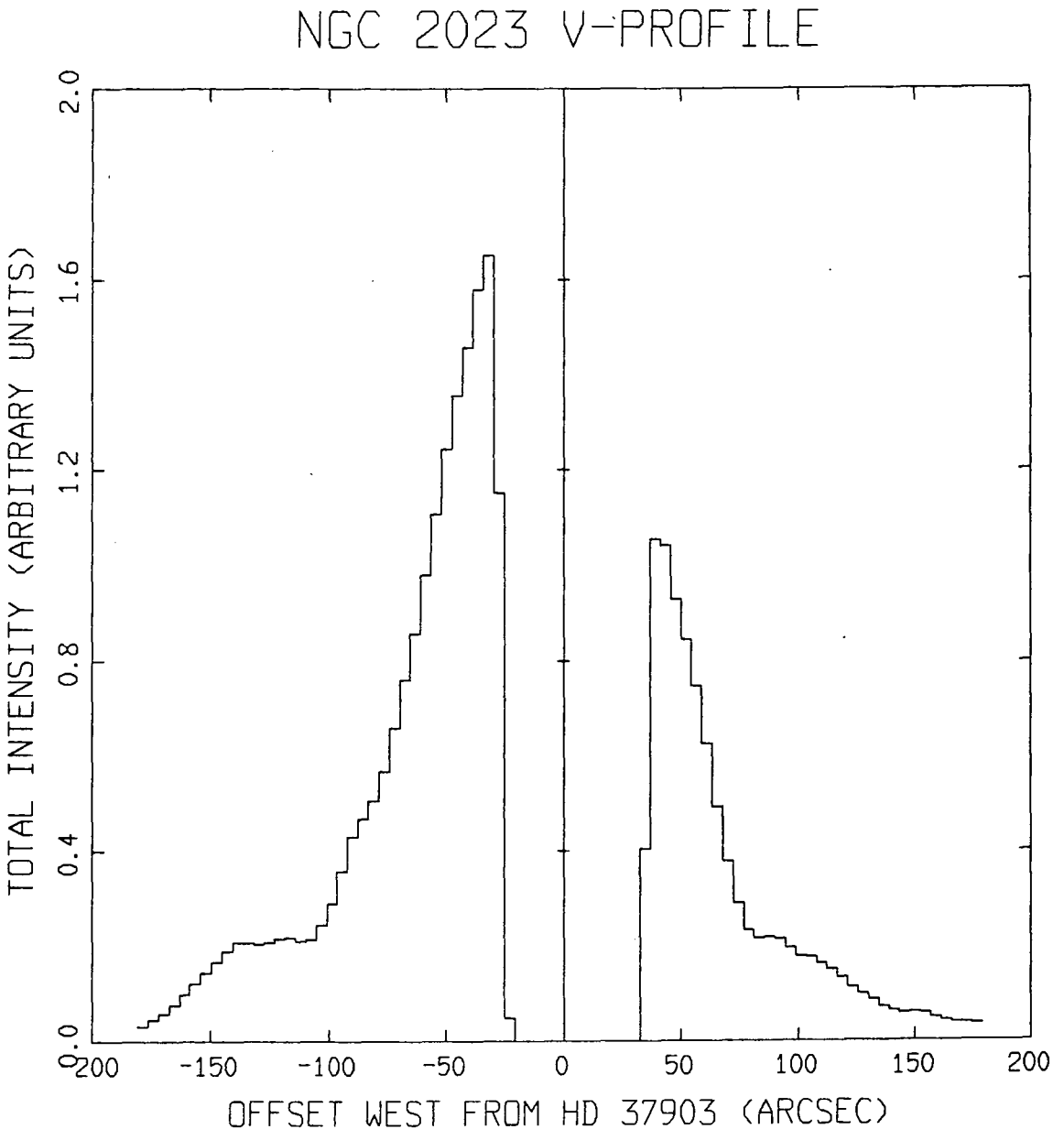

Fig. C6. Total intensity (V) trace through HD 37903 in an east-west direction.

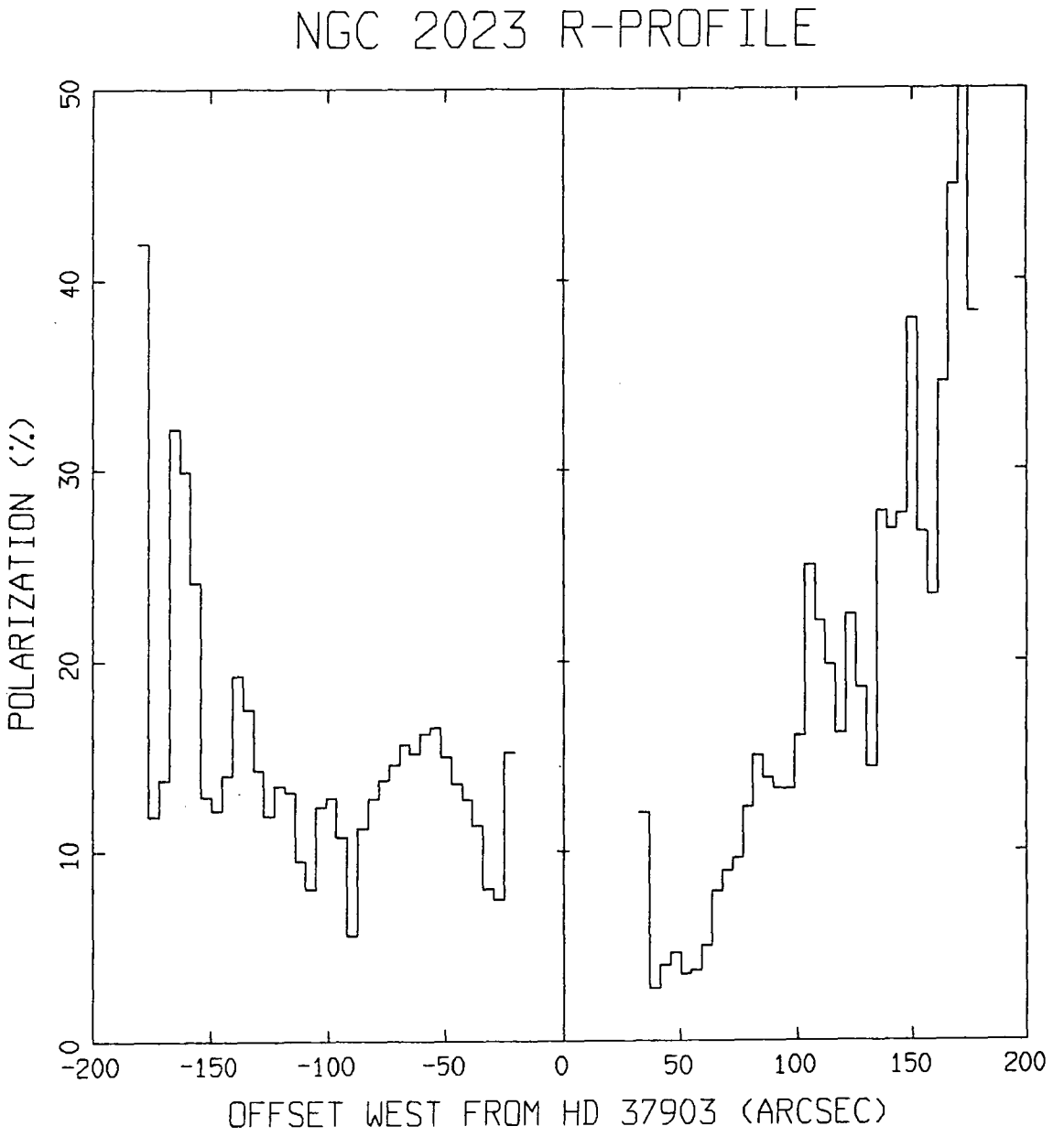

Fig. C7. Polarization (R) trace through HD 37903 in an east-west direction.

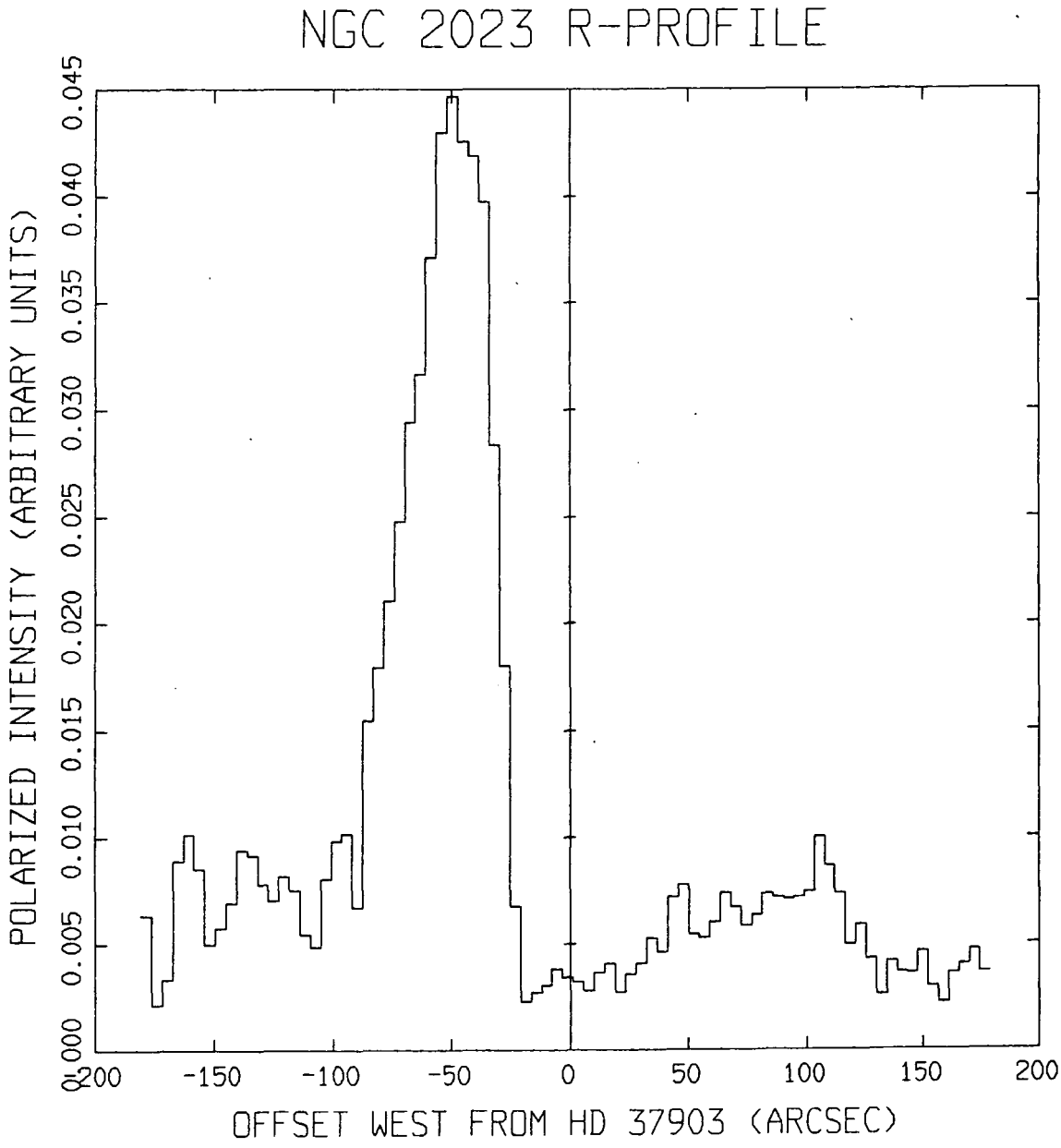

Fig. C8. Polarized intensity (R) trace through HD 37903 in an east-west direction.

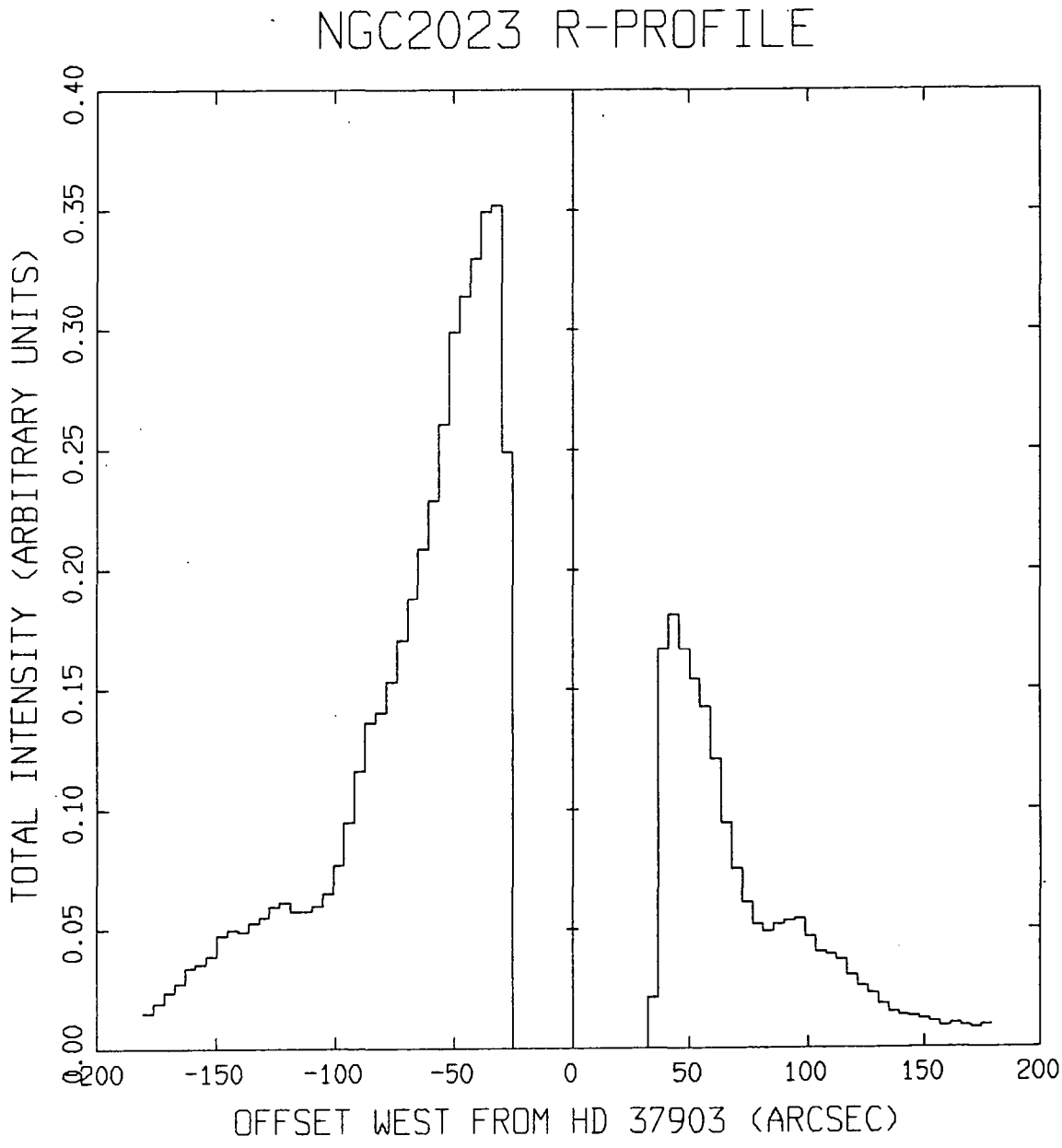

Fig. C9. Total intensity (R) trace through HD 37903 in an east-west direction.

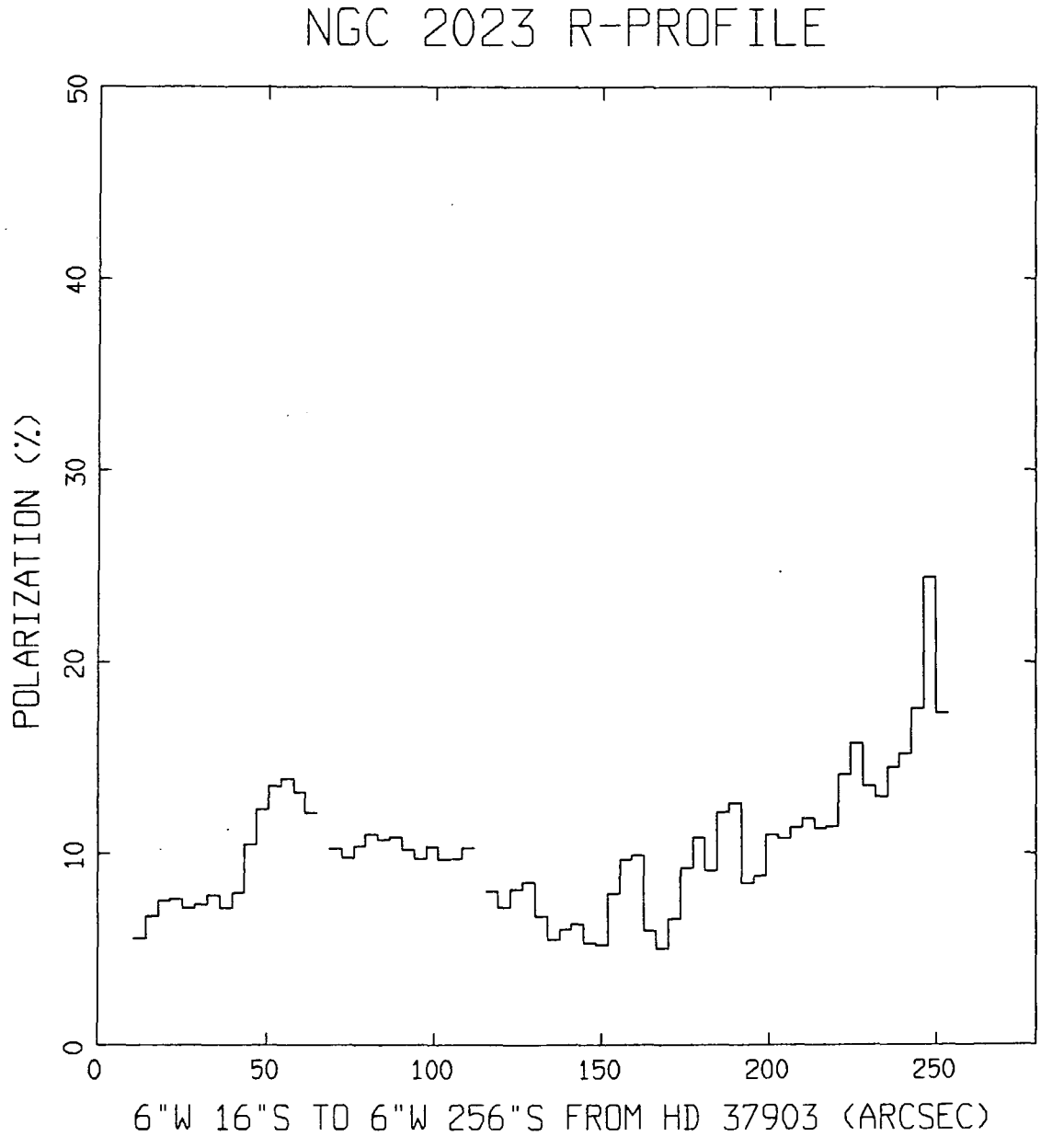

Fig. C10. Polarization (R) trace through HD 37903 in a north-south direction.

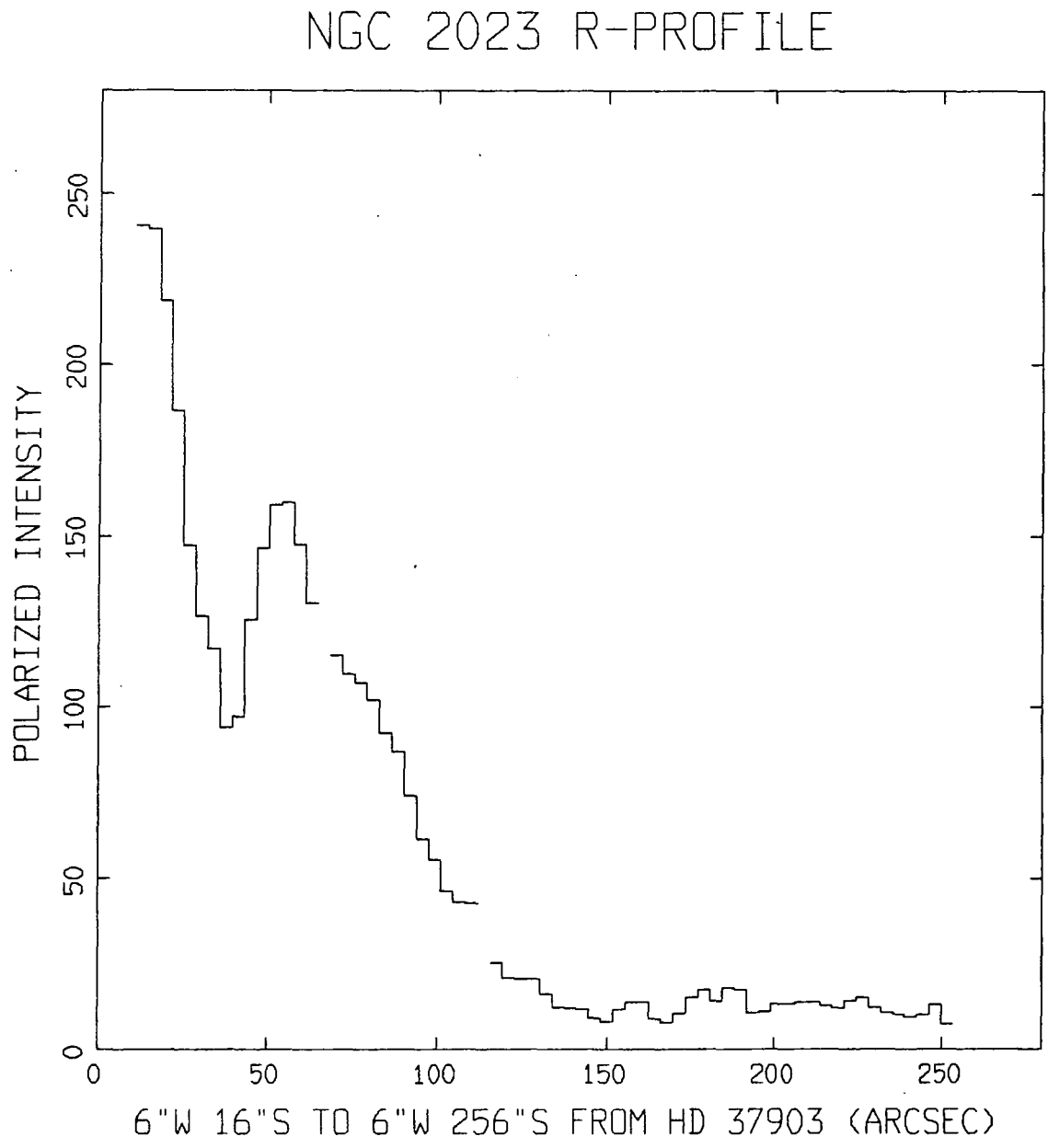

Fig. C11. Polarized intensity (R) trace through HD 37903 in a north-south direction.

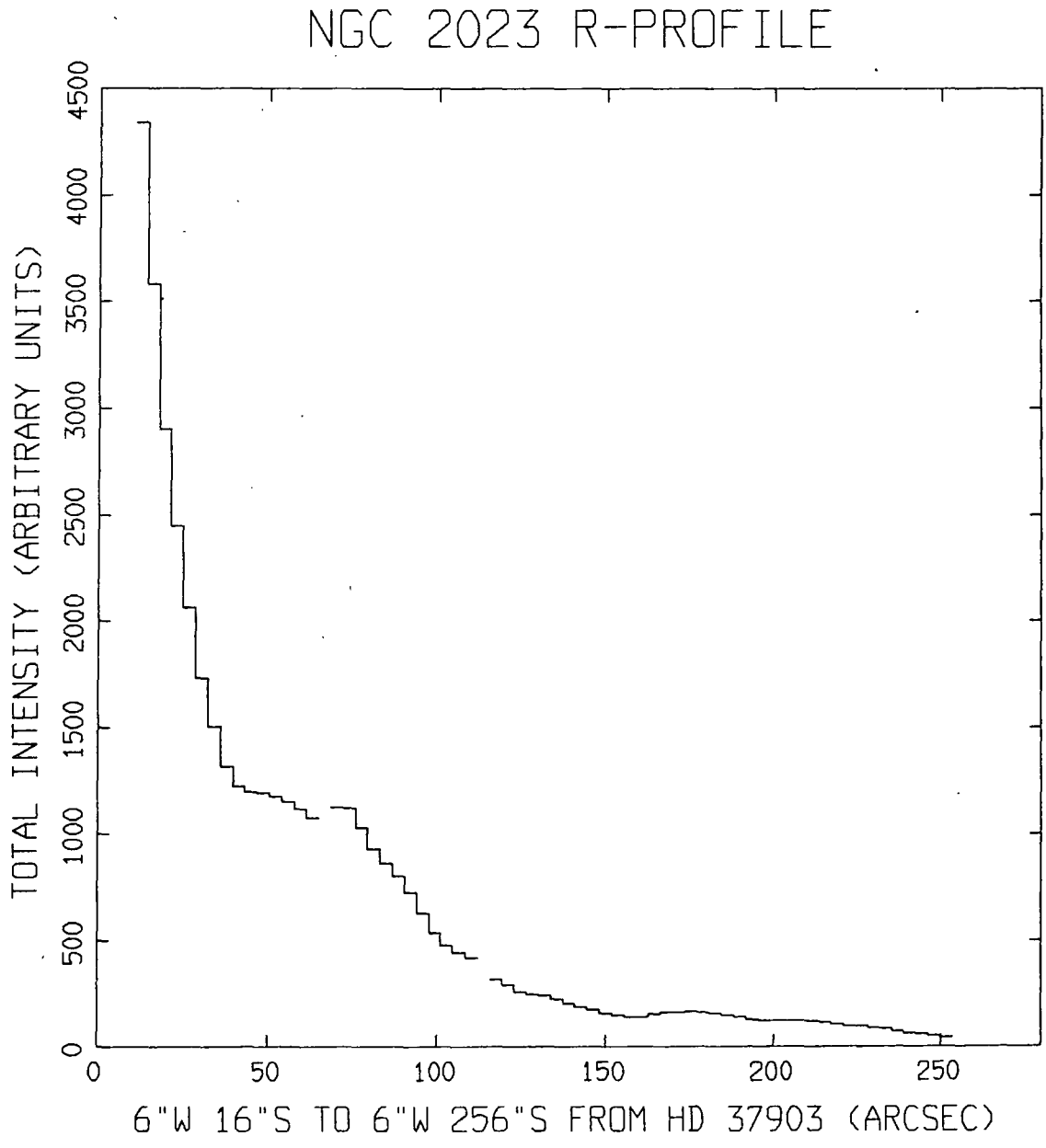

Fig. C12. Total intensity (R) trace through HD 37903 in a north-south direction.

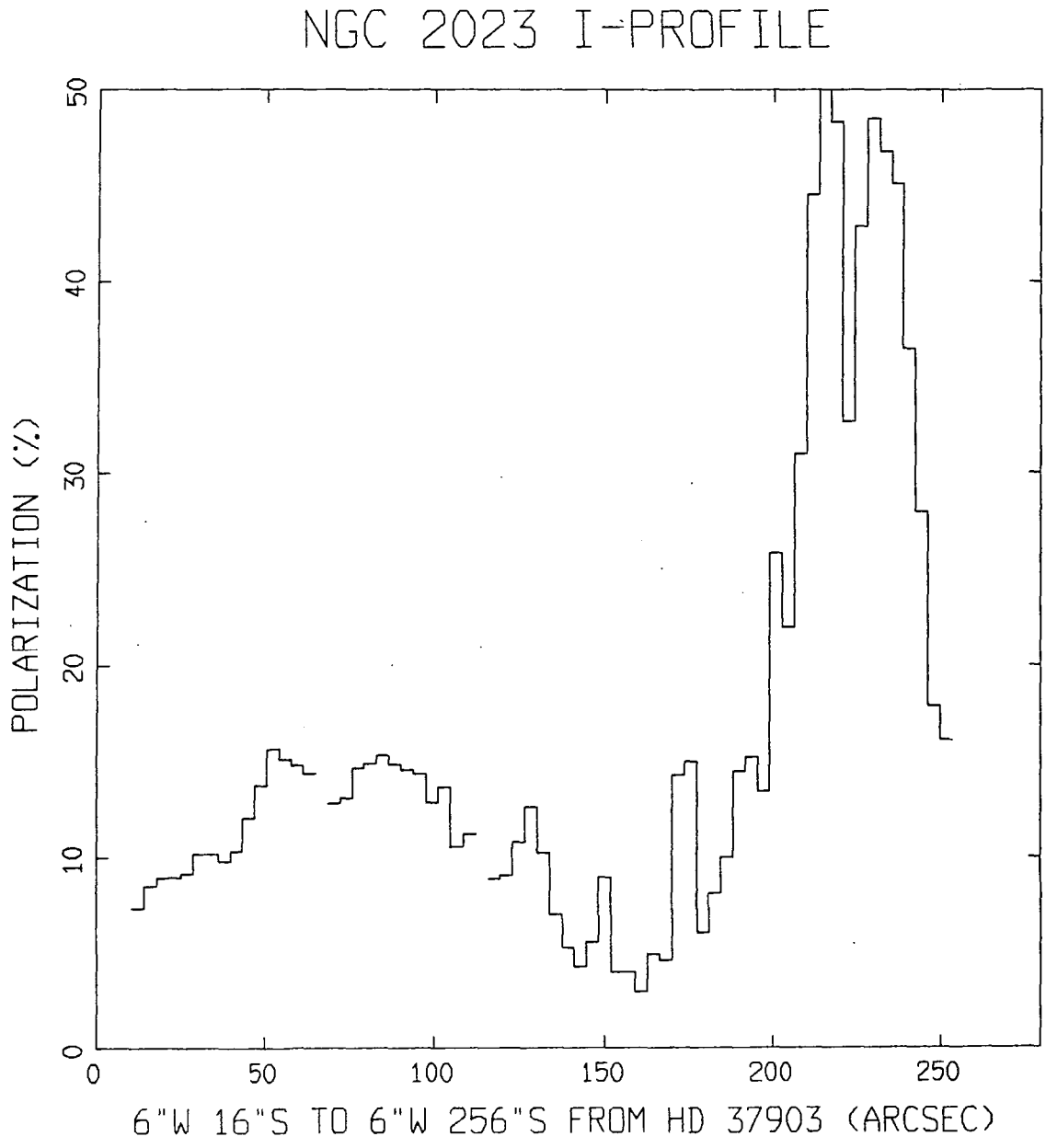

Fig. C13. Polarization (I) trace through HD 37903 in a north-south direction.

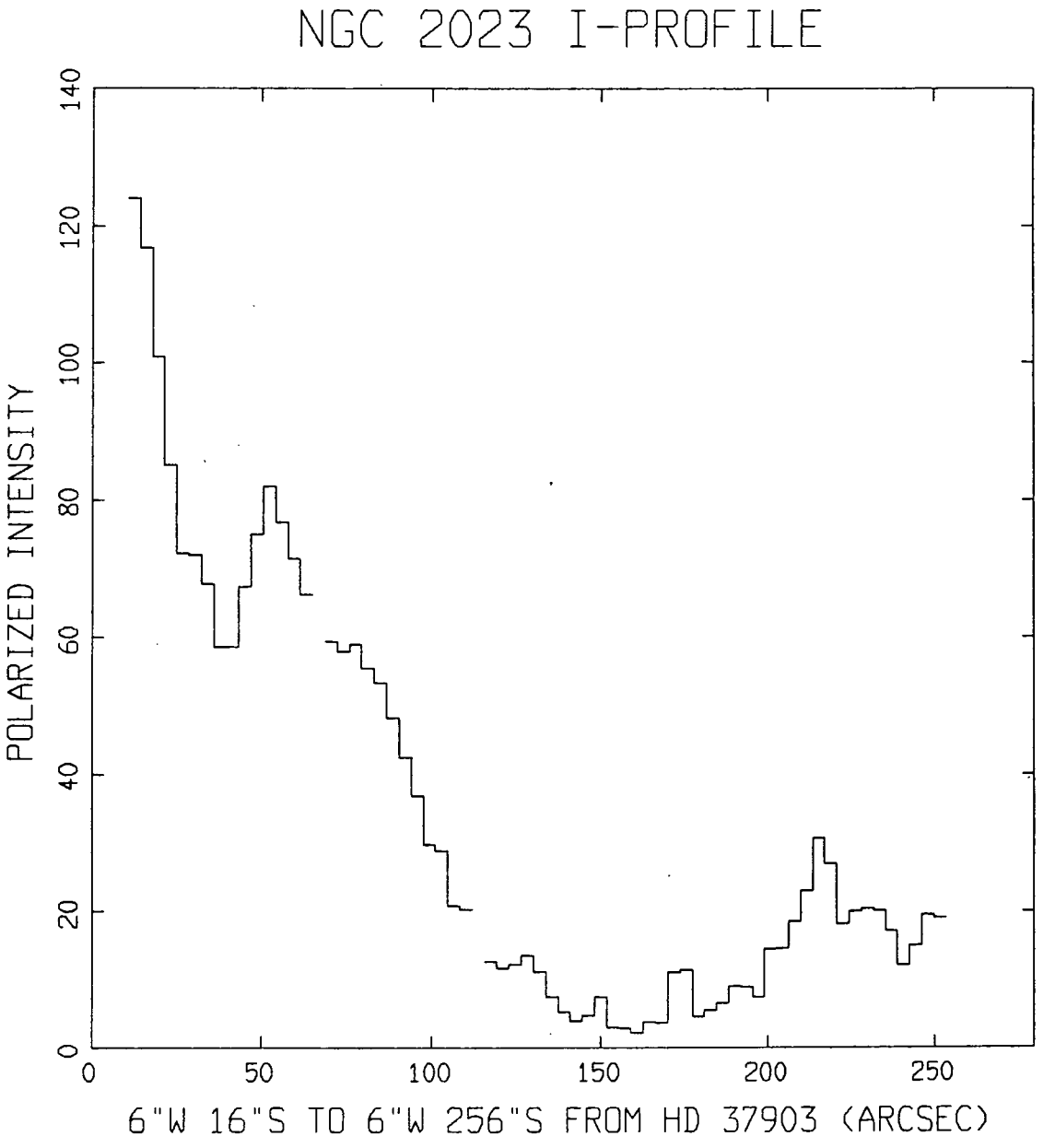

Fig. C14. Polarized intensity (I) trace through HD 37903 in a north-south direction.

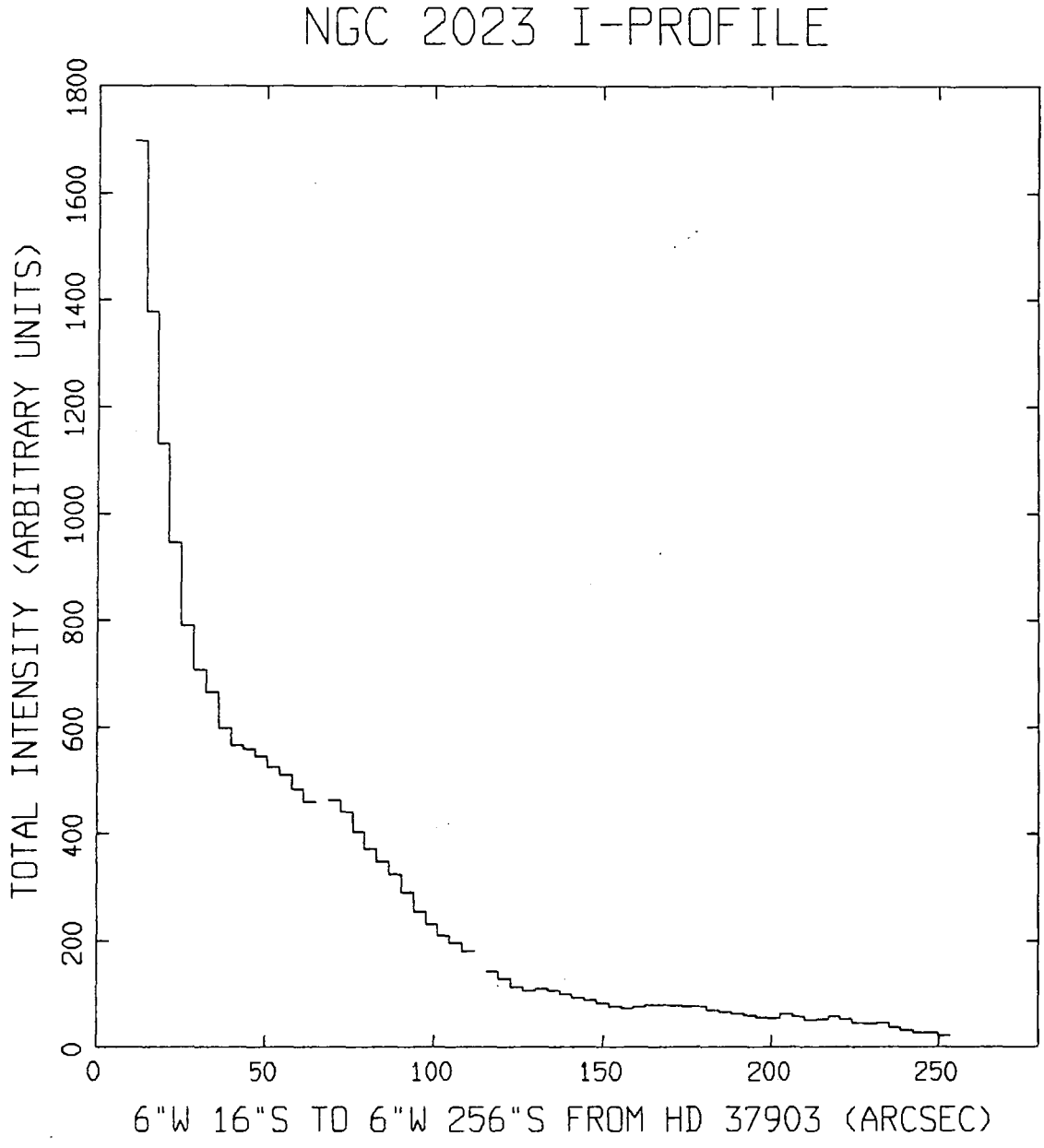

Fig. C15. Total intensity (I) trace through HD 37903 in a north-south direction.

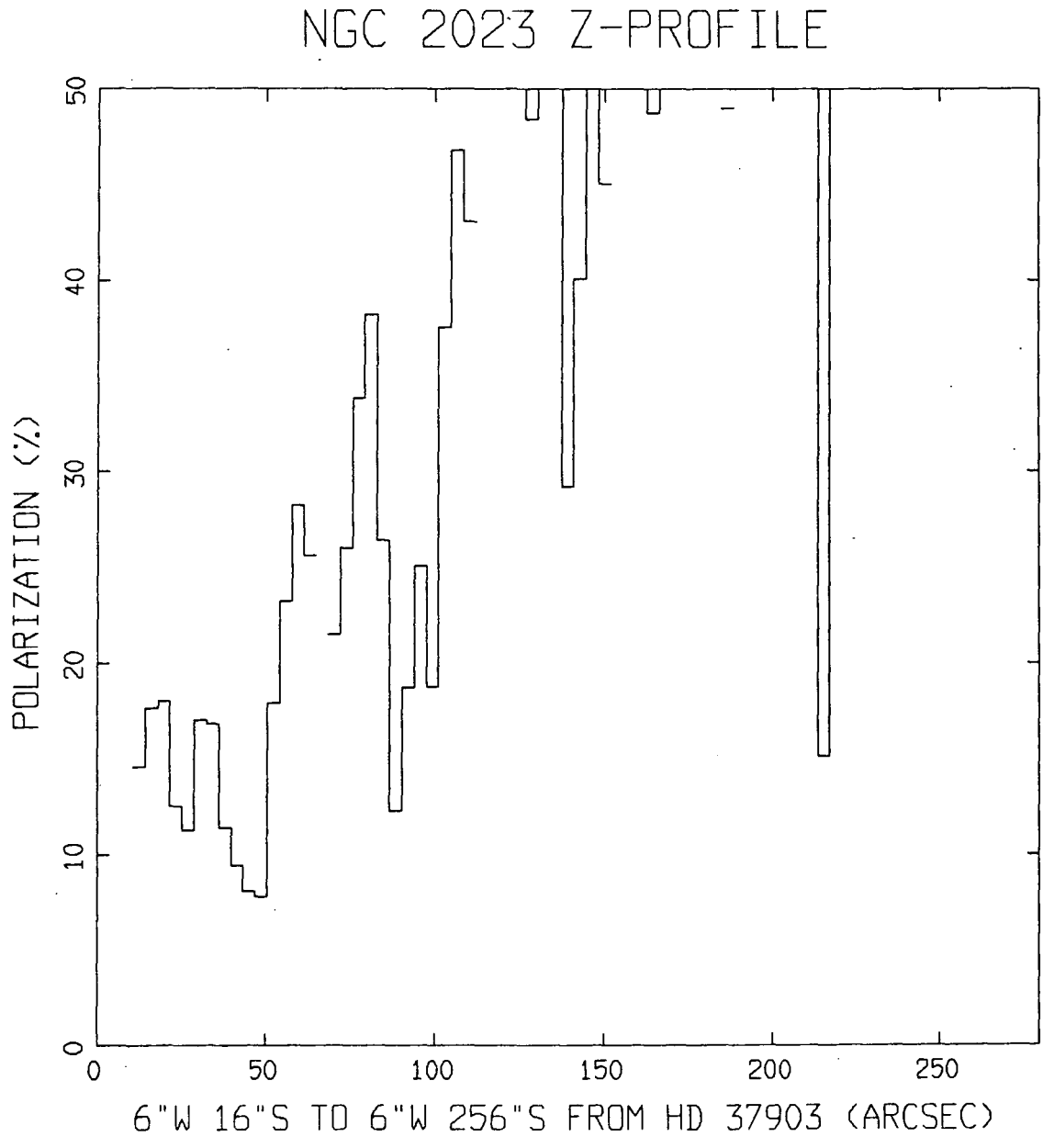

Fig. C16. Polarization (Z) trace through HD 37903 in a north-south direction.

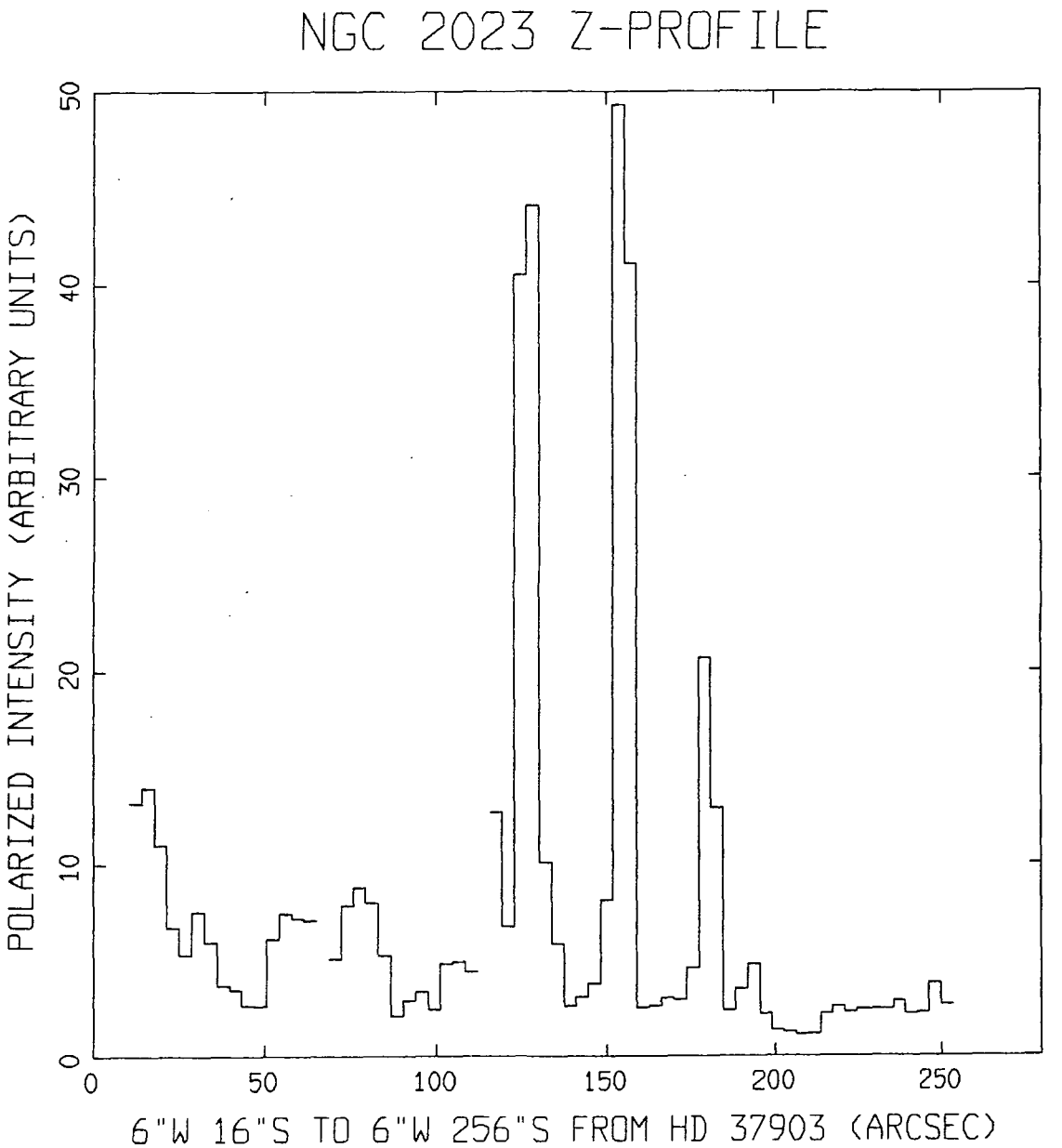

Fig. C17. Polarized intensity (Z) trace through HD 37903 in a north-south direction.

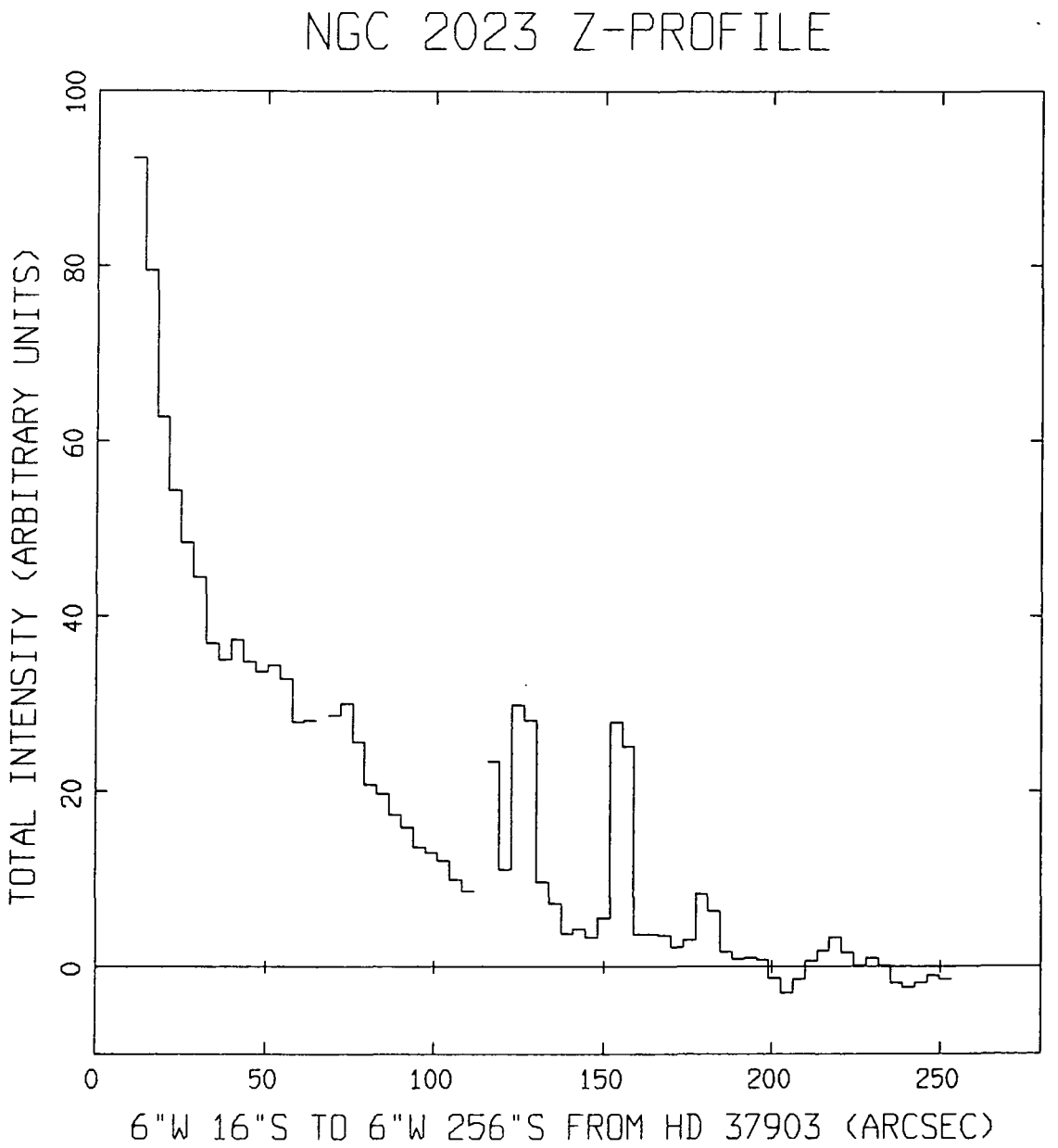

Fig. C18. Total intensity (Z) trace through HD 37903 in a north-south direction.

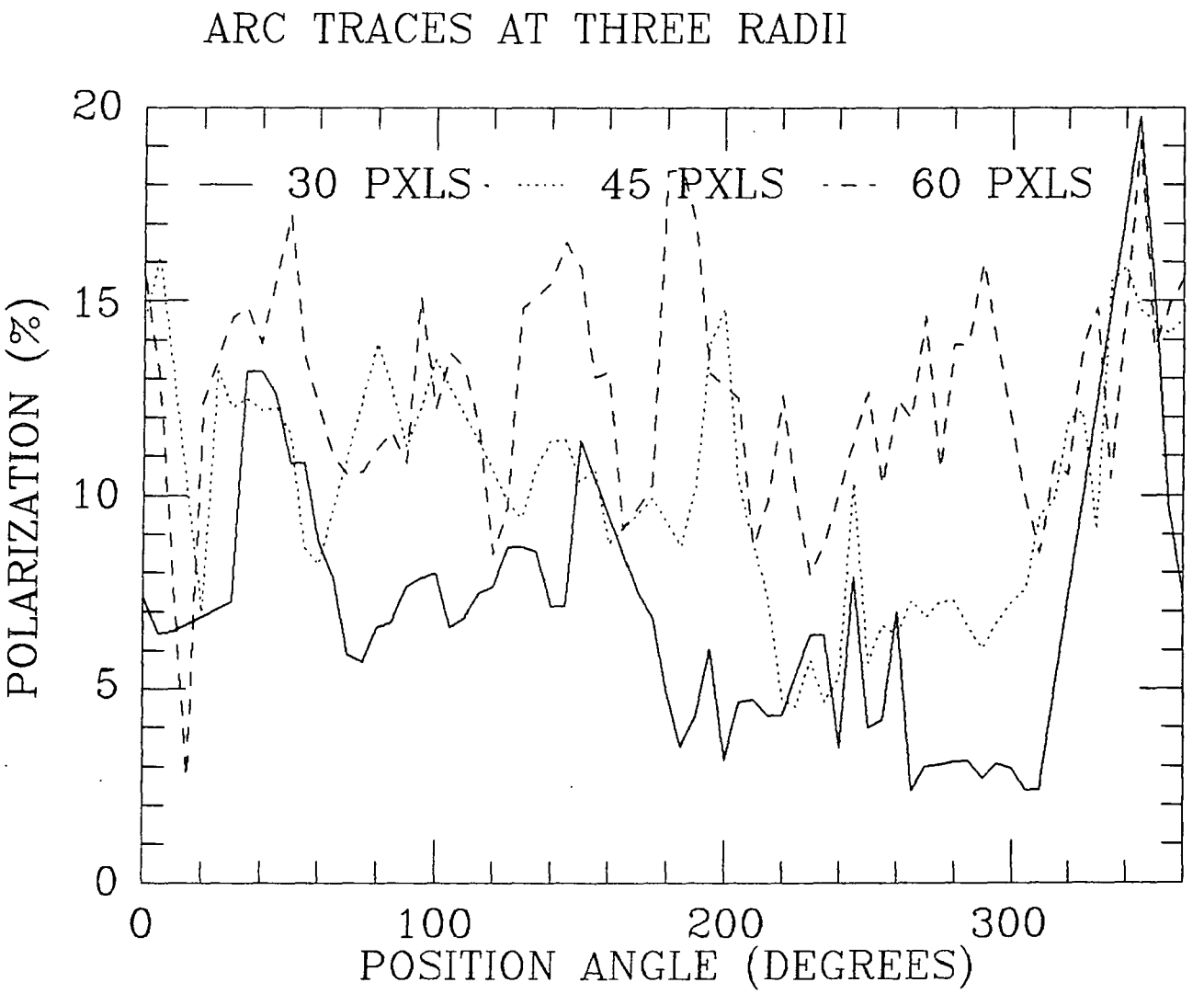

Fig. C19. Arc traces of degree of polarization about HD 37903.